MICROGELS FOR SINGLE-CELL CULTURING OF NEURONS AND CHONDROCYTES

by

Jacob Preston Fredrikson

A dissertation submitted in partial fulfillment
of the requirements for the degree

of

Doctor of Philosophy

in

Chemical Engineering

MONTANA STATE UNIVERSITY
Bozeman, Montana

May 2023

©COPYRIGHT

by

Jacob Preston Fredrikson

2023

All Rights Reserved

DEDICATION

I dedicate this dissertation to my incredible parents who have never wavered in their support.

ACKNOWLEDGEMENTS

I would like to acknowledge my advisor Dr. Connie Chang for her support and guidance. I would additionally like to thank the members of the Chang Lab who contributed to my work, while not all of you are listed contributors, all of you have helped in a major way. Thank you to Dr. Anja Kunze for access to your microscope and fantastic lab members. Thank you to the Center for Biofilm Engineering and Montana Nanotechnology Facility for access to equipment. Thank you to my committee for guidance and support throughout graduate school. Each of you contributed in so many ways to my work. Thank you to Luke Domanico and Dr. Emma Loveday for making me into a biologist of some sort. Thank you to all of my roommates and friends who helped to keep me sane and gave me an unforgettable experience in Bozeman. Finally, thank you to my wonderful wife for her love and support through everything.

This work was made possible by funding provided by the National Science Foundation, National Institute of Health, Montana State University Office of the Provost, Defense Advanced Research Projects Agency, Imaging and Chemical Analysis Laboratory (ICAL) at Montana State University, and the Center for Biofilm Engineering (CBE) at Montana State University. This work was performed in part at the Montana Nanotechnology Facility, a member of the National Nanotechnology Coordinated Infrastructure (NNCI), which is supported by the National Science Foundation (Grant# ECCS-2025391).

TABLE OF CONTENTS

1. INTRODUCTION 1

Introduction 1
Funding 4
Dissertation Overview 5
Works Cited 8

2. LITERATURE REVIEW 11

Microgels for Tissue Engineering 11
Microgels vs. Hydrogels 11
Composition and Structure of Microgels 13
Microgel Gelation and Fabrication Techniques 14
Incorporation of Cells with Microgels 16
Other Applications 17
Human Articular Cartilage Function, Organization, and Properties 17
Matrix-Assisted Chondrocyte Implantation (MACI) 21
Herpes Simplex Virus Type 1 24
Models for Studying HSV-1 27
Single Cell Virology Techniques 28
Works Cited 32

3. METABOLOMIC PROFILING AND MECHANOTRANSDUCTION OF SINGLE CHONDROCYTES ENCAPSULATED IN ALGINATE MICROGELS 37

Manuscript Contributions of Authors 37
Manuscript Information Page 38
Abstract 39
Introduction 40
Methods 43
Chondrocyte Harvest and Culture 43
PDMS Microfluidic Device Fabrication 43
Preparation of Precursor Solutions 44
Oil Preparation 44
Alginate Precursor Preparation (A) 44
Alginate Precursor Preparation (B) 45
Cell Encapsulation in Microgels 45
Cell Culture in Microgels 46

TABLE OF CONTENTS CONTINUED

Cell Viability Assay....46
Fluorescence Imaging and Analysis....46
Immunofluorescence Staining and Confocal Imaging....47
Monolayer Controls....47
Microgel-Encapsulated Chondrocytes....47
Encapsulation in High-Stiffness Agarose, Mechanical Stimulation, and Metabolite Extraction....48
Untargeted Metabolic Profiling....49
Rheology....50
Statistical Analysis....50
Results and Discussion....50
Chondrocyte Encapsulation in Alginate Microgels And Dynamic Compression Workflow....50
Immunofluorescence Staining of PCM Formation in Alginate Microgels....53
Immunofluorescence Staining of Pericellular Matrix Formation in Monolayers....54
Auto-Fluorescence of PCM Formation in Alginate Microgels....55
Chondrocyte Viability in Alginate Microgels....58
Elastic Moduli Characterization of Hydrogel Constructs....58
Metabolomic Profiling of Hydrogel Constructs Containing Compressed And Uncompressed Monolayer and Microgel Cells....58
Conclusions....66
Supplementary Materials....67
Author Contributions....68
Funding....68
Institutional Review Board Statement....68
Informed Consent Statement....69
Data Availability Statement....69
Acknowledgments....69
Works Cited....69

4. PERICELLULAR MATRIX FORMATION AND ATOMIC FORCE MICROSCOPY OF SINGLE PRIMARY HUMAN CHONDROCYTES CULTURED IN ALGINATE MICROGELS....74

Manuscript Contributions of Authors....74
Manuscript Information Page....75
Abstract....76
Introduction....77
Results....79

TABLE OF CONTENTS CONTINUED

Analysis of PCM Formation from Single PHCs Encapsulated Within Alginate Microgels 80
Elastic Moduli (*G'*) of Individual PHCs Released from Alginate Microgels and Measured Using AFM 85
Heterogeneous Outcomes of PCM Formation in Microgels 88
Discussion 92
Methods 94
Primary Human Chondrocyte Harvest and Cell Culture 94
SW1353 Cell Culture 95
PDMS Microfluidic Device Fabrication 95
AFM Well-Trap Fabrication 96
Preparation of Microfluidic and Microgel Reagents 96
Cell Encapsulation and Culture in Microgels 97
Autofluorescence Imaging and Analysis 97
Alginate Dissolution and Chondron Isolation 98
Immunofluorescence Staining and Imaging 98
Force Curve Acquisition and Analysis 99
Funding 100
Informed Consent Statement 100
Acknowledgments 100
Conflicts of Interest 101
Works Cited 101

5. DROPLET-BASED MICROFLUIDICS FOR SINGLE NEURON GROWTH AND INFECTION WITH HERPES SIMPLEX VIRUS – 1 105

Manuscript Contributions of Authors 105
Manuscript Information Page 106
Abstract 107
Introduction 108
Results 109
Single Cell Infection Outcomes of Vero Cells with HSV-1 OK15 112
Growth of Single Mouse Superior Cervical Ganglia Neurons in Microgels 115
Single-cell Infection of SCG Neurons 117
Timing and Outcomes of Viral Gene Expression in Individual SCG Neurons 117
Discussion 121
Methods 124
Vero Cell Culture 124
Mouse Superior Cervical Ganglia Neuron Dissociation 125
Herpes Simplex Virus-Type 1 OK15 Characterization and Productions 125

TABLE OF CONTENTS CONTINUED

Microfluidic Device Fabrication....125
Microgel Production and Cell Encapsulation/Seeding....126
Immunofluorescence Staining and Imaging....127
In-Drop Infection Procedures....127
End-Point Imaging of Inoculated Cells....129
Time-Lapse Imaging of Inoculated Cells....129
HSV-1 Diffusion with Matrigel Experiments....129
Data Analysis and Statistics....130
Percentage of YFP Positive Cells....130
Timing of YFP and RFP Detection....130
Works Cited....131

6. CONCLUSIONS AND OUTLOOK....134

Conclusions....134
Outlook....140
Works Cited....143

APPENDICES....145

Appendix A: Supplemental Information for Chapter 3: Metabolomic Profiling and Mechanotransduction of Single Chondrocytes Encapsulated in Alginate Microgels....146

Appendix B: Supplemental Information for Chapter 4: Pericellular Matrix Formation and Atomic Force Microscopy of Single Primary Human Chondrocytes Cultured In Alginate Microgels....163

Appendix C: Supplemental Information for Chapter 5: Droplet Based Microfluidics for Single Neuron Growth And Infection with Herpes Simplex Virus – 1....166

Appendix D: Granular Matrigel: Restructuring a Trusted Extracellular Matrix Material for Improved Permeability....170
Manuscript Contributions of Authors....170

TABLE OF CONTENTS CONTINUED

Manuscript Information Page 172
Abstract 173
Introduction 173
Materials and Methods 174
Microfluidic Device Fabrication 174
Fabrication of Matrigel Microgels 174
Two-Step Centrifugation of Matrigel Microgels 174
Microscopy Imaging 175
Structural Analysis of Granular Matrigel 175
Permeability Experiments 175
Cell migration Experiments 175
Organoid and DC Culture 175
Results and Discussion 176
Matrigel Microgels of Various Diameters 176
Porous Structure of Granular Matrigel 176
Improved Permeability of Granular Matrigel 177
Granular Matrigel Application for 3D Cell Culture Scaffold 179
Granular Matrigel for Co-Culture Model Applications 179
Conclusions 181
Acknowledgments 181
Conflict of Interest 181
Funding 181
References 182

REFERENCES CITED 184

LIST OF TABLES

Table Page

A.1. Elastic and Storage Moduli of Alginate and Agarose.....155

A.2. All Significant Metabolomic Pathways Found.....156

LIST OF FIGURES

Figure Page

2.1. 2-D versus 3-D Culture 12

2.2. Example Microgels 14

2.3. CLEX for Cell Encapsulation 16

2.4. Schematic of Human Articular Cartilage 19

2.5. Structure of PCM 20

2.6. The Classical Tissue Engineering Paradigm 23

2.7. HSV-1 Infection Cycle 25

2.8. HSV-1 Gene Expression Cycle 27

2.9. Single-Cell Virology Strategies 29

2.10. Workflow of a Drop-Based Viral Infectivity Assay 31

3.1. Experimental Workflow for Chondrocyte Mechanotransduction 52

3.2. SW1353 and PHC Collagen VI Staining 54

3.3. SW1353 Autofluorescence 56

3.4. Heatmaps of Top 25 Metabolites and 2-D Scores Plot of PCA Analysis 60

3.5. 2-D Scores and Volcano Plots 62

4.1. Experimental Workflow of PHC AFM 80

4.2. PHC Autofluorescence 82

4.3. PCH Microgel Collagen VI Staining 84

4.4. PHC AFM Graphs 87

LIST OF FIGURES CONTINUED

Figure Page

4.5. PHC *G'* Heterogeneity 90

5.1. Experimental Workflow for SCG Infection 111

5.2. In-Drop Vero Cell Infection 113

5.3. SCG Growth and In-Drop Infection 116

5.4. Timing of Viral Gene Expression from SCG Neurons Infected In-Drop 119

A.1. Supplemental SW1353 Autofluorescence Images 147

A.2. Elastic and Storage Moduli of Alginate and Agarose 148

A.3. Median Metabolites across All Experimental Groups 149

A.4. Median Metabolites across All Experimental Groups Clusters 1 and 2 150

A.5. Median Metabolites across All Experimental Groups Clusters 3 and 4 151

A.6. Median Metabolites across All Experimental Groups Clusters 5 and 6 152

A.7. Median Metabolites across All Experimental Groups Clusters 7 153

A.8. Venn Diagram of Significant Pathways for each Group 154

B.1. Supplemental PHC Autofluorescence Images 164

B.2. PHC and SW1353 Autofluorescence Comparison 164

B.3. *G'* versus CV Linear Regression for PHCs 165

C.1. Representative Images of Vero Cells Infected In-Drop on Microgels 167

LIST OF FIGURES CONTINUED

Figure Page

C.2. HSV-1 Diffusion in Matrigel 167

C.3. Representative Images of SCG Neuron Infected In-Drop on Microgels 168

C.4. Timing of Viral Gene Expression in Vero Cells 169

D.1. Matrigel Drop Making 177

D.2. Structure of Concentrated Matrigel Microgels 178

D.3. DC Migration through Granular Matrigel 179

D.4. Time-Lapse Microscopy of DC Migration Through Granular Matrigel 180

D.5. Granular Matrigel for Long-Term Organoid Culture 180

D.6. Granular Matrigel Organoid-Immune Cell Co-Culture 181

ABSTRACT

Tissue engineering is a multidisciplinary field that combines engineering and life sciences to restore, improve, or generate biological substitutes to replace damaged tissues or organs. This is often performed using hydrogels that serve as scaffolds for the growth and maintenance of target tissues. Hydrogels, crosslinked polymer networks composed primarily of water, are excellent tissue mimics with highly tunable mechanical and biochemical properties. Hydrogels can be fabricated at the microscale, termed microgels, using drop-based microfluidics, which enables the precise control of cell density within the microgels down to a single cell. Encapsulating cells in microgels allows for the manipulation of microgels after production for single cell analyses. In this dissertation, human articular cartilage (HAC) cells and neurons are cultured within and upon microgel particles that serve as microscale tissue models for the study of chondrocyte matrix production and Herpes Simplex Virus type -1 (HSV-1) infection studies.

HAC is the load-bearing tissue that lines the interfaces of joints and is responsible for shock and wear resistance. Chondrocytes, the cells in HAC, are responsible for producing and maintaining HAC The chondrocyte pericellular matrix (PCM) regulates the metabolism and mechanical strain of the cells, which is critical to cellular function and cartilage homeostasis However, the PCM is challenging to produce *in vitro*. The first half of this work applies microgels for PCM formation in chondrocytes. Immunofluorescence and high-performance liquid chromatography-mass spectrometry data demonstrate that chondrocytes grown in alginate microgels form a collagen VI-rich PCM, significantly altering the cells' metabolic response to dynamic compression. Atomic force microscopy data demonstrates that when chondrocytes are grown in alginate microgels for ten days, the elastic modulus of the PCM increases an order of magnitude.

HSV-1 is a human pathogen that invades the peripheral nervous system. Understanding the complexities of HSV-1 infection at the single-cell level could lead to better therapeutics and reduced disease outcomes. Drop-based microfluidics (DBM) has recently been adapted for studying single-cell viral infection but has not been applied to neurons and HSV-1. The second half of this work develops a method for growing individual neurons in microgels. These microgel-embedded neurons are isolated, encapsulated with precise inoculating doses of HSV-1 using DBM, and the kinetics of viral gene expression are tracked in individual neurons using a fluorescent-recombinant HSV-1 virus. The data demonstrate that microgels provide a solid scaffold for neuronal development that supports single-cell productive HSV-1 infection within droplets.

CHAPTER ONE

INTRODUCTION

Introduction

Tissue engineering is an interdisciplinary field that focuses on generating and restoring bodily tissues by applying engineering and life sciences [1–3]. Initially, tissue engineering began with the primary goal of restoring bodily function to patients; however, the field has expanded to include developing ex vivo tissues for applications such as translational science and drug discovery [2,3]. Tissue engineering techniques typically rely on combining target tissue cells, biomolecules, and a scaffold to create cell-laden constructs in vitro [2,3]. The choice of scaffold is critical to creating healthy tissue.

Common scaffolds used in tissue engineering are hydrogels which are swollen, cross-linked polymer networks composed primarily of water and excellent extracellular matrix (ECM) tissue mimics [2–4]. The mechanical and biochemical properties of the hydrogels can be tuned by changing the polymer composition, gelation method, and various other factors to best mimic the desired ECM [4]. However, the millimeter and centimeter scale hydrogels termed 'bulk' hydrogels in this work, typically used in tissue engineering applications, have several downsides, such as difficulties controlling cell density, manipulating individual cells, or creating multi-functional materials [5,6]. In addition, cells cultured in these bulk hydrogels may also suffer from diffusion limitations as cells may be located centimeters away from the nutrient source [5,6].

A solution to these downsides is to reduce the length scale of the bulk hydrogels to the microscale, producing particles termed 'microgels'. Microgels typically have the same biochemical and mechanical properties as their bulk analogs yet also have favorable transport characteristics for tissue engineering due to the high surface area to volume ratio and comparatively small length scale [5,6]. Additionally, microgels often function as individual cell units in which single cells are either encapsulated or seeded onto the microgels allowing for the facile transfer of individual cells between growth environments through the washing and manipulation of the microgels [5,6]. These combined factors make microgels ideal growth environments for many cell types. This thesis presents work focusing on developing microgels for single-cell biological assays and tissue engineering. This work applies microgels to two fields of tissue engineering: Human articular cartilage and neural tissue engineering.

First, this thesis explores the engineering of human articular cartilage (HAC). HAC is the soft load-bearing tissue that lines the interfaces of joints and is responsible for friction reduction and wear resistance from everyday activities such as walking, running, and jumping [7]. The functionality of HAC stems from the unique cellular and bio-mechanical composition of the matrix which makes up the cartilage. The HAC is primarily composed of chondrocytes, the extracellular matrix (ECM), the pericellular matrix (PCM), and other minor matrix regions, such as the territorial cellular matrix. The cartilage is primarily composed of the ECM, a hydrated matrix of collagen and proteoglycans with significant zonal variations in biomechanical properties due to the orientation of the collagen networks in each zone [7,8]. The PCM is primarily composed of type-VI collagen and closely encapsulates the chondrocytes in the cartilage, providing a uniform strain environment for the cells throughout the zonal variations in

the ECM [9,10]. The functionality of articular cartilage stems from the unique bio-mechanical composition of the cells and matrix which makes up the cartilage. After acute injuries to articular cartilage or during diseases such as osteoarthritis, the ECM and PCM of the cartilage begin to break down, causing pain and loss of joint function [11,12]. Due to the low cell density, avascular nature, and many other factors, HAC is limited in its ability for self-repair [13,14].

The first half of this thesis specifically focuses on methods for developing and studying HAC *in vitro*. Conventional methods for culturing chondrocytes rely on tissue culture plastic to expand and grow cells. However, when cultured on tissue culture plastic, chondrocytes quickly dedifferentiate and lose their ability to produce cartilage [15–20]. When grown in 3-D hydrogels such as alginate and agarose, chondrocytes have been shown to retain their chondrocyte phenotypes or even differentiate back into chondrocytes after monolayer culture [14,21,22]. However, the large hydrogels typically used are poorly suited for tissue engineering and in vitro studies of cartilage due to their large length scale making it difficult to manipulate cells [5,6]. Here we apply microgels as an alternative to monolayer and bulk culturing methods of chondrocytes. This thesis will focus on the PCM formed during microgel culture, its chemical and mechanical composition, and the PCM's effect on the chondrocytes' metabolic response to mechanical stimulation.

Second, this thesis explores the engineering of neural tissue models for herpes simplex virus-1 (HSV-1) studies. HSV-1 is a prevalent human pathogen, infecting 70% of the global adult population and causing recurrent orofacial herpetic lesions and, in severe cases, morbid encephalopathies [23]. Infections begin in the orofacial epithelia, where it then invades the peripheral nervous system (PNS). Disease pathologies arise in the PNS, and the infected neurons

harbor HSV-1 for the host's lifetime. Notably, the neuroinvasion of HSV-1 enables the evasion of sterilizing immunity and complicates the implementation of antiviral therapeutics. A further understanding of the complexities of HSV-1 infection of the nervous system could lead to better therapeutics and a reduction in disease outcomes and neuropathologies.

The second half of this thesis specifically focuses on methods for growing isolated neurons for studying single-cell HSV-1 infections. Current methods for studying HSV-1 in vitro rely on traditional biological techniques where cells are cultured and infected in a well-plate, enabling spread of infection between neighboring cells [24–27]. These population-level infection approaches may obscure the heterogeneous dynamics of neuronal infection that may not be observed using well-plate methods. Growing and infecting single neurons eliminates the confounding effects of mixed infection dynamics in a population of cells. However, there are minimal methods for culturing isolated neurons, and the throughput of these methods is limited. Further, these cells are often grown in well plates where the cells cannot be transferred between environments [28,29]. Here, we use microgels as a novel method to culture and manipulate individual neurons. This thesis will focus on the maturation and HSV-1 infection dynamics of single neurons grown in microgels.

In summary, this thesis explores applying microgels for *in vitro* pericellular matrix formation in human primary chondrocytes and the study of HSV-1 infection dynamics in single neurons.

Funding

This research was funded by the Montana State University Office of the Provost, the National Science Foundations (NSF) Career grants 1753352 and 1554708, the National Institutes of

Health (NIH) grants R01AR073964 and U01 EB029242, and the Defense Advanced Research Projects Agency (DARPA) grant W911NF-17-2-0034. The research was conducted at Montana State University (MSU) (Montana, USA), the Imaging and Chemical Analysis Laboratory (ICAL) at Montana State University (Montana, USA), and the Center for Biofilm Engineering (CBE) at Montana State University (Montana, USA).

Dissertation Overview

The remainder of this thesis is organized into six chapters; Chapter 2 consists of a literature review providing background information and a summary of topics covered in this thesis.

Chapter 3 describes a drop-based microfluidics approach to culture single SW1353 chondrocytes in alginate microgels for cell-directed PCM synthesis, closely mimicking the *in vivo* microenvironment. Throughout the study, the effects of microgels as a growth environment and the effects of ascorbic acid on matrix formation were investigated. We found that chondrocytes formed PCM over 10 days in these single-cell 3-D microenvironments. This PCM was visualized using epifluorescence imaging of matrix auto-fluorescence and confocal imaging of immuno-chemistry-stained collagen VI. In addition, mechanotransduction studies were performed, in which single-cell microgels mimicking the cartilage PCM were embedded in high-stiffness agarose. Finally, physiological dynamic compression was applied to the cells in a custom-built bioreactor, and metabolites were extracted and analyzed using High-performance liquid chromatography-mass spectrometry (HPLC-MS). We found that microgels exhibited distinct metabolomic profiles from uncompressed and monolayer controls. These studies will impact future work in chondrocyte tissue engineering and dynamic compression studies. This

work was published in the journal *Cells*, on March 5th, 2022, and is titled "*Metabolomic Profiling and Mechanotransduction of Single Chondrocytes Encapsulated in Alginate Microgels*".

Chapter 4 describes a method for growing pericellular matrix from primary human chondrocytes (PHCs) *in vitro* and analyzing its mechanical properties. In this study, PHCs were encapsulated and grown in alginate microgels using drop-based microfluidics. PCM formation was analyzed using epifluorescence imaging of matrix auto-fluorescence and immuno-chemistry-stained collagen VI. When grown in alginate microgels, we found that PHCs form a robust, collagen VI-rich PCM. Compared to the SW1353 cells in chapter 3, the auto-fluorescence single of the PHC increased ~5 times faster. The mechanical properties of the *in vitro* formed PCM were measured over time using atomic force microscopy. We found that the elastic modulus (G') of the chondrons, the PCM – chondrocyte constructs, increased an order of magnitude over 10 days in culture, nearly reaching the elastic modulus of in *vivo* PHCs. We also found two distinct populations of chondrocytes; one whose elastic modulus did not change from day 1 and one whose drastically increased over 10 days in culture. This work will impact future work in chondrocyte tissue engineering and regenerative medicine. The title of this work is "*Pericellular Matrix Formation and Atomic Force Microscopy of Single Primary Human Chondrocytes* ".

Chapter 5 describes a drop-based microfluidics approach for culturing and infecting single mouse primary superior cervical ganglia (SCG) neurons with herpes simplex virus-1 (HSV-1). In this study, we developed a method for growing individual neurons in microgels where DBM allows for precise control over cell density to achieve one neuron per microgel.

These Matrigel-embedded neurons were encapsulated with a precise inoculating dose of HSV-1 using DBM. Using a fluorescent-recombinant HSV-1 virus, we tracked the kinetics of viral gene expression across increasing inoculating doses in individual neurons. Our data demonstrate that the microgels provide a solid surface for neuronal growth and development that supports single-cell productive HSV-1 infection within droplets. First, Vero cells are used as a model cell line for HSV-1 infection in microgels. The effects of cell location on the likelihood of infection are studied, and it was found that HSV-1 cannot diffuse through Matrigel; therefore, the cell must be exposed to the surface of the gel for HSV-1 infection to occur. SCG neurons are then grown and matured in microgels for seven days and stained for phosphorylated neurofilament H to show that the neurons are mature. Neurons are then individually infected with HSV-1 OK15 in drops, where we use time-lapse epifluorescence microscopy to track the progression of viral gene expression. We find that neurons expressed viral genes earlier and were far likelier to successfully proceed to late-gene expression when the inoculating dose was highest. This work will impact single-cell virology and neuronal tissue engineering. The title of this work is "*Droplet-Based Microfluidics for Single Neuron Growth and Infection with Herpes Simplex Virus – 1* ".

Chapter 6 concludes this thesis. The chapter will discuss future outlooks and the greater impacts of this research.

Appendices A-C provide supplemental information for the manuscripts in Chapters 3-5. Appendix D contain additional work completed during this Ph.D. not included in the manuscripts in Chapters 3-5. Additional works include the publication "*Granular Matrigel: restructuring a*

trusted extracellular matrix material for improved permeability" by Mahdieh et al. and published in the peer-reviewed journal Biomedical Materials Volume 17 article number 4.

Works Cited

1. Vacanti JP, Langer R. Tissue engineering: the design and fabrication of living replacement devices for surgical reconstruction and transplantation. Lancet. 1999;354 Suppl 1: SI32-4.

2. Gaharwar AK, Singh I, Khademhosseini A. Engineered biomaterials for in situ tissue regeneration. Nature Reviews Materials. 2020;5: 686–705.

3. Esdaille CJ, Washington KS, Laurencin CT. Regenerative engineering: a review of recent advances and future directions. Regen Med. 2021;16: 495–512.

4. Caliari SR, Burdick JA. A practical guide to hydrogels for cell culture. Nat Methods. 2016;13: 405–414.

5. Xu Y, Zhu H, Denduluri A, Ou Y, Erkamp NA, Qi R, et al. Recent Advances in Microgels: From Biomolecules to Functionality. Small. 2022;18: e2200180.

6. Caldwell AS, Aguado BA, Anseth KS. Designing Microgels for Cell Culture and Controlled Assembly of Tissue Microenvironments. Adv Funct Mater. 2020;30. doi:10.1002/adfm.201907670

7. Muir H. The chondrocyte, architect of cartilage. Biomechanics, structure, function and molecular biology of cartilage matrix macromolecules. Bioessays. 1995;17: 1039–1048.

8. Eschweiler J, Horn N, Rath B, Betsch M, Baroncini A, Tingart M, et al. The Biomechanics of Cartilage-An Overview. Life. 2021;11. doi:10.3390/life11040302

9. Wilusz RE, Sanchez-Adams J, Guilak F. The structure and function of the pericellular matrix of articular cartilage. Matrix Biol. 2014;39: 25–32.

10. Zhang Z. Chondrons and the pericellular matrix of chondrocytes. Tissue Eng Part B Rev. 2015;21: 267–277.

11. Alexopoulos LG, Haider MA, Vail TP, Guilak F. Alterations in the mechanical properties of the human chondrocyte pericellular matrix with osteoarthritis. J Biomech Eng. 2003;125: 323–333.

12. Danalache M, Kleinert R, Schneider J, Erler AL, Schwitalle M, Riester R, et al. Changes in stiffness and biochemical composition of the pericellular matrix as a function of spatial chondrocyte organisation in osteoarthritic cartilage. Osteoarthritis Cartilage. 2019;27: 823–832.

13. Jacobi M, Villa V, Magnussen RA, Neyret P. MACI - a new era? Sports Med Arthrosc Rehabil Ther Technol. 2011;3: 10.

14. Huang BJ, Hu JC, Athanasiou KA. Cell-based tissue engineering strategies used in the clinical repair of articular cartilage. Biomaterials. 2016;98: 1–22.

15. Ghosh S, Scott AK, Seelbinder B, Barthold JE, Martin BMS, Kaonis S, et al. Dedifferentiation alters chondrocyte nuclear mechanics during in vitro culture and expansion. Biophys J. 2022;121: 131–141.

16. von der Mark K, Gauss V, von der Mark H, Müller P. Relationship between cell shape and type of collagen synthesised as chondrocytes lose their cartilage phenotype in culture. Nature. 1977;267: 531–532.

17. Darling EM, Athanasiou KA. Rapid phenotypic changes in passaged articular chondrocyte subpopulations. J Orthop Res. 2005;23: 425–432.

18. Benya PD, Padilla SR, Nimni ME. Independent regulation of collagen types by chondrocytes during the loss of differentiated function in culture. Cell. 1978;15: 1313–1321.

19. Mayne R, Vail MS, Mayne PM, Miller EJ. Changes in type of collagen synthesized as clones of chick chondrocytes grow and eventually lose division capacity. Proc Natl Acad Sci U S A. 1976;73: 1674–1678.

20. Costa E, González-García C, Gómez Ribelles JL, Salmerón-Sánchez M. Maintenance of chondrocyte phenotype during expansion on PLLA microtopographies. J Tissue Eng. 2018;9: 2041731418789829.

21. Jeon JE, Schrobback K, Meinert C, Sramek V, Hutmacher DW, Klein TJ. Effect of preculture and loading on expression of matrix molecules, matrix metalloproteinases, and cytokines by expanded osteoarthritic chondrocytes. Arthritis Rheum. 2013;65: 2356–2367.

22. Amr M, Mallah A, Yasmeen S, Van Wie B, Gozen A, Mendenhall J, et al. From Chondrocytes to Chondrons, Maintenance of Phenotype and Matrix Production in a Composite 3D Hydrogel Scaffold. Gels. 2022;8. doi:10.3390/gels8020090

23. Duarte LF, Farías MA, Álvarez DM, Bueno SM, Riedel CA, González PA. Herpes Simplex Virus Type 1 Infection of the Central Nervous System: Insights Into Proposed Interrelationships With Neurodegenerative Disorders. Front Cell Neurosci. 2019;13. doi:10.3389/fncel.2019.00046

24. Liu W, He H, Zheng S-Y. Microfluidics in Single-Cell Virology: Technologies and Applications. Trends Biotechnol. 2020;38: 1360–1372.

25. Loveday EK, Zath GK, Bikos DA, Jay ZJ, Chang CB. Screening of Additive Formulations Enables Off-Chip Drop Reverse Transcription Quantitative Polymerase Chain Reaction of Single Influenza A Virus Genomes. Anal Chem. 2021;93: 4365–4373.

26. Drayman N, Patel P, Vistain L, Tay S. HSV-1 single-cell analysis reveals the activation of anti-viral and developmental programs in distinct sub-populations. Elife. 2019;8. doi:10.7554/eLife.46339

27. Wilson AC. Impact of Cultured Neuron Models on α-Herpesvirus Latency Research. Viruses. 2022;14. doi:10.3390/v14061209

28. Tierney WM, Vicino IA, Sun SY, Chiu W, Engel EA, Taylor MP, et al. Methods and Applications of Campenot Trichamber Neuronal Cultures for the Study of Neuroinvasive Viruses. Methods Mol Biol. 2022;2431: 181–206.

29. Shipley MM, Mangold CA, Kuny CV, Szpara ML. Differentiated Human SH-SY5Y Cells Provide a Reductionist Model of Herpes Simplex Virus 1 Neurotropism. J Virol. 2017;91. doi:10.1128/JVI.00958-17

CHAPTER TWO

LITERATURE REVIEW

Microgels for Tissue Engineering

Microgels vs. Hydrogels

Microgel is the broad term for all hydrogels of the microscale, single to hundreds of microns. Microgels have been developed for many applications, ranging from robotics to cosmetics and food processing [1–3]. However, this work focuses on applying microgels to bio-, biomedical-, and tissue engineering.

Microgels, like mm to cm scale hydrogels, termed 'bulk' hydrogels in this work, are excellent 3-D tissue mimics [1,3,4]. Many elements of the in vivo extracellular matrix can be recapitulated in hydrogels [1,3–5]. Hydrogels possess mechanical properties similar to most in vivo tissues and support cell adhesion and protein sequestration [1,3,4]. Compared to 2-D systems such as petri dishes, culturing cells in 3-D promotes cell morphologies and polarization, which resemble physiological cells (Figure 2.1)[4]. Primary cells grown in 2-D also tend to lose differentiated phenotypes, whereas cells grown in 3-D maintain or even regain differentiated phenotypes [4,6–8].

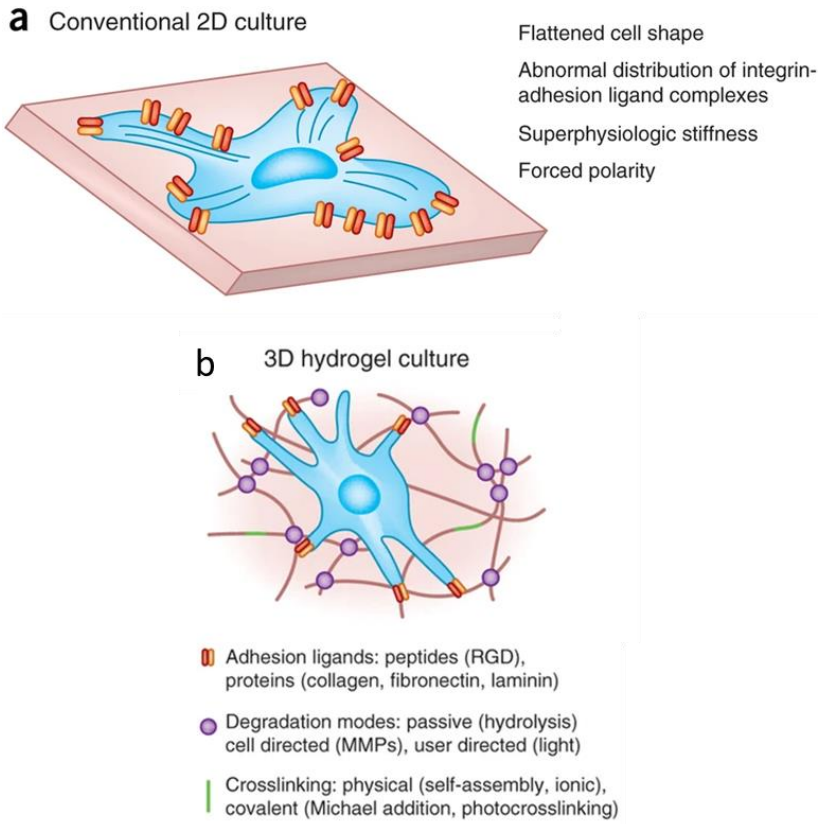


Figure 2.1: (a) Conventional 2D culture on superphysiologically stiff plastic or glass substrates leads to cells displaying aberrant phenotypes. (b) 3D hydrogels can be engineered to present a more realistic microenvironment to cells. Hydrogel design variables are indicated. Adapted from Ref. 4 with permission from the Journal [4]

However, microgels offer several advantages compared to bulk hydrogels: 1) Cells can be encapsulated in microgels at precise cell densities. Each microgel acts as an individual cell unit that can be manipulated or assayed at the single-cell level [1,3]. 2) Reducing the length scale of the hydrogels from the mm/cm scale to the microscale decreases the length scale and increases the surface-to-volume ratio of the hydrogels [1,3]. This small length scale decreases diffusion lengths and facilitates the delivery of nutrients and other bio-active compounds to the encapsulated cells [1,3]. Microgels can be assembled through various techniques to create porous

structures with similar size and cell density to bulk hydrogels but are far more permeable to nutrient diffusion [1,3]. 3) Microgels can be produced in a high throughput manner to create hundreds of thousands to millions of particles in seconds [1,3,9]. 4) Microgels are more easily injectable than their bulk analogs due to their collective shear-thinning behavior, making them favorable for bio-inks and tissue engineering [1,3] .

Composition and Structure of Microgels

'Microgel' comprises a broad range of microscale hydrogels which can be further broken down into more specific categories. In regards to composition, microgels are either homogenous or heterogeneous (Figure 2.2) [1]. Homogeneous microgels are chemically uniform throughout the volume of the microgels and are often composed of one single polymer type (Figure 2.2). However, the shape of the microgels can vary, with spherical and rod-shaped microgels being the most common structures (Figure 2.2) [1]. Conversely, Heterogeneous microgels do not have uniform compositions throughout the gel and are often composed of multiple polymer types [1]. Examples of heterogeneous microgels include core-shell, multicore, and janus particles (Figure 2.2) [1]. Homogenous and heterogeneous microgels both have advantages over the other, depending on the application. For example, Homogeneous spherical microgels are beneficial in applications where uniform cell culture is desired. In contrast, janus particles can benefit applications where coculture of two different cell types is desired.

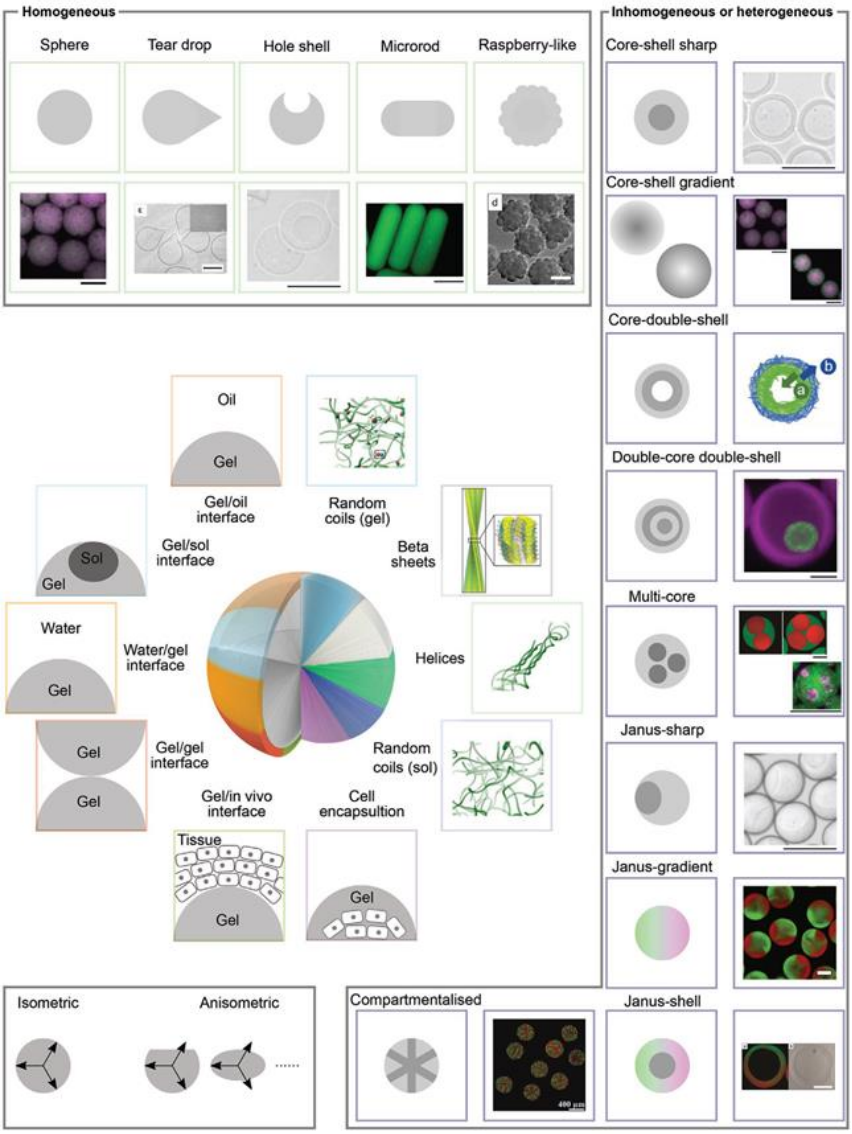


Figure 2.2: Microgels with different morphologies or structures, such as spheres, tear-drop, hole–shell, core–shell, Janus, compartmentalized, rod, and raspberry-like shapes. Scale bars = 200 μm (tear-drop), 500 μm (microrod), 0.3 μm (submicron, raspberry-like), 400 μm (compartmentalized), and 100 μm (all other). The microgel/environment interfaces can include gel/oil, gel/sol, gel/water, gel/gel, and gel/ tissue interfaces. The internal structures of the building blocks can be random coils, alpha helices, beta sheets, etc. [1]

Microgel Gelation and Fabrication Techniques

The type of microgels and the crosslinking chemistry used are subject to the desired application and fabrication technique. Similar to their bulk analogs, microgels can be produced

from synthetic or natural polymers with various gelation methods [1]. The type of polymer used depends on the application; for example, collagen and gelatin-based microgels have been shown to maintain the multipotency of mesenchymal stem cells, whereas agarose has been shown to bias mesenchymal stem cells towards chondrogenic differentiation [1]. The gelation technique is often chosen for cell viability and compatibility with the fabrication technique. For example, ultraviolet-light-based gelation mechanisms have been shown to decrease viability of exposed cells [1]. Common methods for microgel gelation include UV-light, thermal, and ionic gelation [1,3]. Again, the fabrication method for microgels is highly dependent on the application. Electrospraying, for example, produces large volumes of microgels but with heterogeneous size distributions [1]. Alternatively, drop-based microfluidics (DBM) generates microgels of more uniform size but is limited in volumetric throughput (Figure 2.3) [1,3]. Common methods for microgel fabrication include DBM, electrospraying, vortexing emulsions, micropatterning, and ink-jet printing analogous methods [1,3]. Heterogeneous microgels are most commonly produced with DBM as the method allows for the precise manipulation of the different polymer compositions [1].

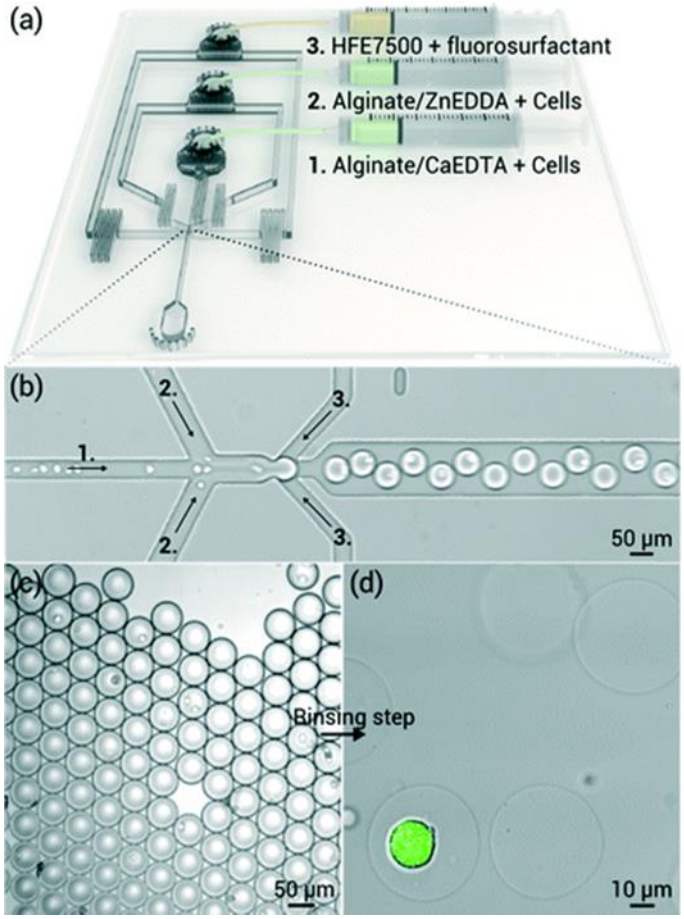


Figure 2.3: A droplet-based microfluidic device was used for encapsulation of cells in alginate microbeads with a new cell friendly and device compatible gelling mechanism. (a) A schematic of the microfluidic coflow device. (b) Micrograph of the region of the device at which the encapsulation of cells occurs. (c) Micrograph of collected microgels suspended in the carrier oil with fluorosurfactant. (d) Confocal image of encapsulated pre-osteoblast cells in microgels after rinsing and resuspending in cell medium to remove the oil and surfactant. Adapted from Ref. 9 with permission from the Journal [9]

Incorporation of Cells with Microgels

Cells can be incorporated either in or on microgels. Microgels are grown within microgels by suspending the cells in the precursor solutions before microgel formation, while cells are added after microgel formation to be grown on the microgels [1,3,9,10]. At this point,

many cell types have been cultured using microgels. A non-comprehensive list includes hepatocytes, fibroblasts, cancer cell lines, osteocytes, chondrocytes, mesenchymal stem cells, induced pluripotent stem cells, and embryonic stem cells [1,3,9,10]. In addition, cell aggregates such as stem cell spheroids, neurospheres, and organoids have been cultured in microgels [1,3,9,10].

Other Applications

Within bioengineering, microgels have more applications than described here. Microgels can also be used in additive manufacturing, gene delivery, drug delivery, and various other applications [1–3]. Microgels serve as promising bio-inks in 3-D printing applications, improving permeability and printability of otherwise viscous materials. Microgels are integral to single-cell sequencing techniques such as InDrops and Drop-seq [1]. Finally, microgels can be designed to degrade with time, temperature, or light, allowing for the controlled release of drugs in medications [1,3].

Human Articular Cartilage Function, Organization, and Properties

Human articular cartilage (HAC) is the soft load-bearing tissue that lines the interface diarthrodial of joints. In diarthrodial joints, the ends of adjoining bones are covered with a thin cartilaginous sheet and joined by a joint capsule called the synovial capsule. The primary function of HAC is to provide a smooth, nearly frictionless surface for joint articulation [11–13]. HAC is a specialized form of cartilage called hyaline cartilage which differs from fibrocartilage and elastic cartilage in composition and mechanical properties [11–13]. Hyaline cartilage in HAC can be considered a biphasic medium containing a fluid and solid phase exhibiting

viscoelastic behavior [11]. The fluid phase, which makes up ~80% of the weight of the cartilage, is composed primarily of water [11–13]. The solid phase comprises the remainder of the weight and is a porous, permeable network of collagen and proteoglycans [11–13]. Much of the functionality of HAC stems from the unique biomechanical composition of this solid phase which is made of two main components: chondrocytes, the cells responsible for maintaining and producing HAC, and the collagen-proteoglycan extracellular matrix (ECM), which is responsible for the unique mechanical function of HAC [11–13].

HAC is typically 2-4 mm thick and generally organized into four zones within its depths: the superficial, middle, deep, and calcified zones [11–13]. Each zone has unique biomechanical properties and collagen organization (Figure 2.4). The cartilage's superficial zone has collagen fibers aligned parallel to the surface of the cartilage and is responsible for most of the resistance to sheer in HAC [11–13]. The collagen fibers in the deep zone of the cartilage are primarily aligned perpendicular to the surface and are responsible for most of the resistance to compressive forces in HAC [11–13]. The middle zone acts as bridging material between the superficial and deep zones, whereas the calcified zone anchors the cartilage to the subchondral bone [11–13].

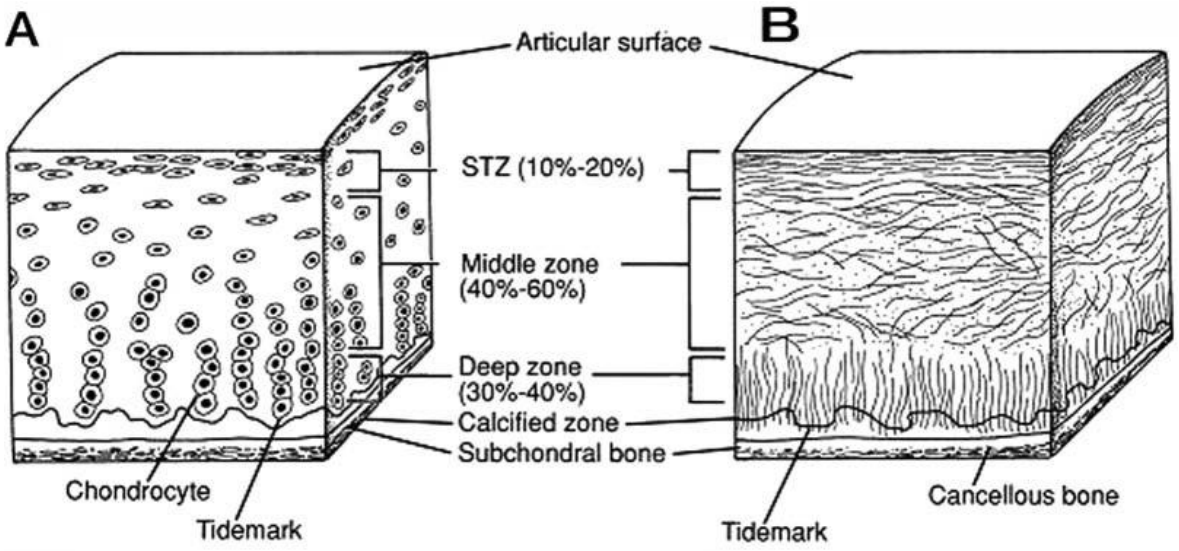


Figure 2.4: Schematic, cross-sectional diagram of healthy articular cartilage: A, cellular organization in the zones of articular cartilage; B, collagen fiber architecture. Adapted from Ref. 12 with permission from the Journal [12]

The chondrocytes in each cartilage zone vary in density, shape, and organization [14–16]. The chondrocytes in each zone are responsible for maintaining the cartilage in their immediate vicinity and thus produce different amounts and types of matrix depending on the zone of the cartilage [17,18]. Additionally, the chondrocytes are typically immobile within the cartilage and have limited cell-to-cell communication [11].

HAC is organized into four zones along its depths but is additionally organized in several distinct regions based on the proximity to the chondrocytes. The two major regions are the extracellular matrix (ECM) and the pericellular matrix (PCM), while other minor matrix regions, such as the territorial matrix, exist (Figure 2.5) . The ECM makes up the majority of the cartilage and is responsible for its mechanical properties. The PCM makes up a small percentage of the cartilage but closely surrounds each chondrocyte in a cocoon-like manner. The PCM is thought

to provide a uniform strain environment for chondrocytes across regions of mechanical diversity in the cartilage [15,16]. It additionally functions as a regulator of biochemical cues to the cells [15,16]. In total, the PCM is thought to influence chondrocyte metabolism and cartilage homeostasis [15,16].

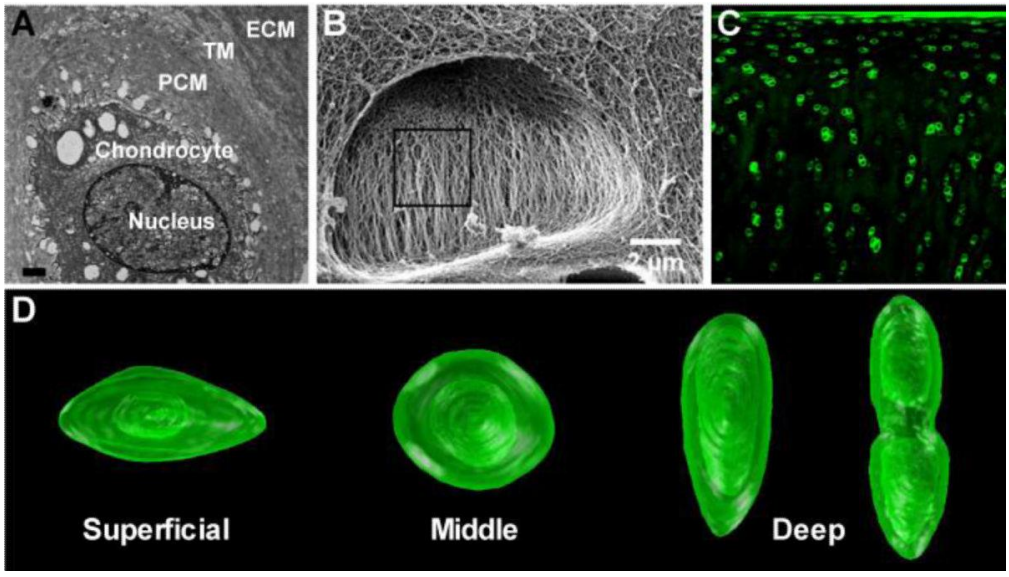


Figure 2.5: Structure and morphology of the PCM. (A) Transmission electron microscopy (TEM) showing the chondrocyte within the pericellular, territorial, and extracellular matrices (scale bar = 1 μm). (B) Helium ion microscopy of a cell void within a cross-section of articular cartilage showing the basket-like morphology of the collagen in the pericellular matrix. (C) Immunohistochemistry for type VI collagen in the full thickness of articular cartilage. (D) Three-dimensional reconstruction of articular cartilage chondrons defined by type VI collagen. Adapted from Ref. 15 with permission from the Journal [15]

The PCM is defined by the exclusive presence of collagen VI, a vital protein stabilizing chondrocyte phenotypes and critical for chondrocyte viability [15,16,19]. In chondrocytes that have dedifferentiated, the expression of collagen VI is greatly diminished but restored after redifferentiation [15,16,19]. The mechanical properties of the PCM are primarily influenced by collagen VI and perlecan, with typical in vivo PCM possessing elastic moduli ranging from 25 to

205 kPa, two orders of magnitude stiffer than the chondrocytes but an order of magnitude lower than the surrounding ECM [13,15,16,18–23].

HAC is an avascular material with low cell density which dramatically limits its ability for self-repair [24,25]. Injuries to the cartilage often are followed by the surrounding healthy cartilage deteriorating due to increased stresses, further exacerbating the injuries [24,25]. In osteoarthritis (OA), the ECM and PCM further break down increasing stresses on the chondrocytes [13,20]. Researchers have turned to tissue engineering to combat cartilage injuries and OA. Engineering cartilage poses many challenges, as cartilage production cannot be accomplished using traditional tissue culture methods [25]. When grown on tissue culture plastic, chondrocytes quickly dedifferentiate into osteocytes and fibroblasts, thus losing their ability to produce cartilage [6,7,18,26–28]. Hydrogel culture has been shown to help retain chondrocyte phenotypes and even redifferentiate cells back into chondrocytes [8,25,29]. When cultured in hydrogels, bovine chondrocytes were seen to begin PCM formation within 1 week and, in 6-12 weeks, began showing healthy cartilage formation [10,15,23]. Ng et al. showed that when cultured in bulk alginate gels, the PCM produced by bovine chondrocytes had an elastic modulus of 4.15 kPa after 28 days in culture [23].

Matrix-Assisted Chondrocyte Implantation (MACI)

Injuries to human artificial cartilage (HAC) have limited ability for self-repair due to the lack of vascularization and the lack of cells available to regenerate the wounded cartilage [24,25]. Following injury surrounding cartilage further deteriorates, exacerbating stresses and accelerating the degradation process [24,25]. Eventually, this deterioration leads to clinical osteoarthritis (OA). Treatment options are limited, with techniques such as microfracture and

abrasion therapy often used for minor cartilage defects [24–26]. However, these techniques are limited in their ability to regenerate large chondral defects [24–26]. They often form fibrocartilage which has limited resistance to sheer forces and is mechanically inferior to hyaline cartilage [24–26]. Autologous chondrocyte implantation (ACI) and the next-generation treatment matrix-assisted chondrocyte implantation (MACI) offers an alternative method to repair cartilage defects [24–26]. MACI has shown highly positive short-term results 3-5 years after surgery [24–29]. Information regarding long-term results 10+ years after surgery is limited but promising [28].

MACI is generally a three-step procedure (Figure 2.6). In MACI, a surgeon removes a small portion of healthy cartilage weighing approximately 300 mg from a non-weight-bearing region of the knee from the patient [24,25,27,29]. The chondrocytes are isolated through enzymatic digestion of the cartilage, which yields approximately 300,000 cells [27,29]. The cells are then cultured on tissue culture plastic for 3-6 weeks to expand the number of available chondrocytes [27,29]. After culture, the chondrocytes are incorporated into a type-I/III collagen membrane [24,25,27,29]. The surgeon then places the membrane over the chondral defect and seals the wound with fibrin glue [24,25,27,29]. The seeding of the chondrocytes onto the membrane has been seen to be advantageous over injecting suspended chondrocytes beneath the flap [27,29]. Injecting suspended cells has been seen to result in uneven cell distribution and cell leakage [27,29].

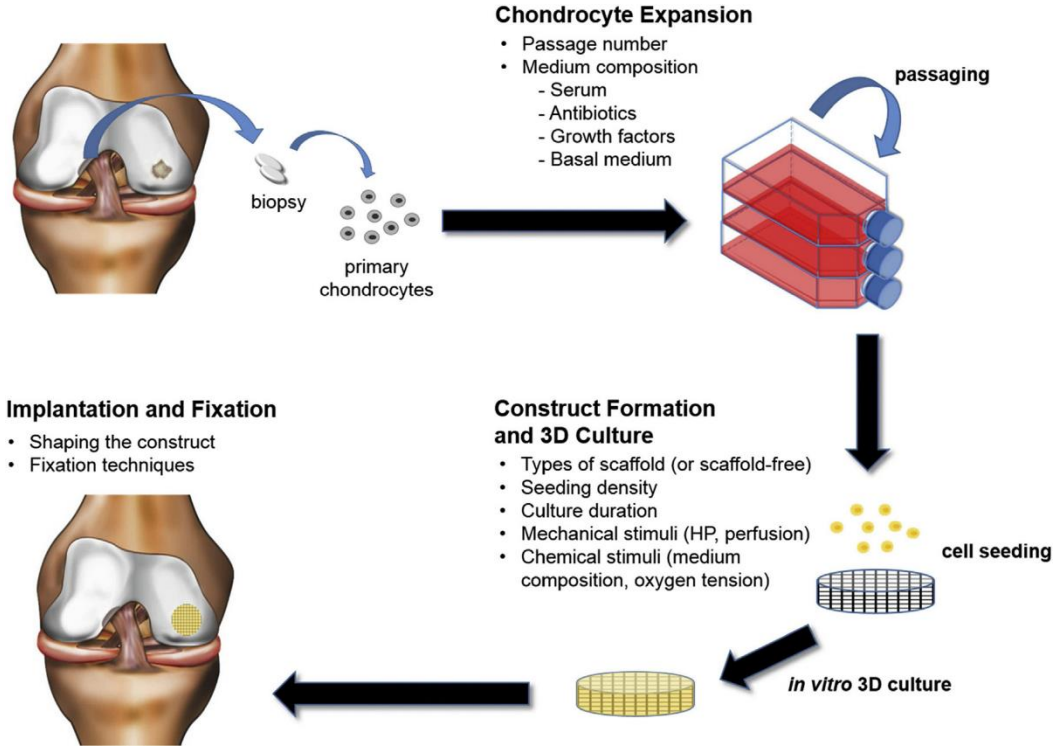


Figure 2.6: The classical tissue engineering paradigm used for the fabrication of the reviewed cartilage products. Various factors can be manipulated in each stage, as listed. Adapted from Ref. 25 with permission from the Journal [25]

Post-surgery recovery follows three phases. Over the first 6 weeks post-surgery, cells proliferate and adhere to the subchondral bone [27,29]. During this period, patients are greatly restricted in the weight bearing and movement they can sustain to not damage the unprotected chondrocytes. During the next 4-6 months, the cells begin releasing matrix components producing a putty-like tissue that allows patients to begin some weight bearing [27,29]. The final stage of recovery begins in the next 6-12 months, where the cartilage progressively hardens and gains characteristics similar to the surrounding healthy cartilage [27,29]. While most patients can return to regular activity at this point, this may take up to three years in some patients [27,29].

While MACI has shown promising results in most patients, the technique has a few weaknesses. First, the expansion process for the harvested chondrocytes is done on tissue culture plastic, where chondrocytes have been shown to differentiate into osteocytes and fibroblasts, which cannot produce hyaline cartilage [6,7,18,26–28]. Secondly, the need for the cells to adhere to the collagen membrane and the subchondral bone forces recovery to rely on cellular migration for the cells to regain their spatial organization in the various cartilage zones [11,17,24,27,29,33,34]. Finally, recovery times and, specifically, the time a patient must remain non-weight bearing are long [24,28,29]. This extended recovery is partially due to the chondrocyte being implanted without a surrounding matrix which may protect them from impact forces [16,19,20,24,27–29]. When chondrocytes are cultured on tissue culture plastic, in addition to dedifferentiation, they produce minimal matrix [8].

Herpes Simplex Virus Type 1

Herpes Simplex Virus Type 1 (HSV-1) is an enveloped dsDNA virus belonging to the family of alphaherpesviruses. Over 60% of the world's population is estimated to be infected with HSV-1, and an estimated 33% of the population has experienced symptomatic HSV-1 [35]. In most cases, HSV-1 causes mild oral and facial lesions, but in severe cases can cause morbid encephalopathies.

HSV-1 infections begin in the epithelium, where it gains access to the peripheral nervous system (PNS) and travels to the neurons' cell bodies via retrograde transport (Figure 2.7). Upon infecting the nervous system, HSV-1 establishes a persistent infection for the lifetime of the host. Upon viral replication in the PNS, HSV-1 travels back to the epithelium through anterograde transport, where symptoms often appear as 'cold sores' [35–37].

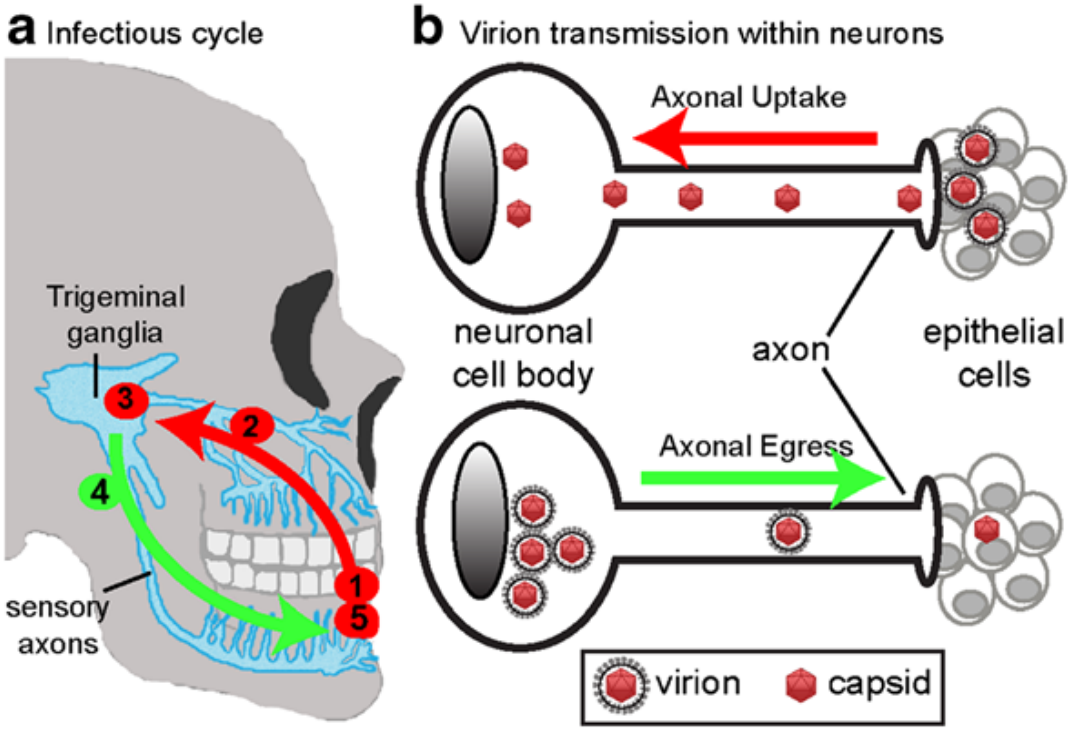


Figure 2.7: The infectious cycle. a (1) Primary infection often occurs in the oral mucosal epithelium of a naïve host. (2) Mucosal epithelial cells transmit infection, via sensory axons, to neuronal cell bodies in the trigeminal ganglia. (3) A latent infection is established in a subset of sensory neurons for an indeterminate period. (4) Latent genomes periodically reactivate and transmit infection, via axons, to epithelial cells. (5) Reinfection of epithelial cells results in formation of recurrent mucosal lesions. b Infection of neurons will result in directed transport of virions within axons. As described in step 2, infected epithelial cells transmit virions into sensory axons. Viral capsids are intracellularly transported within the axon to the neuronal nucleus. Capsids will dock at the nuclear pore and inject their viral genomes. Those genomes will undergo either latent or productive neuronal infection. As described in step 4, reactivated genomes produce progeny virions in the neuronal cell body. Fully assembled virions (enclosed within a vesicle not depicted) transport within the axon to sites of synaptic contact. Virions will egress from the axon and infect closely-associated cells. Adapted from Ref. 58 with permission from the Journal [58]

HSV-1 is unique in its ability to establish lifelong infection and evade sterilizing response from the immune system. Once HSV-1 has infected the nervous system, the virus will enter a hibernation-like state termed latency. During latency, HSV-1 is transcriptionally silent except for the viral RNA transcript, latency-associated transcript (LAT) [36,38]. It is thought that LAT

influences the suppression of apoptosis within neurons, further contributing to its survivability [36,38]. However, the factors contributing to cells entering a latent state and transitioning back to a lytic infection are poorly understood, making the development of therapeutics difficult.

HSV-1 follows three viral gene expression cascades; productive infection, latent infection, and reactivation to lytic infection [36,38]. The productive infection phase takes place in a single replicative cycle where genes are classified as immediate-early (IE), early (E), and late genes (L) (Figure 2.8) [36,38]. In typical HSV-1 infection, IE peptide levels peak between 3-4 hpi while E peptides peak 5-7 hpi [38]. The L peptides continue to increase up until 12 hpi [38]. Both E and L protein synthesis rely on IE protein synthesis, meaning that infections cannot progress to the late stages without the IE proteins [38]. Latent infection is more complicated and poorly understood than the initial stage of productive infection. Latent infection is defined by the silencing of viral genes, except for LAT [36]. The data imply that LAT accumulation can begin even after viral gene expression and that IE proteins may even be required for LAT expression [36]. Reactivation from latent infection to lytic infection is a two-step process where first, silent DNA initiates its expression, and infectious particles are assembled [36]. Following particle assembly, viral particles are transported via anterograde transport to cells, where they initiate a productive infection that follows the expected gene cascade [36].

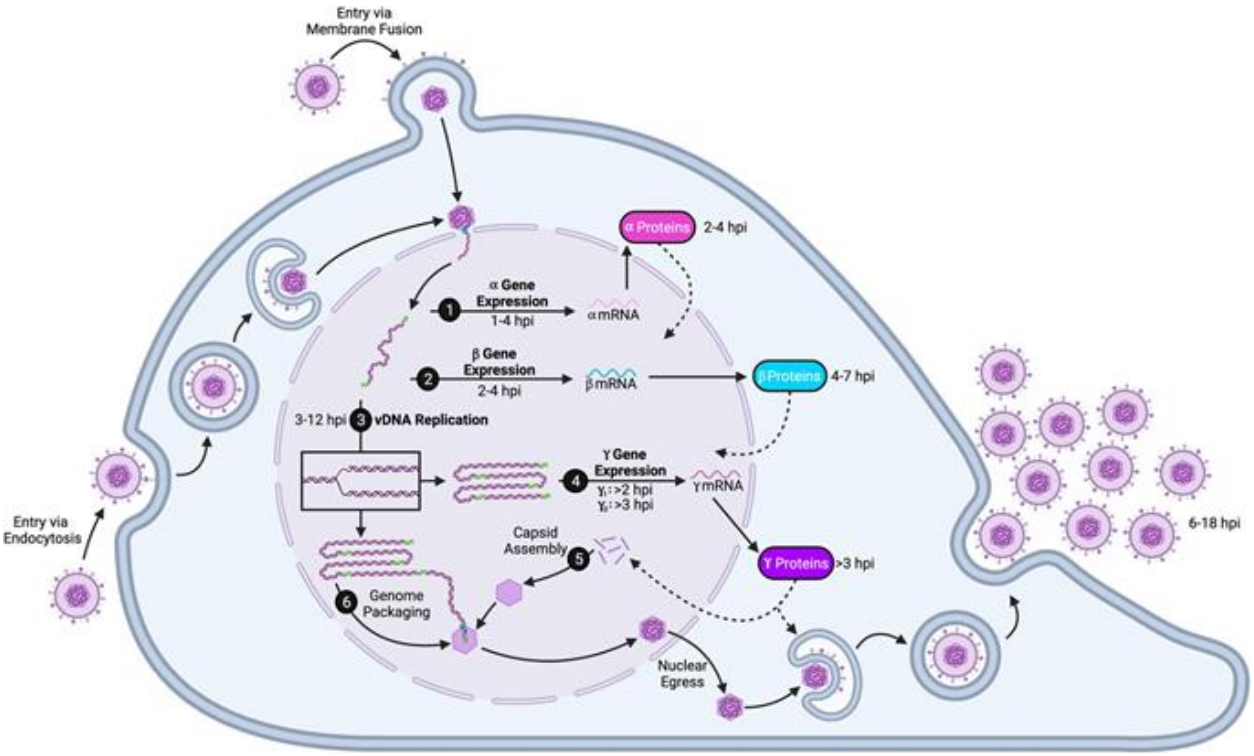


Figure 2.8: The HSV-1 infectious cycle. Virions enter the cell via fusion with the host-cell membrane or endocytosis. The capsid docks at the nuclear pore and viral DNA enters the nucleus through the portal in the capsid. The HSV-1 genome is then expressed: (1) α genes are expressed upon entry; (2) α gene products drive β transcription; (3) after β protein expression, vDNA replication occurs; (4) γ1gene expression is amplified, and γ2gene expression is enabled by DNA replication; (5) capsid proteins, which are γ gene products, assemble; and then (6) replicated genomes are packaged into capsids through the portal. Packaged capsids leave the nucleus through nuclear egress and move through the secretory pathway, obtain an envelope spiked with viral glycoproteins, and nascent virions are released from the cell by exocytosis. Adapted from Ref. 38 with permission from the Journal [38]

Models for Studying HSV-1

Many models exist for studying HSV-1 infection. Primarily, HSV-1 is studied in vivo in mouse and rabbit models, but in vivo models are expensive, limited in throughput, limited in application, and confounded by heterogeneous cell populations [39]. In vitro models offer an alternative method to in vivo methods. Current in vitro models typically involve culturing

primary neurons or cell lines on tissue culture plastic [40–43]. Trichamber microfluidic devices have gained popularity for their ability to inoculate axons independently from the soma of neurons and coculture neurons, and other cell types [40] These methods are sufficient for elucidating population-level infection responses but may obscure the heterogeneous dynamics of infection that may not be observed using well-plate methods [44–46]. Additionally, these in vitro methods are all two-dimensional assays with a stiff substrate which does little to recapitulate the native environment of the cells [4,47–51]

Single-Cell Virology Techniques

Single-cell biology, and more specifically, single-cell virology, have emerged as a promising method for assaying rare virological outcomes in the past decade [44,52,53]. Cells and viruses are both heterogeneous subjects [44]. Host cells have heterogeneous gene expression and immune responses, altering viral entry and replication [44]. In addition, viruses themselves are highly heterogeneous, with high mutation rates and large numbers of defective particles [44]. Together, this heterogeneity leads to diverse outcomes of infection, and understanding these outcomes would lead to better therapeutics and reduced disease outcomes.

Single-cell virology typically relies on microwell plate assays which are low in throughput and application [44,52,53]. Microfluidics has emerged as a technology that addresses the limited throughput and application of well-plates [44,52,53]. Microfluidic well-traps, valve, and droplet systems have all gained traction as methods for investigating viruses at the single-cell level. Examples include but are not limited to the use of well-trap and valve systems to investigate viral infection dynamics in HIV, VSV, and PV (Figure 2.9) [44]. Each system has

strengths and weaknesses regarding its applications, such as ease of manipulation, throughput, or the type of assays possible.

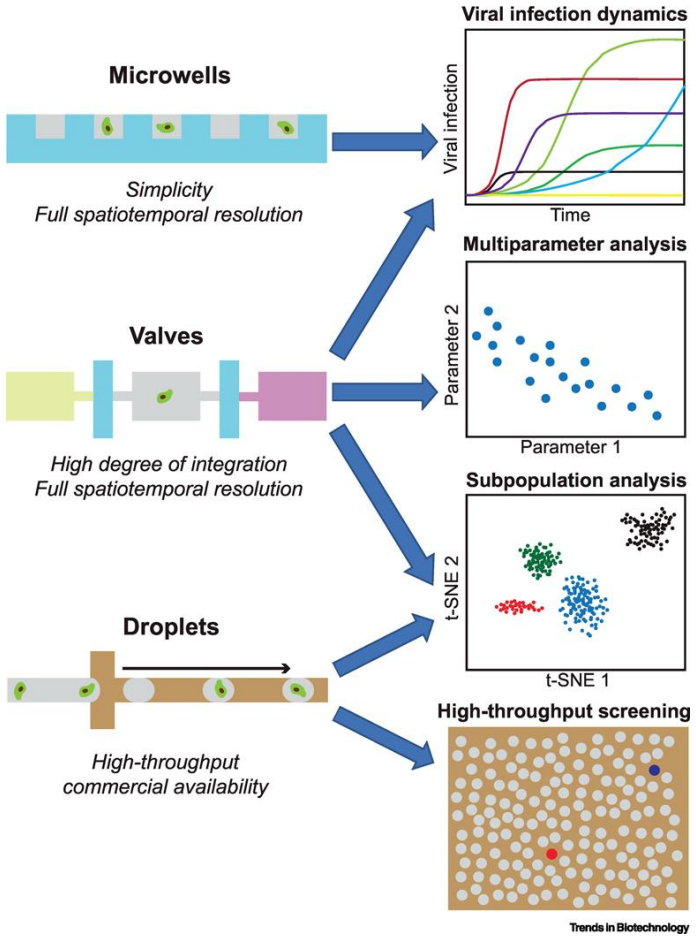


Figure 2.9: Microwell-, valve-, and droplet-based strategies are applied in virology studies. Features and typical application opportunities of these methods are presented. Abbreviations: t-SNE 1 and t-SNE 2, dimension 1 and dimension 2 of the data space with t-distributed stochastic neighbor embedding (t-SNE) technique for dimensionality reduction. Adapted from Ref. 44 with permission from the Journal [44]

The remainder of this work will focus on droplet-based assays for their relevance in later chapters. Droplet-based microfluidics (DBM) generates hundreds to thousands of monodisperse, water-in-oil droplets per second [54]. Depending on applications and microfluidic device design,

drops can contain single-cells, precise inoculating doses, and other reagents [54]. This effectively creates millions of single-cell replicates, which can be manipulated and assayed as desired [54]. Multiple groups have used DBM to combine viruses and single-cells for various applications, such as measuring output of H1N1 infections and detecting rare recombinant noroviruses (Figure 2.10) [45,55,56]. Droplet systems can be assayed in many ways. Fluorescence-based assays are ideal as imaging and high throughput fluorescence droplet detection allow for the quantification of the fluorescence intensity in each individual droplet [54,57]. One fluorescence-based technique, Droplet-based PCR, has recently emerged as a feasible way to run millions of single-cell PCR reactions simultaneously [57]. Other technologies, such as Drop-seq and GemCode, have emerged for performing single-cell sequencing in droplets [44,52,53].

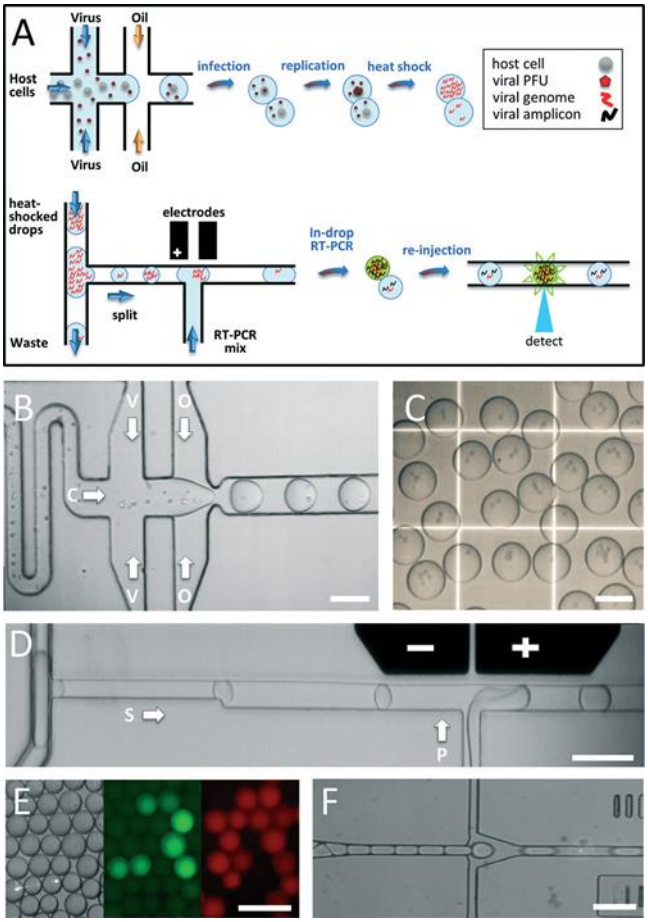


Figure 2.10: Workflow of the drop-based viral infectivity assay. A) Schematic description of the assay. Viruses that infect host cells within drops pro- duce many copies of their genome so that when fractions of these drops are merged with RT-PCR mix and amplified, many amplicons of the viral genome are produced and their marker fluoresce is at high intensity. By contrast, in drops where no infection occurred, very few viral templates if at all exist in the fractions of the original drops and the number of amplicons generated after a limited number of PCR cycles is significantly lower, as is the fluorescence of their marker. B) Viruses (V) and host cells (C) are co-encapsulated in oil (O) using a microfluidic drop-making device. C) An image of the resulting drops showing that each contain about 1–2 cells. D) After incubation, drops are re-injected into the "split and inject" device, where a small volume is split (S) from each drop and merged using electro-coalescence with RT-PCR mix (P). E) After off-chip in-drop amplification the drops remain monodisperse (left), those containing viral amplicons fluoresce at 520 nm (middle) and those containing tracer Rhodamine fluorescence at 586 nm (right). F) The drops are re-injected into a microfluidic drop reader device with a laser and a Photo-Multiplier (PMT) aligned to the channel for the detection of drop fluorescence. All scale bars are 100 μm.

Works Cited

1. Xu Y, Zhu H, Denduluri A, Ou Y, Erkamp NA, Qi R, et al. Recent Advances in Microgels: From Biomolecules to Functionality. Small. 2022;18: e2200180.

2. Scheffold F. Pathways and challenges towards a complete characterization of microgels. Nat Commun. 2020;11: 4315.

3. Caldwell AS, Aguado BA, Anseth KS. Designing Microgels for Cell Culture and Controlled Assembly of Tissue Microenvironments. Adv Funct Mater. 2020;30. doi:10.1002/adfm.201907670

4. Caliari SR, Burdick JA. A practical guide to hydrogels for cell culture. Nat Methods. 2016;13: 405–414.

5. Broguiere N, Isenmann L, Hirt C, Ringel T, Placzek S, Cavalli E, et al. Growth of Epithelial Organoids in a Defined Hydrogel. Adv Mater. 2018;30: e1801621.

6. Ghosh S, Scott AK, Seelbinder B, Barthold JE, Martin BMS, Kaonis S, et al. Dedifferentiation alters chondrocyte nuclear mechanics during in vitro culture and expansion. Biophys J. 2022;121: 131–141.

7. von der Mark K, Gauss V, von der Mark H, Müller P. Relationship between cell shape and type of collagen synthesised as chondrocytes lose their cartilage phenotype in culture. Nature. 1977;267: 531–532.

8. Jeon JE, Schrobback K, Meinert C, Sramek V, Hutmacher DW, Klein TJ. Effect of preculture and loading on expression of matrix molecules, matrix metalloproteinases, and cytokines by expanded osteoarthritic chondrocytes. Arthritis Rheum. 2013;65: 2356–2367.

9. Håti AG, Bassett DC, Ribe JM, Sikorski P, Weitz DA, Stokke BT. Versatile, cell and chip friendly method to gel alginate in microfluidic devices. Lab Chip. 2016;16: 3718–3727.

10. Fredrikson JP, Brahmachary PP, Erdoğan AE, Archambault ZK, Wilking JN, June RK, et al. Metabolomic Profiling and Mechanotransduction of Single Chondrocytes Encapsulated in Alginate Microgels. Cells. 2022;11. doi:10.3390/cells11050900

11. Eschweiler J, Horn N, Rath B, Betsch M, Baroncini A, Tingart M, et al. The Biomechanics of Cartilage-An Overview. Life. 2021;11. doi:10.3390/life11040302

12. Sophia Fox AJ, Bedi A, Rodeo SA. The basic science of articular cartilage: structure, composition, and function. Sports Health. 2009;1: 461–468.

13. Muir H. The chondrocyte, architect of cartilage. Biomechanics, structure, function and molecular biology of cartilage matrix macromolecules. Bioessays. 1995;17: 1039–1048.

14. Darling EM, Wilusz RE, Bolognesi MP, Zauscher S, Guilak F. Spatial mapping of the biomechanical properties of the pericellular matrix of articular cartilage measured in situ via atomic force microscopy. Biophys J. 2010;98: 2848–2856.

15. Wilusz RE, Sanchez-Adams J, Guilak F. The structure and function of the pericellular matrix of articular cartilage. Matrix Biol. 2014;39: 25–32.

16. Zhang Z. Chondrons and the pericellular matrix of chondrocytes. Tissue Eng Part B Rev. 2015;21: 267–277.

17. Lee DA, Noguchi T, Knight MM, O'Donnell L, Bentley G, Bader DL. Response of chondrocyte subpopulations cultured within unloaded and loaded agarose. J Orthop Res. 1998;16: 726–733.

18. Darling EM, Athanasiou KA. Rapid phenotypic changes in passaged articular chondrocyte subpopulations. J Orthop Res. 2005;23: 425–432.

19. Zelenski NA, Leddy HA, Sanchez-Adams J, Zhang J, Bonaldo P, Liedtke W, et al. Type VI Collagen Regulates Pericellular Matrix Properties, Chondrocyte Swelling, and Mechanotransduction in Mouse Articular Cartilage. Arthritis Rheumatol. 2015;67: 1286–1294.

20. Alexopoulos LG, Haider MA, Vail TP, Guilak F. Alterations in the mechanical properties of the human chondrocyte pericellular matrix with osteoarthritis. J Biomech Eng. 2003;125: 323–333.

21. Danalache M, Kleinert R, Schneider J, Erler AL, Schwitalle M, Riester R, et al. Changes in stiffness and biochemical composition of the pericellular matrix as a function of spatial chondrocyte organisation in osteoarthritic cartilage. Osteoarthritis Cartilage. 2019;27: 823–832.

22. Arnold KM, Sicard D, Tschumperlin DJ, Westendorf JJ. Atomic Force Microscopy Micro-Indentation Methods for Determining the Elastic Modulus of Murine Articular Cartilage. Sensors . 2023;23. doi:10.3390/s23041835

23. Ng L, Hung H-H, Sprunt A, Chubinskaya S, Ortiz C, Grodzinsky A. Nanomechanical properties of individual chondrocytes and their developing growth factor-stimulated pericellular matrix. J Biomech. 2007;40: 1011–1023.

24. Jacobi M, Villa V, Magnussen RA, Neyret P. MACI - a new era? Sports Med Arthrosc Rehabil Ther Technol. 2011;3: 10.

25. Huang BJ, Hu JC, Athanasiou KA. Cell-based tissue engineering strategies used in the clinical repair of articular cartilage. Biomaterials. 2016;98: 1–22.

26. Benya PD, Padilla SR, Nimni ME. Independent regulation of collagen types by chondrocytes during the loss of differentiated function in culture. Cell. 1978;15: 1313–1321.

27. Mayne R, Vail MS, Mayne PM, Miller EJ. Changes in type of collagen synthesized as clones of chick chondrocytes grow and eventually lose division capacity. Proc Natl Acad Sci U S A. 1976;73: 1674–1678.

28. Costa E, González-García C, Gómez Ribelles JL, Salmerón-Sánchez M. Maintenance of chondrocyte phenotype during expansion on PLLA microtopographies. J Tissue Eng. 2018;9: 2041731418789829.

29. Amr M, Mallah A, Yasmeen S, Van Wie B, Gozen A, Mendenhall J, et al. From Chondrocytes to Chondrons, Maintenance of Phenotype and Matrix Production in a Composite 3D Hydrogel Scaffold. Gels. 2022;8. doi:10.3390/gels8020090

30. Minas T, Peterson L. Advanced techniques in autologous chondrocyte transplantation. Clin Sports Med. 1999;18: 13–44, v–vi.

31. Colombini A, Libonati F, Lopa S, Peretti GM, Moretti M, de Girolamo L. Autologous chondrocyte implantation provides good long-term clinical results in the treatment of knee osteoarthritis: a systematic review. Knee Surg Sports Traumatol Arthrosc. 2022. doi:10.1007/s00167-022-07030-2

32. Batty L, Dance S, Bajaj S, Cole BJ. Autologous chondrocyte implantation: an overview of technique and outcomes. ANZ J Surg. 2011;81: 18–25.

33. McLeod MA, Wilusz RE, Guilak F. Depth-dependent anisotropy of the micromechanical properties of the extracellular and pericellular matrices of articular cartilage evaluated via atomic force microscopy. J Biomech. 2013;46: 586–592.

34. Darling EM, Zauscher S, Guilak F. Viscoelastic properties of zonal articular chondrocytes measured by atomic force microscopy. Osteoarthritis Cartilage. 2006;14: 571–579.

35. Duarte LF, Farías MA, Álvarez DM, Bueno SM, Riedel CA, González PA. Herpes Simplex Virus Type 1 Infection of the Central Nervous System: Insights Into Proposed Interrelationships With Neurodegenerative Disorders. Front Cell Neurosci. 2019;13. doi:10.3389/fncel.2019.00046

36. Roizman B, Zhou G. The 3 facets of regulation of herpes simplex virus gene expression: A critical inquiry. Virology. 2015;479–480: 562–567.

37. Kratchmarov R, Enquist LW, Taylor MP. Us9-Independent Axonal Sorting and Transport of the Pseudorabies Virus Glycoprotein gM. J Virol. 2015;89: 6511–6514.

38. Heath JR, Dembowski JA. Fashionably late: Temporal regulation of HSV-1 late gene transcription. PLoS Pathog. 2022;18: e1010536.

39. Kollias CM, Huneke RB, Wigdahl B, Jennings SR. Animal models of herpes simplex virus immunity and pathogenesis. J Neurovirol. 2015;21: 8–23.

40. Tierney WM, Vicino IA, Sun SY, Chiu W, Engel EA, Taylor MP, et al. Methods and Applications of Campenot Trichamber Neuronal Cultures for the Study of Neuroinvasive Viruses. Methods Mol Biol. 2022;2431: 181–206.

41. Shipley MM, Mangold CA, Kuny CV, Szpara ML. Differentiated Human SH-SY5Y Cells Provide a Reductionist Model of Herpes Simplex Virus 1 Neurotropism. J Virol. 2017;91. doi:10.1128/JVI.00958-17

42. Wilson AC. Impact of Cultured Neuron Models on α-Herpesvirus Latency Research. Viruses. 2022;14. doi:10.3390/v14061209

43. Rafael D, Tomer E, Kobiler O. A Single Herpes Simplex Virus 1 Genome Reactivates from Individual Cells. Microbiol Spectr. 2022;10: e0114422.

44. Liu W, He H, Zheng S-Y. Microfluidics in Single-Cell Virology: Technologies and Applications. Trends Biotechnol. 2020;38: 1360–1372.

45. Loveday EK, Sanchez HS, Thomas MM, Chang CB. Single-Cell Infection of Influenza A Virus Using Drop-Based Microfluidics. Microbiol Spectr. 2022;10: e0099322.

46. Drayman N, Patel P, Vistain L, Tay S. HSV-1 single-cell analysis reveals the activation of anti-viral and developmental programs in distinct sub-populations. Elife. 2019;8. doi:10.7554/eLife.46339

47. Ju Y-E, Janmey PA, McCormick ME, Sawyer ES, Flanagan LA. Enhanced neurite growth from mammalian neurons in three-dimensional salmon fibrin gels. Biomaterials. 2007;28: 2097–2108.

48. Franze K, Janmey PA, Guck J. Mechanics in neuronal development and repair. Annu Rev Biomed Eng. 2013;15: 227–251.

49. Cullen DK, Lessing MC, LaPlaca MC. Collagen-dependent neurite outgrowth and response to dynamic deformation in three-dimensional neuronal cultures. Ann Biomed Eng. 2007;35: 835–846.

50. Balgude AP, Yu X, Szymanski A, Bellamkonda RV. Agarose gel stiffness determines rate of DRG neurite extension in 3D cultures. Biomaterials. 2001;22: 1077–1084.

51. Frega M. 3D Neuronal Networks: State of the Art. In: Frega M, editor. Neuronal Network Dynamics in 2D and 3D in vitro Neuroengineered Systems. Cham: Springer International Publishing; 2016. pp. 45–57.

52. Basiri A, Heidari A, Nadi MF, Fallahy MTP, Nezamabadi SS, Sedighi M, et al. Microfluidic devices for detection of RNA viruses. Rev Med Virol. 2021;31: 1–11.

53. Simpson C, Lee SS, Lee C-S, Yamauchi Y. Microfluidics: an Untapped Resource in Viral Diagnostics and Viral Cell Biology. Current Clinical Microbiology Reports. 2018;5: 245–251.

54. Zath G, Sperling RA, Hoffman CW, Bikos DA, Abbasi R, Abate AR, et al. Rapid Parallel Generation of a Fluorescently Barcoded Drop Library from a Microtiter Plate Using the Plate-Interfacing Parallel Encapsulation (PIPE) Chip. Lab Chip. 2022 [cited 8 Nov 2022]. doi:10.1039/D2LC00909A

55. Tao Y, Rotem A, Zhang H, Chang CB, Basu A, Kolawole AO, et al. Rapid, targeted and culture-free viral infectivity assay in drop-based microfluidics. Lab Chip. 2015;15: 3934–3940.

56. Tao Y, Rotem A, Zhang H, Cockrell SK, Koehler SA, Chang CB, et al. Artifact-free quantification and sequencing of rare recombinant viruses by using drop-based microfluidics. Chembiochem. 2015;16: 2167–2171.

57. Loveday EK, Zath GK, Bikos DA, Jay ZJ, Chang CB. Screening of Additive Formulations Enables Off-Chip Drop Reverse Transcription Quantitative Polymerase Chain Reaction of Single Influenza A Virus Genomes. Anal Chem. 2021;93: 4365–4373.

58. Herr AE, Hain KS, Taylor MP. Limitations on the Multiplicity of Cellular Infection During Human Alphaherpesvirus Disease. Current Clinical Microbiology Reports. 2017;4: 167–174

CHAPTER THREE

METABOLOMIC PROFILING AND MECHANOTRANSDUCTION OF SINGLE CHONDROCYTES ENCAPSUALTED IN ALGINATE MICROGELS

Contribution of Authors and Co-Authors

Manuscript in Chapter 3

Author: Jacob P. Fredrikson

Contributions: J.P.F. designed research, performed research, analyzed data, and wrote the manuscript

Co-Author: Priyanka P. Brahmachary

Contributions: P.P.B. designed research, performed research, and wrote the manuscript

Co-Author: Ayten E. Erdoğan

Contributions: A.E.E performed research, analyzed data, and wrote the manuscript

Co-Author: Zachary K. Archambault

Contributions: Z.K.A performed research

Co-Author: James N. Wilking

Contributions: J.N.W. designed research, performed research, and analyzed data

Co-Author: Ronald K. June

Contributions: R.K.J. designed research and wrote the manuscript

Co-Author: Connie B. Chang

Contributions: C.B.C. designed research and wrote the manuscriptt

Manuscript Information

Jacob P. Fredrikson, Priyanka P. Brahmachary, Ayten E. Erdoğan, Zachary K. Archambault,

James N. Wilking, Ronald K. June, Connie B. Chang

Cells

Status of Manuscript:
___ Prepared for submission to a peer-reviewed journal
___ Officially submitted to a peer-reviewed journal
___ Accepted by a peer-reviewed journal
_x_ Published in a peer-reviewed journal

Multidisciplinary Digital Publishing Institute
Volume 11 Issue 5
10.3390/cells11050900

Abstract

Articular cartilage is comprised of two main components, the extracellular matrix (ECM) and the pericellular matrix (PCM). The PCM helps to protect chondrocytes in the cartilage from mechanical loads, but in patients with osteoarthritis, the PCM is weakened resulting in increased chondrocyte stress. As chondrocytes are responsible for matrix synthesis and maintenance, it is important to understand how mechanical loads affect cellular responses of chondrocytes. Many studies have examined the chondrocyte response to in vitro mechanical loading by embedding chondrocytes 3D hydrogels. However, these experiments are mostly performed in the absence of PCM which may obscure important responses to mechanotransduction. Here, drop-based microfluidics is used to culture single chondrocytes in alginate microgels for cell-directed PCM synthesis that closely mimics the in vivo microenvironment. Chondrocytes form PCM over 10 days in these single cell 3-D microenvironments. Mechanotransduction studies were performed in which single cell microgels mimicking the cartilage PCM were embedded in high stiffness agarose. After physiological dynamic compression in a custom-built bioreactor, microgels exhibited distinct metabolomic profiles from both uncompressed and monolayer controls. These results demonstrate the potential of single cell encapsulation in alginate microgels to advance cartilage tissue engineering and basic chondrocyte mechanobiology.

Introduction

Osteoarthritis (OA) is the most common degenerative joint disease which affects over 250 million people worldwide [1]. In osteoarthritis, the articular cartilage, the soft load-bearing tissue that lines the interfaces of joints, begins to deteriorate [2]. This is associated with pain and loss of joint function. The tissue in human articular cartilage is composed of two main components: the extracellular matrix (ECM) and the pericellular matrix (PCM). The cartilage is primarily comprised of ECM, a hydrated matrix of collagen and proteoglycans [2]. The rest of the cartilage consists of PCM, which is primarily comprised of type VI collagen and closely encapsulates the chondrocytes, like a cocoon, directly applying stimuli for chondrocyte mechanotransduction [3]. In normal circumstances, cartilage experiences mechanical loads that vary in frequency and amplitude from activities such as walking, running, and jumping [4]. The PCM protects the chondrocytes from these mechanical loads, but in patients with OA, the PCM is weakened resulting in increased chondrocyte stress [5]. As chondrocytes are responsible for matrix synthesis and maintenance, it is important to understand how mechanical loads affect cellular responses of chondrocytes, including their metabolic responses [6].

Many studies have examined the in vitro cellular response of chondrocytes to stress by embedding cells in a stiff agarose gel and applying a load to the gel [7-10]. However, these experiments are mostly performed in the absence of PCM, which may obscure important cellular responses involved in mechanotransduction [3]. Chondrocytes in vivo are naturally surrounded by a three-dimensional (3-D) matrix which has been previously reported to have elastic moduli between 25 and 200 kPa [5,11,12]. Three-dimensional agarose models have achieved similar elastic moduli in the range of 20 to 50 kPa with concentrations of 3-5% w/w of low gelling

temperature agarose in phosphate buffered saline [9]. However, the cells in these models lack a surrounding PCM and may not accurately represent the in vivo functions of the PCM. Thus, the cells do not experience physiologically relevant microenvironments provided by the PCM [3,9]. When cultured in millimeter-scale alginate beads, chondrocytes exhibit phenotypes more similar to in vivo conditions [13-15]. These phenotypes include increased glycosaminoglycan (GAG) and collagen synthesis, both of which are components of both the PCM and ECM [14]. In alginate, chondrocytes synthesize a PCM, yet the elastic moduli of alginate (~1 kPa) cannot reach the elastic moduli of the PCM, which can more accurately depict in vivo mechanical loads in high-stiffness agarose [16-19]. One method of retaining the PCM around the cells is to first grow the cells in a 3-D matrix of alginate and then use various digestive processes to isolate the cells [14]. However, this second digestion may have adverse effects on chondrocytes.

Therefore, there remains a need for a technique in which cells can undergo PCM formation in alginate without a secondary digestion prior to constructing a bulk 3-D matrix. With such a technique, cells can be embedded into a stiffer agarose matrix while retaining properties that better mimic the in vivo microenvironment. One such method is the use of drop-based microfluidics to encapsulate single cells in microscale hydrogels. This approach utilizes fluid flow through microchannels to create monodisperse picoliter-sized microgel droplets. By flow-focusing an inner alginate hydrogel precursor with an outer oil phase, alginate microgels can be fabricated at kilohertz rates [19]. This method has been used to encapsulate numerous mammalian cell types [19,20]. These microgels provide nearly homogenous, highly tunable, 3-D growth environments for cells. Compared to bulk hydrogels, microgels have fewer nutrient limitations and favorable nutrient transfer characteristics due to the high surface area to volume

ratio and small length scale [21]. The individual microgels are easily manipulated through pipetting and centrifugation, allowing for the facile transfer of encapsulated cells between growth environments.

Here, we demonstrate that drop-based microfluidics enables the culture of single chondrocytes in alginate microgels for cell-directed PCM synthesis that closely mimics the in vivo microenvironment. When encapsulated into a stiff agarose construct, these microgel-encapsulated chondrocytes create a cartilage model that includes components of both the PCM in the collagen VI, which surrounds the cells, and ECM in the stiff agarose, providing a more physiologically relevant compression model. Chondrocytes form PCM over 10 days in these single cell microenvironments in comparison to cells grown in a monolayer environment which do not form PCM. We investigated the effects of cyclical dynamic compression on cells cultured in microgels and as monolayers by encapsulating single-cell microgels and monolayer controls in high-stiffness agarose to mimic the cartilage PCM. After physiological dynamic compression, microgels exhibited distinct metabolomic profiles from both uncompressed and monolayer controls [8]. These microgel-encapsulated chondrocytes develop PCM similar to that of the endogenous PCM and have distinct metabolomic profiles compared to monolayer controls. Upon metabolomic pathway analysis, microgel-encapsulated chondrocytes have up-regulated pathways related to amino acid synthesis and central energy metabolism. These results demonstrate the potential of single-cell encapsulation in alginate microgels to advance cartilage tissue engineering and basic chondrocyte mechanobiology through single cell matrix formation studies and more realistic cartilage models.

Methods

Chondrocyte Harvest and Culture

Primary human chondrocytes were obtained from Stage IV osteoarthritis patients undergoing total joint replacement under IRB approval using established methods [22,23]. Cells were isolated by digestion with Collagenase Type I (2 mg/mL)(Gibco) for 14 h at 37 °C. Isolated chondrocytes were cultured for 10 days in Dulbecco's Modified Eagle's medium (DMEM) (Gibco) supplemented with Fetal Bovine Serum (FBS)(10% v/v) (Bio-Techne) and penicillin (10,000 I.U./mL) and streptomycin (10,000 μg/mL)(Sigma) (hereafter referred to as complete media) in 5% CO_2 at 37 °C. Chondrocytes were passaged at 90% confluency and seeded at a density of 1 x 10^5 cells onto 25 x 25 mm microscope coverslips (Fisherbrand). Coverslips with the attached cells were placed in a 60 x 15 mm tissue culture dish containing complete media supplemented with L-sodium ascorbate (50 μg/mL) (Sigma) and incubated for 10 days. Media was exchanged every other day. Monolayers grown in complete media lacking L-sodium ascorbate for 10 days at 37 °C were used as controls. Cells were imaged on days 0, 5, and 10 for collagen production. Similarly, SW1353 chondrocytes, obtained from ATCC, were seeded on microscope coverslips at a density of 1 x 10^5 cells and cultured in complete media supplemented with L-sodium ascorbate (50 μg/mL) for 10 days in 5% CO_2 at 37 °C and imaged on days 0, 5, and 10. Monolayers grown in complete media lacking L-sodium ascorbate for 10 days at 37 °C were used as controls. SW1353 cells were used between passages 5-20 and primary chondrocytes were used between passages 2-5 post-harvest.

PDMS Microfluidic device fabrication

Polydimethylsiloxane (PDMS) microfluidic devices were fabricated using standard soft-lithography techniques [24]. Negative master molds were fabricated on 3-inch diameter silicon wafers (University Wafer ID: 447) using UV crosslinked Nano SU-8-100 photoresist (Microchem) patterned with photomasks printed on high-resolution transparent plastic film (CAD/Art Inc.). Two-component Sylgard 184 PDMS (Dow SYLGARD 184) was mixed at a 10:1 ratio by mass, poured over wafers in a 100 mm petri dish (Fisherbrand), and degassed. The devices baked at 55 °C for at least 4 h. The cured devices were cut from the master and ports were punched using a 0.75 mm ID biopsy punch (Well Tech). The devices were plasma bonded to 3 x 2 in glass slides (VWR) for drop makers and 25 x 25 mm type 0 coverslips (VWR) for imaging arrays by exposing the PDMS and glass to oxygen plasma for 1 min at high power, 45 watts, and 700 mTorr oxygen pressure using a plasma cleaner (Harrick Scientific Corp PDC-002). The bonded devices were baked at 55 °C for at least 1 h to increase the strength of the plasma bond. Following baking, drop makers were filled with a hydrophobic treatment (PPG Industries Aquapel) for 5 min, flushed with air, and baked at 55 °C again for 1 h.

Preparation of Precursor Solutions

Oil Preparation. The surfactant Krytox 157 FSH (4% w/w)(Miller-Stephenson) was added to the fluorinated oil, HFE 7500 (3M Novec). The solution was filtered through a 0.2 µm hydrophobic polytetrafluoroethylene (PTFE) syringe filter (GVS).

Alginate Precursor Preparation (A). $CaCl_2$ (80 mM)(ACROS Organics), Na_2EDTA (Ethylenediaminetetraacetic acid)(80 mM)(Fisher Chemical), and MOPS (40 mM)(VWR) were mixed with ultra-pure water (50 mL)(18.2 MΩ●cm, MilliQ) and the pH was adjusted to 7.2

using NaOH (2 M)(VWR). Sodium alginate (1.5% w/w)(Sigma, 9005-38-3) was added to the solution (10 mL) and the solution was filtered through a 0.2 µm hydrophilic polyethersulfone (PES) syringe filter (MilliporeSigma Millex).

Alginate Precursor Preparation (B). $Zn(CH_3CO_2)_2$ (80 mM)(Alfa Aesar), EDDA (Ethylenediaminediacetic acid)(80 mM)(TCI Chemicals), and MOPS (40 mM) were mixed with ultra-pure water (50 mL)(18.2 MΩ●cm, MilliQ) and the pH was adjusted to 7.2 using NaOH (2 M). Sodium alginate (1.5% w/w) was added to the solution (10 mL) and the solution was filtered through a 0.2 µm PES syringe filter.

Cell Encapsulation in Microgels

To prepare cells for encapsulation, cells were removed from monolayers using of Trypsin-EDTA (2 mL) and suspended in media. Cells were centrifuged at 500 x g for 5 min (Thermo Scientific ST-16) and washed with of phosphate buffered saline (PBS)(1X, 10 mL) twice. In order to minimize the number of empty drops, cells were then suspended in alginate precursor solution 'A' at 5 x 10^6 cells/mL (final concentration 2.5 x 10^6 cells/mL) and loaded into 1 or 3 mL syringes (BD luer lock). Following previous protocols, cells were encapsulated in 100 µm diameter alginate microgels [19]. The continuous flow rate used was QOil = 2000 µL/h and the dispersed phase flow rates used were QAlgA = QAlgB = 250 µL/h. Microgels were produced in parallel by running two drop making devices for 4 h to encapsulate at least 1 x 10^7 cells. After encapsulation and gelation, microgels were washed with HFE 7500 (500 µL) and 1H,1H,2H,2H-Perfluoro-octonal (PFO)(20% v/v) (VWR) in HFE 7500 (100 µL) for each 125 µL of microgels 2-3 times to remove the surfactant. Microgels were collected from the oil phase with PBS (1X, 500 µL) and suspended in the appropriate media (see the following section).

Cell Culture in Microgels

Approximately 200 µL of microgels containing ~1.3 cells/microgel were placed in each well plate of a six well plate (Falcon) and covered with media (2 mL). Cells were either cultured with complete media or complete media supplemented with L-sodium ascorbate (50 µg/mL) to promote collagen synthesis. Every 3 days, media was exchanged by collecting the contents of each well, centrifuging at 500 x g for 2 min, removing the supernatant, and suspending the microgels in new media (2 mL).

Cell Viability Assay

After 10 days of culture, microgel encapsulated SW1353 cells (100 µL) were mixed with PBS (1X, 800 µL) and of Trypan Blue (100 µL)(Corning). 10 µL of the solution was pipetted onto a hemocytometer (Reichert) to quantify live and dead cells. Each measurement contained 10-40 cells for a total of approximately 260-280 cells for both microgels with and without ascorbate.

Fluorescence Imaging and Analysis

SW1353 cells were imaged using an epi-fluorescent microscope (Leica DMi-8) with a 40 X objective over 10 days to capture brightfield and auto-fluorescence (ex. 350 nm/em. 470 nm). For autofluorescence imaging, each day, 30 µL of microgels and media were flowed into a microfluidic chamber with a height greater than microgel diameter. Approximately 20 cells per growth condition, monolayer and microgels with or without ascorbate, were imaged. The background intensity was subtracted from each image using Fiji ImageJ and the fluorescence intensity of each cell was measured using the Fiji ImageJ distribution of TrackMate [25,26].

Immunofluorescence Staining and Confocal Imaging

Monolayer Controls. Primary chondrocytes and SW1353 cells grown in monolayers on microscope coverslips were fixed in Paraformaldehyde (4% v/v) – PBS (1X) for 10 min at room temperature followed by three 5 min washes of PBS (1X). Cells were permeabilized with a blocking solution containing Triton X-100 (0.1% v/v) - Bovine Serum Albumin (1% v/v) – PBS (1X) for 30 min at room temperature. Cells were then incubated with the primary antibody to collagen VI (Rabbit Polyclonal Anti-collagen VI antibody, ab6588 from Abcam) in Triton X-100 (0.1% v/v) - Bovine Serum Albumin (1% v/v) – PBS (1X) for 1 h at room temperature. After three 5 min washes with PBS (1X), cells were incubated with a mixture of the secondary antibody Donkey anti-Rabbit IgG H&L Alexa Fluor®488 (Abcam), VibrantTMDyeCycle™ Violet Stain for Nuclei (Invitrogen), and MitoTracker™ Red CMXRos (Invitrogen) for mitochondrial detection in Triton X-100 (0.1% v/v) - Bovine Serum Albumin (1% v/v) – PBS (1X) for 1 h at room temperature. Cells were washed 3 times with PBS (1X) and the coverslip was mounted on a glass slide with ProLong™ Diamond Antifade Mountant (Invitrogen). Digital images were acquired on a Leica TCS SP8 confocal microscope with the Leica Application Suite Advanced Fluorescence software.

Microgel-encapsulated Chondrocytes. Alginate beads with encapsulated chondrocytes were spun down at 500 x g for 2 min, washed with PBS (1X), and then fixed with Paraformaldehyde (4% v/v) – PBS (1X) for 15 min at room temperature. Paraformaldehyde-fixed microgel-encapsulated cells were permeabilized with a blocking solution containing Triton X-100 (1.0% v/v) - Bovine Serum Albumin (3% v/v) – PBS (1X) for 30 min at room temperature. Microgels were then incubated with primary antibody to collagen VI (Rabbit

Polyclonal Anti-collagen VI antibody, ab6588 from Abcam) in Triton X-100 (1.0% v/v) - Bovine Serum Albumin (3% v/v) – PBS (1X) for 1 h at room temperature. Following three washes of 5 min each with PBS (1X), encapsulated samples were incubated with a mixture of secondary antibody Donkey anti-Rabbit IgG H&L Alexa FluorR488 (Abcam), Vibrant™DyeCycle™ Violet Stain for Nuclei (Invitrogen), and MitoTracker™ Red CMXRos (Invitrogen) for mitochondrial detection in Triton X-100 (1.0% v/v) - Bovine Serum Albumin (3% v/v) – PBS (1X) for 1 h at room temperature. Microgel constructs were washed three times with PBS (1X). 100 µl of the alginate beads were cytospun onto single frosted adhesive slides (Tanner Scientific) using a Thermo Scientific Cytospin™ 4 Cytocentrifuge for immunocytochemistry and mounted with ProLong™ Diamond Antifade Mountant (Invitrogen).

Encapsulation in High Stiffness Agarose, Mechanical Stimulation, and Metabolite Extraction

After 9 days in culture, microgels and SW1353 cells from each condition were mixed with low melting temperature agarose (Sigma Aldrich) at a final agarose concentration of 4.5% w/w [9,27]. Final cell concentrations for each condition were 1 x 10^6 cells/mL with each gel being a 0.5 mL cylinder 12.75 mm in height. The agarose was allowed to cool to room temperature to form a gel. The agarose gels were each placed in individual wells of a 12-well plate (Falcon) and cultured for 2 days in appropriate experimental conditions. After 2 days, each gel was loaded onto a custom-built bioreactor at 37 °C, 5% CO_2, and 95% relative humidity in PBS and preloaded at 5% strain [8]. After 30 min, 2% cyclic strain at 1.1 Hz was applied for 15 min. Gels were washed with PBS and frozen for 1 min with liquid nitrogen. Gels were then crushed and placed in a -80 °C freezer for 1 h. Gels were removed from the freezer and a 1 mL solution of equal volumes HPLC-grade methanol (Fisher Chemical) and acetone (Sigma Aldrich)

was added to each sample. Samples were vortexed every 5 min for 20 min and kept at -20 °C overnight. The next day samples were centrifuged at 13,000 rpm for 10 min at 4 °C (Thermo Scientific Sorvall Legend X1R). The supernatant was removed and placed in a speed-VAC (Savant SC110) for 6.5 h. The resulting pellet was suspended in a 1:1 mixture of HPLC grade water (Fisher Chemical) and acetonitrile (Fisher Chemical) and placed in a -80 °C freezer until used for HPLC-MS.

Untargeted Metabolic Profiling

Changes in cellular activity were studied using untargeted metabolomic profiling by HPLC-MS (high-performance liquid chromatography coupled to mass spectrometry). Chromatography was performed in normal phase with established protocols using a Cogent Diamond Hydride HILIC 150 x 2.1 mm column in an Agilent 1290 UPLC system [28]. Mass spectrometry was performed using an Agilent 6538 Q-TOF. Metabolites with a median intensity of zero across all experimental groups were excluded from analysis. Undetected remaining metabolites (i.e., intensity of zero) were replaced with a value of one half the minimum peak intensity for statistical analyses. Statistical analysis was performed in Metaboanalyst. Data were first log transformed and standardized. Metabolomic profiles between experimental groups were compared using principal components analysis (PCA), hierarchical clustering, volcano plot analysis, and pathway enrichment analysis. Significance was assessed with false discovery rate corrections using a significance level of 0.05 selected a priori.

Rheology

The storage and loss moduli of each gel used was measured using a TA Instruments AR-G2 parallel plate rheometer. Gel mixtures were poured into 2 mL molds and gelled. They were then loaded onto the rheometer and 1% strain was applied from 100 to 0.1 rad/s.

Statistical Analysis

SW1353 cell viabilities were compared using a Welch Two Sample t-test in R [29,30]. The rate of autofluorescence increase was calculated using a weighted multiple linear regression in R [29,30]. Each measurement was weighted by the inverse variance of the mean of each sample.

Results and Discussion

Chondrocyte encapsulation in alginate microgels and dynamic compression workflow

Previous studies have investigated the effects of alginate macrogels on the formation of pericellular matrix (PCM), but while these macrogels support the formation of PCM, they have insufficient stiffness to mimic the in vivo elastic modulus surrounding chondrocytes which is between 25 and 200 kPa [13-15]. Here, drop-based microfluidics was used to encapsulate single cells (SW1353 and primary human chondrocytes) in alginate microgels (Figure 1A). To produce alginate microgels in a biocompatible manner, the competitive ligand exchange crosslinking (CLEX) method for crosslinking alginate was used [19]. Briefly, 1.5% w/w alginate is mixed with two solutions of 80 mM Ca-EDTA and Zn-EDDA. Upon mixing of the two precursor solutions, Zn^{2+} binds to EDTA, releasing Ca^{2+} which crosslinks the alginate. After 9 days in culture, alginate microgels were concentrated via centrifugation, suspended in 4.5% w/w

agarose, and gelled (Figure 1B). The agarose constructs were allowed to equilibrate over two days to ensure that the process of creating the agarose constructs did not affect the metabolic activity of the cells [9]. The agarose constructs were then placed in a custom-built bioreactor and then subjected to physiological dynamic compression (Figure 1C) [8]. Following compression, metabolites were extracted from the chondrocytes and analyzed using HPLC-MS.

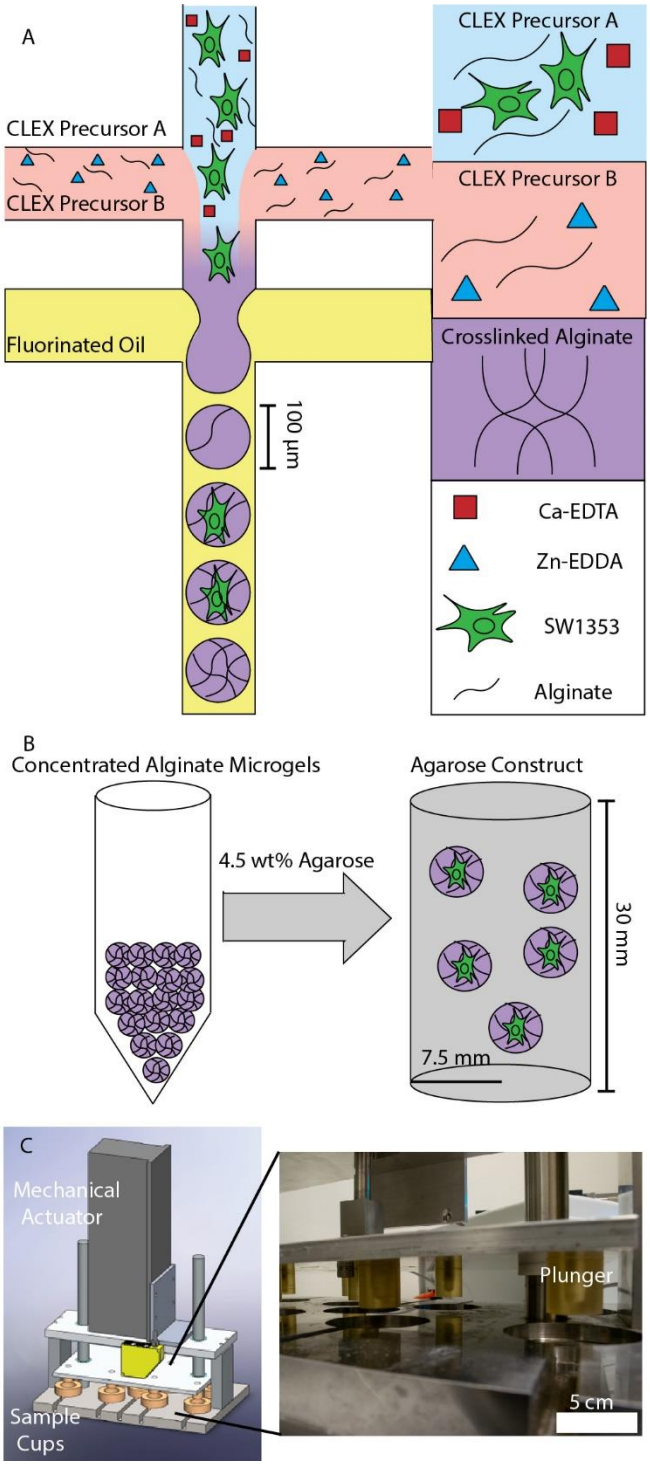


Figure 1. Experimental Workflow: (A) Schematic of alginate microgel production. Cell-laden CLEX precursor A is mixed with CLEX precursor B and flow focused with 4% FSH surfactant in HFE 7500 oil. (B) After 9 days of culture, concentrated alginate microgels are mixed with agarose to a final agarose concentration of 4.5% w/w and 80% v/v. (C) After 2 days, a custom built bioreactor applied 2% cyclic strain after a 5% strain preload to the agarose constructs.

Immunofluorescence staining of PCM formation in alginate microgels

To visualize the PCM formation, we compared two different cell lines, the SW1353 human chondrosarcoma cell line and human primary chondrocytes (HPC) harvested from human knees. Cells were fixed on days 0, 5, and 10, and stained using polyclonal anti-collagen VI antibodies for the primary component of the PCM, collagen VI. Confocal microscopy was used to image collagen formation surrounding single cells. When cultured with ascorbate, which is known to increase collagen production [31], the HPC cells encapsulated in three-dimensional microgels produced more collagen VI compared to HPCs cultured in monolayers, SW153 cells encapsulated in microgels, and SW153 cells encapsulated as monolayers (Figure 2). The HPC cells produced collagen VI that closely surrounds the outside of the cell. A thin, approximately 1 μm, thickness of collagen formed around most of the HPC cells in microgels by day 5 (Figure 2 B), and by day 10, the collagen layer ranged from 2 to 5 μm thick surrounding the entire perimeter of the cell (Figure 2 C). Similarly, the SW1353 cells cultured in microgels showed collagen VI staining by day 5. By day 10, the majority of the cell was covered with collagen VI when ascorbate was present in the media (Figure 2 D-F). However, the SW1353 cells produced less collagen VI than the HPC cells and the resulting collagen VI had a less cocoon-like appearance. When cultured without ascorbate, the HPC and SW1353 cells showed similar trends with more collagen production in microgels than monolayers, but less collagen production than when cultured with ascorbate (data not shown).

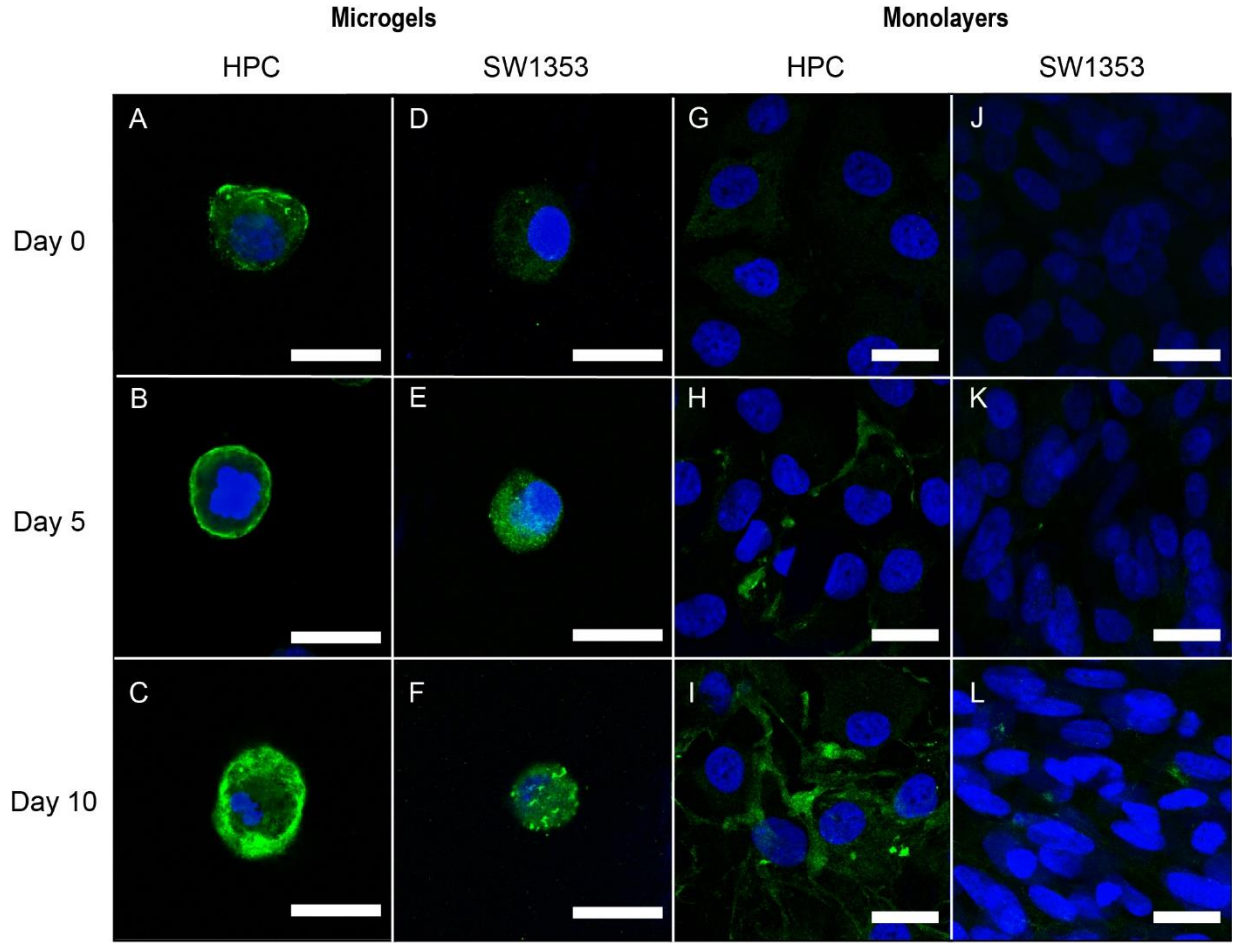


Figure 2. Human Primary Chondrocyte (HPC) and SW1353 cells in 1.5% w/w alginate microgels and monolayers cultured with 50 µg/mL ascorbate. Cells were stained for collagen VI (green), mitochondria (red), and nuclei (blue). Cells were imaged on days 0, 5, and 10. Scale bars are 20 µm.

Immunofluorescence staining of pericellular matrix formation in monolayers

As a control study, we verified that the formation of PCM in typical two-dimensional (2D) cellular monolayers was undetectable in these conditions [32]. SW1353 cells cultured in 2D monolayers showed no collagen VI on day 0 and had negligible collagen VI staining by day 10 when ascorbate was present in the media, indicating a lack of PCM formation (Figure 2 G-I). In

contrast, HPC cells cultured in 2D monolayers with ascorbate produced a small amount of collagen VI (Figure 2 J-L). While the HPC cells cultured in monolayers produced collagen VI, this collagen was typically located in small concentrated regions and did not surround the cells compared to cells when cultured in microgels or naïve cells in the endogenous PCM (Figure 2I) [3]. SW1353 and HPC cultured as monolayers without ascorbate showed low levels of collagen VI compared to when cultured with ascorbate (data not shown).

Auto-fluorescence of PCM formation in alginate microgels

In addition to immuno-fluorescence staining, we quantified collagen formation by measuring the auto-fluorescence signal produced from SW1353 cells under epi-fluorescence imaging. Collagen, a main component of the PCM, shows substantial auto-fluorescence upon excitation from light ranging from UV to blue (365 - 415 nm) [33-35]. Although collagen VI is a specific marker of chondrocyte PCM formation, other types of collagen (I, II, IV) can also auto-fluorescence, but we are not able to distinguish types of collagen using this method [3,33-35]. Therefore, this label-free approach enables general collagen-based PCM formation to be quantified over time. Only SW1353 cells were studied as they are more readily available compared to the human primary chondrocytes. Each day over 10 days, SW1353 cells grown in microgels and monolayers with and without ascorbate were imaged for auto-fluorescence. Similar to immuno-fluorescence staining, the SW1353 cells cultured in microgels produced the most collagen. We show representative images of single cells grown in alginate microgels which display an increase in auto-fluorescence of the PCM over time (Figure 3A). The auto-fluorescence signal closely surrounding the cell is similar to the endogenous PCM where collagen VI surrounds the cell in a cocoon-like manner [3]. As a control experiment, we verified

that when SW1353 cells were cultured in monolayer with and without ascorbate, there was not a noticeable auto-fluorescence signal indicating the absence of collagen (Figure S1 A-B).

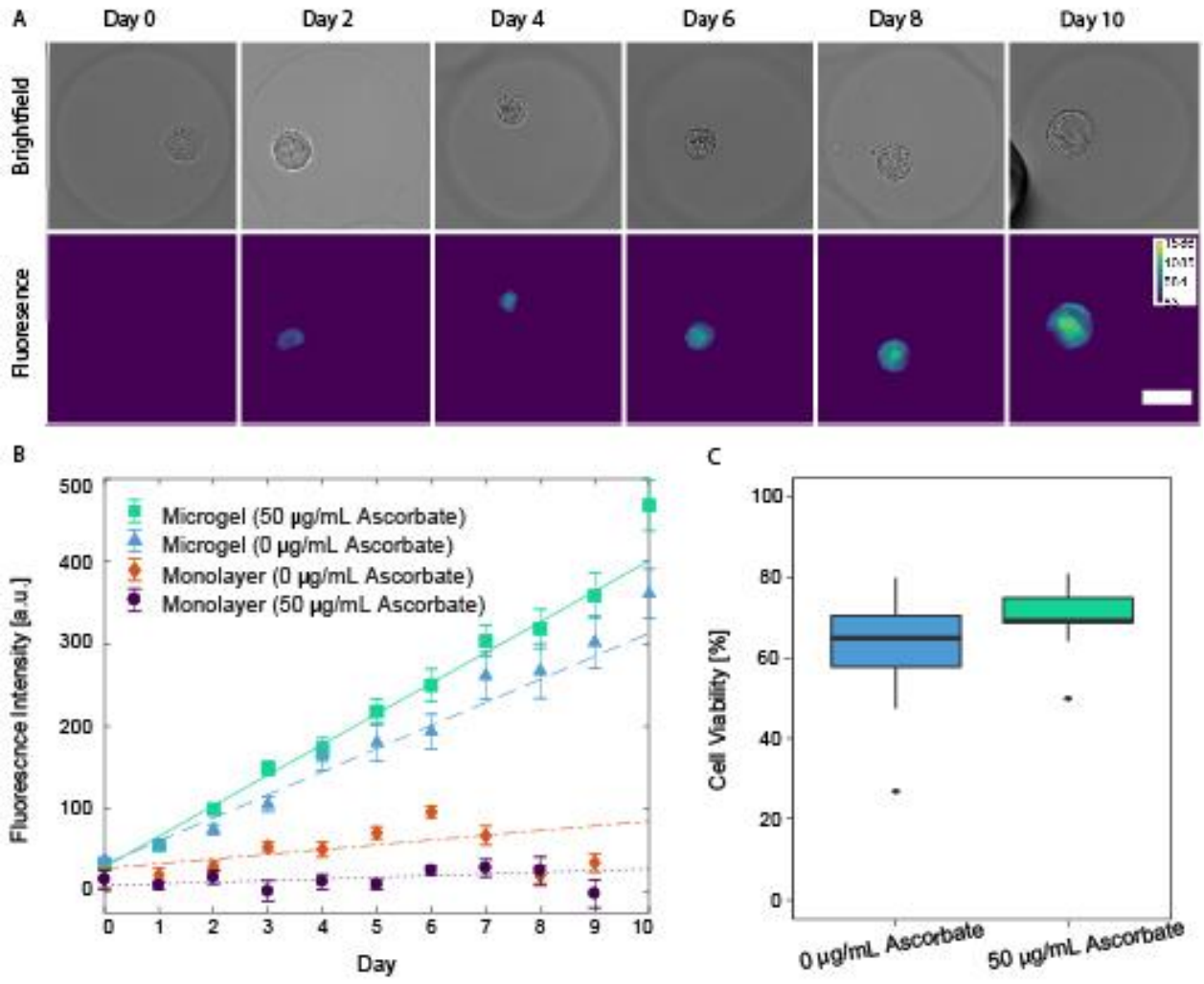


Figure 3. (A) Brightfield and fluorescence images (ex. 350/em. 470) of SW1353 cells encapsulated in alginate microgels and cultured with 50 µg/mL ascorbate. Scale bar is 25 µm. (B) Measured mean fluorescence intensities of imaged SW 1353 cells plotted with a weighted multiple linear regression. SW1353 cells encapsulated in microgels cultured without ascorbate (blue triangle, dashed), encapsulated in microgels cultured with ascorbate (green square, solid), monolayers cultured without ascorbate (orange diamond, dashed-dotted), monolayers cultured with ascorbate (purple circle, dotted). (C) 10 day cell viability for SW1353 cells encapsulated in alginate microgels. Cell viability between cells cultured with or without ascorbate in microgels do not vary (p-value = 0.0957).

As another control experiment, we verify that when ascorbate is not present in the media, there is a decrease in the rate of change in PCM auto-fluorescence signal compared to when ascorbate is present. Representative images of SW1353 cells grown in microgels without ascorbate still showed an increase in auto-fluorescence signal over time (Figure S1C); however, upon quantitative image analysis, a significant decrease in the rate of auto-fluorescence signal change was observed compared to SW1353 cells grown in microgels with ascorbate. When SW1353 cells were cultured in microgels with ascorbate, the auto-fluorescence signal increased 37.1 ± 2.4 a.u./day (Figure 3B, green squares). In contrast, when SW1353 cells were cultured in microgels without ascorbate the auto-fluorescence signal increased 28.0 ± 2.8 a.u./day (Figure 3B, blue triangles), a decrease of 9.1 ± 3.6 a.u./day (p-value = 6.91×10^{-7}). The control monolayer SW1353 cells, when cultured with ascorbate, showed negligible increases in auto-fluorescence signal over time with the signal increasing 2.0 ± 2.0 a.u./day (Figure 3B, purple circles). This is a 35.1 ± 3.0 a.u./day decrease compared to SW1353 cells cultured in microgels with ascorbate ($p < 2 \times 10^{-16}$). The presence of ascorbate did not significantly change the rate of auto-fluorescence increase in monolayers ($p < 0.016$, Figure 3B, orange diamonds).

Overall, collagen production in the PCM showed similar trends with both immunofluorescence and auto-fluorescence. Collagen production increases in microgels compared to monolayers, both with and without ascorbate present. These data indicate that single-cell encapsulation of chondrocytes within alginate microgels, regardless of ascorbate, dramatically increases collagen production compared to monolayer controls.

Chondrocyte Viability in Alginate Microgels

After 10 days of culture in alginate microgels, SW1353 cell viability was evaluated using a dead stain (Trypan Blue exclusion). When 50 µg/mL ascorbate was present in the media, the cell viability was 70.3 ± 4.3%. Without ascorbate, the cell viability was 62.4 ± 7.7% (Figure 3C). The difference in cell viability was not significantly different with and without ascorbate in the media (p-value = 0.0957, Welch two sample t-test), indicating that 50 µg/mL of ascorbate does not affect SW1353 viability in alginate microgels.

Elastic Moduli Characterization of Hydrogel Constructs

To create agarose-alginate constructs, 1.5% w/w alginate microgels were suspended in a 4.5% w/w agarose solution, poured into a cylindrical mold, and gelled. To quantify the mechanical properties of these hydrogels with and without embedded microgels, the storage and loss moduli of the 1.5% w/w alginate, the 4.5% w/w agarose, and the 4.5% w/w agarose with 20% v/v 1.5% w/w alginate microgels were measured on a parallel plate rheometer (Table S1). The 1.5% w/w alginate ($G' \sim 660$ Pa, $G'' \sim 35$ Pa, $\omega = 1$ rad/s) had storage and elastic moduli two orders of magnitude lower than the agarose ($G' \sim 32$ kPa, $G'' \sim 2.3$ kPa, $\omega = 1$ rad/s) (Figure S2). There was no significant difference between the stiffness of the agarose gels with and without embedded alginate microgels indicating that bulk mechanical properties were not affected by microgel encapsulation.

Metabolomic Profiling of Hydrogel Constructs containing compressed and uncompressed monolayer and microgel cells

To examine the effects of microgel encapsulation on chondrocyte mechanotransduction, SW1353 cells were encapsulated in alginate microgels, the microgels were suspended in a 4.5%

w/w agarose solution, poured into a cylindrical mold, and gelled (Figure 1 B). Metabolomic profiling was performed on compressed and uncompressed constructs. Dynamic compression at 1.1 Hz was applied using a custom-built bioreactor for 15 minutes (Figure 1 C) [8]. Sample groups included cells encapsulated in microgels before embedding in agarose and monolayer control cells encapsulated directly into agarose after monolayer culture. Thus, four conditions of SW1353 cells in agarose were compared: cells in microgels that were compressed and uncompressed and cells from monolayers that were compressed and uncompressed as a control. Using heatmaps, principal components analysis, and volcano plots, distinct metabolic profiles between these four conditions were found using HPLC-MS (Figures 4-5). Both hierarchical clustering and principal components analysis (PCA) found substantial differences between the metabolomic profiles of microgels and monolayer chondrocytes independent of compression (Figure 4). Hierarchical clustering of the top 25 metabolites that differ between all groups shows a large cluster of metabolites are downregulated in uncompressed microgels (Figure 4A light purple columns) and another cluster is up-regulated in compressed monolayer. (Figure 4A bright green columns).

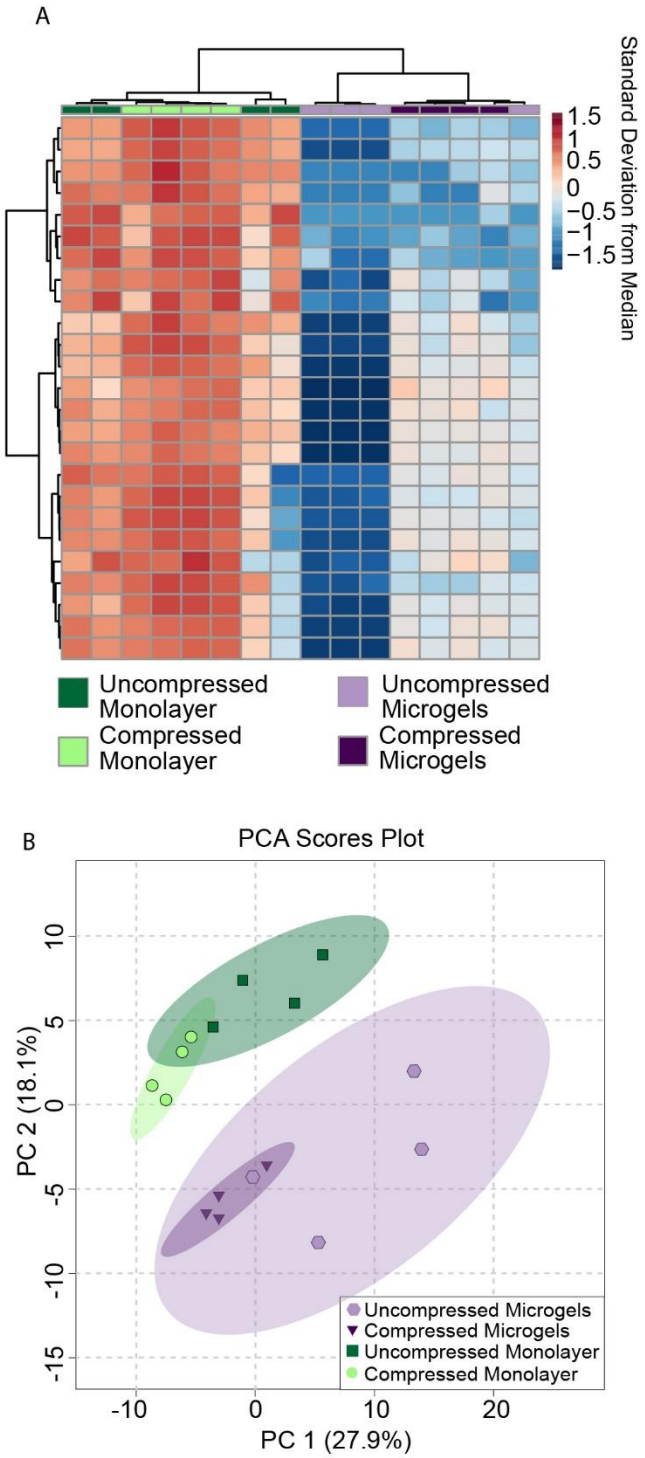


Figure 4. (A) Heat map of top 25 metabolites from SW1353 cells. (B) 2-D scores plot of PCA analysis for metabolites from SW1353 cells cultured with complete media supplemented with 50µg/mL L-sodium ascorbate.

PCA is an unsupervised method to assess overall variation and potential similarity between samples among different experimental groups. The microgel and monolayer groups display clear separation when projected onto the principal components, indicating that these groups have distinct metabolomic profiles (Figure 4B green monolayer compared to purple microgels). These groups also show moderate overlap between compressed and uncompressed samples that is further analyzed using two sample PCA analysis and volcano plots (Figure 5).

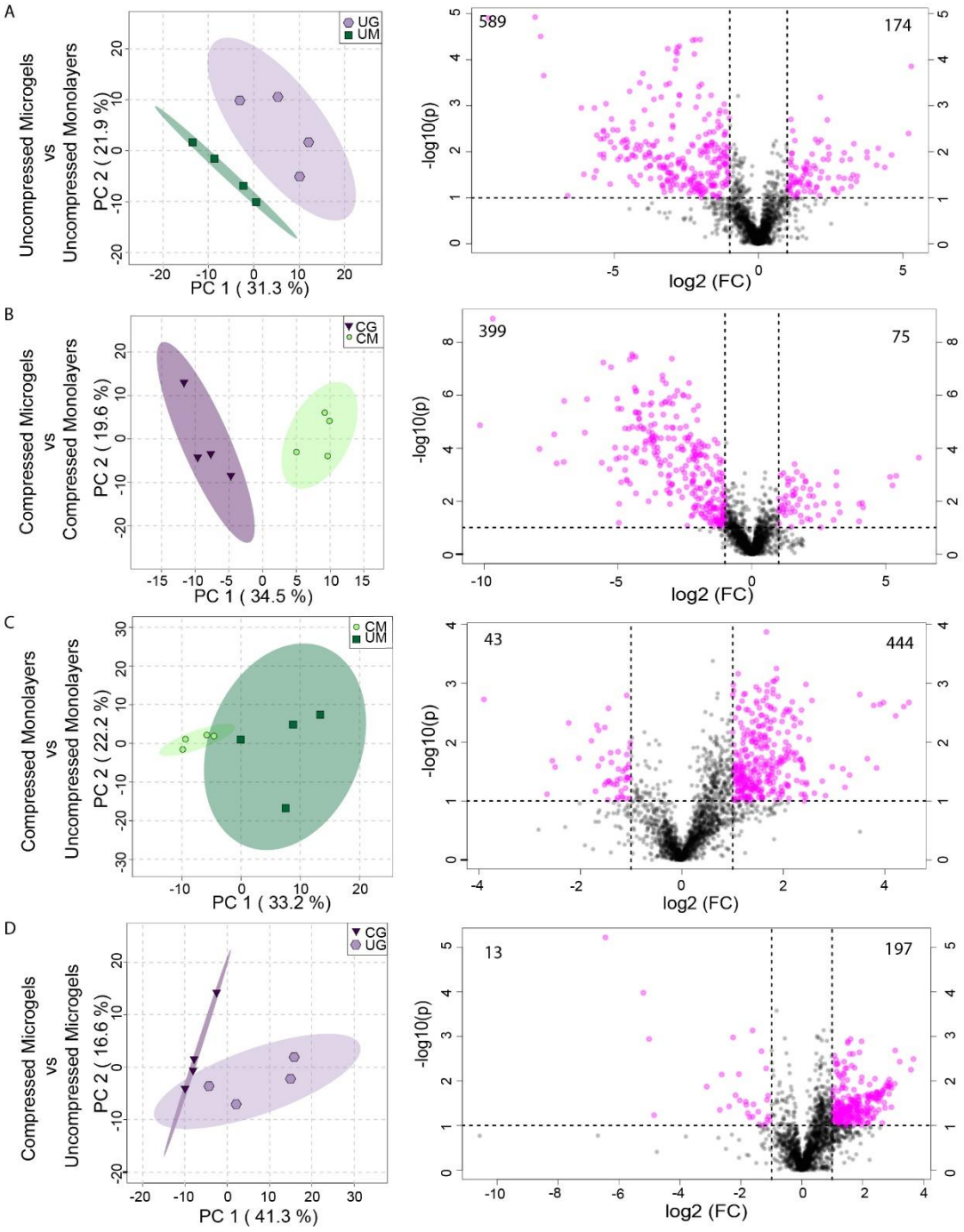


Figure 5. 2-D score plots for PCA analysis (left) and volcano plots (right) for metabolites from SW1353 cells. (A) Uncompressed Monolayers (UM) vs. Uncompressed Microgels (UG). (B) Compressed Microgels (CG) vs. Compressed Monolayers (CM). (C) Uncompressed Monolayers vs. Compressed Monolayers. (D) Compressed Microgels vs. Uncompressed Microgels. All comparisons are made for cells cultured in complete media supplemented with 50 μg/mL L-

sodium ascorbate. The numbers in the corners of the volcano plots denote the number of down- (left) and up- (right) regulated metabolites.

There were substantial differences between metabolomic profiles of uncompressed microgel and uncompressed monolayer samples, as seen in the volcano plots, where the x-axis is the relative fold change in metabolite presence and the y-axis is the negative logarithm of the p-value for each metabolite. Significantly different metabolites are shown in pink, with 174 metabolites up-regulated in uncompressed microgels and 589 up-regulated in uncompressed monolayer (Figure 5A, right). Furthermore, there were substantial differences between the profiles of compressed microgels and compressed monolayer cells upon pairwise comparison (Figure 5B). Metabolomic profiles differed between compressed microgels and compressed monolayers with 75 metabolites up-regulated in microgels and 399 metabolites up-regulated in monolayer samples (Figure 5B, right). Within both the monolayer and microgel groups, compression induced a robust metabolomic response for SW1353 chondrocytes (Figure 5 C-D). Furthermore, compressed samples showed decreased variability in metabolomic profiles, as previously observed [8,22]. Dynamic compression in microgels induced upregulation of 197 metabolites and downregulation of 13 metabolites when compared with uncompressed controls (Figure 5 D, right). Finally, microgels had distinct compression-induced responses from compressed monolayer controls (Figure 5B).

To identify patterns of coregulated metabolites between groups, hierarchical clustering was applied to the median metabolite intensities. This analysis was performed across all eight experimental groups, microgels and monolayers cultured with and without ascorbate that are compressed and uncompressed, to capture all potential experimental features. This median

clustering also found similarity between uncompressed microgels cultured with ascorbate and compressed microgels without ascorbate, indicating that compression can mimic the effects of ascorbate on chondrocytes metabolomic profiles (Figure S3-7).

To determine the biological relevance of coregulated metabolites, each cluster from the median heatmap (Figure S3) was assessed for cellular pathways. The resulting up-regulated pathways (false discovery rate corrected p-values <0.05) were from four main groups: compressed microgels cultured with ascorbate (Figure S5A Cluster #3), compressed monolayers cultured with ascorbate (Figure S7 Cluster #7), compressed monolayers cultured without ascorbate (Figures S4B and S5B Clusters #2 and 4), and uncompressed monolayers cultured without ascorbate (Figure S6B Cluster #6). Key pathway results are presented here with complete results in the supplemental information (Figure S8 and Table S2).

We detected many pathways solely up-regulated in the compressed microgels cultured with ascorbate (Figure S5A Cluster #3). Here, the main pathways are associated with amino acid, energy, and hormone-related metabolism. Two vitamin B pathways are also significantly up-regulated – vitamin B6 and vitamin B5 metabolism. Vitamin B6 is involved in more than 140 different metabolic reactions in the cell and more importantly for this case, the supplementation of vitamin B6 reduces pro-inflammatory responses by suppressing pro-inflammatory cytokines IL-6 and TNF-alpha in patients with rheumatoid arthritis [36]. Meanwhile, vitamin B5 has potential for maintaining bone homeostasis [37]. Vitamin B5 is required to synthesize Coenzyme A, an essential cofactor for fatty acid metabolism that is also a known regulator of chondrocyte maturation [38,39].

Interestingly, many pathways relating to the ECM and PCM were up-regulated in compressed microgels cultured with ascorbate. The chondrocyte ECM and PCM are primarily composed of collagen. Collagen contains many glycine and proline residues. The data show that arginine and proline metabolism were up-regulated in compressed microgels, including proline upregulation. This pathway involves the biosynthesis and metabolism of several amino acids, including arginine, ornithine, proline, citrulline, and glutamate in mammals [40]. Additionally, N-glycan biosynthesis was up-regulated in compressed microgels cultured with ascorbate. Matrix proteoglycans utilize N-glycans and provide much of the compressive strength of cartilage by regulating the matrix hydration through interactions with water. The compressed microgels cultured with ascorbate and the compressed monolayer cultured with ascorbate both share the pathway for glycine, serine, alanine and threonine metabolism. These amino acids are also needed to synthesize PCM and ECM. Together, these pathways and the microscopy images suggest that collagen and matrix synthesis are likely up-regulated in compressed microgels cultured with ascorbate. Furthermore, both compression and cultured condition play a role in ECM and PCM production, but further mechanistic studies are necessary to determine how these key environmental stimuli drive matrix production.

Other common pathways between compressed microgel and monolayer samples with ascorbate are butanoate metabolism and glutathione metabolism. The former is responsible for L-glutamate degradation followed by a series of reactions that produce CoA-conjugated compounds. The latter is considered a major antioxidant and one of the indicators of cellular oxidative stress. While both groups show the same metabolite again (pyroglutamic acid), the

monolayer compressed group expresses trypanothione compared to the microgel compressed group, which expresses gamma-glutamylcysteine.

In compressed monolayers cultured with ascorbate (Figure S7 Cluster #7), upregulation of many CoA-conjugated metabolites were detected, including Palmityl-CoA, Linoleoyl-CoA, and Arachidonyl-CoA. Importantly, Acetyl-CoA is a downstream product of these Acyl-CoA metabolites and regulates chondrocyte maturation [39]. Acetyl-CoA provides acetyl groups to the citric acid cycle, a key component of energy metabolism. Energy pathways also play an important role in the development, maintenance and repair of extracellular matrix (ECM) [41]. These results further confirm previous studies which found that compression is a key factor for modeling chondrocyte mechanotransduction [9].

Conclusions

Chondrocytes were encapsulated in alginate microgels, imaged over ten days, and evaluated for collagen formation. These data indicate that collagen VI production is greatly increased in microgels compared to monolayer cultures. Primary human chondrocytes produced more collagen VI than SW1353 cells when cultured in microgels or monolayers as observed using immunofluorescence with confocal microscopy and auto-fluorescence using epifluorescence microscopy. Thus, these results indicate that chondrocytes are more likely to form a PCM comprised of collagen VI in 3-D alginate microgels than in monolayers. Additionally, chondrocytes were encapsulated in physiologically stiff agarose gels and subjected to physiological dynamic compression. The cells cultured in microgels had substantially different metabolomic profiles compared to cells cultured in monolayers. Compression induced a robust metabolic response in both monolayer controls and microgel-encapsulated chondrocytes. Upon

metabolomic pathway analysis, the microgel encapsulated chondrocytes were found to have up-regulated pathways related to amino acid synthesis and central energy metabolism. Together, these pathways and the microscopy images suggest that collagen and matrix synthesis is increased in microgels compared to monolayers.

In summary, we show that microgels created using drop-based microfluidics can provide a robust 3-D culture environment for individual chondrons in vitro. Encapsulation of the cells in small volumes of alginate enables the development of type VI collagen-rich PCM surrounding individual cells. This novel method eliminates the use of potentially harmful digestive processes that are typically applied to isolate single cells in traditional bulk alginate culture in order to isolate cells with developed PCM. We demonstrate that these single cell microgels can be embedded into physiologically stiff agarose for studying the metabolic response to compression. This is the first instance of chondrons encapsulated in alginate microgels and embedded in physiologically stiff agarose, enabling more realistic in vitro models of chondrocyte mechanotransduction that better mimic in vivo structure. These microscale constructs allow the manipulation of thousands of single cells in microenvironments that can be embedded into other hydrogels of interest. We expect that this work will have an impact on future studies of chondrocyte mechanotransduction and tissue engineering.

Supplementary Materials

The following supporting information can be downloaded at: https://www.mdpi.com/article/10.3390/cells11050900/s1, Figure S1: Brightfield and fluorescence images of SW1353 cells; Figure S2: Storage and loss moduli versus angular frequency of hydrogels; Figure S3: Median metabolites across all experimental groups; Figure

S4: Median metabolites across all experimental group for clusters 1 and 2; Figure S5: Median metabolites across all experimental group for clusters 3 and 4; Figure S6: Median metabolites across all experimental group for clusters 5 and 6; Figure S7: Median metabolites across all experimental group for cluster 7; Figure S8: Venn diagram of significant pathways for each group; Table S1: Storage and loss moduli versus angular frequency of hydrogels; Table S2: All significant pathways found and the corresponding gamma values and matched metabolites.

Author Contributions

Conceptualization, J.P.F., R.K.J. and C.B.C.; Methodology, J.P.F., P.P.B., A.E.E., R.K.J. and C.B.C.; Software, J.P.F. and A.E.E.; Validation, J.P.F., P.P.B. and A.E.E.; Formal Analysis, J.P.F. and A.E.E.; Investigation, J.P.F., P.P.B., A.E.E., Z.K.A. and J.N.W.; Resources, R.K.J. and C.B.C.; Data Curation, J.P.F. and A.E.E.; Writing—Original Draft Preparation, J.P.F., P.P.B., A.E.E., R.K.J. and C.B.C.; Writing—Review & Editing, J.P.F., P.P.B., A.E.E., R.K.J. and C.B.C.; Visualization, J.P.F. and A.E.E.; Supervision, R.K.J. and C.B.C.; Project Administration, R.K.J. and C.B.C.; Funding Acquisition, R.K.J. and C.B.C. All authors have read and agreed to the published version of the manuscript.

Funding

This research was funded by the National Institutes of Health [R01AR073964 to RKJ] and National Science Foundation [CAREER 1753352 to CBC, 1554708 to RKJ]. The funding sources had no role in the design or execution of the study.

Institutional Review Board Statement

After review by the Montana State University Institutional Review Board, this study was performed under the NIH Exemption 4 Human Subjects Research.

Informed Consent Statement

Patient consent was waived as a 4B exemption on 13 October 2011, by the Montana State University Institutional Review Board

Data Availability Statement

The data presented in this study are available as supplementary files and on request from the corresponding author.

Acknowledgments

We thank the Montana State University Proteomics, Metabolomics, and Mass Spectrometry Facility for the use of equipment. The facility in was made possible in part by the MJ Murdock Charitable Trust, the National Institute of General Medical Sciences of the National Institutes of Health under Award Numbers P20GM103474 and S10OD28650, and the MSU Office of Research, Economic Development and Graduate Education.

Works Cited

1. Hunter, D.J.; Nevitt, M.; Losina, E.; Kraus, V. Biomarkers for osteoarthritis: current position and steps towards further validation. Best Pract Res Clin Rheumatol 2014, 28, 61-71, doi:10.1016/j.berh.2014.01.007.

2. Muir, H. The chondrocyte, architect of cartilage. Biomechanics, structure, function and molecular biology of cartilage matrix macromolecules. Bioessays 1995, 17, 1039-1048, doi:10.1002/bies.950171208.

3. Wilusz, R.E.; Sanchez-Adams, J.; Guilak, F. The structure and function of the pericellular matrix of articular cartilage. Matrix Biol 2014, 39, 25-32, doi:10.1016/j.matbio.2014.08.009.

4. Harris, M.D.; Anderson, A.E.; Henak, C.R.; Ellis, B.J.; Peters, C.L.; Weiss, J.A. Finite element prediction of cartilage contact stresses in normal human hips. J Orthop Res 2012, 30, 1133-1139, doi:10.1002/jor.22040.

5. Alexopoulos, L.G.; Haider, M.A.; Vail, T.P.; Guilak, F. Alterations in the mechanical properties of the human chondrocyte pericellular matrix with osteoarthritis. J Biomech Eng 2003, 125, 323-333, doi:10.1115/1.1579047.

6. Salinas, D.; Mumey, B.M.; June, R.K. Physiological dynamic compression regulates central energy metabolism in primary human chondrocytes. Biomech Model Mechanobiol 2019, 18, 69-77, doi:10.1007/s10237-018-1068-x.

7. Chowdhury, T.T.; Arghandawi, S.; Brand, J.; Akanji, O.O.; Bader, D.L.; Salter, D.M.; Lee, D.A. Dynamic compression counteracts IL-1beta induced inducible nitric oxide synthase and cyclo-oxygenase-2 expression in chondrocyte/agarose constructs. Arthritis Res Ther 2008, 10, R35, doi:10.1186/ar2389.

8. Jutila, A.A.; Zignego, D.L.; Hwang, B.K.; Hilmer, J.K.; Hamerly, T.; Minor, C.A.; Walk, S.T.; June, R.K. Candidate mediators of chondrocyte mechanotransduction via targeted and untargeted metabolomic measurements. Arch Biochem Biophys 2014, 545, 116-123, doi:10.1016/j.abb.2014.01.011.

9. Jutila, A.A.; Zignego, D.L.; Schell, W.J.; June, R.K. Encapsulation of chondrocytes in high-stiffness agarose microenvironments for in vitro modeling of osteoarthritis mechanotransduction. Ann Biomed Eng 2015, 43, 1132-1144, doi:10.1007/s10439-014-1183-5.

10. McCutchen, C.N.; Zignego, D.L.; June, R.K. Metabolic responses induced by compression of chondrocytes in variable-stiffness microenvironments. J Biomech 2017, 64, 49-58, doi:10.1016/j.jbiomech.2017.08.032.

11. Darling, E.M.; Wilusz, R.E.; Bolognesi, M.P.; Zauscher, S.; Guilak, F. Spatial mapping of the biomechanical properties of the pericellular matrix of articular cartilage measured in situ via atomic force microscopy. Biophys J 2010, 98, 2848-2856, doi:10.1016/j.bpj.2010.03.037.

12. McLeod, M.A.; Wilusz, R.E.; Guilak, F. Depth-dependent anisotropy of the micromechanical properties of the extracellular and pericellular matrices of articular cartilage evaluated via atomic force microscopy. J Biomech 2013, 46, 586-592, doi:10.1016/j.jbiomech.2012.09.003.

13. Hauselmann, H.J.; Fernandes, R.J.; Mok, S.S.; Schmid, T.M.; Block, J.A.; Aydelotte, M.B.; Kuettner, K.E.; Thonar, E.J. Phenotypic stability of bovine articular chondrocytes after long-term culture in alginate beads. Journal of Cell Science 1994, 107, 17-27.

14. Stoddart, M.J.; Ettinger, L.; Hauselmann, H.J. Generation of a scaffold free cartilage-like implant from a small amount of starting material. J Cell Mol Med 2006, 10, 480-492, doi:10.1111/j.1582-4934.2006.tb00413.x.

15. Randau, T.M.; Schildberg, F.A.; Alini, M.; Wimmer, M.D.; Haddouti el, M.; Gravius, S.; Ito, K.; Stoddart, M.J. The effect of dexamethasone and triiodothyronine on terminal differentiation of primary bovine chondrocytes and chondrogenically differentiated mesenchymal stem cells. PLoS One 2013, 8, e72973, doi:10.1371/journal.pone.0072973.

16. Stokke, B.T.; Draget, K.I.; Smidsrød, O.; Yuguchi, Y.; Urakawa, H.; Kajiwara, K. Small-Angle X-ray Scattering and Rheological Characterization of Alginate Gels. 1. Ca−Alginate Gels. Macromolecules 2000, 33, 1853-1863, doi:10.1021/ma991559q.

17. Yuguchi, Y.; Urakawa, H.; Kajiwara, K.; Draget, K.I.; Stokke, B.T. Small-angle X-ray scattering and rheological characterization of alginate gels. 2. Time-resolved studies on ionotropic gels. Journal of Molecular Structure 2000, 554, 21-34, doi:10.1016/s0022-2860(00)00556-1.

18. Bassett, D.C.; Håti, A.G.; Melø, T.B.; Stokke, B.T.; Sikorski, P. Competitive ligand exchange of crosslinking ions for ionotropic hydrogel formation. Journal of Materials Chemistry B 2016, 4, 6175-6182, doi:10.1039/c6tb01812b.

19. Hati, A.G.; Bassett, D.C.; Ribe, J.M.; Sikorski, P.; Weitz, D.A.; Stokke, B.T. Versatile, cell and chip friendly method to gel alginate in microfluidic devices. Lab Chip 2016, 16, 3718-3727, doi:10.1039/c6lc00769d.

20. Utech, S.; Prodanovic, R.; Mao, A.S.; Ostafe, R.; Mooney, D.J.; Weitz, D.A. Microfluidic Generation of Monodisperse, Structurally Homogeneous Alginate Microgels for Cell Encapsulation and 3D Cell Culture. Adv Healthc Mater 2015, 4, 1628-1633, doi:10.1002/adhm.201500021.

21. McGuigan, A.P.; Bruzewicz, D.A.; Glavan, A.; Butte, M.J.; Whitesides, G.M. Cell encapsulation in sub-mm sized gel modules using replica molding. PLoS One 2008, 3, e2258, doi:10.1371/journal.pone.0002258.

22. Zignego, D.L.; Hilmer, J.K.; June, R.K. Mechanotransduction in primary human osteoarthritic chondrocytes is mediated by metabolism of energy, lipids, and amino acids. J Biomech 2015, 48, 4253-4261, doi:10.1016/j.jbiomech.2015.10.038.

23. Zignego, D.L.; Hilmer, J.K.; Bothner, B.; Schell, W.J.; June, R.K. Primary human chondrocytes respond to compression with phosphoproteomic signatures that include microtubule activation. J Biomech 2019, 97, 109367, doi:10.1016/j.jbiomech.2019.109367.

24. Duffy, D.C.; McDonald, J.C.; Schueller, O.J.; Whitesides, G.M. Rapid Prototyping of Microfluidic Systems in Poly(dimethylsiloxane). Anal Chem 1998, 70, 4974-4984, doi:10.1021/ac980656z.

25. Rueden, C.T.; Schindelin, J.; Hiner, M.C.; DeZonia, B.E.; Walter, A.E.; Arena, E.T.; Eliceiri, K.W. ImageJ2: ImageJ for the next generation of scientific image data. BMC Bioinformatics 2017, 18, 529, doi:10.1186/s12859-017-1934-z.

26. Tinevez, J.Y.; Perry, N.; Schindelin, J.; Hoopes, G.M.; Reynolds, G.D.; Laplantine, E.; Bednarek, S.Y.; Shorte, S.L.; Eliceiri, K.W. TrackMate: An open and extensible platform for single-particle tracking. Methods 2017, 115, 80-90, doi:10.1016/j.ymeth.2016.09.016.

27. Zignego, D.L.; Jutila, A.A.; Gelbke, M.K.; Gannon, D.M.; June, R.K. The mechanical microenvironment of high concentration agarose for applying deformation to primary chondrocytes. J Biomech 2014, 47, 2143-2148, doi:10.1016/j.jbiomech.2013.10.051.

28. Carlson, A.K.; Rawle, R.A.; Wallace, C.W.; Brooks, E.G.; Adams, E.; Greenwood, M.C.; Olmer, M.; Lotz, M.K.; Bothner, B.; June, R.K. Characterization of synovial fluid metabolomic phenotypes of cartilage morphological changes associated with osteoarthritis. Osteoarthritis Cartilage 2019, 27, 1174-1184, doi:10.1016/j.joca.2019.04.007.

29. R Core Team R: A language and environment for statistical

computing, R Foundation for Statistical Computing: Vienna, Austria 2019.

30. Wickham, H. tidyverse: Easily Install and Load the

'Tidyverse', 2017.

31. Daniel, J.C.; Pauli, B.U.; Kuettner, K.E. Synthesis of Cartilage Matrix by Mammalian Chondrocytes In Vitro. III. Effects of Ascorbate. The journal of cell biology 1984, 99.

32. Benya, P.D.; Shaffer, J.D. Dedifferentiated Chondrocytes Reexpress the Differentiated Collagen Phenotype When Cultured in Agarose Gels. Cell 1982, 30, 215-224, doi:Doi 10.1016/0092-8674(82)90027-7.

33. Andersson-Engels, S.; Johansson, J.; Svanberg, K.; Svanberg, S. Fluorescence imaging and point measurements of tissue: applications to the demarcation of malignant tumors and atherosclerotic lesions from normal tissue. Photochem Photobiol 1991, 53, 807-814, doi:10.1111/j.1751-1097.1991.tb09895.x.

34. Hoell, T.; Huschak, G.; Beier, A.; Huttmann, G.; Minkus, Y.; Holzhausen, H.J.; Meisel, H.J. Auto fluorescence of intervertebral disc tissue: a new diagnostic tool. Eur Spine J 2006, 15 Suppl 3, S345-353, doi:10.1007/s00586-006-0157-1.

35. Rigacci, L.; Alterini, R.; Bernabei, P.A.; Ferrini, P.R.; Agati, G.; Fusi, F.; Monici, M. Multispectral Imaging Autofluorescence Microscopy for the Analysis of Lymph-Node Tissues. Photochemistry and Photobiology 2000, 71, doi:10.1562/0031-8655(2000)071<0737:Miamft>2.0.Co;2.

36. Huang, S.C.; Wei, J.C.; Wu, D.J.; Huang, Y.C. Vitamin B(6) supplementation improves pro-inflammatory responses in patients with rheumatoid arthritis. Eur J Clin Nutr 2010, 64, 1007-1013, doi:10.1038/ejcn.2010.107.

37. Ma, Q.; Liang, M.; Tang, X.; Luo, F.; Dou, C. Vitamin B5 inhibit RANKL induced osteoclastogenesis and ovariectomy induced osteoporosis by scavenging ROS generation. American journal of translational research 2019, 11, 5008.

38. Nelson, D.L.; Cox, M.M. Lehniger: Principals of Biochemistry; Company, F.a., Ed.; 2008.

39. Kosai, A.; Horike, N.; Takei, Y.; Yamashita, A.; Fujita, K.; Kamatani, T.; Tsumaki, N. Changes in acetyl-CoA mediate Sik3-induced maturation of chondrocytes in endochondral bone formation. Biochem Biophys Res Commun 2019, 516, 1097-1102, doi:10.1016/j.bbrc.2019.06.139.

40. Kanehisa, M.; Furumichi, M.; Sato, Y.; Ishiguro-Watanabe, M.; Tanabe, M. KEGG: integrating viruses and cellular organisms. Nucleic Acids Res 2021, 49, D545-D551, doi:10.1093/nar/gkaa970.

41. Zhai, G. Alteration of metabolic pathways in osteoarthritis. Metabolites 2019, 9, 11.

CHAPTER FOUR

PERICELLULAR MATRIX FORMATION AND ATOMIC FORCE MICROSCOPY OF SINGLE PRIMARY HUMAN CHONDROCYTES CULTURED IN ALGINATE MICROGELS

Contribution of Authors and Co-Authors

Manuscript in Chapter 4

Author: Jacob P. Fredrikson

Contributions: J.P.F. designed research, performed research, analyzed data, and wrote the manuscript

Co-Author: Priyanka P. Brahmachary

Contributions: P.P.B designed research and performed research,

Co-Author: Ronald K. June

Contributions: R.K.J designed research

Co-Author: Lewis M. Cox

Contributions: L.M.C designed research, performed research, and wrote the manuscript

Co-Author: Connie B. Chang

Contributions: C.B.C designed research and wrote the manuscript

Manuscript Information

Jacob P. Fredrikson, Priyanka P Brahmachary, Ronald K. June, Lewis M. Cox, Connie B. Chang

Advanced Healthcare Materials

Status of Manuscript:
_x_ Prepared for submission to a peer-reviewed journal
____ Officially submitted to a peer-reviewed journal
____ Accepted by a peer-reviewed journal
____ Published in a peer-reviewed journal

Wiley

Abstract

One of the main components of articular cartilage is the chondrocyte's pericellular matrix (PCM) which is critical for regulating mechanotransduction, biochemical cues, and healthy cartilage development. Here, individual primary human chondrocytes (PHC) are encapsulated and cultured in alginate microgels created using drop-based microfluidics. This unique culturing method enables PCM formation and manipulation of individual cells. Over ten days, matrix formation is observed using autofluorescence imaging, and the elastic moduli of the isolated cells are measured using AFM. Matrix production and elastic modulus increase are observed for the chondrons cultured in microgels. Furthermore, the elastic modulus of cells grown in microgels increases ~10× over ten days, nearly reaching the elastic modulus of in vivo PCM. Using a Gaussian mixture model these data show that the population of PHCs grown in microgels exhibit two distinct populations; one with an elastic modulus averaging 9.0 kPa, and a second averaging 38.0 kPa. Overall, this work shows that microgels provide an excellent culture platform for the growth and isolation of PHCs, enabling PCM formation that is mechanically similar to native PCM. The microgel culture platform presented here has the potential to revolutionize cartilage regeneration procedures through the inclusion of in vitro developed PCM.

Introduction

Articular cartilage (AC) is the soft load-bearing tissue lining the interface of joints and is responsible for shock absorption and wear resistance from everyday activities such as walking, running, and jumping [1]. Acute injuries to the AC are limited in their ability to self-repair due to being avascular and the low cell density [2]. As a result, acute injuries to AC often lead to osteoarthritis (OA), the most common degenerative joint disease affecting over 300 million people worldwide [2–4]. Unfortunately, treatment options for acute injuries and OA are limited, and many treatments create mechanically inferior cartilage compared to native AC [2,4,5]. A laboratory-based tissue engineering approach to cartilage regeneration called matrix-assisted autologous chondrocyte transplantation (MACI) is currently one of the most effective treatment options [2,4]. In MACI, a small portion of healthy cartilage is taken from patients; the chondrocytes are isolated from the cartilage and expanded without passaging using standard in vitro cell culture [2,4,6,7]. The cells are then transplanted back into the patient with a membrane often made of porcine collagen I/III [2,4,6,7]. However, MACI has key drawbacks: (1) During expansion on tissue culture plastic, most chondrocytes quickly dedifferentiate into osteocytes and fibroblasts and lose the ability to produce cartilage [8–13]. (2) Expanded cells lack a pericellular matrix (PCM), a 1-5 μm layer of Collagen VI which closely encapsulates the cells in a cocoon-like manner and which is critical for cell viability, regulating mechanotransduction, regulating biochemical cues, and healthy cartilage development [14–18].

Culturing chondrocytes in three-dimensional (3-D) hydrogels, instead of on tissue culture plastic, has been shown to retain the chondrocyte phenotype and even regain it from dedifferentiated cells [5,19]. Additionally, chondrocytes grown in 3-D hydrogels produce PCM

and other matrix components [5,19,20]. However, the large bulk hydrogels typically used to culture cells, on the order of millimeters to centimeters, are poorly suited to MACI [2,21]. The bulk hydrogels are often not injectable, so cells must be extracted from the hydrogels to be compatible with MACI [21]. An alternative to bulk hydrogel culture is microscale hydrogel particles termed microgels. Microgels offer several advantages compared to bulk culture; (1) Microgels are more easily injectable due to their collective shear-thinning behavior [21–23]. (2) Reducing the length scale of the hydrogels to the microscale increases the surface area-to-volume ratio of the hydrogels and decreases diffusion lengths, thus facilitating the delivery of nutrients and other bio-active compounds to the encapsulated cells [21–23]. Our group has previously demonstrated a novel method of encapsulating single primary human chondrocytes (PHCs) in 3-D alginate microgels that are approximately 100 μm in diameter, which enables the cells to remain as chondrocytes and form a collagen VI-rich PCM [14]. Though differences in metabolomic profiles were analyzed, our studies did not determine how mechanically similar the in vitro developed PCM in microgels was compared to in vivo formed PCM. As the PCM directly transfer extracellular mechanical loads to chondrocytes, it is essential to understand the biomechanical properties of in vitro developed PCM [14–18,24].

Here, individual primary human chondrocytes (PHC) isolated from patient knees are encapsulated and cultured in alginate microgels created using drop-based microfluidics. This unique culture method enables PCM formation and manipulation of individual cells [14]. We then remove the alginate using chemical degradation and isolate the single cells into microscale wells created using soft lithography for downstream atomic force microscopy (AFM). Over ten days, matrix formation is observed using autofluorescence imaging, and the elastic moduli of the

isolated cells are measured using AFM. We compare the biochemical and biomechanical properties of cells cultured in monolayers to those cultured in microgels over ten days. We observe a negligible change in both matrix formation and elastic modulus of the chondrons cultured in monolayer. In contrast, matrix production and elastic modulus increase are observed for the chondrons cultured in microgels. Furthermore, the elastic modulus of cells grown in microgels increases ~10× over ten days nearly reaching the elastic modulus of in vivo PCM. We further analyze the AFM data using a Gaussian mixture model and find that the population of PHCs grown in microgels exhibit two heterogeneous outcomes of PCM formation. Specifically, two distinct populations were found; the first had an elastic modulus averaging 9.0 kPa, and the second had an elastic modulus averaging 38.0 kPa, accounting for 54% and 46% of the population, respectively. The second population was mechanically similar to in vivo PCM, which has an elastic modulus of 25-250 kPa [1,11,15–17,24,25]. Overall, we show that the in vitro microgel culture platform enables PHCs to form PCM that is mechanically similar to native PCM.

Results

An overview of the experimental methodology used in this work is presented in Figure 1. Briefly, we present a novel method for culturing individual PHCs within alginate microgels approximately 50 μm in diameter that are dissolved and measured under AFM. PHCs are harvested from donor tissue from patients undergoing knee replacements and encapsulated in alginate microgels using drop-based microfluidics, as we have previously developed (Figure 1A-B)[14]. The 3-D microenvironment of the alginate microgels enables the diffusion of nutrients to the encapsulated single cells and promotes the formation of PCM surrounding PHC chondrons

(Figure 1C). After 10 days in culture, the alginate surrounding the cells is dissolved (Figure 1D), and the cells are gently centrifuged down onto a microscale well-plate created using photolithography (Figure 1E). The mechanical properties of the chondrons are then measured using AFM (Figure 1F).

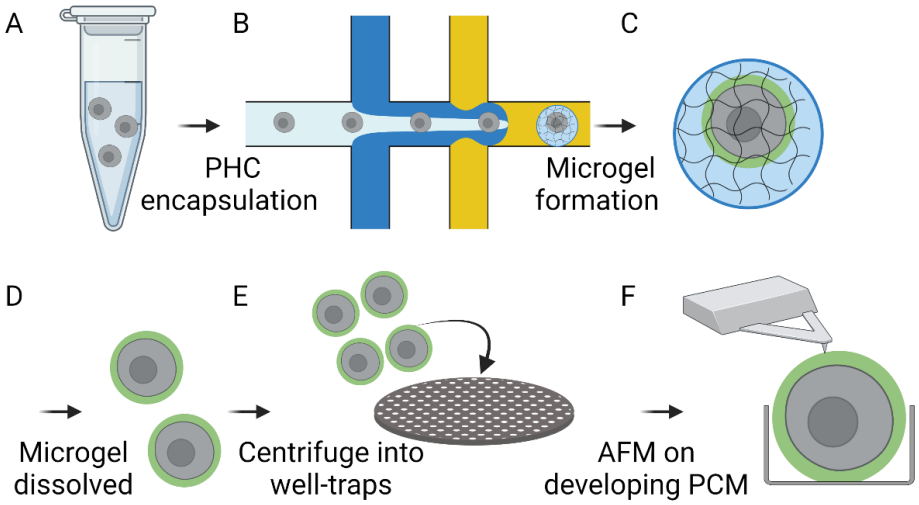


Figure 1: Schematic of Experimental Design; (A) Primary Human Chondrocytes (PHC) are suspended in the alginate precursor at 4 x 10^6 cells/mL. (B) PHCs are encapsulated in alginate microgels using drop-based microfluidics. (C) Microgels are washed and cultured in media for 10 days where chondrocytes form a collagen VI-rich PCM. (D) On days 1, 6, and 10, cells are removed from the microgels using sodium citrate and EDTA washes. (E) The released cells are centrifuged into well-traps created using photolithography. (F) The elastic moduli (G') of the cells are measured using AFM.

Analysis of PCM formation from single PHCs encapsulated within alginate microgels

Collagen VI and many other PCM components are autofluorescent when excited with wavelengths of light ranging from UV to blue (365–415 nm) [14,26–28]. Previously, we measured the formation of PCM in SW1353 cells, a chondrosarcoma cell line, over 10 days in microgel culture using autofluorescence imaging [14]. Results showed increased intensities

surrounding the cells, due to increased matrix protein expression of the cells cultured in alginate microgels compared to monolayer [14]. This label-free approach enabled PCM formation of the cells to be quantified over time while the cells were cultured in 3-D alginate microenvironments. Here, we apply the same methodology to quantify PCM formation of PHC cells isolated from knee replacements of female patients ages 63 to 72 (Bozeman Deaconess Hospital, MSU). As previously described, the isolated PHCs were subsequently cultured in both 3-D microgels and 2-D monolayers, where cells were cultured upon standard tissue culture flasks. Autofluorescence of cells was imaged on days 0, 1, 4, 7, and 10. PHCs grown in 2-D using standard tissue culture are known to produce minimal amounts of collagen VI in the PCM [19]. As a control experiment, we expanded PHCs on tissue culture flasks, and as expected, the autofluorescence images of the cells cultured in monolayers showed no observable signal on day 0 and no change in observable signal at any time point over the 10 days, indicating that the monolayer PHCs were forming minimal matrix components (SI Figure 1). By contrast, when PHCs were grown in microgels formed using drop-based microfluidics, autofluorescence visibly increased at each time point (Figure 2A -B).

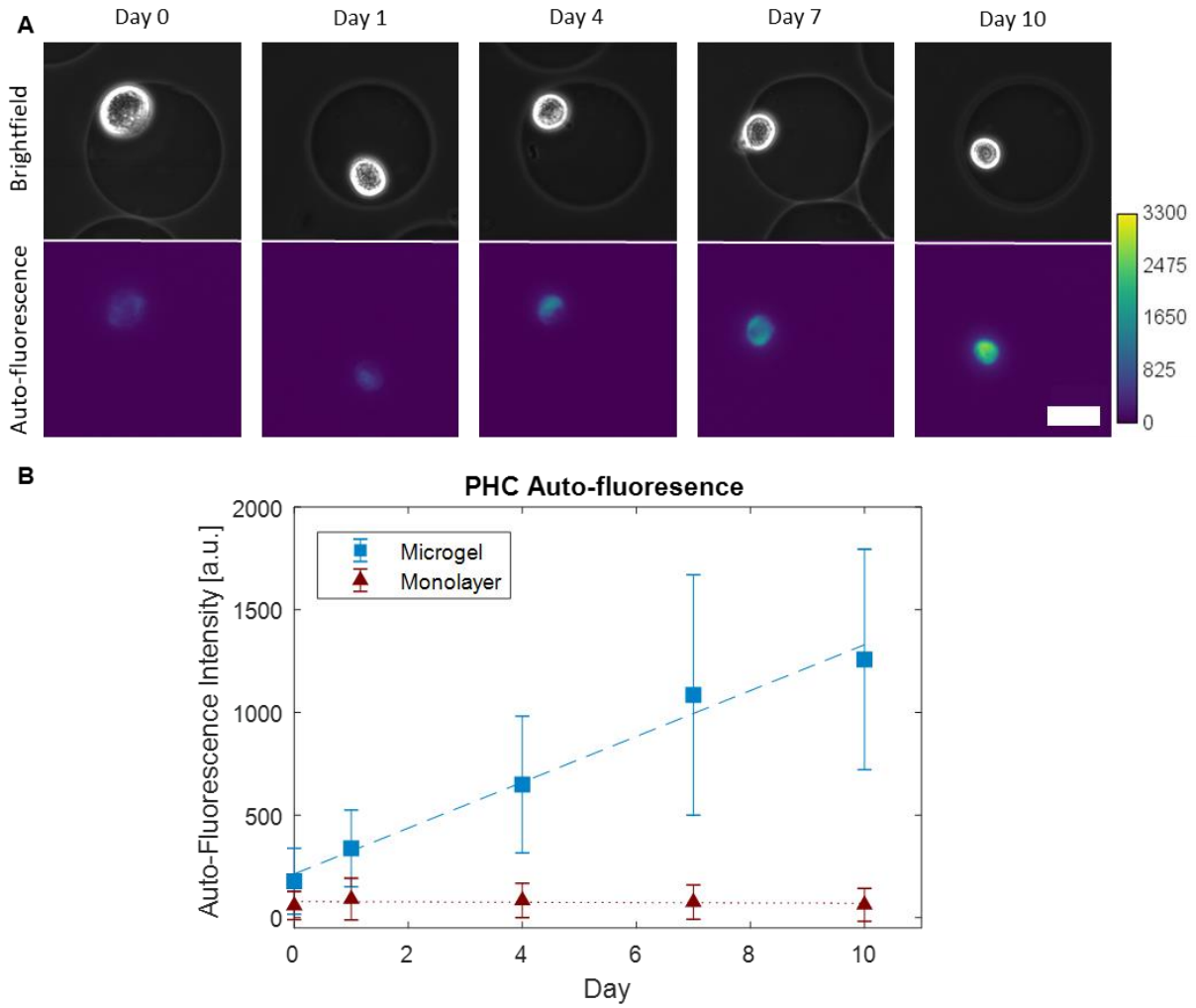


Figure 2: Representative images of single PHC cells cultured in microgels over 10 days using fluorescence imaging; (A) Brightfield and auto-fluorescence images (ex. 375 nm/em. 415 nm) of PHCs encapsulated in alginate microgels and cultured for 10 days. Scale bar is 25 μm. (B) Measured mean fluorescence intensities of imaged PHCs over time with multiple linear regressions. PHCs encapsulated in microgels (Blue squares, dashed) and PHCs grown in monolayers (Red triangles, dotted).

The cells grown in monolayers displayed a non-statistically significant change in fluorescence intensity over the ten days (Multiple linear regression, $p = 0.85$) (Figure 2B, red triangles). These results further confirm that chondrocytes grown in monolayers form minimal matrix components. However, cells grown in microgels showed a linear increase in fluorescence

intensity over time ($p << 0.0001$). Upon quantitative image analysis, the average fluorescence intensity across the area of each cell grown in microgels increased over the 10 days at a rate of 111 ± 12 a.u. /day (Figure 2B, blue squares). These results indicate that PHCs grown in alginate microgels produce matrix components at rates far greater than when grown in monolayer. We also compared PHC and SW1353 growth in monolayer versus microgels as a control experiment. The autofluorescence signal from PHCs grown in microgels increased ~ 70 a.u./day or ~5× faster than SW1353 cells in microgels, reaching a final pixel intensity of 1258 ± 537 a.u. and 347 ± 73 a.u., respectively (SI Figure 2). As expected, these results demonstrate that PHCs produce more matrix components than SW1535 cells, likely due to the PHCs expressing higher levels of anabolic genes that govern matrix production [29].

Our prior work using immunofluorescence has shown that PHCs grown in alginate microgels produce a PCM-like structure of collagen VI [14]. However, these experiments were performed without releasing the PHCs from the microgels. Although progress has recently been made using AFM force curves to image cell organelles without breaching the cell wall, quantifying the elastic moduli of subsurface structures at undetermined distances beneath the imaging surface of the probe tip remains infeasible [38]. To directly measure the elastic modulus of the PCM-like-structure we first dissolved the microgels using sodium citrate and EDTA, typical reagents for dissolving alginate, prior to AFM characterization of elastic modulus. The AFM probe tip is then able to directly actuate the PHCs without alginate impediment. To determine whether the dissolution process affected the structure of the developing PCM, PHCs on days 1, 6, and 10 were fixed and stained for collagen VI using antibodies before and after the dissolution of the alginate microgels. We compare the fluorescence of the cells before and after

microgel dissolution on days 1, 6, and 10. Representative cell images of intact microgels before and after microgel dissolution are seen in Figure 3.

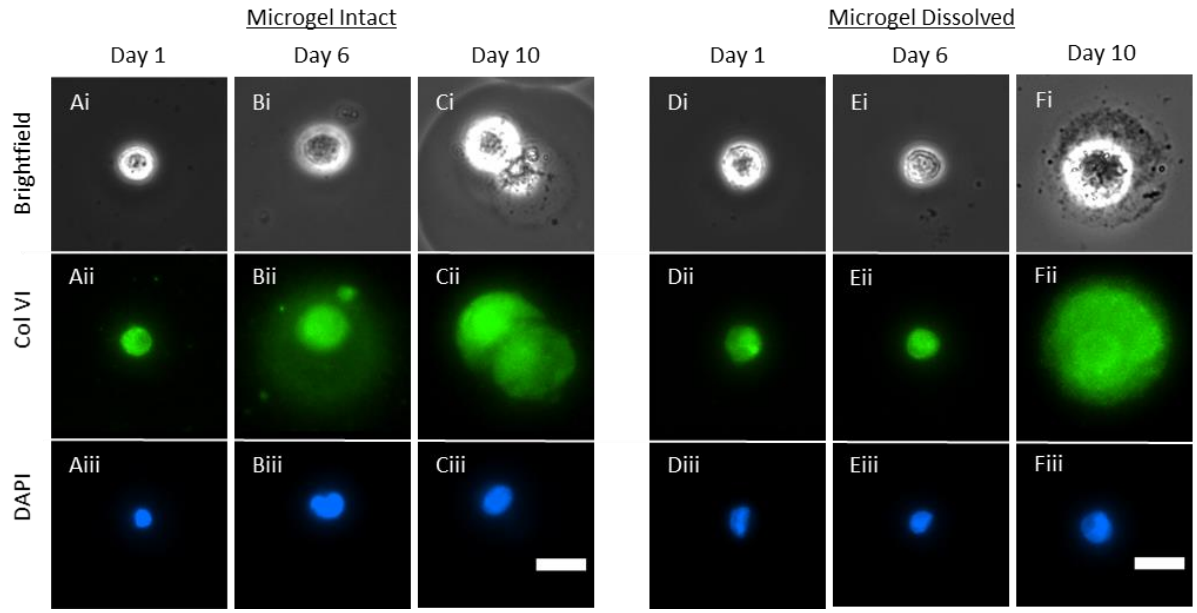


Figure 3: Collagen VI immunofluorescence; Representative Human Primary Chondrocyte (HPC) cultured in 1.5 % w/w alginate microgels with the microgels intact (A-C) and after dissolving the microgels using sodium citrate and EDTA (D-F). Cells were fixed and stained for collagen VI (green) and nuclei (DAPI blue). Cells were imaged on days 1, 6, and 10 to match with AFM time points. Scale bars are 25 μm

Prior to dissolution, a thin layer of collagen VI can be observed surrounding the cell on day 1 (Figure 3A ii), which grows thicker by day 6 (Figure 3Bii), and by day 10, the entire region surrounding the cell shows a significant amount of collagen VI, forming PCM similar to that typically seen in vivo surrounding the cell (Figure 3Cii) . After microgel dissolution on day 1, there appeared to be no difference in collagen VI expression between cells in microgels and cells after dissolution, and a thin layer of collagen VI immediately surrounding each cell remains (Figure 3Aii and 3Dii). Before microgel dissolution on day 6, a faint, more diffuse signal is

observed radiating from the cell (Figure 3Bii). However, after microgel dissolution on day 6, the diffuse signal seen further from the cell in intact microgels is no longer present (Figure 3Bii vs. 3Eii). In fact, only a thin layer of collagen VI immediately surrounding the cell remained (Figure 3Eii), similar to cells in microgels on day 1 (Figure 3Aii). After microgel dissolution on day 10, the region surrounding the cells shows a significant amount of collagen VI immediately enclosing the cell that extends into the surrounding area (Figure 3Cii vs. 3Fii). The PCM is also visible in brightfield once released from the microgel (Figure 3Fi). The matrix is stable and strong enough by day 10 that the dissolution of the microgel does not visibly affect the PCM produced by the PHC.

Elastic moduli (G') of individual PHCs released from alginate microgels and measured using AFM

Understanding the mechanical properties, primarily the elastic modulus (G'), of PCM development in vitro is critical to understanding how the chondrons will respond to mechanical forces if transplanted into patients. Here, AFM was used to measure the elastic moduli of individual PHCs over time after development in alginate microgels. First, the microgels were dissolved to isolate the growing chondrons on days 1, 6, and 10. The isolated chondrons were then suspended in PBS and gently centrifuged into microscale wells ($30 \times 30 \times 10$ μm) on a silicon wafer created using photolithography. The wells enabled single cells to be immobilized for subsequent AFM measurements. As a control study, PHCs grown in monolayers were also removed from 2-D tissue culture with sodium citrate and EDTA and centrifuged into microscale wells.

Once cells were isolated into the microscale wells, AFM measurements were performed on individual cells. Force versus displacement curves were acquired for 20 cells from each donor

(N = 3) on days 1, 6, and 10. In addition, an 8 × 8 force map covering a 1 μm^2 area was acquired for each cell. Representative force curves are shown in Figure 4A and 4B. The indentation depth to reach 2 nN for PHCs cultured in monolayer was compared to PHCs cultured in microgels. Cells cultured in monolayer reached an indentation force of 2 nN at average indentation depths ranging from 1.33 – 1.91 μm on days 1, 6, and 10 (Figure 4A). For chondrons cultured in microgels on day 1, the indentation depths were similar to those of cells cultured on monolayers with average indentation depths of 0.90 μm (Figure 4B, Day 1). However, on days 6 and 10, significant decreases in the indentation depths were observed, with the average indentation depths being 0.51 and 0.33 μm, respectively (Figure 4B, Day 6 and Day 10). This significant decrease in the indentation depth suggests that the chondrons grown in microgels are undergoing matrix production and stiffening.

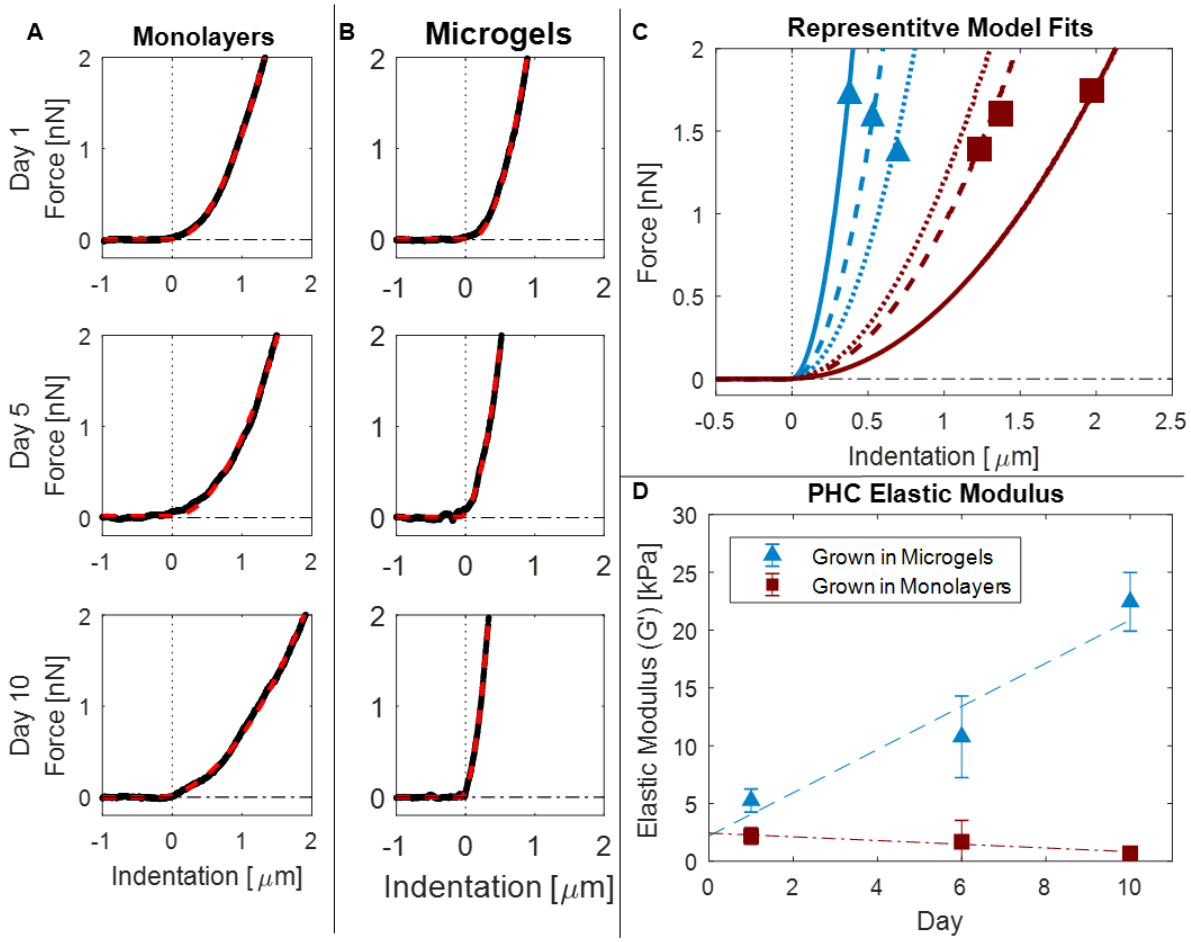


Figure 4: Atomic Force Microscopy Measurements; (A) Representative force vs. indentation curves of PHCs grown in monolayer on days 1, 6, and 10. Modeled Hertz fits are overlaid (red dashed). (B) Representative force vs. indentation curves of PHCs grown in microgels on days 1, 6, and 10. Modeled Hertz fits are overlaid (red dashed). (C) Average Hertz models for cells cultured in microgels (red, squares) and cells cultured in monolayers (blue, triangles) on days 1 (dotted), 6 (dashed), and 10 (solid). (D) Average elastic modulus and the standard deviation plotted for cells cultured in microgels (blue triangles, dashed) and monolayer (red squares, dotted dashes). At each time point, 20 cells were measured for each donor and culture condition (N = 3). When compared with a linear mixed effects model, modeled slopes were significantly different from each other ($p < 0.0001$) while the modeled intercepts were not ($p = 0.49$) Error bars represent the standard deviation between donors.

To calculate *G'* of the cells, the indentation force curves were fit using the standard Hertz model [30], and representative model fits are shown in Figure 4C. The representative model fits for cells grown in monolayers on days 1, 6, and 10 show a slight softening with force vs.

indentation curves becoming flatter as time increases (Figure 4C, red squares). Conversely, the representative model fits for cells grown in microgels on days 1, 6, and 10 show substantial stiffening of the chondrons with force vs. indentation curves becoming steeper as time increases (Figure 4C, blue triangles). Cells originally cultured in monolayer showed an average elastic modulus of 2.1 ± 0.7 kPa on day 1 and a minor decrease in stiffness with an average elastic modulus of 0.7 ± 0.3 kPa on day 10 (Figure 4D, red squares). By contrast, chondrons cultured in microgels showed an average elastic modulus of 5.2 ± 1.0 kPa on day 1 and a significant increase in stiffness with an average elastic modulus of 22.4 ± 2.5 kPa by day 10 (Figure 4D, blue triangles). The data were modeled using a linear mixed effects model to quantify trends in the elastic moduli data. From the linear mixed effects model, we found that over 10 days, the slopes of the two lines were significantly different from each other ($p < 1.0 \times 10^{-30}$); cells grown in monolayers decreased in stiffness at 0.16 ± 0.07 kPa/day, while cells grown in microgels increased in stiffness at 1.87 ± 0.7 kPa/day. Interestingly, cells grown in both monolayers and microgels showed a non-significant difference in the modeled day 0 elastic modulus ($p = 0.49$), suggesting that the observed difference in elastic moduli by day 1 was a factor of culturing over 24 h. These results indicate that microgel culture increases matrix production as quickly as 24 h.

Heterogeneous outcomes of PCM formation in microgels

Chondrocytes are spatially heterogenous with many phenotypic differences between chondrocytes depending upon the location of the cell within the cartilage [11,19,31,32]. The *G'* of the cells grown in microgels were further analyzed, and when the three donors were compared to one another, there was no difference in mean *G'* between donors on days 1, 6, and 10 ($p > 0.5$). Since there was no difference in donors at any time point, *G'* data at each time point of cells

grown in microgels were pooled together. On day 10, cells grown in microgels display a wide distribution of *G'* ranging from 3 to 116 kPa (Figure 5A Day 10). Histograms of all the individual *G'* on day 1 show a normal distribution with no skew (S = 0.08) and with a mean and median, approximately equal at 5.2 and 4.6 kPa, respectively (Figure 5A, Day 1). However, on day 10, the distribution becomes highly skewed (S = 0.44), and significant differences in the mean and median are observed at 22.4 and 12.9 kPa, respectively. These results indicate that on day 10, the mean *G'* is highly dominated by the skewed population.

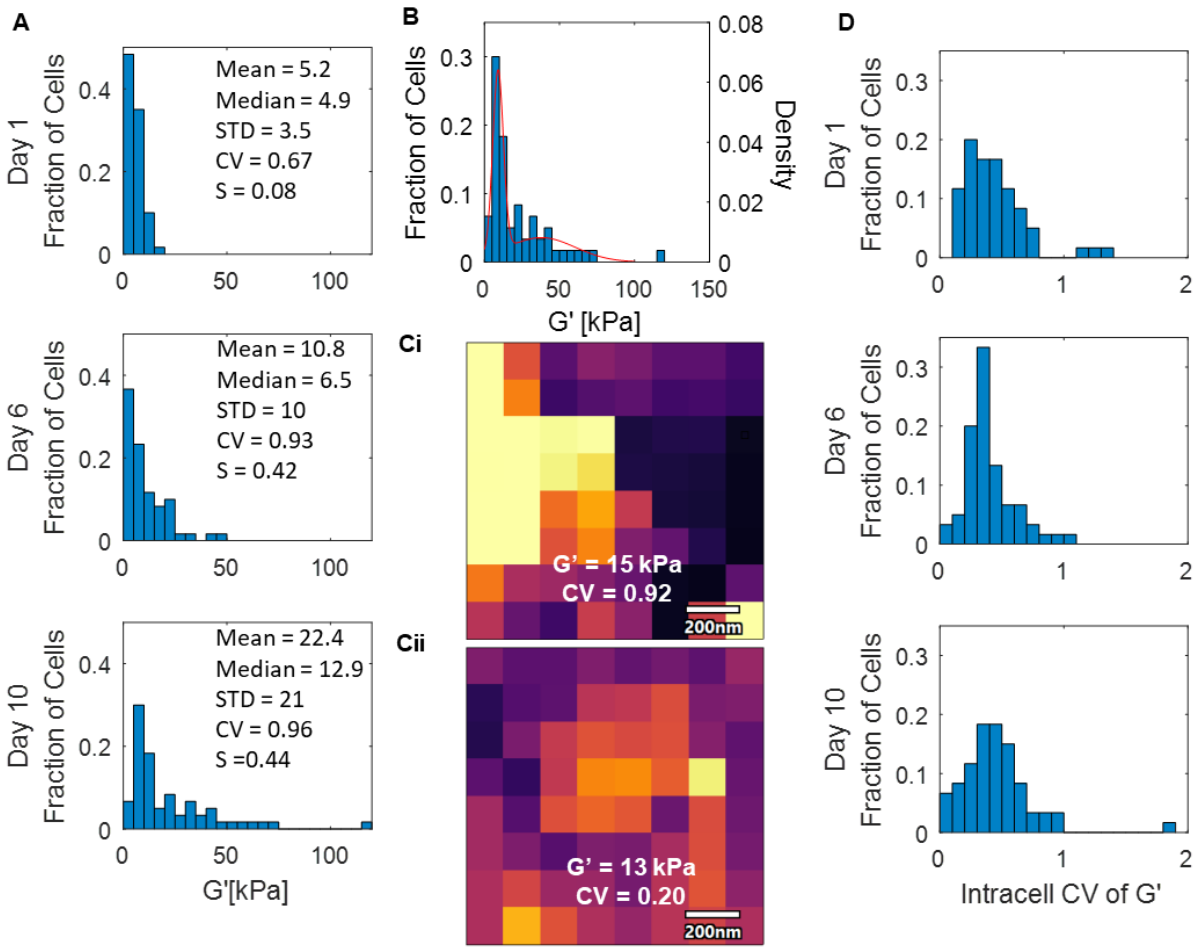


Figure 5: Elastic Moduli Heterogeneity. (A) Histograms of individual *G'* from PHCs grown in microgels on days 1, 6, and 10. 36.7% of cells reached physiological *G'* by day 10 while 26.7% did not change from day 1. (B) Histogram of *G'* for cells grown in microgels on day 10 plotted with the probability distribution function of the Gaussian mixture model with k =2. (C) Representative force maps of PHCs cultured in microgels on day 10 with similar *G'* (15 and 13 kPa) but different coefficients of variation (CV = 0.92 and 0.20). Scale bar is 200 nm. (D) Histograms of the intracell *G'* CV from each cell's force map on days 1, 6, and 10. Cells were cultured in microgels.

Therefore, a Gaussian mixture model (GMM) was applied to understand if the skew in *G'* on day 10 is due to a subpopulation of cells. After a GMM was applied for up to three populations (k =1 AIC = 532, k=2 AIC = 483, k=3 AIC = 486), the model found that two distinct distributions had the best fit with the first population mean at 9.0 ± 3.5 kPa, accounting for

53.8% of the population, and the second population mean at 38 ± 7.5 kPa, accounting for 46.2% of the population (Figure 5B). These results indicate that one subpopulation, accounting for 53.8% of the population, stiffens only slightly compared to day 1, with a difference in *G'* of approximately 4 kPa. The second subpopulation, accounting for 46.2% of the population, becomes physiologically stiff with *G'* approximately 34 kPa stiffer than on day 1. The second subpopulation is well within the range of native PCM (25-250 kPa) [1,11,15–17,24,25].

In addition to studying different PCM outcomes between cells, AFM enables the study of differences in intracell *G'* for each cell or the heterogeneity in elastic moduli at different points on individual cells. During AFM force curve acquisition, 8 × 8 force maps covering a 1 μm^2 area were acquired for each cell grown in microgels. The force maps were further analyzed, and quantification of the coefficient of variation (CV) for each cell revealed whether the matrix being produced is homogeneous or heterogeneous in *G'* over the 1 × 1 μm probed region. For example, representative force maps for two cells grown in microgels on day 10 are displayed in Figure 5Ci-ii with approximately equal *G'* (15 and 13 kPa). However, the cells display significantly different CVs indicating that the matrix in the probed regions were highly heterogeneous (Figure 5Ci, CV = 0.92) or homogenous (Figure 5Cii, CV = 0.20). Histograms of the intracell heterogeneity for N = 60 cells on days 1, 6, and 10 show a wide range of CV in *G'*, ranging from 0.06 to 1.82 (Figure 5D). Interestingly, the distributions of the intracell *G'* CV did not change over time for the PHCs cultured in microgels ($p > 0.25$). To understand whether the CV correlated with *G'*, linear regressions were applied to cells grown in microgels on days 1, 6, and 10. The linear regression revealed that on day 1, there was no relationship between the average *G'* and the CV of the cell ($p = 0.57$) (SI Figure 3 Day 1). However, on days 6 and 10, a positive

correlation between *G'* and the CV of the cell ($p = 0.018$ and 0.000018) was found, indicating that the matrix produced by cells with high *G'* was more likely to be heterogeneous than cells which did not produce a stiff matrix (SI Figure 3, Day 6 and Day 10).

Discussion

In this work we present a novel methodology for culturing single chondrocytes isolated from human knees within alginate microgels created using drop-based microfluidics, which enables a robust PCM to be formed around each cell over a 10 day incubation period. After dissolving the alginate surrounding the cells, the biochemical and mechanical properties of the cells were analyzed using autofluorescence, immunofluorescence, and AFM. We first monitored and quantified matrix formation in microgels using autofluorescence imaging. A significant increase in the autofluorescence signal of PHCs cultured in microgels was observed, compared to PHCs cultured in monolayer with negligible change in signal. As PHCs produce less collagen I, II, IV, and VI when cultured in monolayer compared to when cultured in 3-D, the difference in autofluorescence is consistent with the expected levels of collagen production. Measuring cellular autofluorescence enables matrix production to be measured over time without disturbing cells, unlike other assays such as immunofluorescence staining. Additionally, this analysis method enables quantification between different cell types. We discovered that the PHC autofluorescence signal increases nearly 5× faster than SW1353 cells, furthering the evidence to support that even osteoarthritic PHCs produce far more collagen than SW1353 cells.

The mechanical properties of chondrons grown in microgels were measured over 10 days. We found that the *G'* of cells cultured in microgels rapidly increased nearly 10× over 10

days in culture, with the average *G′* nearly reaching *G′* values seen in vivo (25 - 250 kPa) [1,11,15–17,24,25] . We additionally saw an increase in *G′* beginning as early as 24h in culture. Conversely, PHCs cultured in monolayers saw a negligible change in *G′* over 10 days. These results suggest that microgels are an excellent growth environment for single-cell PHCs, allowing them to form PCM similar to native PCM. Interestingly, the distribution of *G′* from PHCs grown in microgels on day 10 was heterogeneous, suggesting that subpopulations of cellular PCM production may exist. To determine the existence of these subpopulations, the *G′* data from cells grown in microgels on day 10 were analyzed with a Gaussian mixture model, and two distinct subpopulations of cells were found with means centered on 9 ± 3.5 and 38 ± 7.5 kPa. Each subpopulation accounted for approximately half of the cells, suggesting that half of the PHCs were responsible for most of the matrix formation in this study. One potential explanation is that the chondrocytes in this study were extracted from the entirety of full-thickness knee cartilage, which has diverse chondrocyte populations with chondrocytes in the deep zone experiencing higher compressive forces compared to chondrocytes in the superficial zone [1,11,19,31,32]. The subpopulations observed in our experiments could be due to the heterogeneity of cells within the cartilage, but additional studies targeting particular locations within the cartilage would be needed to confirm this. Future work comparing isolated populations from cartilage zones (e.g. superficial versus deep) and cultured in microgels could lead to insights into the ability to isolate more advantageous cells for cartilage repair.

These results demonstrate that microgel culture offers a superior alternative to traditional methods for growing and expanding chondrocytes in vitro that can be applied to innovating regenerative medicine techniques. The microgels allow chondrocytes to quickly form a

developed PCM in as short as 10 days. In MACI, cells are cultured for 3-6 weeks and by applying this microgel method for the final two weeks of culture, cells can potentially be implanted with a more developed PCM without altering total culturing time. Additionally, techniques such as MACI rely on the adherence of cells to a membrane scaffold to prevent cell leakage and improve cell viability. Microgels are easily injectable and would decrease the reliance on cellular adherence to membranes, as the microgels are less likely to leak due to their size [2,4,21,23]. Further, using non-invasive autofluorescence measurements, chondrocytes that produce the most matrix components can potentially be isolated and expanded to accelerate recovery times in regenerative cartilage procedures. Overall, we show that microgels provide an excellent culture platform for the growth and isolation of PHCs, enabling PCM formation that is mechanically similar to native PCM. The microgel culture platform presented here has the potential to revolutionize cartilage regeneration procedures by enhancing the growth of PCM surrounding individual chondrocytes.

Methods

Primary human chondrocyte harvest and cell culture

Primary Human Chondrocytes (PHCs) were obtained from female Stage-IV osteoarthritis patients ages 63-72 undergoing total joint replacement under IRB approval using established methods (N = 3/experiment) [33,34]. Isolated chondrocytes were seeded onto 60 × 15 mm tissue culture dishes and were maintained in Dulbecco's Modified Eagle's medium (DMEM) (Gibco, Waltham, MA, USA) supplemented with Fetal Bovine Serum (FBS) (10% v/v) (Bio-Techne, Minneapolis, MN, USA), penicillin (10,000 I.U./mL), and streptomycin (10,000 μg/mL) in 5% CO_2 at 37 °C. PHCs were passaged at 90% confluence and used in all experiments between

passages 1-4. For autofluorescence imaging and AFM experiments, cells were cultured with DMEM supplemented with FBS (10% v/v), penicillin (10,000 I.U./mL), streptomycin (10,000 μg/mL), and 50 μg/mL sodium ascorbate in 5% CO_2 at 37 °C.

SW1353 cell culture

SW1353 chondrocytes, a cell line initiated from a human chondrosarcoma and obtained from the American Type Culture Collection (ATCC, Manassas, VA, USA), were cultured using standard tissue culture techniques [14]. SW1353 cells were seeded onto 60 × 15 mm tissue culture dishes and were maintained in DMEM supplemented with FBS (10% v/v), penicillin (10,000 I.U./mL), and streptomycin (10,000 μg/mL) in 5% CO_2 at 37 °C. SW1353 cells were passaged at 90% confluence and used in all experiments between passages 5-20. For autofluorescence imaging experiments, cells were cultured with DMEM supplemented with FBS (10% v/v), penicillin (10,000 I.U./mL), streptomycin (10,000 μg/mL), and 50 μg/mL sodium ascorbate in 5% CO_2 at 37 °C.

PDMS microfluidic device fabrication

Negative master molds for the microfluidic devices were prepared using standard photolithography techniques [14]. Negative master molds were made with Nano SU-8-100 photoresist (Microchem, Round Rock, TX, USA) on 3” silicon wafers (University Wafer Inc., Boston, MA, USA University Wafer ID: 447). The microgel dropmaker was fabricated to be 50 μm in height. Devices were treated with (tridecafluoro-1,1,2,2-tetrahydrooctyl) trichlorosilane (1 v/v%) (Gelest) in NOVEC HFE 7500 fluorinated oil (3M, Saint Paul, MN, USA) and left for solvent evaporation overnight at 55 °C.

AFM well-trap fabrication

The well-traps were fabricated with Nano SU-8-100 photoresist (Microchem, Round Rock, TX, USA) on 3" silicon wafers (University Wafer Inc., Boston, MA, USA University Wafer ID: 447) using standard photolithography techniques [14]. To fit on the AFM, wafers were cut into ~ 1 × 1 cm pieces using a diamond-tipped scribe. Wells were designed as 30 × 30 × 10 μm rectangular prisms with heights of 10 μm. Developed well-traps were rinsed with phosphate buffered saline (PBS) prior to use.

Preparation of microfluidic microgel reagents

To make the continuous/oil phase, the surfactant Krytox 157 FSH (4% w/w) (Miller-Stephenson, Danbury, CT, USA) was added to NOVEC HFE 7500 fluorinated oil (3M, Saint Paul, MN, USA) [14]. The solution was filtered through a 0.2 μm hydrophobic polytetrafluoroethylene (PTFE) syringe filter to remove dust and other contaminants.

Two dispersed phase alginate precursor solutions were made as previously described [14,35]. The first (Alginate - precursor A) by mixing $CaCl_2$ (80 mM), Na_2EDTA (Ethylenediaminetetraacetic acid) (80 mM) (Fisher Chemical, Hampton, NH, USA), and 3-(Morpholin-4-yl) propane-1-sulfonic acid (MOPS) (40 mM) (VWR, Randor, PA, USA) with ultra-pure water (18.2 MΩ●cm). The second (Alginate - precursor B) was made by mixing Zn $(CH_3CO_2)_2$ (80 mM), EDDA (Ethylenediaminediacetic acid) (80 mM) (TCI Chemicals, Tokyo, Japan), and MOPS (40 mM) with ultra-pure water (50 mL) (18.2 MΩ●cm). The pH of both solutions was adjusted to 7.2 using NaOH (10 M). Sodium alginate (1.5% w/w) (Sigma, St. Louis, MO, USA, 9005-38-3) was mixed with each solution, then each was filtered through a 0.2 μm PES syringe filter (Argos Technologies).

Cell encapsulation and culture in microgels

To prepare cells for microgel encapsulation, cells were removed from monolayers using Trypsin-EDTA and then suspended in DMEM supplemented with FBS (10% v/v), penicillin (10,000 I.U./mL), and streptomycin (10,000 μg/mL))to inactivate the trypsin [14]. Cells were centrifuged at 500 × g for 5 min and washed 3× with PBS. The cells were then suspended in alginate-precursor A at 4×10^6 cells/mL and loaded into 1 mL syringes. Cells were encapsulated in 50 μm diameter alginate microgels following previous protocols [14,35]. The continuous flow rate used was Q_{Oil} = 2000 μL/h and the dispersed phase flow rate used was $Q_{AlgA} = Q_{AlgB}$ = 250 μL/h. After encapsulation and gelation, the microgels were washed with equal volumes of 1H,1H,2H,2H-Perfluoro-octanal (PFO) (647-42-7, VWR) in HFE7500 (20% v/v) and PBS to drops. The microgels were collected from the PBS and suspended in DMEM supplemented with FBS (10% v/v), penicillin (10,000 I.U./mL), streptomycin (10,000 μg/mL)), and 50 μg/mL sodium ascorbate. Microgels were added to 6 well plates at 1×10^6 cells/well and the volume brought to 2 mL with media. Sodium ascorbate was added every 3 days to supplement the media. Cells were incubated in 5% CO_2 at 37 °C.

Autofluorescence imaging and analysis

Cells were imaged using an epi-fluorescence microscope (Nikon Ti2 Eclipse) with a 20× objective over 10 days to capture bright field and autofluorescence (ex. 375nm/ em. 415nm). Cells were imaged on days 0, 1, 4, 7, and 10. To image cells in microgels, 5 μL of microgels and media were pipetted onto a PTFE-printed microscope slide. To image cells in monolayers, cells were grown on 35 mm glass-bottom dishes (MatTek). Approximately 20 cells from each donor (N = 3) were imaged per condition for each time point. The background intensity was subtracted

from each image using Fiji ImageJ and the fluorescence intensity of each cell was measured using the Fiji ImageJ distribution of TrackMate [36,37]. Autofluorescence curves were analyzed using a multiple linear regression model in Matlab.

Alginate dissolution and chondron isolation

To isolate chondrons from the alginate microgels, microgels were collected from the media via centrifugation for 1 min at 200 × g and vortexed for 2 min with sodium citrate (50mM) and EDTA (80mM) in PBS. The chondrons were then collected via centrifugation for 5 min at 500 × g and washed 3× in PBS.

Immunofluorescence staining and imaging

After days 1, 6, and 10 in culture, PHCs grown in microgels were collected in microcentrifuge tubes and washed with PBS. The sample was split with half the cells remaining in microgels and half the cells being removed from microgels by dissolving the alginate. Cells were fixed with paraformaldehyde (PFA) (4% v/v) in PBS for 15 min at room temperature and washed 3× with PBS. Cells were blocked Bovine Serum Albumin (BSA) (2% w/v) in PBS at room temperature for 1 h and then washed 3× with PBS. Cells were permeabilized with Triton-X (0.1% w/v) and BSA (0.125% w/v) in PBS and then washed 3× with BSA (0.125% w/v) in PBS. The microgels were then incubated with the primary antibody to collagen VI (5 µg/mL) (Rabbit Polyclonal Anti-collagen VI antibody, ab6588 from Abcam, Boston, MA, USA), Triton-X (0.1% w/v), and BSA (0.125% w/v) in PBS, incubated at room temperature overnight and then washed 3× with BSA (0.125% w/v) in PBS. A 1mL mixture of secondary antibody (Donkey anti-Rabbit IgG H&L Alexa FluorR488) (5µg/mL) (Abcam, Boston, MA, USA), Triton-X (0.1% w/v), and

BSA (0.125% w/v) in PBS, and Hoechst 33342 Solution (20 μg/mL) (ThermoFisher Scientific, USA)/PBS were added for 1 h at 37 °C and then washed 3× with 0.125% BSA-PBS.

Cells and microgels were loaded onto glass slides and imaged on a custom-built Nikon Ti2 epi-fluorescent microscope. Cells were imaged in Phase Contrast/DAPI/GFP. A total of 3-10 cells were imaged per condition.

Force curve acquisition and analysis

Cells grown in microgels were prepared for AFM by first collecting the microgels on days 1, 6, and 10, and dissolving the alginate microgels. Cells were then washed with PBS and placed into the well-traps by pipetting the cell suspension onto the trap and centrifuging at 2000 × g for 1 min.

Cells grown in monolayer were prepared for AFM by collecting the cells using a cell scraper and sodium-citrate (50mM)/EDTA (80mM) in PBS. Cells were then washed with PBS and placed into the well-traps by pipetting the cell suspension onto the traps and centrifuging at 2000 × g for 1 min.

The cell-laden traps were placed in an AFM (Sypher S, Asylum Research) outfitted with a droplet holding stage and qp-BioAC AFM probe (Nanosensors). The cantilever with a 0.1 N/m spring constant was selected for force curve collection and calibrated using the Sader method [39]. Force curves were performed using extension and retraction speeds of 1 μm/s and a maximum force of 2 nN. Applying a Hertzian contact model to force-distance data calculates average quasi-static contact modulus of the substrate volume actuated under the probe tip (referred to as elastic modulus in this work), and the 2nN max force was selected to minimize indentation depth and confine the actuated volume, consistent with AFM cell mechanics

literature [40]. Accordingly, indentation depths did not exceed 10% of the cell diameter. Cells were located in brightfield, and the tip was placed approximately above the middle of the cell. 8 × 8 force maps were acquired for each cell probing over a 1 × 1 μm area. Imaged surfaces were smooth at tip-relevant length scales and no topography-related artifacts were noted. Twenty cells were imaged for each of cells grown in microgels and monolayers on days 1, 6, and 10 for each donor (N = 3). Force curves were analyzed using the Hertz equation to calculate *G'* of each cell [30].

Statistical differences in *G'* between cells grown in monolayer and microgels (Figure 4D) were assessed using a linear mixed effects model. Statistical differences between microgels from each donor were tested with two-sample T-tests. Differences in *G'* of microgels on day 10 were examined using a Gaussian mixture model. Differences in CV of microgels were assessed using through two-sample T-tests and trends between *G'* and CV were tested using linear regressions. All statistics were performed in Matlab (Mathworks, USA).

Representative force curves and maps were generated in the Igor Pro software package and Matlab.

Funding

This research was funded by the National Institutes of Health [R01AR073964 to RKJ] and National Science Foundation [CAREER 1753352 to CBC, 1554708 to RKJ]. The funding sources had no role in the design or execution of the study

Informed Consent Statement

The Montana State University Institutional Review Board (IRB) defined these studies as exempt (exemption 4B) on 13 October 2011. Patient consent was provided using an IRB approved consent form.

Acknowledgments

This work was performed in part at the Montana Nanotechnology Facility, a member of the National Nanotechnology Coordinated Infrastructure (NNCI), which is supported by the National Science Foundation (Grant# ECCS-2025391).

Conflicts of Interest

June owns stock in Beartooth Biotech, which was not involved in this study.

Works Cited

1. Muir H. The chondrocyte, architect of cartilage. Biomechanics, structure, function and molecular biology of cartilage matrix macromolecules. Bioessays. 1995;17: 1039–1048.

2. Huang BJ, Hu JC, Athanasiou KA. Cell-based tissue engineering strategies used in the clinical repair of articular cartilage. Biomaterials. 2016;98: 1–22.

3. Safiri S, Kolahi A-A, Smith E, Hill C, Bettampadi D, Mansournia MA, et al. Global, regional and national burden of osteoarthritis 1990-2017: a systematic analysis of the Global Burden of Disease Study 2017. Ann Rheum Dis. 2020;79: 819–828.

4. Jacobi M, Villa V, Magnussen RA, Neyret P. MACI - a new era? Sports Med Arthrosc Rehabil Ther Technol. 2011;3: 10.

5. Amr M, Mallah A, Yasmeen S, Van Wie B, Gozen A, Mendenhall J, et al. From Chondrocytes to Chondrons, Maintenance of Phenotype and Matrix Production in a Composite 3D Hydrogel Scaffold. Gels. 2022;8. doi:10.3390/gels8020090

6. Minas T, Peterson L. Advanced techniques in autologous chondrocyte transplantation. Clin Sports Med. 1999;18: 13–44, v–vi.

7. Batty L, Dance S, Bajaj S, Cole BJ. Autologous chondrocyte implantation: an overview of technique and outcomes. ANZ J Surg. 2011;81: 18–25.

8. Benya PD, Padilla SR, Nimni ME. Independent regulation of collagen types by chondrocytes during the loss of differentiated function in culture. Cell. 1978;15: 1313–1321.

9. Mayne R, Vail MS, Mayne PM, Miller EJ. Changes in type of collagen synthesized as clones of chick chondrocytes grow and eventually lose division capacity. Proc Natl Acad Sci U S A. 1976;73: 1674–1678.

10. von der Mark K, Gauss V, von der Mark H, Müller P. Relationship between cell shape and type of collagen synthesised as chondrocytes lose their cartilage phenotype in culture. Nature. 1977;267: 531–532.

11. Darling EM, Athanasiou KA. Rapid phenotypic changes in passaged articular chondrocyte subpopulations. J Orthop Res. 2005;23: 425–432.

12. Costa E, González-García C, Gómez Ribelles JL, Salmerón-Sánchez M. Maintenance of chondrocyte phenotype during expansion on PLLA microtopographies. J Tissue Eng. 2018;9: 2041731418789829.

13. Ghosh S, Scott AK, Seelbinder B, Barthold JE, Martin BMS, Kaonis S, et al. Dedifferentiation alters chondrocyte nuclear mechanics during in vitro culture and expansion. Biophys J. 2022;121: 131–141.

14. Fredrikson JP, Brahmachary PP, Erdoğan AE, Archambault ZK, Wilking JN, June RK, et al. Metabolomic Profiling and Mechanotransduction of Single Chondrocytes Encapsulated in Alginate Microgels. Cells. 2022;11. doi:10.3390/cells11050900

15. Alexopoulos LG, Haider MA, Vail TP, Guilak F. Alterations in the mechanical properties of the human chondrocyte pericellular matrix with osteoarthritis. J Biomech Eng. 2003;125: 323–333.

16. Wilusz RE, Sanchez-Adams J, Guilak F. The structure and function of the pericellular matrix of articular cartilage. Matrix Biol. 2014;39: 25–32.

17. Zhang Z. Chondrons and the pericellular matrix of chondrocytes. Tissue Eng Part B Rev. 2015;21: 267–277.

18. Zelenski NA, Leddy HA, Sanchez-Adams J, Zhang J, Bonaldo P, Liedtke W, et al. Type VI Collagen Regulates Pericellular Matrix Properties, Chondrocyte Swelling, and Mechanotransduction in Mouse Articular Cartilage. Arthritis Rheumatol. 2015;67: 1286–1294.

19. Jeon JE, Schrobback K, Meinert C, Sramek V, Hutmacher DW, Klein TJ. Effect of preculture and loading on expression of matrix molecules, matrix metalloproteinases, and cytokines by expanded osteoarthritic chondrocytes. Arthritis Rheum. 2013;65: 2356–2367.

20. Ng L, Hung H-H, Sprunt A, Chubinskaya S, Ortiz C, Grodzinsky A. Nanomechanical properties of individual chondrocytes and their developing growth factor-stimulated pericellular matrix. J Biomech. 2007;40: 1011–1023.

21. Caldwell AS, Aguado BA, Anseth KS. Designing Microgels for Cell Culture and Controlled Assembly of Tissue Microenvironments. Adv Funct Mater. 2020;30. doi:10.1002/adfm.201907670

22. Caliari SR, Burdick JA. A practical guide to hydrogels for cell culture. Nat Methods. 2016;13: 405–414.

23. Xu Y, Zhu H, Denduluri A, Ou Y, Erkamp NA, Qi R, et al. Recent Advances in Microgels: From Biomolecules to Functionality. Small. 2022;18: e2200180.

24. Danalache M, Kleinert R, Schneider J, Erler AL, Schwitalle M, Riester R, et al. Changes in stiffness and biochemical composition of the pericellular matrix as a function of spatial chondrocyte organisation in osteoarthritic cartilage. Osteoarthritis Cartilage. 2019;27: 823–832.

25. Arnold KM, Sicard D, Tschumperlin DJ, Westendorf JJ. Atomic Force Microscopy Micro-Indentation Methods for Determining the Elastic Modulus of Murine Articular Cartilage. Sensors . 2023;23. doi:10.3390/s23041835

26. Rigacci L, Alterini R, Bernabei PA, Ferrini PR, Agati G, Fusi F, et al. Multispectral imaging autofluorescence microscopy for the analysis of lymph-node tissues. Photochem Photobiol. 2007;71: 737–742.

27. Hoell T, Huschak G, Beier A, Hüttmann G, Minkus Y, Holzhausen HJ, et al. Auto fluorescence of intervertebral disc tissue: a new diagnostic tool. Eur Spine J. 2006;15 Suppl 3: S345-53.

28. Andersson-Engels S, Johansson J, Svanberg K, Svanberg S. Fluorescence imaging and point measurements of tissue: applications to the demarcation of malignant tumors and atherosclerotic lesions from normal tissue. Photochem Photobiol. 1991;53: 807–814.

29. Gebauer M, Saas J, Sohler F, Haag J, Söder S, Pieper M, et al. Comparison of the chondrosarcoma cell line SW1353 with primary human adult articular chondrocytes with regard to their gene expression profile and reactivity to IL-1beta. Osteoarthritis Cartilage. 2005;13: 697–708.

30. Kontomaris SV, Malamou A, Stylianou A. The Hertzian theory in AFM nanoindentation experiments regarding biological samples: Overcoming limitations in data processing. Micron. 2022;155: 103228.

31. Lee DA, Noguchi T, Knight MM, O'Donnell L, Bentley G, Bader DL. Response of chondrocyte subpopulations cultured within unloaded and loaded agarose. J Orthop Res. 1998;16: 726–733.

32. McLeod MA, Wilusz RE, Guilak F. Depth-dependent anisotropy of the micromechanical properties of the extracellular and pericellular matrices of articular cartilage evaluated via atomic force microscopy. J Biomech. 2013;46: 586–592.

33. Zignego DL, Hilmer JK, June RK. Mechanotransduction in primary human osteoarthritic chondrocytes is mediated by metabolism of energy, lipids, and amino acids. J Biomech. 2015;48: 4253–4261.

34. Zignego DL, Hilmer JK, Bothner B, Schell WJ, June RK. Primary human chondrocytes respond to compression with phosphoproteomic signatures that include microtubule activation. J Biomech. 2019;97: 109367.

35. Håti AG, Bassett DC, Ribe JM, Sikorski P, Weitz DA, Stokke BT. Versatile, cell and chip friendly method to gel alginate in microfluidic devices. Lab Chip. 2016;16: 3718–3727.

36. Tinevez J-Y, Perry N, Schindelin J, Hoopes GM, Reynolds GD, Laplantine E, et al. TrackMate: An open and extensible platform for single-particle tracking. Methods. 2017;115: 80–90.

37. Rueden CT, Schindelin J, Hiner MC, DeZonia BE, Walter AE, Arena ET, et al. ImageJ2: ImageJ for the next generation of scientific image data. BMC Bioinformatics. 2017;18: 529.

38. C. R. Guerrero, P. D. Garcia, R. Garcia, Subsurface Imaging of Cell Organelles by Force Microscopy. ACS Nano 13, 9629–9637 (2019).

39. J. E. Sader, J. W. M. Chon, P. Mulvaney, Calibration of rectangular atomic force microscope cantilevers. Rev. Sci. Instrum. 70, 3967–3969 (1999).

40. N. Gavara, A beginner's guide to atomic force microscopy probing for cell mechanics. Microsc. Res. Tech. 80, 75–84 (2017).

CHAPTER FIVE

DROPLET BASED MICROFLUIDICS FOR SINGLE NERUON GROWTH AND INFECTION WITH HERPES SIMPLEX VIRUS - 1

Contribution of Authors and Co-Authors

Manuscript in Chapter 5

Author: Jacob P. Fredrikson

Contributions: J.P.F. designed research, performed research, analyzed data, and wrote the manuscript

Co-Author: Luke F. Domanico

Contributions: L.F.D. designed research, performed research, and wrote the manuscript

Co-Author: Shawna L. Pratt

Contributions: S.L.P performed research and wrote the manuscript

Co-Author: Emma K. Loveday

Contributions: E.K.L designed research, performed research, and wrote the manuscript

Co-Author: Matt P. Taylor

Contributions: M.P.T. designed research and wrote the manuscript

Co-Author: Connie B. Chang

Contributions: C.B.C designed research and wrote the manuscript

Manuscript Information

Jacob P. Fredrikson, Luke F. Domanico, Shawna L. Pratt, Emma K. Loveday, Matthew P.

Taylor, Connie B. Chang

PNAS

Status of Manuscript:
_x_ Prepared for submission to a peer-reviewed journal
____ Officially submitted to a peer-reviewed journal
____ Accepted by a peer-reviewed journal
____ Published in a peer-reviewed journal

National Academy of Sciences

Abstract

Modern approaches to study single-cell HSV-1 infection have enabled high-resolution observation of viral gene expression and cellular dynamics that impact the outcome of infection. Often, these approaches are temporally restricted to data acquisition at single-timepoints and do not allow observation of critical events throughout the progression of HSV-1 replication. We developed a drop-based microfluidic system of single-cell culturing that allows real-time observation and quantitation of HSV-1 infection. Single primary mouse superior cervical ganglia are individually cultured by embedding the cells in Matrigel-microgels that support neuronal growth and maturation. After maturation, the microgel-embedded neurons are subsequently infected with HSV-1 using a co-flow inoculation that simultaneously emulsifies single neurons with viral inoculum. The co-flow device allows controlled manipulation of HSV-1 inoculum that achieves dose-dependent infection of single neurons. Using a dual-fluorescent recombinant HSV-1 that reports immediate early (IE) and late (L) gene expression, we track the progression of viral replication in single neurons via live-cell fluorescence microscopy. HSV-1 infection of single neurons progresses to fulminant infection in-drop, and replication kinetics are inoculating dose-dependent. Specifically, onset of IE gene expression is detected earlier in single neurons infected at higher inoculating doses. In total, we present a new, high-throughput DBM approach to study single-cell HSV-1 infections of primary neurons, adaptable for further temporal analysis of HSV-1 gene expression.

Introduction

Conventional in vitro methods for studying viral infection rely on traditional biological techniques where cells are cultured and infected in a well plate (1, 2). These population-level infection approaches may overlook the heterogeneous dynamics of infection that are obscured by productive replication in a sub-population of cells (1, 3–6). Single cell methods drive increased understanding of infectious virus production, viral kinetics, and genetic variability (5–12). Drop-based microfluidics (DBM) is a well-established technology that has recently been adapted for studying single-cell viral infection (1, 4, 13, 14). DBM is a high-throughput single-cell assay technique in which a microfluidic device is used to create an emulsion of monodisperse, picoliter-sized drops of water-in-oil. For in-depth, high-throughput analysis of viral and cellular heterogeneity, techniques such as DBM can utilize millions of single cells for various experimental procedures (1, 4, 13). However, DBM has been limited in the types of cells and viruses that could be studied (13).

Herpes Simplex Virus type -1 (HSV-1) is a prevalent human pathogen that typically infects the orofacial epithelia and then invades the peripheral nervous system (PNS) where disease pathologies arise. HSV-1 replication employs a regimented, temporally defined cascade of events, represented by the expression of three classes of viral genes in the order of immediate early (IE), early (E), and late (L) genes (15, 16). Understanding the complexities of HSV-1 replication in neurons can lead to better therapeutics and a reduction in disease outcomes and neuropathologies. To understand HSV-1 infection in single neurons eliminates the confounding effects of mixed infection dynamics in a population of cells (1).

The direct application of DBM methods to study HSV-1 infection in neurons imposes new challenges. Aqueous drops lack a solid scaffold needed to grow and differentiate primary cells for single cell infection studies. Specifically, primary neurons require a solid substrate that supports neurite development and growth, limiting their usability in an aqueous drop environment (17). There remains a need to develop novel techniques in which single cells can be cultured on a surface, yet still remain in an individual microenvironment for single cell analyses.

Thus, to address the need for a solid surface to support single cell growth and development, we used DBM to generate micron scale collagen hydrogel beads, termed microgels (18, 19). Microgels provide a homogenous, highly tunable, biomimetic, growth environment for cells (18, 19). Microgels have been previously used to multiple culture cell types such as neurospheres, embryonic stem cells and induced pluri-potent stem cell aggregates but have not been previously used to culture single neurons (18–21). Here, we developed a method for growing individual neurons in microgels where DBM allows for the precise control over cell density to achieve one neuron per microgel. These microgel-embedded neurons were encapsulated with a precise inoculating dose of HSV-1 using DBM. Using a recombinant fluorescent-reporter virus, we tracked the kinetics of HSV-1 gene expression across increasing inoculating doses in individual neurons. Our data demonstrates that the microgels provide a solid surface for neuronal growth and development that supports productive single-cell HSV-1 infection within drops.

Results

We have developed a drop-based microfluidics approach for the growth and differentiation of individual primary neurons to investigate HSV-1 infection dynamics. Here we present a

workflow for our experiments. Individual SCG neurons are suspended in a Matrigel precursor solution that is then processed into ~100 μm diameter microgels using DBM (Figure 1A). The microgel embedded neurons are cultured for one week to allow for growth and development of neurite extensions (Figure 1A). The microgels are subsequently emulsified into larger drops with viral inoculum; a co-flow inoculation where cells and virus are encapsulated simultaneously. The use of a co-flow microfluidic workflow allows controlled delivery of a viral inoculating dose therefore achieving a superior single cell infection (Figure 1B). The drops are incubated for 16 hours post infection (hpi). To visualize infection dynamics and replication kinetics, a dual-fluorescent HSV-1 recombinant, OK-15, is employed (22). OK15 possesses a CMV-driven yellow fluorescent protein (YFP) and a VP26-mCherry fusion (22). Detection of OK15-expressed YFP reports onset of immediate early (IE) viral gene expression upon infection, and subsequent OK15-expressed mCherry detection in the nucleus correlates with Late (L) gene expression and virion assembly (Figure 1C)(22). To observe infection dynamics at the single cell level we immobilized drops on a specialized microfluidic device that allows for incubation and imaging for fluorescent protein detection over the course of infection (Figure 1D) (23, 24).

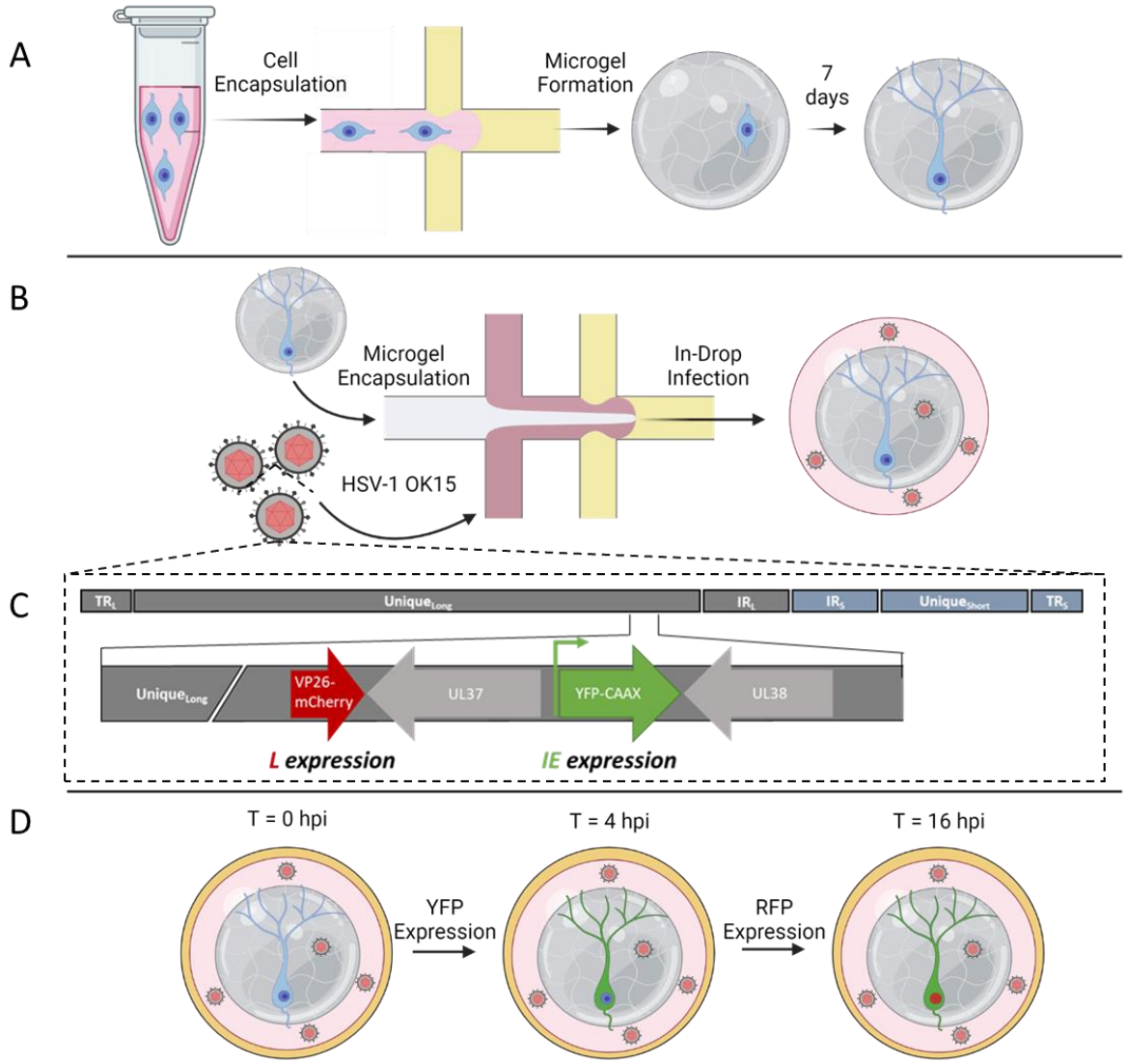


Figure 1: Experimental schematic for the encapsulation, growth, and infection of individual neurons within microfluidic drops. (A) SCG neurons are suspended in liquid matrigel and emulsified in fluorinated oil. The drops are incubated at 37 °C for 35 minutes to gel the microgels. The gels and neurons are washed and placed in media for 7 days for neuronal maturation. (B) After 7 days the neurons are coflow inoculated with viral inoculum and emulsified in fluorinated oil. (C) To visualize infection dynamics and replication kinetics, a dual-fluorescent HSV-1 recombinant, OK-15, is employed. OK15 possesses a CMV-driven yellow fluorescent protein (YFP) and a VP26-mCherry fusion (22). Detection of OK15-expressed YFP reports onset of IE viral gene expression upon infection, and subsequent OK15-expressed mCherry detection in the nucleus correlates with L gene expression and assembly. (D) Drops are incubated in a dropspot chamber for 16 hpi and imaged for YFP and RFP.

Single Cell Infection Outcomes of Vero Cells with HSV-1 OK15

To understand the potential interactions between cells, microgels, and viruses, we studied HSV-1 infection of Vero cells in microgels. Vero cells are an epithelial cell line that is highly susceptible and permissive to HSV-1 infections and has been conventionally used to propagate and study HSV-1 infection in vitro (2).

We first evaluated whether the location of the cell in relation to the microgel alters the likelihood of a cell becoming infected. Vero cells were either grown within microgels, on microgels, or placed in suspension prior to being inoculated with virus at 10 pfu/drop using a co-flow microfluidic device (Figure 2A). To visualize virus infection in Vero cells, we used OK15-expressed YFP detection as our reporter infection (22). Vero cells suspended in drops show 50.0 ± 3.7 % YFP positive detection at 16 hpi (Figure 2Bi and 2D). Vero cells seeded onto prefabricated microgels and allowed to adhere for 4 hours prior to inoculation in drops show 76.8 ± 5.0% YFP positive detection at 16 hpi (Figure 2Bii and 2D, SI Figure 1). Vero cells embedded within microgels show only 1.7 ± 1.4% YFP positive detection at 16 hpi. (Figure 2Ci-ii and 2D). Interestingly, the cells that did express YFP were all found at the edge of the microgel, a random event from the drop making process. No cells enclosed within the microgel expressed YFP (Figure 2Ci-ii).

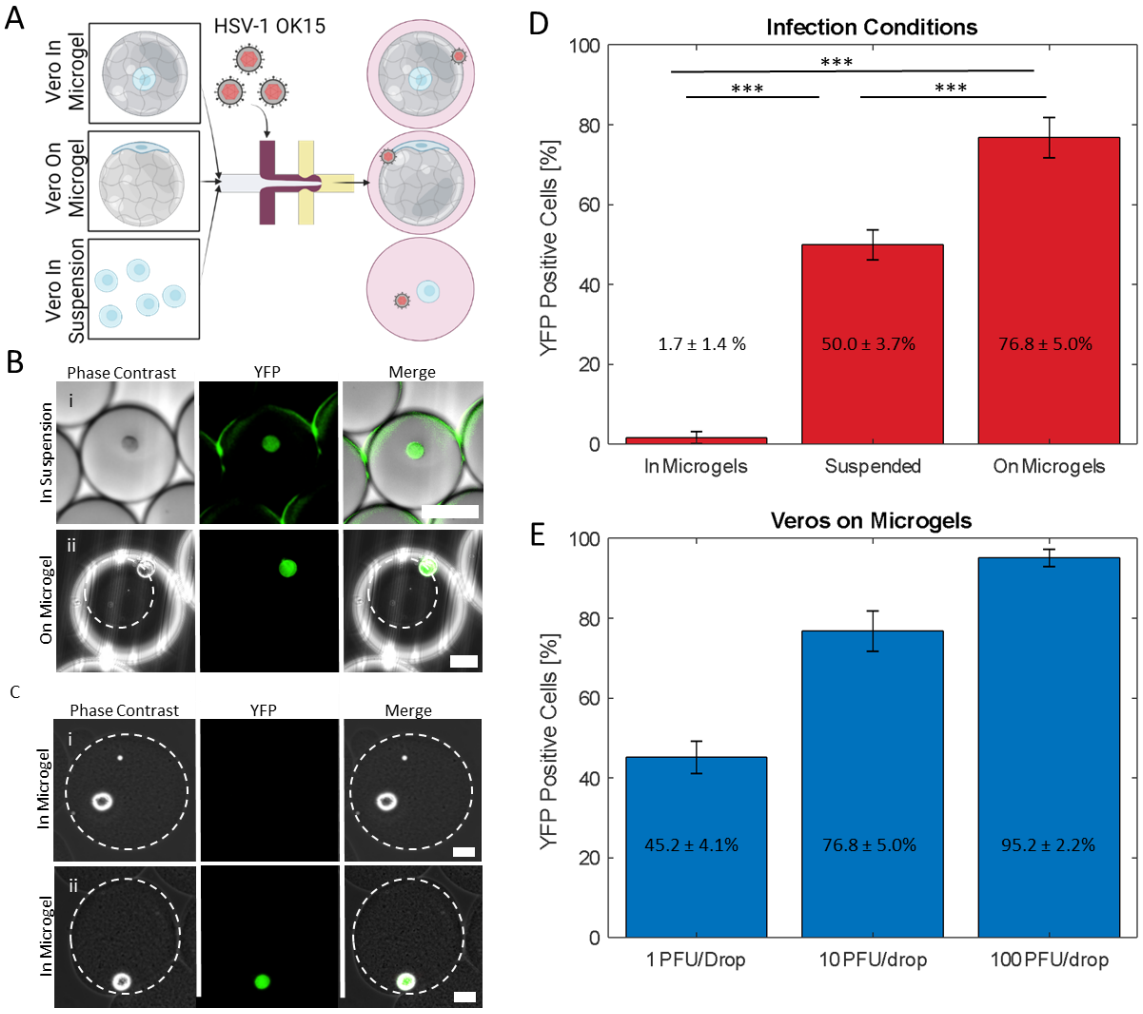


Figure 2: (A) Schematic of experimental design for Vero cell infections. (B) Representative images of infected Vero cells (i) in suspension and (ii) on microgels. Scale bar is 50 µm (C) Representative images of Vero cells in microgels (i) near the middle of the gel (ii) and near the surface. Scale bar is 25 µm. (D) Bar graphs of the percentage of YFP positive cells from Vero cells which were suspended in media, seeded onto matrigel microgels, or encapsulated inside of microgels. Cells were individually infected with HSV-1 OK15 within microfluidic drops at a virus concentration of 10 PFU/drop. All comparisons are significantly different (multiple comparison pairwise t-test, in microgels-suspension, $p = 9.3 \times 10^{-6}$; in microgels-on microgels, $p = 7.8 \times 10^{-7}$; suspension-on microgels, $p= 2.7 \times 10^{-4}$)(N = 3 replicates; In microgels, $n_{average}$ = 162 cells; On microgels, $n_{average}$ = 224; Suspension, $n_{average}$= 329) . (E) Bar graphs of the percentage of YFP positive cells from Vero cells which were seeded onto matrigel microgels. Cells were individually infected with HSV-1 OK15 within microfluidic drops at virus concentrations of 1, 10, and 100 PFU/drop. As inoculating dose increased, the percentage of cells where YFP was detected increased. This trend was statistically significant (One-way ANOVA $p = 1.3 \times 10^{-5}$)(N = 3 replicates; 1 PFU/drop, $n_{average}$ = 303 cells; 10 PFU/drop, $n_{average}$ = 224 ; 100 PFU/drop, $n_{average}$ = 179).

We hypothesize that the comparatively large number of Vero cells embedded in microgels without detectable YFP is due to the inability of virions to penetrate/diffuse through Matrigel (25, 26). While Matrigel is a porous material, the pore size is approximately 150 nm, nearly the same size as the 150-250 nm diameter HSV-1 virion (27). To test our hypothesis that HSV-1 diffusion through Matrigel is limited, the interaction between VP26-mCherry labeled virions and Matrigel was observed on a confocal microscope. Over 1.5h, we observed no HSV-1 virions diffusing past the interface of the Matrigel (SI Figure 2). Additionally, we saw no accumulation of virions at the interface indicating that the HSV-1 particles were not adhering to or penetrating the gel and becoming immobilized (SI Figure 2). This demonstrates that HSV-1 virions do not diffuse through the Matrigel. Thus, only cells which are located near or on the surface of Matrigel microgels are accessible to HSV-1 infection.

After making these observations, we further characterized the co-flow inoculation system in HSV-1 OK15 infection of Vero cells cultured on the surface of microgels. Cells were inoculated with doses ranging from 1, 10, and 100 pfu/drop. As inoculating dose increased, the percentage of cells where YFP was detected increased from 45.2 ± 4.1% at 1 pfu/drop to 76.8 ± 5.0% at 10 pfu/drop and 95.2 ± 2.2% at 100 pfu/drop (Figure 2E). These changes were statistically significant ($p = 1.3 \times 10^{-5}$ df = 8), as tested by one-way ANOVA. This observation is consistent with the expectations that increasing inoculating dose leads to greater extents of infection (28).

These above results show that microgels provide a 3-D scaffold which can be used to culture and infect adherent cell lines in DBM-based assays. In comparison to embedded cells, Vero cells cultured on the microgel have increased accessibility to HSV-1 infection and yield the

highest percentage of detected infection. Cells that are not on the surface of the microgels were unlikely to become infected with HSV-1 as the virions do not diffuse through Matrigel. The reduced infection observed in suspended Vero cells is hypothesized to be caused by changes in either cellular susceptibility or permissiveness to HSV-1 infection.

Growth of Single Mouse Superior Cervical Ganglia Neurons in Microgels

Using the system developed above, we then employed our 3-D microgel culturing system for the in vitro growth and development of single primary mouse Superior Cervical Ganglia (SCG) neurons. In contrast to adherent epithelial cells like Vero, dissociated SCG neurons require structural support to promote neurite development and growth during microfluidic manipulation. Neurites, including axons and dendrites, are critical to neuronal homeostasis, metabolic regulation, and synaptic signaling (17, 29). To support neurite development, SCG neurons were embedded in Matrigel microgels using DBM (Figure 3A). Following Matrigel-embedding, cultured neurons matured over seven days (Figure 3A).

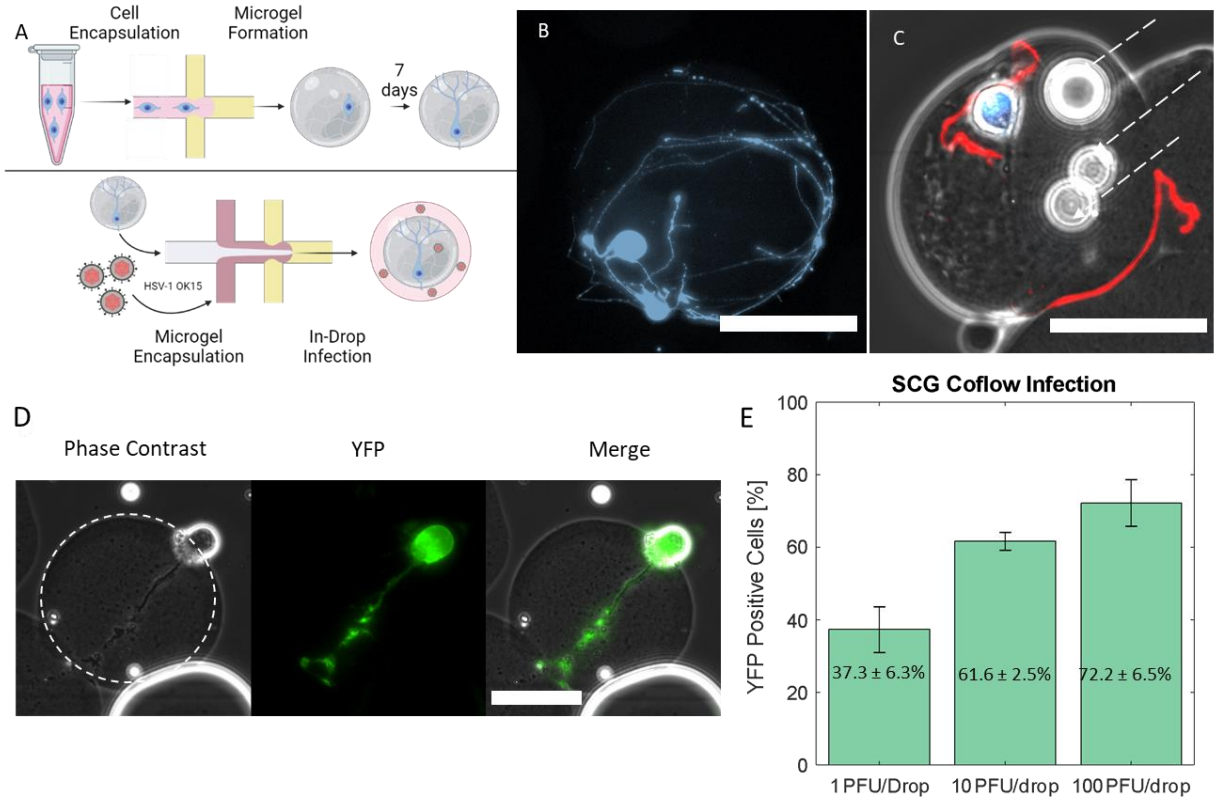


Figure 3: (A) Schematic of experimental design for SCG maturation and infection. (B) A representative image of a live SCG neuron grown in a microgel and stained with Calcien AM. False colored blue. Scale bar is 50 µm. (C) A SCG neuron grown in a Matrigel microgel for 7 days and labeled using immunofluorescence for phosphorylated neuro-filament H (Red) and Nuclei (Blue). The white arrows denote residual oil from drop making. Scale bar is 50 µm. (D) A representative image of an SCG neuron infected in a microfluidic drop with HSV-1 OK15 after breaking the emulsion for improved imaging. The dashed white circle outlines the microgel. Scale bar is 50 µm (E) Bar graphs of the percentage of YFP positive cells after infecting isolated SCG neurons in drops with HSV-1 OK15 at 1, 10, and 100 PFU/drop. Inoculating dose significantly impacted YFP detection (1-Way ANOVA $p = 5.9 \times 10^{-4}$)(N = 3 replicates; 1 PFU/drop, $n_{average}$ = 183 cells; 10 PFU/drop, $n_{average}$ = 164 ; 100 PFU/drop, $n_{average}$ = 128).

After seven days in culture, the neuronal somas migrated to peripheral regions of the microgels and robust neurites were detected within or on the external curvature of the microgels (Figure 3B). To confirm that the embedded neurons reached physiological maturity, we performed immunofluorescence staining for phosphorylated neuro-filament H (N-F), an axonal protein indicating neuronal maturity. Robust N-F signal was detectable in the axons of SCG

neurons grown in Matrigel microgels (Figure 3C). These results indicate that microgels provide an adequate growth environment for individual neurons to grow and mature.

Single-cell Infection of SCG Neurons

Following seven days of culturing primary SCG neurons in microgels, we investigated the capacity for single-cell HSV-1 OK15 infection. Embedded neurons were infected in drops with inoculating doses of 1, 10, or 100 pfu/drop and imaged for YFP detection (Figure 3A). At 16 hpi, SCG neurons demonstrated YFP detection (Figure 3D, SI Figure 3). At the lowest viral concentration, 1 pfu/drop, 37.3 ± 6.3% of SCG neurons expressed YFP 16hpi (Figure 3E). At the same time point, SCG neurons infected at 10 and 100 pfu/drop saw much higher percentages of infection with 61.6 ± 2.5 and 72.2 ± 6.6% of YFP detected in cells, respectively (Figure 3E). To assess if inoculating dose determines YFP positivity, we performed a one-way ANOVA and found that inoculating dose significantly impacted YFP detection across 1, 10 and 100 pfu/drop inoculations ($p = 5.9 \times 10^{-4}$ df = 8). Our results demonstrate that primary SCG neurons cultured in microgels and infected in microfluidic drops are susceptible to HSV-1 infection and support viral gene expression as reported by YFP detection.

Timing and Outcomes of Viral Gene Expression in Individual SCG Neurons

Here, we sought to observe viral gene expression kinetics in single neurons through detection of YFP for IE gene expression and RFP for L gene expression. To monitor and quantify the timing of viral gene expression of single neurons infected with HSV-1 OK15, mature Matrigel-embedded neurons were encapsulated with viral inoculum and applied to a microfluidic chamber, termed a drop-spot (Figure 4A). The drop-spot immobilizes drops and

allows temporal tracking and fluorescence quantification of single-cells (23). Images of infected neurons were acquired every 15 minutes for 16 hours, with image acquisition starting within 1 hour post droplet inoculation (0hpi) (Figure 4B). The timing of FP detection is determined by the time at which the fluorescent pixel intensity passes the background threshold value (Figure 4C).

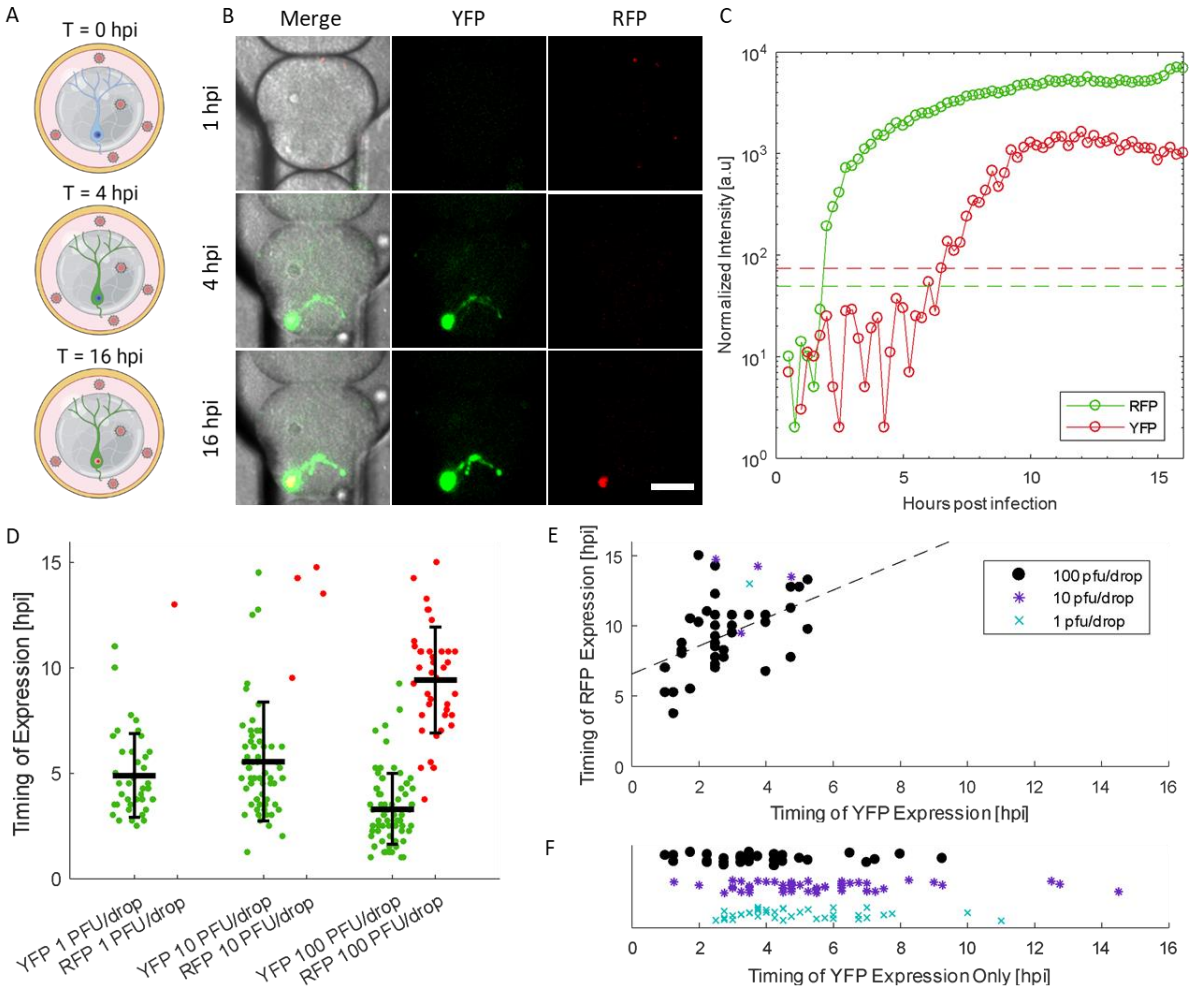


Figure 4: (A) Schematic of experimental design for temporal tracking of YFP and RFP (B) Representative images of an infected neuron expressing YFP and RFP in a dropspot chamber. Scale bar is 50 µm. (C) Representative YFP (green circles) and RFP (red circles) intensities measured from the cell in 'B' plotted with the threshold of YFP (green) and RFP (red) detection. (D) Timing of YFP and RFP expression in individual neurons plotted with the mean and standard deviation. Timing of YFP detection decreased with increased inoculating dose (1-way ANOVA $p = 1.1 \times 10^{-7}$). (E) YFP vs RFP expression timing in individual neurons. (1 PFU/drop - blue X, 10 PFU/drop - purple star, 100 pfu/drop - black circle) (Linear regression $t_{RFP+} = 6.6 + t_{YFP+}$ $p = 0.002$ $R^2 = 0.23$). (F) YFP expression timing in neurons which did not express RFP. (1 PFU/drop - blue X, 10 PFU/drop - purple star, 100 pfu/drop - black circle).

To understand how inoculating dose impacts detection of HSV-1 IE and L fluorescent proteins in single neurons, Matrigel-embedded neurons were infected at 1, 10, and 100 pfu/drop

and imaged in the drop-spot for 16 hours. Neurons infected at 1 pfu/drop saw an onset of YFP detection at 4.9 ± 2.0 hpi (Figure 4D). Neurons infected at 10 pfu/drop saw an onset of YFP detection at 5.5 ± 2.8 hpi (Figure 4D). Neurons infected at 100 pfu/drop had the earliest onset of YFP detection 3.3 ± 1.7 hpi (Figure 4D). From a 1-Way ANOVA we found that timing of YFP detection decreased with increased inoculating dose ($p = 1.1 \times 10^{-7}$ df = 166) (Figure 4D) demonstrating that inoculating dose significantly impacts the onset of HSV-1 gene expression in single neurons.

Neurons were further monitored for RFP detection and we saw that only 2.6 and 6.5% of YFP positive cells become YFP and RFP positive at 1 and 10 pfu/drop respectively (Figure 4D). However, neurons infected at 100 pfu/drop resulted in much higher rates with 55.7 % of YFP positive cells becoming YFP and RFP positive by 16hpi (FIgure 4D). The average timing of RFP detection in cells infected at 100 PFU/drop was 9.4 ± 2.5 hpi (FIgure 4D). This demonstrates that in our single-neuron DBM culturing and infection system, we can observe dose-dependent progression of HSV-1 infection in real time.

From our time-lapse data, we can calculate the timing between YFP and RFP detection of single neurons. At 100 PFU/drop we observed an average time between YFP and RFP detection of 6.6 ± 2.2 hours (Figure 4E). To understand if timing of YFP detection effects the timing of RFP detection we implemented a linear regression model which predicts that single neurons will become detectably RFP positive 6.6 ± 1.8 h after onset of YFP detection ($t_{RFP+} = 6.6 + t_{YFP+}$ p =0.002). However, correlation between YFP detection and conversion to YFP/RFP detection was poor ($R^2 = 0.23$) indicating that timing of YFP detection is a poor indicator for the timing of RFP

detection. Furthermore, the onset of YFP detection in cells that did not express detectable RFP was found in the range of 1.25 - 16 hpi (Figure 4F)

To assess the utility of this system in the conventional Vero cell line, we monitored and quantified the timing of viral gene expression of single Vero cells infected with HSV-1 OK15. Similarly as above, Vero cells were cultured on microgels, encapsulated with viral inoculum and then applied to the drop-spot. We see similar trends that were observed in single neurons in single Vero cells. From a 1-Way ANOVA we found that timing of YFP detection decreased with increased inoculating dose in single vero cells ($p = 1.9 \times 10^{-35}$ df = 649) (SI Figure 4A). Similar to neurons, 1.9 and 4.6% of YFP positive vero cells became YFP/RFP positive at 1 and 10 pfu/drop while 64.2% of YFP positive vero cells became YFP/RFP positive at 100 pfu/drop (SI Figure 4A). These experiments affirm the use of DBM culturing and live-cell tracking of HSV-1 across different cell types susceptible to HSV-1 infection.

In total, we demonstrate the use of HSV-1 OK15 to observe progression of HSV-1 infection at the single-cell level in Vero cells and primary SCG neurons. We find that inoculating dose influences progression of HSV-1 infection. Specifically, at higher inoculating doses, cells are YFP positive earlier and are more likely to become YFP and RFP positive.

Discussion

We employed a drop-based microfluidic (DBM) approach to isolate, culture and infect epithelial cells and primary neurons with HSV-1. We utilized Matrigel microgels to enable culturing, development, and maturation of primary neurons and adherent epithelial cells. We then encapsulated individually grown cells with viral inoculum, using a microfluidic co-flow device, enabling isolation and manipulation of individually-infected cells for downstream assays.

In total, we achieved single-cell infection in a system that enables real time analysis of HSV-1 infection kinetics and outcome at the single-cell level.

The aqueous drops employed in typical DBM lack a solid scaffold for cells to adhere, grow and mature. Specifically, primary neurons require a solid substrate that supports neurite development and growth, limiting their usability in an aqueous drop environment. We embedded primary SCG neurons in Matrigel microgels to culture neurons in a system that provides a solid scaffold for individual neuronal differentiation and is compatible with DBM. When embedded in Matrigel microgels and cultured for 7 days, we saw that SCG neurons grew robust neuronal extensions which followed the external curvature of the microgels. By immunofluorescence imaging of phosphorylated-neurofilament H, SCG neuron maturation and axonal development is achieved by 7 days in culture. This technology develops a high throughput method of culturing single-neuron useful for applications of neurobiology. These results are consistent with other applications of microgels to various cell types where microgels provide a scaffold for the differentiation of primary cells (18, 19).

As the infected neuron is a focal point of HSV-1 persistence, morbidity and mortality, it is important to understand how HSV-1 infection progresses in primary neurons (2). We achieved 72.2 ± 6.6% infection of individual neurons grown in microgels when inoculated at 100 PFU/drop, with 55.7% of infected neurons achieving RFP positivity by 16 hpi. Recent single-cell transcriptomic work has captured heterogeneity in HSV-1 infection of neurons, highlighting the diversity in cellular state that yields a myriad of infection phenotypes at a single time point (3, 30). Our system enables visualization of single neuron infection throughout HSV-1 replication. We captured a wide distribution of onset of YFP detection in single-neurons, ranging from 1.25-

16 hpi and saw that at higher inoculating doses YFP was detectable earlier. This could be the result of distal axonal HSV-1 entry of the single neuron, or alternatively, a heterogeneous establishment of infection. Similarly, we observed large differences in the time it takes a YFP positive cell to become RFP positive. These results support the interpretation that HSV-1 infection of neurons proceeds in a kinetically diverse manner. Our data also shows that all RFP positive were detectably YFP positive before 6 hpi. These observations suggest that a sub-population of infected neurons becomes 'stalled' in that viral gene expression has begun, but replication is not achieved.

We are the first to demonstrate in-drop infection of single primary neurons cultured in Matrigel-microgels. To further understand the complexities of the microgel in-drop infection system, we investigated the spatial impact between the microgel, the susceptible cell and viral inoculum. We hypothesized that cells cultured within the microgel were inaccessible to infection, as reported by minimal YFP detection at 10 PFU/drop. Our particle-diffusion data demonstrates no virion diffusion through the Matrigel interface. However, cells cultured on the surface of the microgel were found to be accessible to HSV-1 and achieved a maximum of 95.2 ± 2.2% infection, suggesting that epithelial cells cultured in-microgel are limited in their spatial accessibility to HSV-1 infection.

Traditional approaches to DBM cell culturing do not employ a surface for cellular adhesion in-drop relying on suspension cells to study viral infection and replication (4, 31, 32). To further investigate the benefits of microgels in a drop-based infection system, we sought to assess suspension-cell infection in our system. We observed an approximate 35% reduction in

infection when cells were cultured in suspension compared to on microgels, further supporting our approach of on-microgel culturing of epithelial cells in a DBM infection system.

We developed a drop-based microfluidic system that supports the growth and maturation of single primary neurons and epithelial cells. We utilized a co-flow inoculation approach that enables infection and real-time observation of single-cells through the progression of HSV-1 replication. From growth to viral replication, this work utilizes single-cells isolated via drop-based microfluidics. Our DBM-based single-cell approach captures discrete events of heterogeneity within a population that would be missed by single-cell analysis of bulk culturing (4). The resolution that this approach yields will develop critical insights into underrepresented variables relevant to HSV-1 infection, such as the cryptic cellular and viral factors contributing to the suppression of viral gene expression necessary to establish the latent infection of neurons.

While we apply microgels to the study of HSV-1, this technique can be further applied to other viruses and cell types and has the unique capability to advance single-cell neurobiology by giving a high throughput method for culturing individual primary neurons in a highly reproducible manner. The system is amenable to downstream processing of the drops for assays such as single-cell RNA-sequencing, but provides the advantage of analyzing individually-grown and infected cells (4).

Materials and Methods

Vero Cell Culture

Vero cells purchased from ATCC were maintained and subcultured in Dulbecco's Modified Eagle's Medium (DMEM) supplemented with 10% fetal bovine serum (v/v) and 1% penicillin/streptomycin in 5% CO_2 at 37 °C.

Mouse Superior Cervical Ganglia Neuron Dissociation

Mouse Superior Cervical Ganglia (SCG) were excised from embryos at 14 days post gestation from pregnant C57Bl/6 mice. All protocols for isolating SCGs were approved by the Institutional Animal Care and Use Committee (protocol 2022-52-IA) at Montana State University. Briefly, Isolated SCGs were washed with HBSS and resuspended in 0.25 mg/mL trypsin in HBSS for dissociation, and incubated for 15 minutes in a 37 ℃ water bath. Tripsinized SCGs were centrifuged and resuspended in 1 mg/mL trypsin inhibitor (Gibco 9035-81-8) in HBSS, then incubated for 5 minutes in a 37 ℃ water bath. Next, SCGs were centrifuged and resuspended in complete neurobasal and dissociated by trituration using a 5 mL pasteur pipette (33).

Herpes Simplex Virus-Type 1 OK15 Characterization and Production

HSV-1 OK15 was constructed, isolated and characterized as previously described (OK15 publication). OK15 viral stock was produced by propagation in ATCC vero cells, and viral stock titer was determined by plaque assay on ATCC vero cells.

Microfluidic Device Fabrication

Negative master molds for the microfluidic devices were prepared using standard photolithography techniques (34). Negative master molds were made with Nano SU-8-100 photoresist (Microchem, Round Rock, TX, USA) on 3 silicon wafers (University Wafer Inc., Boston, MA, USA University Wafer ID: 447). The microgel drop-maker and the suspension cell coflow inoculating device were fabricated to be 100 μm tall. The co-flow microgel inoculating drop-maker and the dropspot chambers were fabricated to be 150 μm tall. Devices were fabricated using standard soft lithography techniques (34). Devices were treated with

(tridecafluoro-1,1,2,2-tetrahydrooctyl) trichlorosilane (1 v/v%) (Gelest) in a fluorinated oil NOVEC HFE 7500 (3M, Saint Paul, MN, USA) and left for solvent evaporation at 55 °C.

Microgel Production and Cell Encapsulation/Seeding

Matrigel microgels were produced through drop-based microfluidics using previously established protocols (35). Briefly, liquid Matrigel at 4°C and 1.5% w/w RAN (008-Fluorosurfactant, RAN Biotechnologies, MA, US) in HFE 7500 were loaded into luer lock syringes and injected into the 100 μm drop-maker using syringe pumps. The flow rates used were $Q_{Matrigel}$ = 100 μL/h and Q_{HFE} = 900 μL/h. All equipment and reagents were placed into a fridge at 4 °C to keep the matrigel from gelling prematurely. Drops were collected in microcentrifuge tubes and incubated at 37 °C for 35 min to gel the drops. The resulting microgels were washed with equal volumes of 1H,1H,2H,2H-Perfluoro-octanal (PFO) - HFE 7500 (20% v/v) and PBS to drops. The cleaned microgels were then collected in PBS.

In experiments where Vero cells or dissociated SCG neurons were encapsulated in microgels, cells were suspended in the liquid Matrigel at 1×10^6 cells/$mL_{Matrigel}$ prior to drop making. After the resulting microgels were collected in PBS they were placed in well plates with the appropriate growth medium. Vero cells were maintained in DMEM - 10% FBS - 1% penicillin/streptomycin in 5% CO_2 at 37 °C for 4 h before experimentation. SCG neurons were grown in complete neurobasal composed of Gibco neurobasal, 1X B27, 60ng/mL 2.5S NGF and 1% penicillin/streptomycin + glutamate in 5% CO_2 at 37 °C for 7 days prior to experimentation to allow maturation and neurite growth. 24 h after encapsulation, SCGs were supplemented with 1uM Cytosine-**β**-D arabinofuranoside (Sigma C6645), a cytostatic DNA polymerase inhibitor that is cytolethal to dividing, non-neuronal cells.

In experiments where Vero cells were seeded onto the microgels, empty microgels were mixed with 1×10^6 cells/$mL_{Matrigel}$ in a well plate. Cells were allowed to adhere for 4 h prior to experimentation.

Immunofluorescence Staining and Imaging

After 7 days in culture, neurons grown in microgels were collected in microcentrifuge tubes and washed with PBS. Cells were fixed with 1% glutaraldehyde for 1 min and washed 3× with PBS. Cells were blocked with 2% BSA /PBS at room temperature for 1 h and then washed 3× with PBS. Cells were permeabilized with 0.1% Triton-X / 0.125% BSA / PBS and then washed 3× with 0.125% BSA/PBS. The primary Antibody, anti-Phosphorylated Neurofilament H (NF-H) (BioLegend) was added at 5 μg/mL, incubated at room temperature overnight and then washed 3× in 0.125% BSA/PBS. The secondary antibody, Goat anti Mouse IgG (H+L), DyLight 550 (#84540 Thermo Fisher) and Hoechst 33342 Solution (ThermoFisher Scientific, USA) were added at 5 μg/mL and 20 μg/mL respectively for 1 h at 37 °C and then washed 3× with 0.125% BSA/PBS .

Cells and microgels were loaded onto glass slides and imaged on a custom built Nikon TI2 epi-fluorescent microscope. Cells were imaged in Phase Contrast/DAPI/RFP.

In-Drop Infection Procedures

Cells were infected in drops using drop-based microfluidics.

To infect cells seeded onto or cultured in microgels, microgels were collected from well plates and pelleted by centrifuging the microgels at 200 ×g for 1 min. The pelleted microgels were loaded into luer lock syringes.

HSV-1 OK15 was diluted into the appropriate media. For Vero infections, HSV-1 OK15 was diluted in DMEM - 10% FBS - 1% penicillin/streptomycin. For SCG infections HSV-1 OK15 was diluted in complete neurobasal composed of Gibco neurobasal, 1X B27, 60ng/mL 2.5S NGF and 1% penicillin/streptomycin + glutamate. HSV-1 OK15 was diluted at concentrations of 1.1×10^6 , 1.1×10^7 and 1.1×10^8 pfu/mL resulting in inoculating conditions of 1, 10 and 100 pfu/drop respectively. The virus solutions were loaded into individual luer lock syringes. 1.5% RAN in HFE was prepared and loaded into a luer lock syringe.

The three syringes were loaded onto syringe pumps and injected into the appropriate inlet channels of the microfluidic co-flow microgel inoculation device. Flow rates were Q_{HFE} = 2500 μL/h, and $Q_{Matrigel}$= Q_{Vrius} = 250 μL/h. Drops were collected into microcentrifuge tubes and either placed in an incubator at 37 °C for end-point imaging or injected into dropspot chambers for time-lapse imaging.

To infect Vero cells suspended in media, Vero cells were removed from subculture using Trypsin - EDTA and washed in PBS. Cells were suspended in DMEM - 10% FBS - 1% penicillin/streptomycin at 1×10^6 cells/mL and loaded into a luer lock syringe. HSV-1 OK15 was diluted into DMEM - 10% FBS - 1% penicillin/streptomycin at a concentration of 3.8×10^7 pfu/mL resulting in an inoculating condition of 10 pfu/drop. The virus solution was loaded into an individual luer lock syringe. 1.5% RAN in HFE was prepared and loaded into a luer lock syringe. The three syringes were loaded onto syringe pumps and injected into the appropriate inlet channels of the co-flow suspension cell inoculating drop-maker. Flow rates were Q_{HFE} = 2000 μL/h, and Q_{Cells}= Q_{Vrius} = 250 μL/h. Drops were collected into microcentrifuge tubes and placed in an incubator at 37 °C for end-point imaging.

End-Point Imaging of Inoculated Cells

To visualize in-drop infection, drops were loaded into capillary tubes and imaged on a custom built Nikon TI2 epi-fluorescent microscope. Cells were imaged in Phase Contrast/FITC/TRITC.

To quantify the percentage of infected cells at16 hpi, the drops containing infected cells were broken using 20% v/v PFO-HFE. Breaking the emulsion allowed for easier visualization and quantification of cells. The broken supernatant containing infected cells was pipetted onto a PTFE printed microscope slide and imaged on a custom built Nikon TI2 epi-fluorescent microscope. Cells were imaged in Phase Contrast/FITC/TRITC.

Time-Lapse Imaging of Inoculated Cells

To track the progression of single cells from YFP negative to YFP positive and then YFP and RFP positive, drops containing infected cells were loaded into dropspot devices with modified aluminum capsules (23). The capsules were placed in a microscope stage top incubation chamber (OKOlab) at 37 °C. Using custom built Nikon TI2 microscopes, images in Phase Contrast/ YFP/RFP were taken every 15 min for 16 h. Tile scans of each chamber were taken to capture as many cells as possible. Image acquisition began within 1 hour post inoculation.

HSV-1 Diffusion with Matrigel Experiments

To evaluate HSV-1 OK15 diffusion through Matrigel, a time-lapse imaging series of virions interacting with the Matrigel interface was performed via inverted laser scanning confocal microscopy (iCLSM) (Stellaris DMI8, Leica.) Matrigel (20 μL) was pipetted onto a 35 mm glass-bottom dish (MatTek) and gelled at 37 °C, forming a hemisphere of solid gel on the

glass surface. PBS was added to the glass-bottom dish to submerge the Matrigel. The PBS and Matrigel containing dish was placed on the microscope stage, and a time-lapse imaging series (XYT) was initiated, with the focal point centered on the Matrigel-PBS interface. At time=0, HSV-1 OK15 at 1×10^8 pfu/mL was added to the dish. Images were acquired at 63X every 10 min for 90 min in two channels: a transmitted light channel (brightfield) and a fluorescence channel (mRFP).

Data Analysis and Statistics

Percentage of YFP Positive Cells. To quantify the percentage of YFP positive cells, end-point images were analyzed using Fiji ImageJ (36). Cells were found in brightfield. The background intensity of the YFP channel was subtracted from the image and the percentage of YFP positive cells was quantified. Experiments were repeated 3 times (N=3). Cell counts for Vero cells embedded in microgels ranged from 79 -280 cells/ replicate. Cell counts for Vero cells grown on microgels ranged from 165 - 390 cells/ replicate. Cell counts for Vero cells in suspension ranged from 228 - 456 cells/ replicate. Cell counts for SCG neurons ranged from 84 - 209 cells/ replicate.

Timing of YFP and RFP Detection. To quantify timing of YFP and RFP detection, time-lapse images were analyzed using Fiji ImageJ (36). Cells were difficult to identify in brightfield so cells were identified by finding YFP positive cells at 16 hpi. Once located, a 30 μm diameter circular region of interest (ROI) was drawn around each individual cell. The maximum pixel intensity in YFP and RFP for the ROI was then measured for each timeframe. The frame 1 maximum pixel intensity of each ROI was subtracted from the subsequent frames for that ROI. The noise threshold was found to be 50 a.u. for YFP and 75 a.u. for RFP. The timing of YFP and

RFP detection were defined as the first time frame the YFP and RFP pixel intensities in each ROI were greater than the noise threshold for two consecutive frames. For SCG time-lapse studies, experiments were repeated 3-4 (N=3-4) times with a total of 174 cells analyzed. For Vero time-lapse studies experiments were repeated 4 times (N=4) with a total of 669 cells analyzed.

1-Way ANOVAs and linear regressions were performed in Matlab.

Works Cited

1. C. Simpson, S. S. Lee, C.-S. Lee, Y. Yamauchi, Microfluidics: an Untapped Resource in Viral Diagnostics and Viral Cell Biology. Current Clinical Microbiology Reports 5, 245–251 (2018).

2. A. C. Wilson, Impact of Cultured Neuron Models on α-Herpesvirus Latency Research. Viruses 14 (2022).

3. N. Drayman, P. Patel, L. Vistain, S. Tay, HSV-1 single-cell analysis reveals the activation of anti-viral and developmental programs in distinct sub-populations. Elife 8 (2019).

4. W. Liu, H. He, S.-Y. Zheng, Microfluidics in Single-Cell Virology: Technologies and Applications. Trends Biotechnol. 38, 1360–1372 (2020).

5. A. B. Russell, E. Elshina, J. R. Kowalsky, A. J. W. Te Velthuis, J. D. Bloom, Single-Cell Virus Sequencing of Influenza Infections That Trigger Innate Immunity. J. Virol. 93 (2019).

6. A. B. Russell, C. Trapnell, J. D. Bloom, Extreme heterogeneity of influenza virus infection in single cells. Elife 7 (2018).

7. S. Y. Kupke, et al., Single-Cell Analysis Uncovers a Vast Diversity in Intracellular Viral Defective Interfering RNA Content Affecting the Large Cell-to-Cell Heterogeneity in Influenza A Virus Replication. Viruses 12 (2020).

8. F. S. Heldt, S. Y. Kupke, S. Dorl, U. Reichl, T. Frensing, Single-cell analysis and stochastic modelling unveil large cell-to-cell variability in influenza A virus infection. Nat. Commun. 6, 8938 (2015).

9. Y. Zhu, A. Yongky, J. Yin, Growth of an RNA virus in single cells reveals a broad fitness distribution. Virology 385, 39–46 (2009).

10. F. Guo, et al., Single-Cell Virology: On-Chip Investigation of Viral Infection Dynamics. Cell Rep. 21, 1692–1704 (2017).

11. A. Timm, J. Yin, Kinetics of virus production from single cells. Virology 424, 11–17 (2012).

12. J. Sun, et al., Single cell heterogeneity in influenza A virus gene expression shapes the innate antiviral response to infection. PLoS Pathog. 16, e1008671 (2020).

13. D. García Alonso, M. Yu, H. Qu, L. Ma, F. Shen, Advances in Microfluidics-Based Technologies for Single Cell Culture. Adv Biosyst 3, e1900003 (2019).

14. A. B. Theberge, et al., Microdroplets in microfluidics: an evolving platform for discoveries in chemistry and biology. Angew. Chem. Int. Ed Engl. 49, 5846–5868 (2010).

15. J. R. Heath, J. A. Dembowski, Fashionably late: Temporal regulation of HSV-1 late gene transcription. PLoS Pathog. 18, e1010536 (2022).

16. B. Roizman, G. Zhou, The 3 facets of regulation of herpes simplex virus gene expression: A critical inquiry. Virology 479-480, 562–567 (2015).

17. M. Frega, "3D Neuronal Networks: State of the Art" in Neuronal Network Dynamics in 2D and 3D in Vitro Neuroengineered Systems, M. Frega, Ed. (Springer International Publishing, 2016), pp. 45–57.

18. A. S. Caldwell, B. A. Aguado, K. S. Anseth, Designing Microgels for Cell Culture and Controlled Assembly of Tissue Microenvironments. Adv. Funct. Mater. 30 (2020).

19. Y. Xu, et al., Recent Advances in Microgels: From Biomolecules to Functionality. Small 18, e2200180 (2022).

20. S. Pautot, C. Wyart, E. Y. Isacoff, Colloid-guided assembly of oriented 3D neuronal networks. Nat. Methods 5, 735–740 (2008).

21. D. Jgamadze, et al., Colloids as mobile substrates for the implantation and integration of differentiated neurons into the mammalian brain. PLoS One 7, e30293 (2012).

22. M. T. Luke Domanico, A Dual Fluorescent Recombinant for Live Cell Observation of HSV-1 Replication.

23. S. L. Pratt, et al., DropSOAC: Stabilizing Microfluidic Drops for Time-Lapse Quantification of Single-Cell Bacterial Physiology. Front. Microbiol. 10, 2112 (2019).

24. C. H. J. Schmitz, A. C. Rowat, S. Köster, D. A. Weitz, Dropspots: a picoliter array in a microfluidic device. Lab Chip 9, 44–49 (2009).

25. O. Lieleg, K. Ribbeck, Biological hydrogels as selective diffusion barriers. Trends Cell Biol. 21, 543–551 (2011).

26. J. Witten, K. Ribbeck, The particle in the spider's web: transport through biological hydrogels. Nanoscale 9, 8080–8095 (2017).

27. N. Broguiere, et al., Growth of Epithelial Organoids in a Defined Hydrogel. Adv. Mater. 30, e1801621 (2018).

28. E. M. Cohen, O. Kobiler, Gene Expression Correlates with the Number of Herpes Viral Genomes Initiating Infection in Single Cells. PLoS Pathog. 12, e1006082 (2016).

29. M. Frega, Neuronal Network Dynamics in 2D and 3D in vitro Neuroengineered Systems (Springer International Publishing) (April 5, 2023).

30. H.-L. Hu, et al., Single-cell transcriptomics identifies Gadd45b as a regulator of herpesvirus-reactivating neurons. EMBO Rep. 23, e53543 (2022).

31. E. K. Loveday, H. S. Sanchez, M. M. Thomas, C. B. Chang, Single-Cell Infection of Influenza A Virus Using Drop-Based Microfluidics. Microbiol Spectr 10, e0099322 (2022).

32. H. Zhang, et al., Isolation and Analysis of Rare Norovirus Recombinants from Coinfected Mice Using Drop-Based Microfluidics. J. Virol. 89, 7722–7734 (2015).

33. T. H. Ch'ng, E. A. Flood, L. W. Enquist, Culturing primary and transformed neuronal cells for studying pseudorabies virus infection. Methods Mol. Biol. 292, 299–316 (2005).

34. J. P. Fredrikson, et al., Metabolomic Profiling and Mechanotransduction of Single Chondrocytes Encapsulated in Alginate Microgels. Cells 11 (2022).

35. Z. Mahdieh, et al., Granular Matrigel: restructuring a trusted extracellular matrix material for improved permeability. Biomed. Mater. 17 (2022).

36. C. T. Rueden, et al., ImageJ2: ImageJ for the next generation of scientific image data. BMC Bioinformatics 18, 529 (2017).

CHAPTER SIX

CONCLUSIONS AND OUTLOOK

Conclusions

The research presented in this thesis expanded the application of microgels in tissue engineering. The work presented focused on two specific fields of tissue engineering: articular cartilage and neural tissue engineering. Chapters 3 and 4 focused on applying alginate microgels to chondrocytes and pericellular matrix formation. Chapter 5 focused on applying microgels to neurons and HSV-1 infection dynamics.

In chapters 3 and 4, the capabilities of microgels to advance cartilage engineering and enhance PCM formation from single chondrocytes grown in microgels were investigated. We first showed that SW1353 chondrocytes grown in microgels showed excellent viability after ten days in culture. We then examined the microgels' ability to induce PCM formation in chondrocytes. Collagen VI is a PCM-specific biomarker [1]. Upon immunofluorescence staining for collagen VI, SW1353 cells and primary human chondrocytes both produced distinct collagen VI PCM layers surrounding the cells over ten days in microgel culture. In addition, the PHCs produced far more collagen VI than the SW1353 cells, which was expected due to the genomic differences between the two cell types [2]. In comparison, when grown in monolayer, both cell types produced minimal collagen VI, and what was produced had no PCM-like structure. These results indicated that alginate microgel culture allowed for collagen VI-rich PCM formation.

After establishing that microgels promote PCM production, we presented a non-harmful method to quantify matrix production in real-time. Many PCM and ECM proteins, such as most

collagens, are auto-fluorescent upon UV and blue light exposure [3–5]. Upon exposure to a 405nm light source, both SW1353 cells and PHCs grown in monolayer showed no significant change in auto-fluorescence intensity over ten days in culture. However, when grown in microgels, both SW1353 cells and PHCs displayed a linear increase in auto-fluorescence signal. The rate of change in auto-fluorescence signal was approximately 5 times greater in PHCs than in SW1353 cells, reaching auto-fluorescence intensities of 1258 ± 537 a.u. and 347 ± 73 a.u., respectively. The auto-fluorescence imaging correlated with trends in collagen VI staining. In both imaging techniques, matrix production was minimal when cells were grown in monolayers and significantly increased when grown in microgels. In both techniques, PHCs produced far more matrix components than the SW1353 cells. In total, these two techniques demonstrated how microgels induce the formation of PCM in chondrocytes.

Work in chapter 4 analyzed the mechanical properties of the PCM produced by chondrocytes grown in alginate microgels through atomic force microscopy. PHCs were grown in monolayers and alginate microgels for 10 days. On days 1, 6, and 10, cells were removed from the microgels and monolayers using EDTA-sodium ascorbate and centrifuged into well-traps developed using photolithography. The elastic moduli of the cells were then measured using AFM. PHCs grown in monolayers showed a slight decrease in elastic modulus over the ten days in culture, decreasing from 2.1 ± 0.7 kPa on day 1 to 0.7 ± 0.3 kPa on day 10. In contrast, PHCs grown in microgels stiffened substantially over the ten days in culture. The elastic moduli of the PCM of PHCs grown in microgels increased by 1.87 ± 0.7 kPa/day, reaching a final average elastic modulus of 22.4 ± 2.5 kPa. For reference, in vivo PCM of PHCs has been measured at 25-250 kPa [1,6–9]. The trends seen in the measurements of G' correlate nearly identically to the

auto-fluorescence imaging of the PHCs, with both measurements linearly increasing when cells were grown in microgels and both seeing negligible changes when cells were grown in monolayers. Interestingly, when the elastic moduli data of cells grown in microgels were further analyzed using a Gaussian mixture model, two distinct subpopulations of cells were found on day 10 with means at 9 and 38 kPa. The first subpopulation, centered around 9 kPa, accounted for 54% of the cells and only slightly stiffened compared to the PHCs on day 1, which had an average elastic modulus of 5.2 ± 1.0 kPa. The second subpopulation, centered around 38 kPa, accounted for 46% of the cells and had a PCM elastic modulus similar to in vivo PCM. These results indicated that approximately half of the cells produced far more matrix components than the others. These differences may have been due to the cartilage zone of origin of the cells, but more studies are necessary to elucidate the cause of these subpopulations.

Work in chapter 3 analyzed how microgels affected how chondrocytes respond to physiological dynamic compression. Previous work has shown that dynamic compression is beneficial to chondrocyte function [10]. SW1353 cells grown in microgels or monolayers for ten days were embedded in high-stiffness agarose and compressed using a custom-built bioreactor. The metabolites were extracted and analyzed using HPLC-MS. Interestingly, many pathways relating to the ECM and PCM were up-regulated in cells grown in microgels undergoing physiological dynamic compression. The data showed that arginine and proline metabolism were up-regulated in compressed microgels. This pathway involves the biosynthesis and metabolism of several amino acids, including arginine, ornithine, proline, citrulline, and glutamate. Additionally, N-glycan biosynthesis was up-regulated in compressed microgels. Matrix proteoglycans utilize N-glycans and provide much of the compressive strength of cartilage by

regulating matrix hydration through interactions with water. The compressed microgels also showed upregulation in glycine, serine, alanine, and threonine metabolism pathways. These amino acids are also needed to synthesize PCM and ECM. Due to low HPC availability, the metabolic studies were performed in SW1353 chondrosarcoma cells to optimize the experimental system. Nonetheless, collagen formation observed around PHCs in the alginate microgels yields promising data for future metabolomic studies using PHCs that will provide exciting advances in single-cell chondrocyte microgels to advance osteoarthritis and tissue engineering.

Chapters 3 and 4 demonstrated that alginate microgels provide an excellent growth environment for chondrocytes, promote PCM formation, and alter the chondrocytes' metabolic response to physiological dynamic compression. When grown in alginate microgels, chondrocytes form a collagen VI-rich PCM that forms linearly over ten days. The PCM of the chondrocytes stiffens dramatically over ten days, with approximately half of the cell reaching in vivo G'. The developed PCM was found to alter the chondrocytes' metabolic response to physiological dynamic compression. When embedded in a stiffer agarose gel, the cells with developed PCM expressed higher levels of amino acid and central energy metabolism pathways.

Chapter 5 investigated the capabilities of microgels to advance neural tissue engineering and HSV-1 studies. Through drop-based microfluidics, we sought to culture single neurons to observe viral infection dynamics and outcomes in individual cells. The aqueous drops employed in typical DBM lack a solid scaffold for cells to adhere, grow and mature. We first showed that microgels are a suitable culture platform for mouse superior cervical ganglia neurons and Vero cells. When embedded in Matrigel microgels and cultured for 7 days, we saw that SCG neurons

grew robust neuronal extensions that followed the external curvature of the microgels. By immunofluorescence imaging of phosphorylated-neurofilament H, SCG neuron maturation and axonal development was achieved within 7 days in culture.

We then applied these microgel-embedded cells to the study of HSV-1. A dual-fluorescent HSV-1 recombinant, OK-15, was employed to visualize infection dynamics and replication kinetics. OK15 contains a CMV-driven yellow fluorescent protein (YFP) immediate-early (IE) reporter and a VP26-RFP (red fluorescent protein) fusion late (L) reporter. The detection of OK15-expressed YFP reported the onset of viral gene expression upon infection, and subsequent OK15-expressed RFP demonstrated the expression of structural late genes and the assembly of viral capsids. An early concern was how microgels and microgel-based cell culturing influenced HSV-1 infections. To understand the potential interactions between cells, microgels, and viruses, we explored HSV-1 infection of Vero cells in microgels. We first evaluated whether the location of the cell in relation to the microgel altered the likelihood of a cell becoming infected. Vero cells were either grown within microgels, on microgels, or suspended before being inoculated with virus at 10 pfu/drop. We found that when Vero cells were grown in microgels, the microgel inhibited infection with HSV-1 due to the size exclusion of the virions. However, when Vero cells were cultured on microgels, the cells were found to be highly permissible to infection. Additionally, Vero cells cultured on microgels expressed detectable YFP at significantly higher rates than Vero cells in suspension. This difference was hypothesized to result from cells maintaining critical morphological characteristics when cultured on microgels that encourage cellular susceptibility and permittivity to viral infection and replication. After making these observations, we further characterized HSV-1 OK15 infection of

Vero cells cultured on the surface of microgels. Vero cells were inoculated with 1, 10, and 100 pfu/drop doses. As the inoculating dose increased, the percentage of YFP positive cells increased, reaching a maximum of 95.2 ± 2.2% at 100 pfu/drop. This observation was consistent with the expectations of inoculation dose effects.

Using the system developed with Vero cells, we employed our 3-D microgel culturing and infection system with SCG neurons. Embedded neurons were infected in drops with inoculating doses of 1, 10, or 100 pfu/drop and as in Vero cells. As the inoculating dose increased, the percentage of YFP positive cells increased, reaching a maximum of 72.2 ± 6.6% at 100 pfu/drop.

HSV-1 gene expression progresses in a regimented cascade of three classes of viral genes in the order of IE, E, and L genes [11]. Therefore, we sought to observe viral gene expression kinetics in single neurons infected with HSV-1 OK15. HSV-1 OK15 allows the observation of viral gene expression in real-time by detection of YFP and RFP. Using the Dropspot imaging platform, neurons were imaged for 16 hours, and HSV-1 OK15 expressed fluorescent proteins were observable in real-time [12,13]. Furthermore, we found that the timing of YFP expression decreased with increased inoculating dose demonstrating that inoculating dose significantly impacted the onset of HSV-1 gene expression in single neurons. Neurons were further monitored for RFP expression, and we found that minimal percentages of neurons expressed detectable RFP at inoculating doses of 1 and 10 pfu/drop. However, at 100 pfu/drop, we saw that 55% of neurons expressed detectable RFP. These results demonstrated that in our single-neuron DBM culturing and infection system, we could observe the dose-dependent progression of HSV-1 infection in real-time. Additionally, using this system, we can temporally track the conversion of

single neurons from YFP positive to YFP and RFP positive. When these temporal experiments were repeated in Vero cells, we saw similar trends in single neurons as in single Vero cells.

Chapter 5 demonstrated the use of HSV-1 OK15 to observe the progression of HSV-1 infection in primary SCGs at the single-cell level and Vero cells. We developed a drop-based microfluidic system that supports the growth and maturation of single primary neurons and epithelial cells. We utilized a co-flow inoculation approach that enables infection and real-time observation of single-cells through the progression of HSV-1 replication. From growth to viral replication, this work utilizes single-cells isolated via drop-based microfluidics. Our DBM-based single-cell approach captures discrete events of heterogeneity within a population that would be missed by single-cell analysis of bulk culturing [14]. The resolution that this approach yields will develop critical insights into underrepresented variables relevant to HSV-1 infection, such as the cryptic cellular and viral factors contributing to the suppression of viral gene expression necessary to establish the latent infection of neurons.

Outlook

The two projects presented in this thesis aimed to improve typical culture tissue techniques by applying microgels. In addition, this thesis demonstrated the capabilities of microgels to advance articular cartilage and neural tissue engineering. While these projects specifically explored PCM formation in chondrocytes and HSV-1 infection dynamics in single neurons, many more phenomena exist to study.

In chapters 3 and 4, we demonstrated the capabilities of microgels to advance articular cartilage engineering. While we demonstrated that culturing chondrocytes in microgels induced PCM formation, we did not investigate the effects of microgel culture on ECM production. The

time frames of the experiments were 10 days in chapters 3 and 4. However, if the time frames of the experiments were expanded to time frames up to 8-12 weeks, questions regarding ECM production could also be answered. Further, over 8-12 weeks, the microgels could act as individual cartilage units, and the ability of single chondrocytes to produce functional cartilage could be investigated.

Chapter 3 investigated how PCM affects SW1353 cells' metabolic response to physiological dynamic compression. SW1353 cells are one of the best cell lines for studying chondrocytes; however, they do little to represent the metabolism of primary chondrocytes [2]. Repeating the dynamic compression studies with human primary chondrocytes would reveal new insights into how PCM affects the metabolism of human primary chondrocytes.

In chapters 3 and 4, we showed that increases in auto-fluorescence of chondrocytes correlated with matrix production. Microfluidics provides a unique platform to sort for the brightest chondrocytes through fluorescence-activated droplet sorting [15,16]. Sorting for only chondrocytes that produce the most matrix could help build better cartilage models and improve tissue engineering techniques by only including the most active cells. Studying transcriptional differences between the brightest and dimmest cells would be interesting. Why did some cells produce incredibly stiff PCM while others did not in Chapter 4? Why do some cells produce large amounts of matrix while others do not?

The work in chapters 3 and 4 demonstrated how microgels can advance regenerative medicine techniques such as MACI. However, the studies do not examine whether the microgels would be effective in in vivo models. Translation of the microgels to a mouse model would provide insightful information on to what extend microgels could improve upon MACI. We

hypothesize that growing primary chondrocytes in microgels would decrease recovery times in MACI, but a direct comparison of MACI vs. microgels would be necessary.

In chapter 5, we used microgels and microfluidics as tools to grow and study neurons and HSV-1. However, the applications investigated within the chapter are only the beginning of what can be studied using these tools. For example, the single-neuron infection experiments can be furthered to include studies of drug efficacy in single neurons. One of the most promising outlooks for this work involves the phenomena of latency. Currently, the systems available to study latency are limited in availability and throughput [17]. This system can potentially establish a latent infection in tens of thousands of cells simultaneously, a feat not yet achieved. However, this work did not establish if latent infections were occurring, and further work involving single-cell transcriptomics to confirm the occurrence of latent infections in this system is necessary. Additionally, the work presented here focused on HSV-1 studies specifically. Many more viruses and cell types could be studied using the technology we developed here. For example, human primary lung cells could be grown on microgels to study influenza or coronaviruses.

The work presented in chapter 5 focused on applying singly grown neurons to HSV-1 studies. However, many more applications exist for these single neuron-microgel systems. For example, microgels have been used in many 3-D fabrication techniques [18]. Including singly grown neurons into these microgels could give researchers control over the directionality and assembly of 3-D neural networks with precise control over cell density and location.

In total, this work presented how microgels can be used as tools for human articular cartilage and neural tissue engineering. The work presented here focused explicitly on PCM formation in primary human chondrocytes and HSV-1 infection dynamics in mouse superior cervical ganglia neurons. The tools developed here are far more broadly applicable than the specific applications described. The tools developed can revolutionize many facets of cartilage engineering, neural tissue engineering, and single-cell virology.

Works Cited

1. Wilusz RE, Sanchez-Adams J, Guilak F. The structure and function of the pericellular matrix of articular cartilage. Matrix Biol. 2014;39: 25–32.

2. Gebauer M, Saas J, Sohler F, Haag J, Söder S, Pieper M, et al. Comparison of the chondrosarcoma cell line SW1353 with primary human adult articular chondrocytes with regard to their gene expression profile and reactivity to IL-1beta. Osteoarthritis Cartilage. 2005;13: 697–708.

3. Rigacci L, Alterini R, Bernabei PA, Ferrini PR, Agati G, Fusi F, et al. Multispectral imaging autofluorescence microscopy for the analysis of lymph-node tissues. Photochem Photobiol. 2007;71: 737–742.

4. Hoell T, Huschak G, Beier A, Hüttmann G, Minkus Y, Holzhausen HJ, et al. Auto fluorescence of intervertebral disc tissue: a new diagnostic tool. Eur Spine J. 2006;15 Suppl 3: S345-53.

5. Andersson-Engels S, Johansson J, Svanberg K, Svanberg S. Fluorescence imaging and point measurements of tissue: applications to the demarcation of malignant tumors and atherosclerotic lesions from normal tissue. Photochem Photobiol. 1991;53: 807–814.

6. Muir H. The chondrocyte, architect of cartilage. Biomechanics, structure, function and molecular biology of cartilage matrix macromolecules. Bioessays. 1995;17: 1039–1048.

7. Darling EM, Wilusz RE, Bolognesi MP, Zauscher S, Guilak F. Spatial mapping of the biomechanical properties of the pericellular matrix of articular cartilage measured in situ via atomic force microscopy. Biophys J. 2010;98: 2848–2856.

8. Alexopoulos LG, Haider MA, Vail TP, Guilak F. Alterations in the mechanical properties of the human chondrocyte pericellular matrix with osteoarthritis. J Biomech Eng. 2003;125: 323–333.

9. Zhang Z. Chondrons and the pericellular matrix of chondrocytes. Tissue Eng Part B Rev. 2015;21: 267–277.

10. Zignego DL, Hilmer JK, June RK. Mechanotransduction in primary human osteoarthritic chondrocytes is mediated by metabolism of energy, lipids, and amino acids. J Biomech. 2015;48: 4253–4261.

11. Roizman B, Zhou G. The 3 facets of regulation of herpes simplex virus gene expression: A critical inquiry. Virology. 2015;479–480: 562–567.

12. Schmitz CHJ, Rowat AC, Köster S, Weitz DA. Dropspots: a picoliter array in a microfluidic device. Lab Chip. 2009;9: 44–49.

13. Pratt SL, Zath GK, Akiyama T, Williamson KS, Franklin MJ, Chang CB. DropSOAC: Stabilizing Microfluidic Drops for Time-Lapse Quantification of Single-Cell Bacterial Physiology. Front Microbiol. 2019;10: 2112.

14. Liu W, He H, Zheng S-Y. Microfluidics in Single-Cell Virology: Technologies and Applications. Trends Biotechnol. 2020;38: 1360–1372.

15. Sciambi A, Abate AR. Accurate microfluidic sorting of droplets at 30 kHz. Lab Chip. 2015;15: 47–51.

16. Caen O, Schütz S, Jammalamadaka MSS, Vrignon J, Nizard P, Schneider TM, et al. High-throughput multiplexed fluorescence-activated droplet sorting. Microsyst Nanoeng. 2018;4: 33.

17. Wilson AC. Impact of Cultured Neuron Models on α-Herpesvirus Latency Research. Viruses. 2022;14. doi:10.3390/v14061209

18. Caldwell AS, Aguado BA, Anseth KS. Designing Microgels for Cell Culture and Controlled Assembly of Tissue Microenvironments. Adv Funct Mater. 2020;30. doi:10.1002/adfm.201907670

APPENDICES

APPENDIX A

SUPPLEMETANL INFORMATION FOR CHAPTER 3: METABOLOMIC PROFILING AND MECHANOTRANSDUCTION OF SINGLE CHONDROCYTES ENCAPSUALTED IN ALGINATE MICROGELS

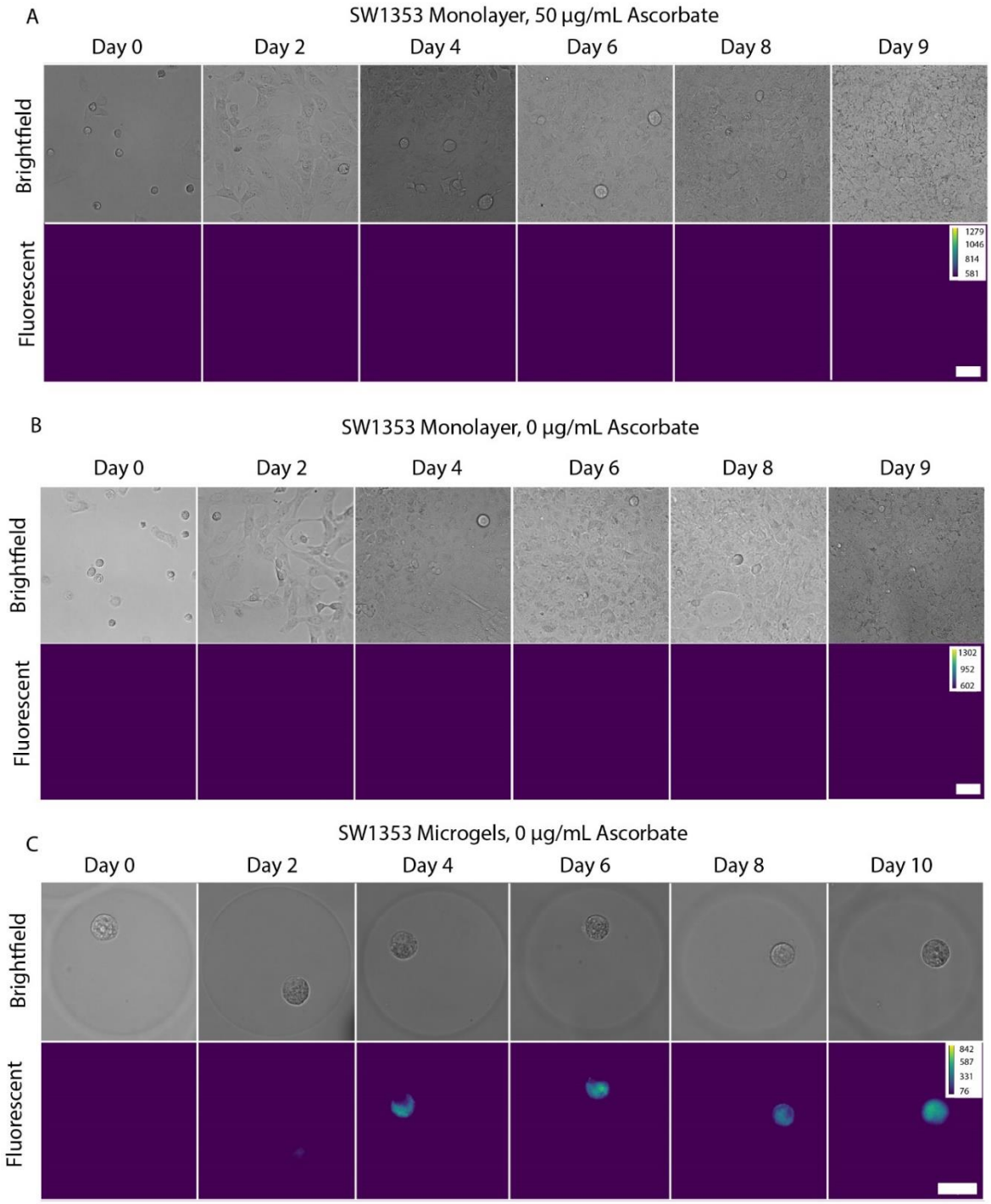


Figure S1. Brightfield and fluorescence images of microgels without and with ascorbate of (A) SW1353 cells grown on monolayers with 50 µg mL-1 ascorbate. Scale bar = 50 µm (B) SW1353 cells grown on monolayers with 0 µg mL-1 ascorbate. Scale bar = 50 µm (C) SW1353 cells encapsulated in alginate microgels and cultured with 0 µg mL-1 ascorbate Scale bar =25 µm

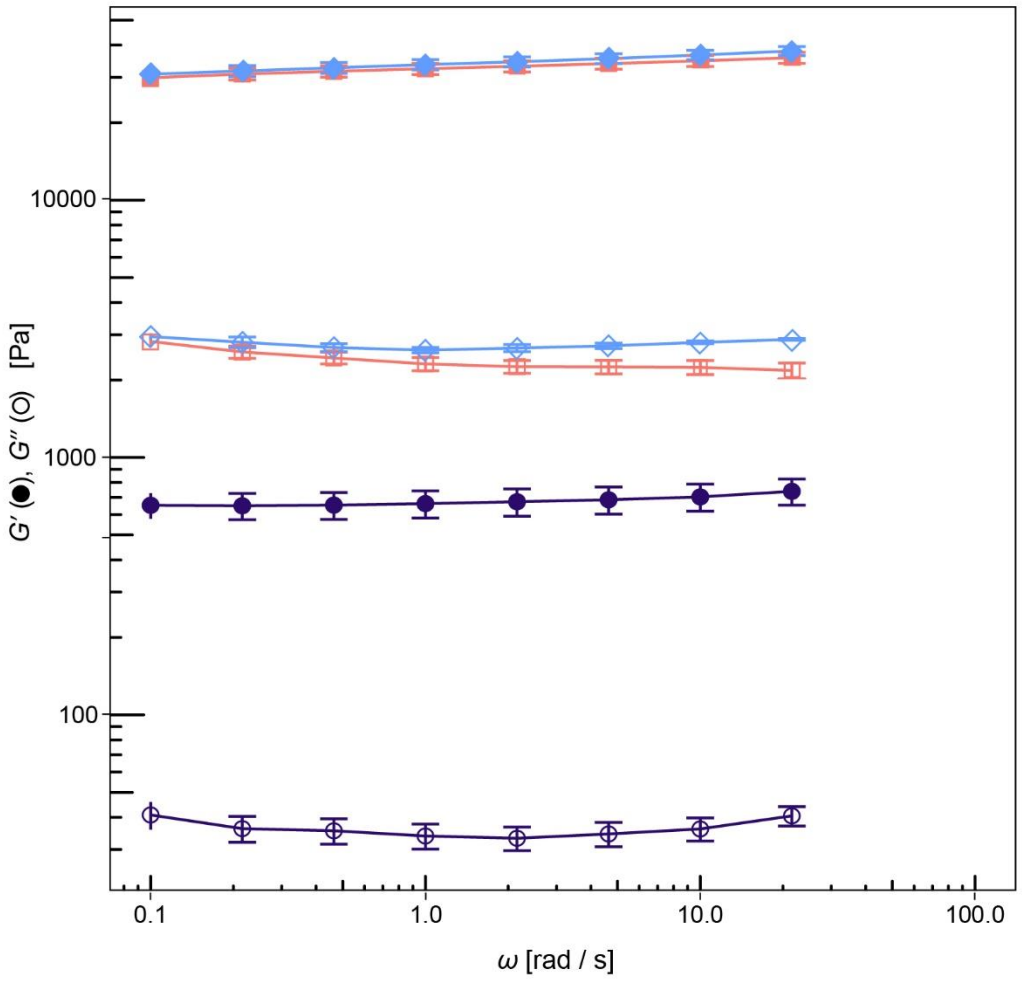


Figure S2. Storage (closed symbols) and loss (open symbols) moduli versus angular frequency, T = 25 °C, for 4.5% w/w agarose (squares), 1.5% w/w alginate (circles), and 4.5% w/w agarose with 20% v/v 1.5% w/w alginate microgels (diamonds).

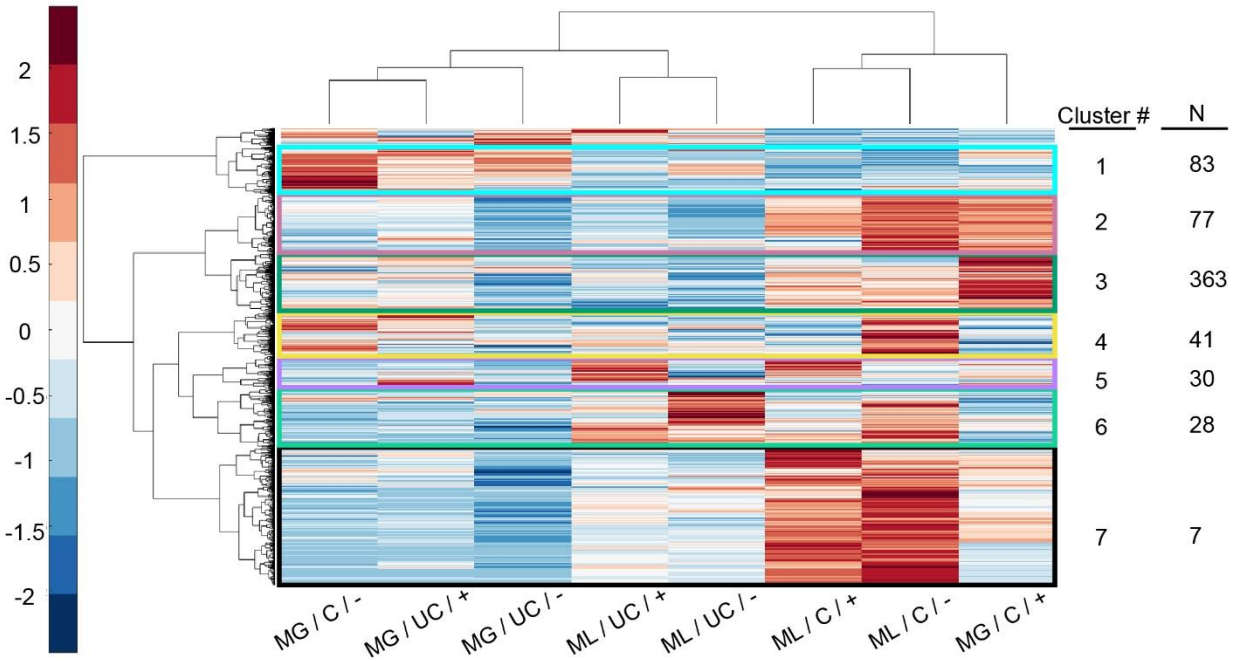


Figure S3. Median metabolites across all experimental groups. Metabolite clusters (colored boxes) were subjected to pathway enrichment analysis, but no significant pathways were found after false discovery rate correction. ML (Monolayer), MG (Microgel), C (Compressed), UC (Uncompressed), + (complete media supplemented with 50 μg mL-1 L-sodium ascorbate), - (complete media lacking L-sodium ascorbate).

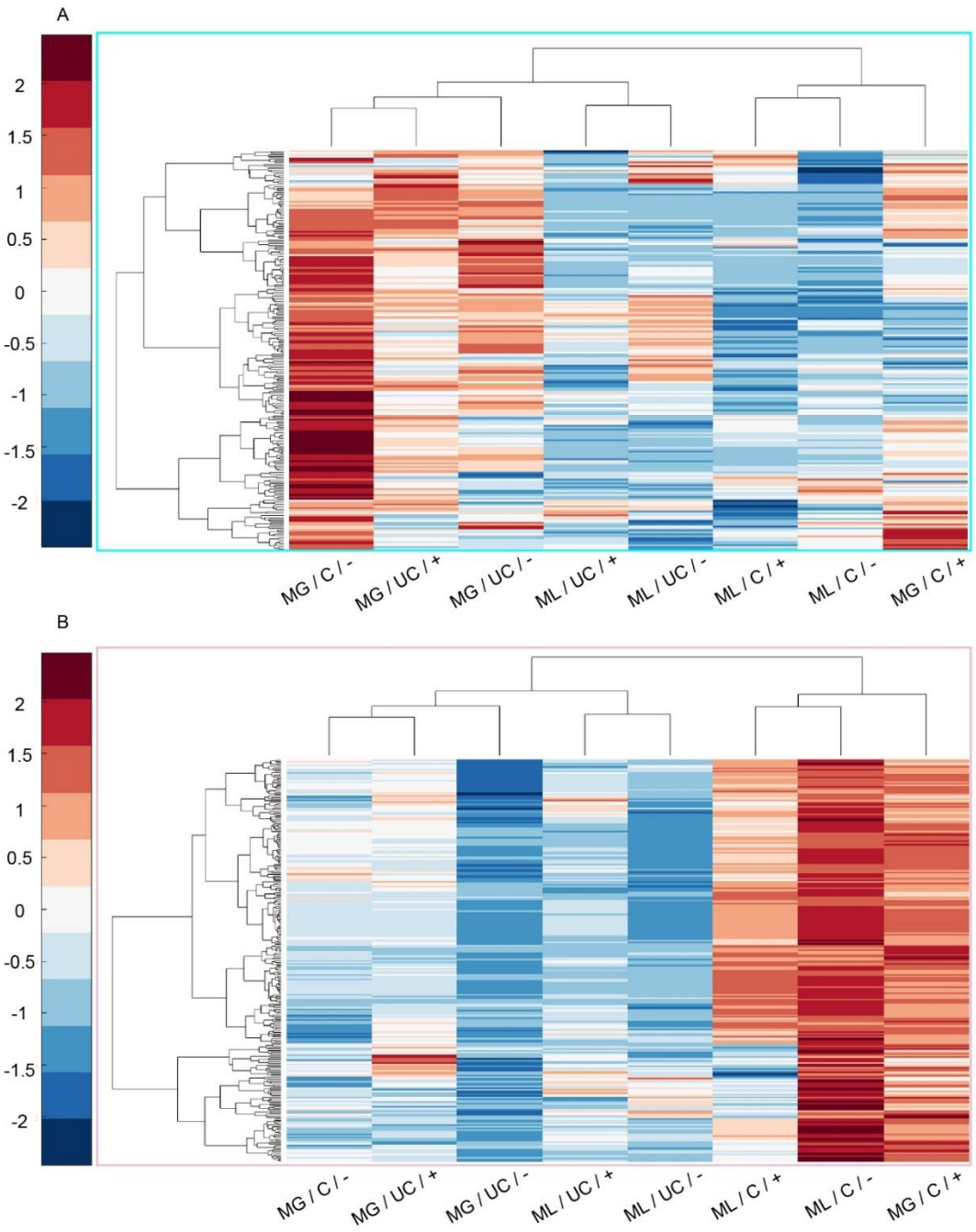


Figure S4. Median metabolites across all experimental group. (A) Metabolite cluster 1 and (B) cluster 2 from SI figure 4 were further subjected to pathway enrichment analysis, but no significant pathways were found after false discovery rate correction. ML (Monolayer), MG (Microgel), C (Compressed), UC (Uncompressed), + (complete media supplemented with 50 µg mL-1 L-sodium ascorbate), - (complete media lacking L-sodium ascorbate).

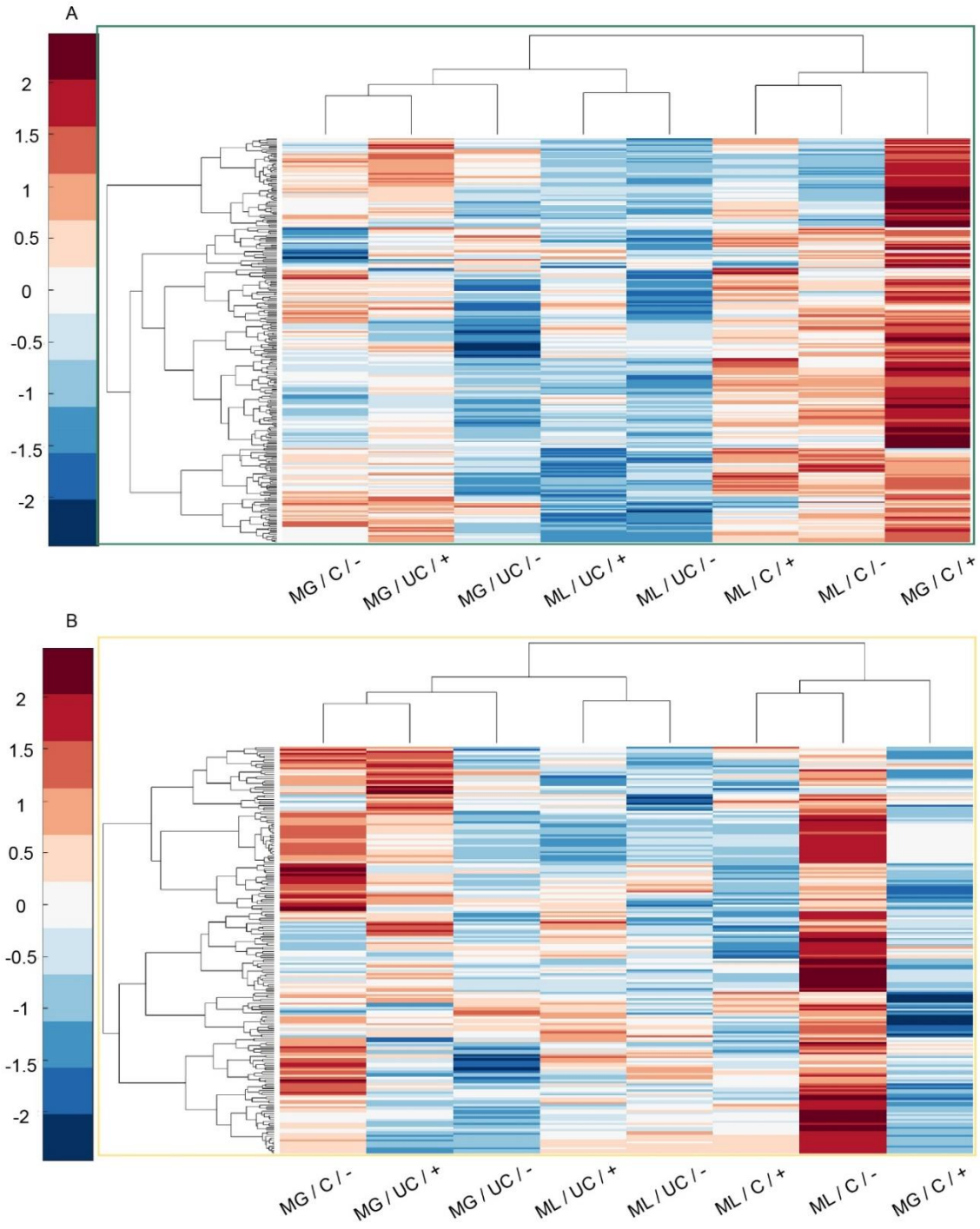


Figure S5. Median metabolites across all experimental group. (A) Metabolite cluster 3 and (B) cluster 4 from SI Figure 4 were subjected to pathway enrichment analysis, but no significant pathways were found after false discovery rate correction. ML (Monolayer), MG (Microgel), C (Compressed), UC (Uncompressed), + (complete media supplemented with 50 µg mL-1 L-sodium ascorbate), - (complete media lacking L-sodium ascorbate).

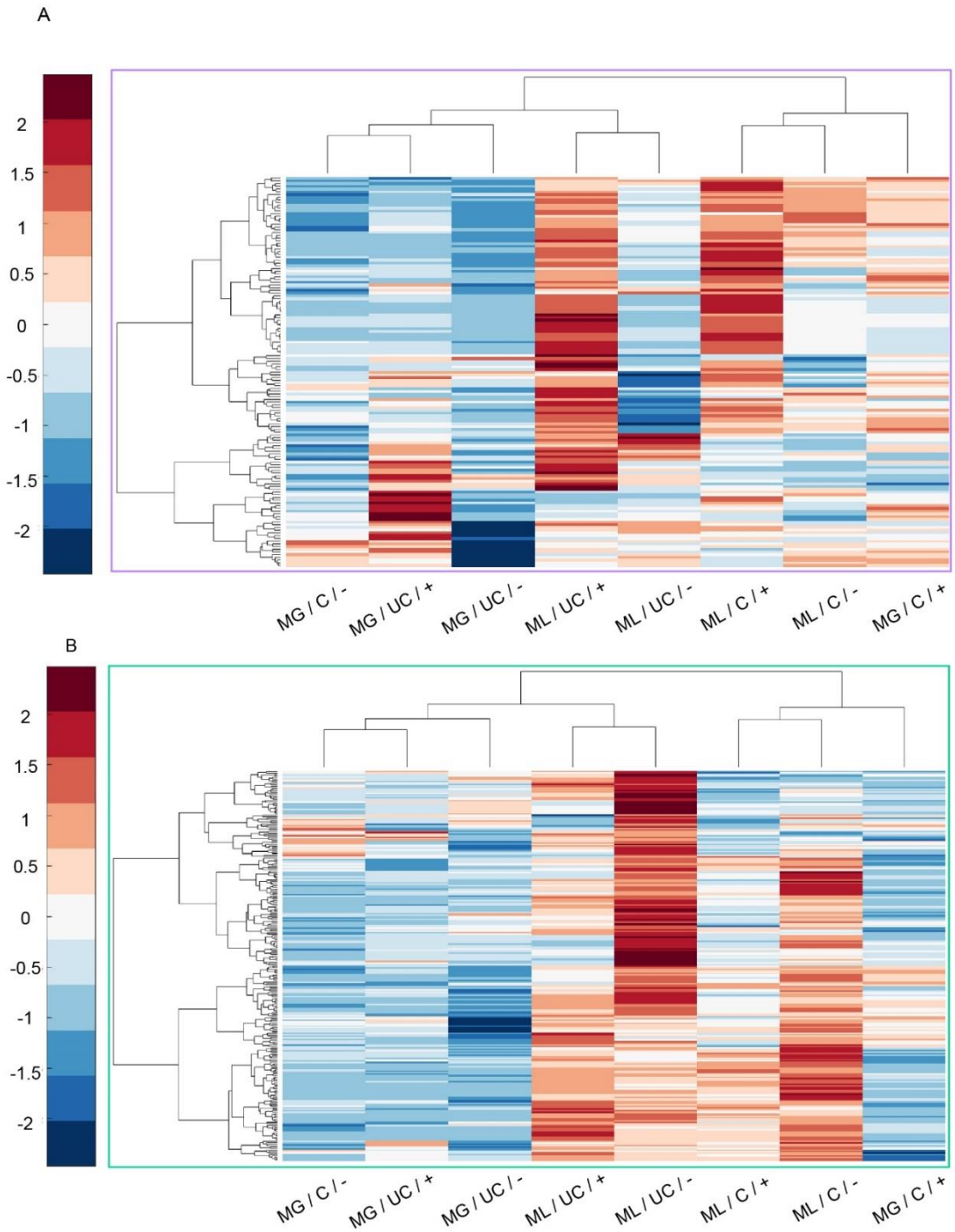


Figure S6. Median metabolites across all experimental group. (A) Metabolite cluster 5 and (B) cluster 6 from SI Figure 4 were subjected to pathway enrichment analysis, but no significant pathways were found after false discovery rate correction. ML (Monolayer), MG (Microgel), C (Compressed), UC (Uncompressed), + (complete media supplemented with 50 μg mL-1 L-sodium ascorbate), - (complete media lacking L-sodium ascorbate).

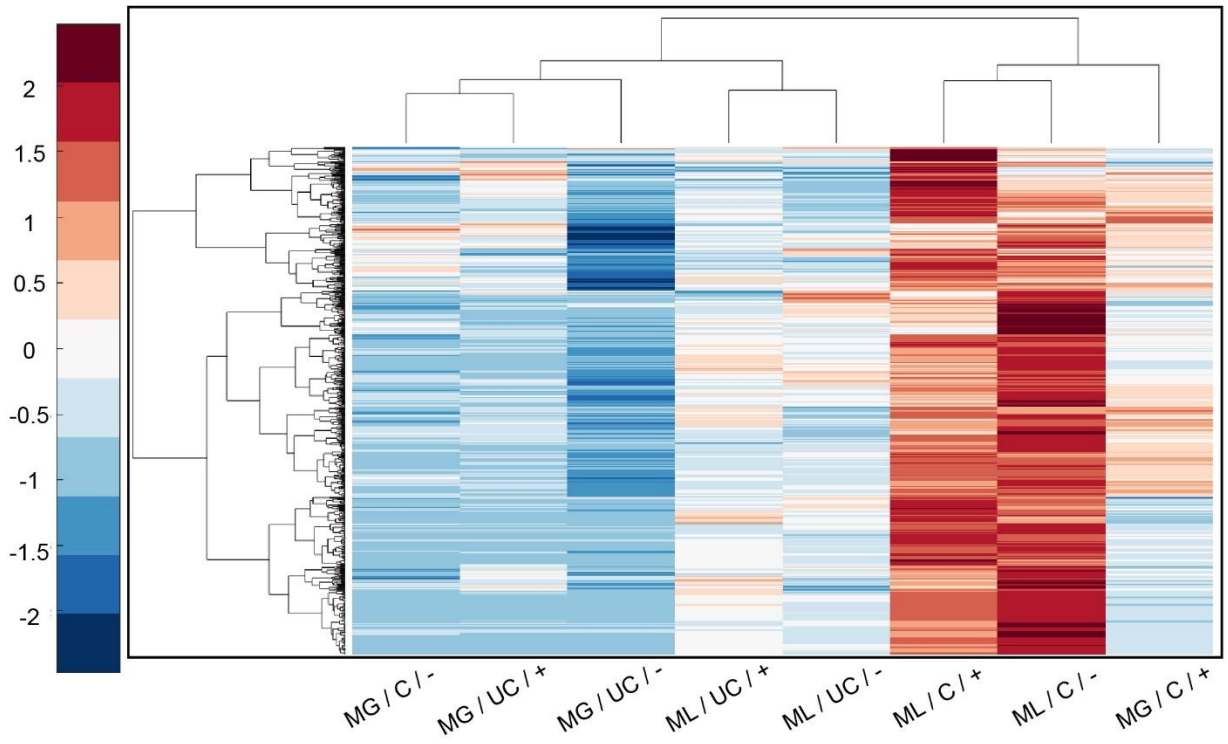


Figure S7. Median metabolites across all experimental group. Metabolite cluster 7 from SI Figure 4 was subjected to pathway enrichment analysis, but no significant pathways were found after false discovery rate correction. ML (Monolayer), MG (Microgel), C (Compressed), UC (Uncompressed), + (complete media supplemented with 50 μg mL-1 L-sodium ascorbate), - (complete media lacking L-sodium ascorbate).

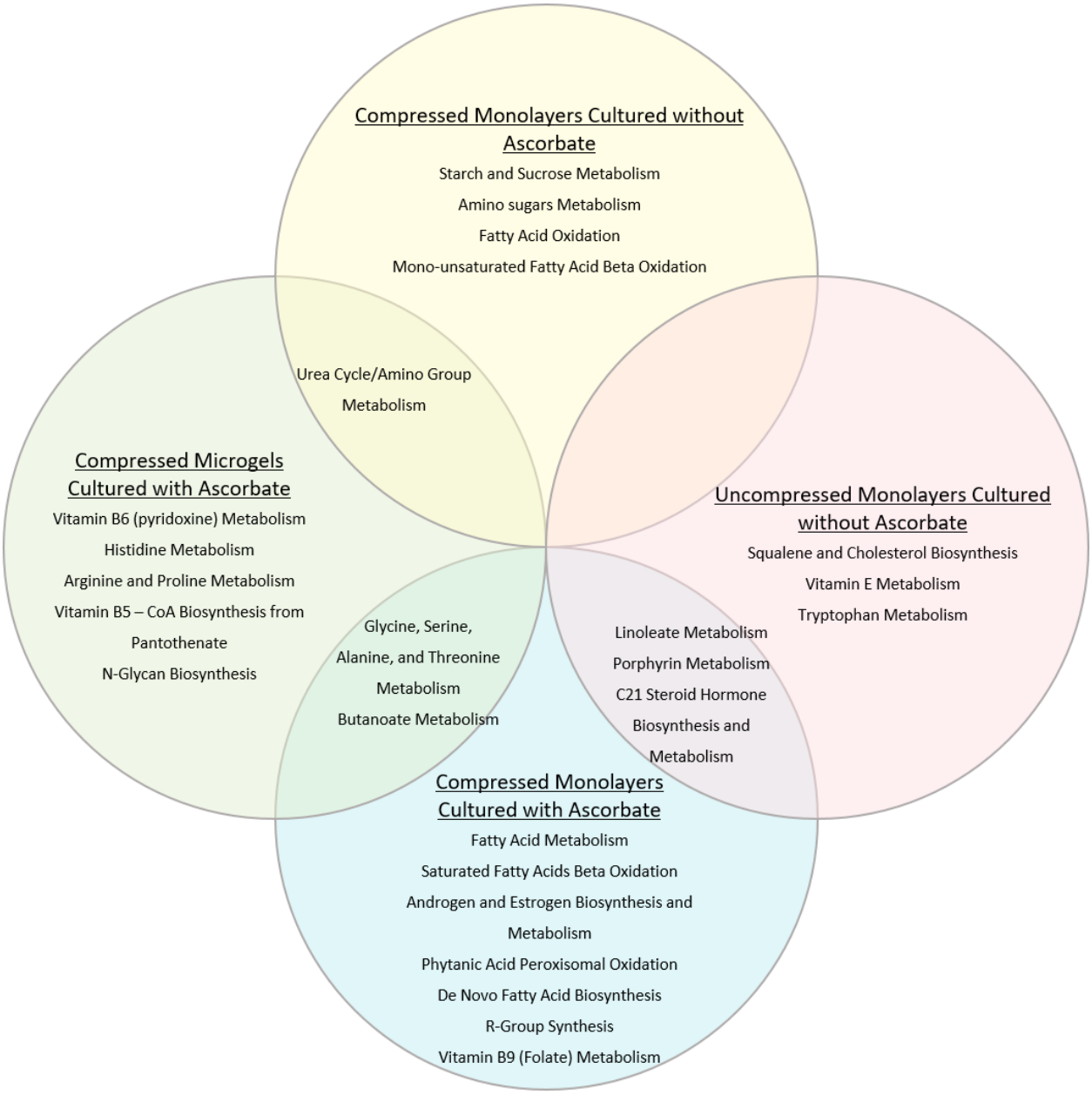


Figure S8. Venn diagram of significant pathways for each group

Hydrogel	ω [rad/s]	G' [Pa]	G'' [Pa]
4.5% w/w Agarose	0.100	3.0E+04 ± 2.9E+03	2.8E+03 ± 2.4E+02
	0.215	3.1E+04 ± 2.7E+03	2.6E+03 ± 2.4E+02
	0.464	3.2E+04 ± 2.8E+03	2.4E+03 ± 2.2E+02
	1.000	3.2E+04 ± 2.8E+03	2.3E+03 ± 2.3E+02
	2.154	3.3E+04 ± 2.8E+03	2.3E+03 ± 2.2E+02
	4.642	3.4E+04 ± 2.9E+03	2.2E+03 ± 2.4E+02
	10.000	3.5E+04 ± 3.0E+03	2.2E+03 ± 2.4E+02
	21.544	3.6E+04 ± 3.0E+03	2.2E+03 ± 2.6E+02
1.5 % w/w Alginate	0.100	6.5E+02 ± 1.8E+02	4.1E+01 ± 1.2E+01
	0.215	6.5E+02 ± 1.9E+02	3.6E+01 ± 1.0E+01
	0.464	6.5E+02 ± 1.9E+02	3.5E+01 ± 9.8E+00
	1.000	6.6E+02 ± 2.0E+02	3.4E+01 ± 9.3E+00
	2.154	6.7E+02 ± 2.0E+02	3.3E+01 ± 8.5E+00
	4.642	6.9E+02 ± 2.0E+02	3.4E+01 ± 9.2E+00
	10.000	7.0E+02 ± 2.1E+02	3.6E+01 ± 9.1E+00
	21.544	7.4E+02 ± 2.1E+02	4.1E+01 ± 8.6E+00
Agarose + 20% v/v Alginate Microgels	0.100	3.1E+04 ± 2.7E+03	2.9E+03 ± 1.6E+02
	0.215	3.2E+04 ± 2.8E+03	2.8E+03 ± 2.3E+02
	0.464	3.3E+04 ± 2.7E+03	2.7E+03 ± 1.6E+02
	1.000	3.4E+04 ± 2.7E+03	2.6E+03 ± 1.0E+02
	2.154	3.4E+04 ± 2.7E+03	2.7E+03 ± 1.5E+02
	4.642	3.5E+04 ± 2.7E+03	2.7E+03 ± 1.1E+02
	10.000	3.7E+04 ± 2.7E+03	2.8E+03 ± 5.9E+01
	21.544	3.8E+04 ± 2.7E+03	2.9E+03 ± 4.2E+01

Table S1. Elastic (*G'*) and Storage (*G''*) moduli of 4.5% w/w agarose, 1.5% w/w alginate, and 4.5 % w/w agarose with 20% v/v 1.5% w/w alginate microgels for varying angular frequencies. Rheology was performed on a TA Instruments AR-G2 rheometer with a parallel plate geometry.

Cluster #2 – Compressed Monolayers Cultured without Ascorbate (Up-regulated)

	Gamma	Matched Metabolites
Starch and Sucrose Metabolism	0.0441	*Maltopentaose *D-Glucose *D-Glucose *Alpha-D-Glucose
Urea cycle/amino group metabolism	0.048281	*Creatinine *L-Arginine *2-(3-Carboxy-3-(methylammonio)propyl)-L-histidine *L-Methionine – the 1st amino group (essential) *Creatine
Aminosugars metabolism	0.048739	*Chitin *(N-acetylneuraminosyl(a2-6)lactosamine) *Phosphoenolpyruvic acid

Cluster #3 – Compressed Microgels Cultured with Ascorbate (Up-regulated)

	Gamma	Matched Metabolites
Vitamin B6 (pyridoxine) metabolism	0.035844	*Pyridoxamine *Pyridoxine

Urea cycle/amino group metabolism	0.036024	*L-Proline *Hippuric acid *Citrulline *4-Acetamidobutanoic acid *4-Aminobutyraldehyde *N-Methylphenylethanolamine *Norepinephrine
Histidine metabolism	0.036669	*5-Formiminotetrahydrofolic acid *Methylimidazoleacetic acid *Carnosine
Glycine, serine, alanine and threonine metabolism	0.040908	*Betaine *2-methylbutyrylglycine *Isovalerylglycine *L-Allothreonine *L-Threonine
Arginine and Proline Metabolism	0.040908	*L-Proline *Citrulline *4-Acetamidobutanoic acid *1-Pyrroline-2-carboxylic acid *4-Aminobutyraldehyde *D-Proline

		*Pyrroline hydroxycarboxylic acid
Vitamin B5 - CoA biosynthesis from pantothenate	0.045044	*4-Phosphopantothenoylcysteine *Pantetheine
Butanoate metabolism	0.045044	*2-Keto-6-acetamidocaproate *5-Aminopentanoic acid
Glutathione Metabolism	0.045044	*Pyroglutamic acid *gamma-Glutamylcysteine
N-Glycan biosynthesis	0.04861	*Uridine diphosphategalactose *Uridine diphosphate glucose *N,N'-Diacetylchitobiosyldiphosphodolichol *Dolichol-20

Cluster #4 - Compressed Monolayers Cultured without Ascorbate (Up-regulated)

	Gamma	Matched Metabolites
Fatty acid oxidation	0.041484	*2,6 dimethylheptanoyl-CoA *Gamma-linolenoyl-CoA *4,8 dimethylnonanoyl-CoA *Trans-Octadec-2-enoyl-CoA * Hexadecenoyl-CoA * Vaccenyl coenzyme A *Octadecenoyl-CoA

Mono-unsaturated fatty acid beta-oxidation	0.047503	* 3-oxolaur-cis-5-enoyl-CoA *Palmitoleoyl-CoA

Cluster #6 - Uncompressed Monolayers Cultured without Ascorbate (Up-regulated)

	Gamma	Matched Metabolites
Linoleate metabolism	0.033754	*LysoPC(18:1(9Z)) *(11S)-11-Hydroperoxylinoleic acid * 9,10-12,13-diepoxy-octadecanoate
Squalene and cholesterol biosynthesis	0.041083	* 4,4-dimethylcholesta-8(9),14-dien-3beta-ol *Presqualene diphosphate *4,4-Dimethyl-5a-cholesta-8,24-dien-3-b-ol *Avenasterol * Delta7-Avenasterol
Porphyrin metabolism	0.04495	*Protoporphyrinogen IX *Uroporphyrin I *Uroporphyrin III
C21-steroid hormone biosynthesis and metabolism	0.04495	*Cholesterol sulfate *Estrone sulfate

Vitamin E metabolism	0.048938	*Phenylacetaldehyde *9'-carboxy-alpha-chromanol
Tryptophan metabolism	0.052097	*Cyclic 3-hydroxymelatonin *6-Hydroxymelatonin *Melatonin radical *Tetrahydrobiopterin

Cluster #7 – Compressed Monolayers Cultured with and without Ascorbate (Up-regulated)

	Gamma	Matched Metabolites
Fatty Acid Metabolism	0.011922	*Tetradecanoyl-CoA *Palmityl-CoA *(2E)-Dodecenoyl-CoA *3-Oxotetradecanoyl-CoA *3-dodecenoyl CoA
Saturated fatty acids beta-oxidation	0.011922	*Tetradecanoyl-CoA *Palmityl-CoA *(S)-3-Hydroxytetradecanoyl-CoA *3-Oxotetradecanoyl-CoA *(S)-3-Hydroxydodecanoyl-CoA *(2E)-Dodecenoyl-CoA
Androgen and estrogen	0.017094	*Estrone sulfate

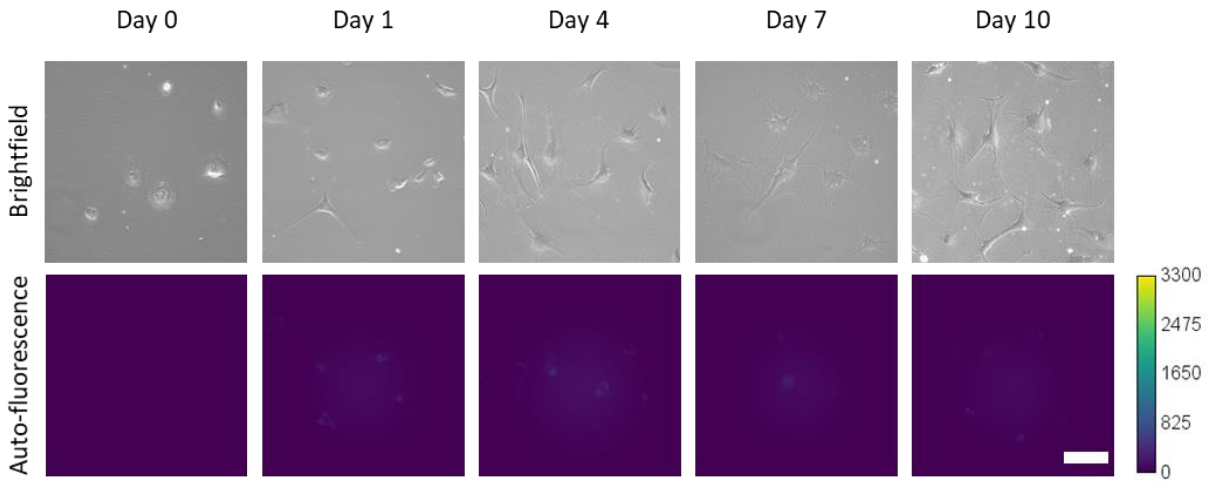
biosynthesis and metabolism		*Trypanothione disulfide *17-beta-Estradiol-3-glucuronide *Androstenedione *Estrone glucuronide
Porphyrin metabolism	0.018407	*Heme O *Coproporphyrin I *Protoporphyrinogen IX *Coproporphyrin III
C21-steroid hormone biosynthesis and metabolism	0.018407	*Androst-4-ene-3,17-dione *Estrone-glucuronide *Estrone sulfate *Androstenedione *17beta-estradiol 3-glucosiduronic acid
Phytanic acid peroxisomal oxidation	0.021904	*Pristanoyl-CoA *4,8,12-Trimethyltridecanoyl-CoA *3(S)-2-hydroxyphytanoyl-CoA *(2R)-pristanoyl-CoA; *(2S)-pristanoyl-CoA *3(R)-hydroxy-pristanoyl-CoA
De novo fatty acid biosynthesis	0.023437	*Palmityl-CoA *Linoleoyl-CoA

		*Tetradecanoyl-CoA; *Arachidonyl-CoA *3-hydroxyoctadecanoyl-CoA *3-hydroxytetracosanoyl-CoA *3-hydroxyeicosanoyl-CoA *3(S)-hydroxy-11-cis-eicosenoyl-CoA *Trans,cis-2,11-eicosadienoyl-CoA
Glycine, serine, alanine and threonine metabolism	0.031029	*Arachidonyl-CoA *Creatine *L-Allothreonine *L-Threonine
R Group Synthesis	0.033308	*Palmityl-CoA *Tetradecanoyl-CoA
Butanoate metabolism	0.033308	*2-Keto-6-acetamidocaproate *5-Acetamidovalerate
Glutathione Metabolism	0.033308	*Pyroglutamic acid *Trypanothione disulfide
Vitamin B9 (folate) metabolism	0.044339	*10-formyltetrahydrofolate-[Glu](5) *Tetrahydrofolyl-[Glu](n)

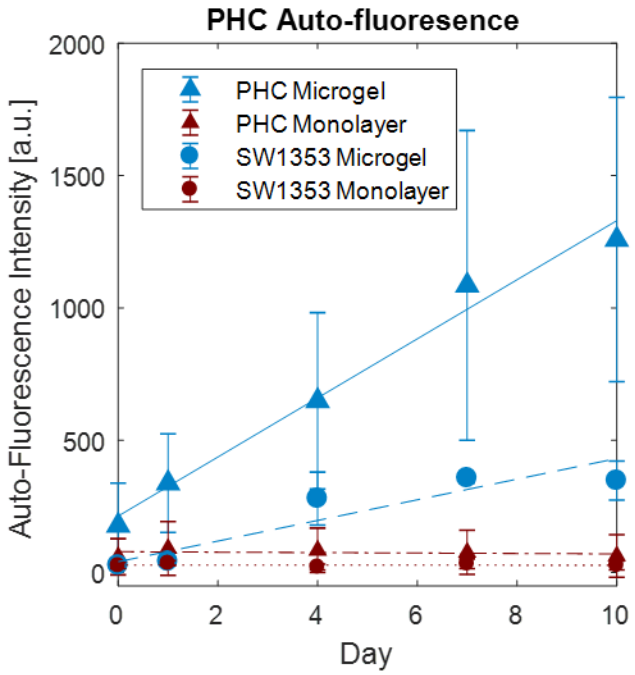
Table S2. All significant pathways found and the corresponding gamma values and matched metabolites.

APPENDIX B

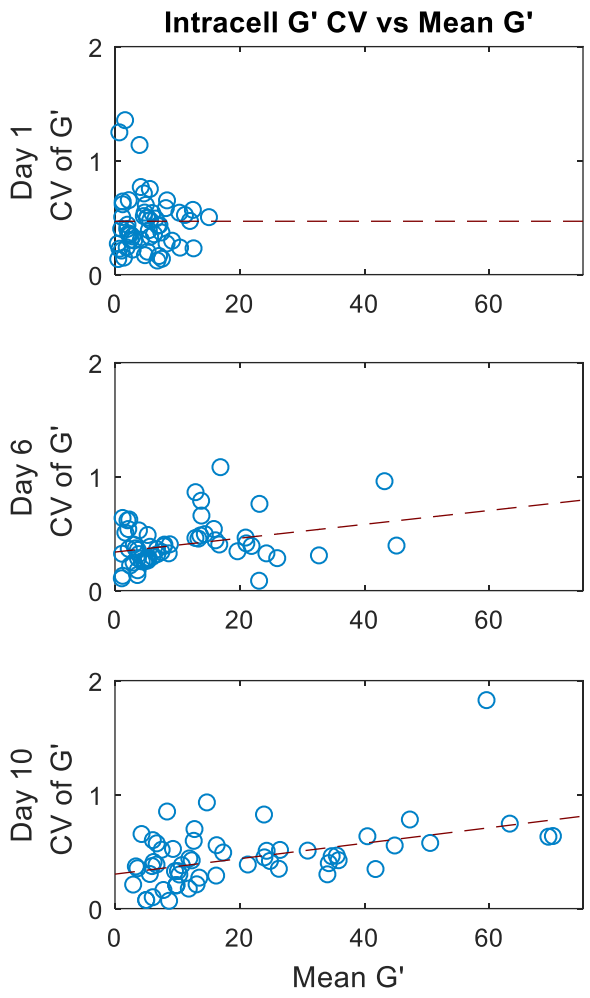
SUPPLEMETANL INFORMATION FOR CHAPTER 4: PERICEULLUAR MATRIX FORMATION AND ATOMIC FORCE MICROSCOPY OF SINGLE PRIMARY HUMAN CHONDROCYTES CULTRED IN ALGINATE MICROGELS



SI Figure 1: Auto-fluorescence imaging; Brightfield and fluorescence images (ex. 350/em. 470) of PHCs encapsulated grown in monolayer and cultured for 10 days. Scale bar is 25 μm.



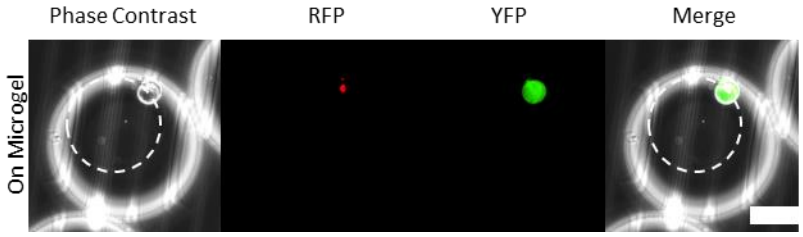
SI Figure 2: Auto-fluorescence imaging; Measured mean fluorescence intensities of imaged PHCs and SW1353 cells over time with weighted multiple linear regressions. PHCs encapsulated in microgels (blue triangles, solid line) and PHCs grown in monolayers (red triangle, dot-dash). SW1353 cells encapsulated in microgels (blue circles, dashed) and SW1353 cells grown in monolayers (red circles, dotted).



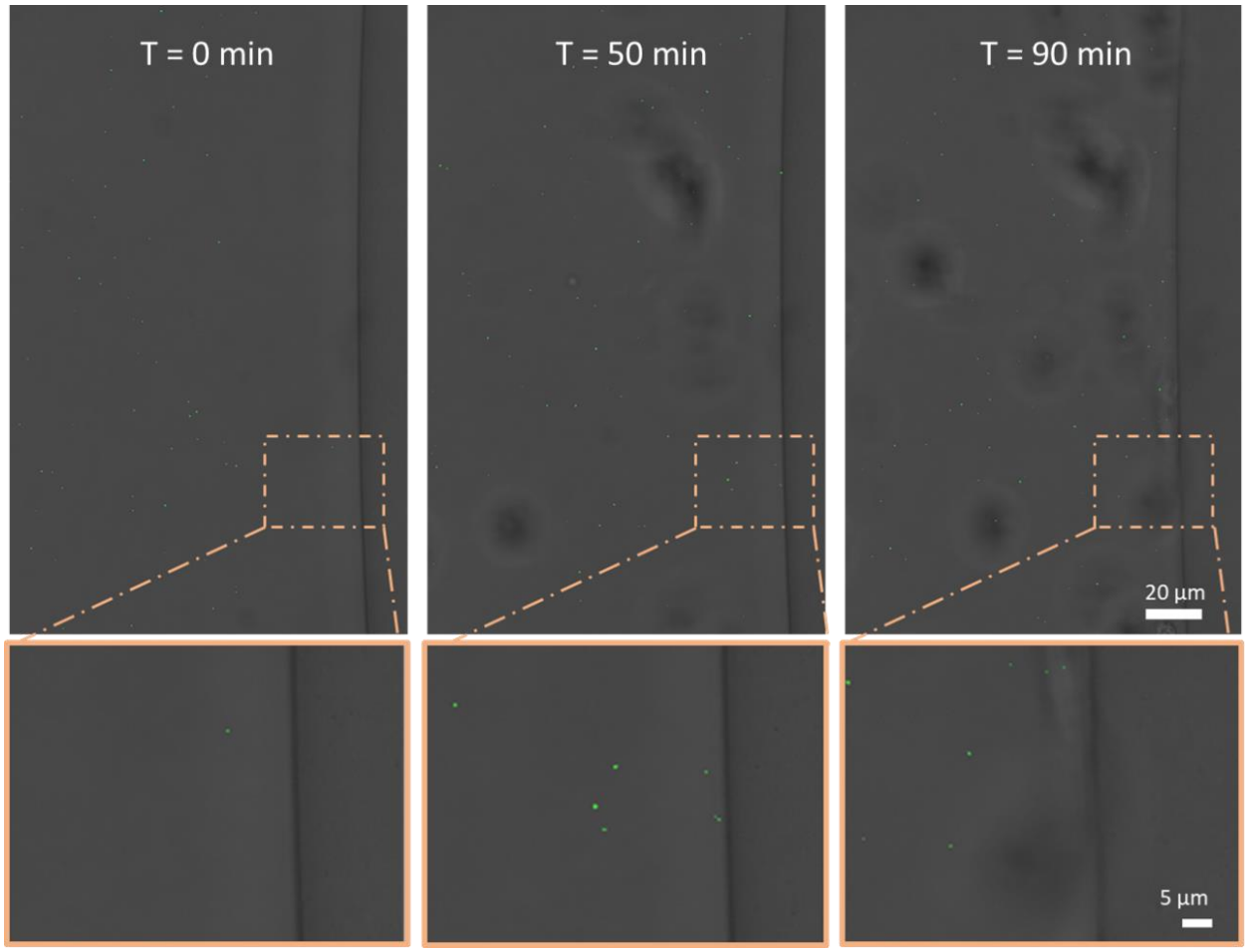
SI Figure 3: The average *G'* for each cell plotted versus its CV for PHCs grown in microgels on days 1, 6, and 10. Dashed lines represent fits from linear regressions. On day 1, intracell CV of *G'* did not correlate with each cell's average *G'* (p =0.57). On days 6 and 10, the intracell CV of *G'* was found to positively correlate with each cell's average *G'* (p = 0.018 and p = 0.000018).

APPENDIX C

SUPPLEMETANL INFORMATION FOR CHAPTER 5: DROPLET BASED MICROFLUIDICS FOR SINGLE NEURON GROWTH AND INFECTION WITH HERPES SIMPLEX VIRUS - 1

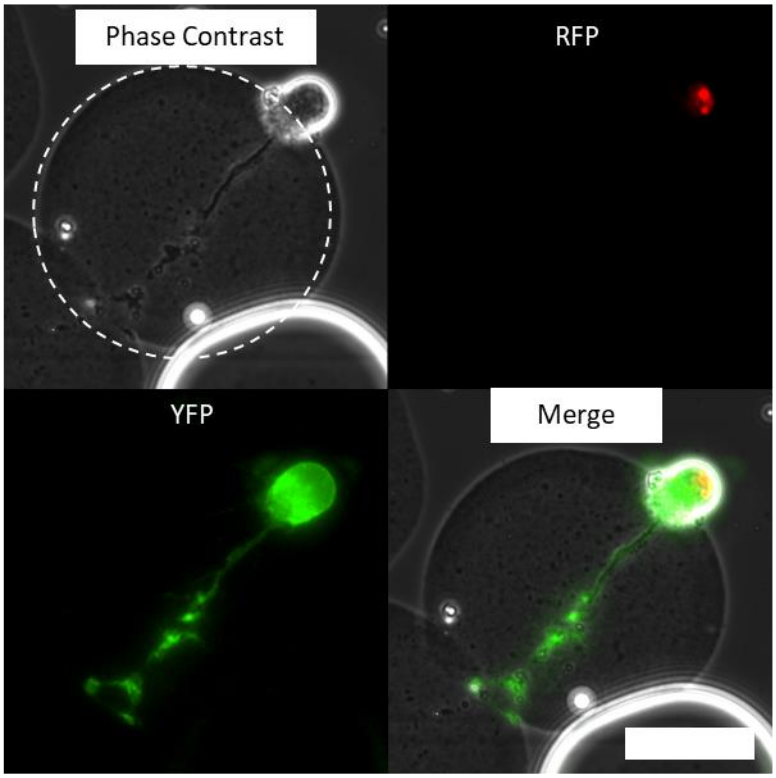


SI Figure 1: Representative images of Vero cells infected in drop on microgels. White circles denote the microgel. Scale bar is 50 µm

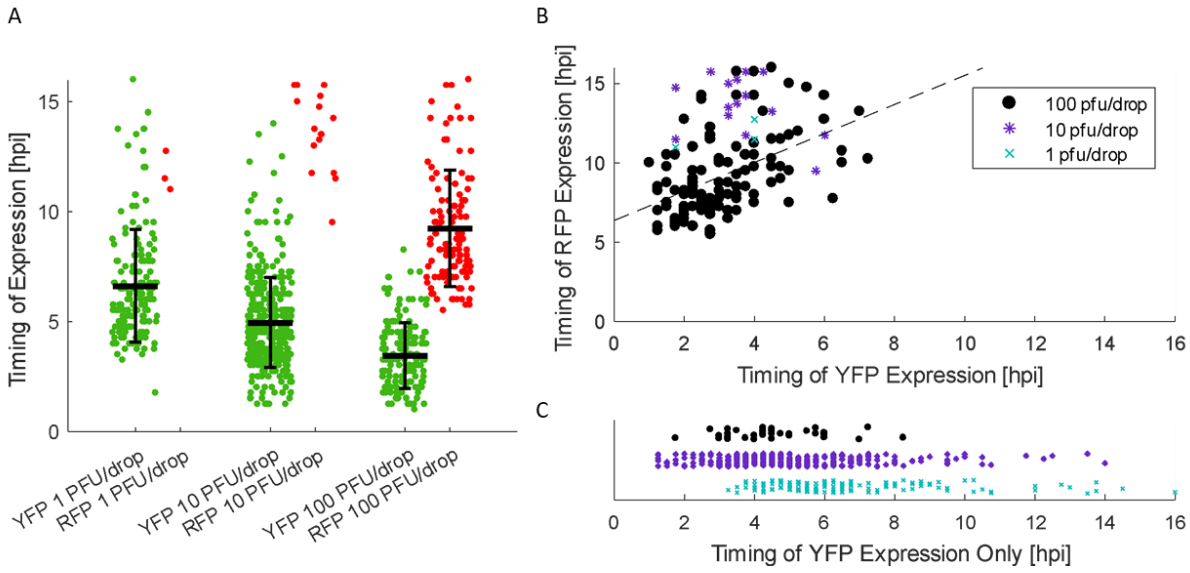


SI Figure 2: To investigate if HSV-1 OK15 can diffuse through Matrigel, confocal time-lapse imaging of virions (green) and Matrigel was performed. 20 µL of Matrigel was pipetted onto a glass-bottom petri dish and gelled at 37 °C. The resulting Matrigel hemisphere was immersed in PBS and the dish was placed onto the confocal microscope. The edge of the Matrigel was located

in brightfield and HSV-1 OK15 at 1×10^8 pfu/mL was added to the dish. Images were acquired at 63× every 10 min for 90 min in brightfield and mRFP (false colored green).



SI Figure 3: A representative image of an SCG neuron infected in a microfluidic drop with HSV-1 OK15 after breaking the emulsion for improved imaging. The white circle outlines the microgel. Scale bar is 50 μm.



SI Figure 4: (A) Timing of YFP and RFP expression in individual Vero cells plotted with the mean and standard deviation. Timing of YFP detection decreased with increased inoculating dose (1-way ANOVA $p = 1.9 \times 10^{-35}$). (B) YFP vs RFP expression timing in individual Vero cells. (1 PFU/drop - blue X, 10 PFU/drop - purple star, 100 pfu/drop - black circle) (Linear regression $t_{RFP+} = 6.4 + 0.9x\ t_{YFP+}$ $p = 1.1 \times 10^{-7}$ $R^2 = 0.22$). (F)YFP expression timing in Vero cells which did not express RFP. (1 PFU/drop - blue X, 10 PFU/drop - purple star, 100 pfu/drop - black circle).

APPENDIX D

GRANULAR MATRIGEL: RESTUCTURING A TRUSTED EXTRACELLULAR MATRIX MATERIAL FOR IMPROVED PERMEABILITY

Contribution of Authors and Co-Authors

Manuscript in Appendix D

Author: Zahra Mahdieh

Contributions: Conceptualization, methodology, formal analysis, investigation, data curation, writing original draft, and writing review and editing

Co-Author: Michelle D. Cherne

Contributions: Investigation, writing original draft, and writing review and editing

Co-Author: Jacob P. Fredrikson

Contributions: Conceptualization, investigation, writing original draft, and writing review and editing

Co-Author: Barkan Sidar

Contributions: Conceptualization, investigation, and Writing-Review & Editing

Co-Author: Humberto S. Sanchez

Contributions: Investigation, writing original draft, and writing review and editing

Co-Author: Connie B. Chang

Contributions: Validation, writing review and editing, and funding acquisition

Co-Author: Diane Bimczok

Contributions: Validation, writing review and editing, and funding acquisition

Co-Author: James N. Wilking

Contributions: Conceptualization, methodology, formal analysis, data curation, writing original draft, writing review and editing, supervision, and funding acquisition

Manuscript Information

Zahra Mahdieh, Michelle D. Cherne, Jacob P Fredrikson, Barkan Sidar, Humberto S. Sanchez,

Connie B. Chang, Diane Bimczok, James N. Wilking

Biomedical Materials

Status of Manuscript:
___ Prepared for submission to a peer-reviewed journal
___ Officially submitted to a peer-reviewed journal
___ Accepted by a peer-reviewed journal
_x_ Published in a peer-reviewed journal

IOP Science
Volume 17 Number 4
10.1088/1748-605X/ac7306

IOP Publishing Biomed. Mater. 17 (2022) 045020 https://doi.org/10.1088/1748-605X/ac7306

Biomedical Materials



PAPER

RECEIVED
1 February 2022

REVISED
6 May 2022

ACCEPTED FOR PUBLICATION
24 May 2022

PUBLISHED
8 June 2022

Granular Matrigel: restructuring a trusted extracellular matrix material for improved permeability

Zahra Mahdieh[1,2], Michelle D Cherne[3], Jacob P Fredrikson[1,2], Barkan Sidar[1,2], Humberto S Sanchez[1,2], Connie B Chang[1,2], Diane Bimczok[3] and James N Wilking[1,2,*]

[1] Department of Chemical and Biological Engineering, Montana State University, Bozeman, MT, United States of America
[2] Center for Biofilm Engineering, Montana State University, Bozeman, MT, United States of America
[3] Department of Microbiology and Cell Biology, Montana State University, Bozeman, MT, United States of America
[*] Author to whom any correspondence should be addressed.

E-mail: jwilking@gmail.com

Keywords: Matrigel, granular microgel, 3D cell culture, cell migration, organoids, microfluidics

Supplementary material for this article is available online

Abstract

Matrigel is a polymeric extracellular matrix material produced by mouse cancer cells. Over the past four decades, Matrigel has been shown to support a wide variety of two- and three-dimensional cell and tissue culture applications including organoids. Despite widespread use, transport of molecules, cells, and colloidal particles through Matrigel can be limited. These limitations restrict cell growth, viability, and function and limit Matrigel applications. A strategy to improve transport through a hydrogel without modifying the chemistry or composition of the gel is to physically restructure the material into microscopic microgels and then pack them together to form a porous material. These 'granular' hydrogels have been created using a variety of synthetic hydrogels, but granular hydrogels composed of Matrigel have not yet been reported. Here we present a drop-based microfluidics approach for structuring Matrigel into a three-dimensional, mesoporous material composed of packed Matrigel microgels, which we call granular Matrigel. We show that restructuring Matrigel in this manner enhances the transport of colloidal particles and human dendritic cells (DCs) through the gel while providing sufficient mechanical support for culture of human gastric organoids (HGOs) and co-culture of human DCs with HGOs.

1. Introduction

Matrigel is a commercialized, protein-based extracellular matrix (ECM) produced by Engelbreth–Holm–Swarm mouse sarcoma cells which is widely used for mammalian cell and tissue culture [1–3]. Matrigel contains many essential ECM components such as collagen, laminin, entactin, the proteoglycan heparan sulfate, and important growth factors which are essential for cell growth and development [4, 5]. Matrigel was first reported in 1975 [6], and, over the past four decades, has been shown to support a wide variety of two- and three-dimensional culture applications, both *in vitro* and *in vivo* [7–10].

Despite Matrigel's widespread use, transport of molecules, cells, and colloidal particles through Matrigel can be limited [11–17]. Matrigel is a polymeric hydrogel with a median pore size, $\xi \approx 0.14$ μm [18], which limits liquid flow; thus, transport of materials through Matrigel occurs primarily by diffusion. Molecules and colloids smaller than ξ diffuse freely, unless they bind to the gel, while molecules and colloidal particles larger than ξ are physically limited by the gel. Living cells experience similar limitations in Matrigel; although mammalian cells are larger than ξ, some cells are able to actively migrate by deforming or degrading the gel [19, 20], while others are physically limited by the gel [21, 22]. These transport limitations can restrict cell growth, viability, and function and limit Matrigel applications [23, 24].

A strategy to address transport limitations within a hydrogel, without modifying the chemistry or composition of the gel, is to physically restructure the material to create mesoscale pores. 'Granular' hydrogels are created by dividing the bulk material into small picoliter-scale volumes and then concentrating

© 2022 IOP Publishing Ltd

IOP Publishing Biomed. Mater. 17 (2022) 045020 Z Mahdieh et al

the resulting microgel spheres to form a porous material [25–27]. The interconnected, liquid-filled pore space of granular hydrogels allows for free diffusion of molecules and colloids, migration of cells, and advective flow [28, 29]. *In vitro* and *in vivo* studies have shown that use of granular hydrogels as scaffolds enables cell infiltration and tissue remodeling [27, 30–32]. Granular hydrogels have been created using a variety of synthetic hydrogels, but granular hydrogels composed of Matrigel have not yet been reported. Restructuring Matrigel in such a manner would enhance transport without modifying the composition or chemistry of the gel and would enable a variety of new applications.

Here we present an approach for structuring Matrigel into a three-dimensional, mesoporous material composed of packed Matrigel microgels, which we call granular Matrigel. We show that restructuring Matrigel in this manner enhances the transport of colloidal particles and human dendritic cells (DCs) through the gel while providing sufficient mechanical support for tissue culture. We concentrate the microgels with centrifugation and use confocal microscopy to characterize the structure and dynamics of granular Matrigel. We find that the microgels interact attractively to form a dense granular gel. We find that the granular Matrigel scaffolds allow for free diffusion of colloidal microspheres and dramatically improved migration of DCs, relative to bulk, non-porous Matrigel, and demonstrate the capability of the scaffolds for supporting the growth of human gastric organoids (HGOs) over 19 days. To demonstrate the potential utility of this material, we co-culture DCs and HGOs in granular Matrigel.

2. Materials and methods

2.1. Microfluidic device fabrication

PDMS microfluidic flow-focusing drop makers [33] were fabricated with standard photolithography techniques [34]. SU-8 photoresist (Microchem SU-8 100, Kayaku Advanced Materials Inc.) was patterned on silicon wafers (ID No. 447, test grade, University Wafer, MA, US) and polydimethylsiloxane (PDMS) (Sylgard® 184, Sigma, MA, US) was poured at a 10:1 mass ratio of polymer to cross-linking agent onto the patterned device master mold. Air was purged from the uncured PDMS by placing the filled mold in a vacuum chamber for at least 1 h. PDMS was cured in an oven at 55 °C for 24 h and then removed from the mold with a scalpel. Ports were punched into the PDMS slab with a 0.75 mm diameter biopsy punch (EMS Rapid-Core, Electron Microscopy Sciences). The PDMS slab was bonded to a glass slide (micro slides 48 382–179, VWR, PA, US) after plasma treatment (Harrick Plasma PDC-001, NY, US) for 60 s at high power (30 W) and 700 mTorr oxygen pressure. Devices were then made hydrophobic by flowing Aquapel Glass treatment (Aquapel, PA, US) through the channels, followed by blowing the channels with air filtered through a 0.2 μm filter (GVS ABLUO™ 25 mm, Fisher Scientific, MA, US) before baking the devices in an oven at 55 °C for 1 h.

2.2. Fabrication of Matrigel microgels

Matrigel drops of different sizes were fabricated using the devices described above. Matrigel (Corning® Matrigel® Matrix, Corning, AZ, US) was used as the drop phase, and a surfactant solution made of 3 wt% RAN (Neat (un-dissolved) 008-Fluorosurfactant, RAN Biotechnologies, MA, US) in 1-methoxyheptafluoropropane (HFE, Novec™ 7500 Engineered Fluid, Sigma, MA, US) was used as the continuous phase. For drop creation, flow rates of 400 and 1200 μl h^{-1} were used for the Matrigel and surfactant solution, respectively. The microfluidic device and precursor materials were first allowed to cool inside a 4 °C fridge to prevent the gelation of Matrigel. Matrigel drops were gelled at 37 °C for 45–60 min to form Matrigel microgels. Afterward, a 2:1 volume ratio of phosphate buffered saline (PBS, 1X, MFCD00131855, Sigma, MA, US) was added to Matrigel microgels. Matrigel microgels were washed by adding 1:1 volume ratio of 20 v/v% 1 H,1 H,2 H,2 H-perfluoro-octanal (99%, PA, US) in HFE, centrifuging at 100 g, and removing the oil phase. The washing process was repeated until no surfactant droplets remained attached to Matrigel microgels. Matrigel microgels were imaged using an epi-fluorescent microscope (Nikon TI-2, NY, US) and a 4x phase contrast objective. To measure microgel size, image analysis was performed using ImageJ [35]. For each drop size, measurements were made on individual Matrigel microgels ($n \approx 100$). A high-speed camera (1000 fps, Edgertronic™, CA, US) was used to image Matrigel drop formation.

2.3. Two-step centrifugation of Matrigel microgels

To form granular Matrigel, microgels were packed with a two-step centrifugation technique. To avoid the accumulation of Matrigel microgels in one corner of the container (384-well plate, flat bottom, tissue culture treated, polystyrene, Eco-Sensa, NC, US), the total volume of required Matrigel microgels was divided in half and each half was sequentially centrifuged in opposite directions by rotating the plate inside the plate-holder of the centrifuge (Z 300 K Universal Centrifuge, Hermle LaborTechnik GmbH, Wehingen, Germany). This technique resulted in a relatively homogenous granular Matrigel packing. For example, to form granular Matrigel with thickness of ~1600 μm in a 384-well plate, 50 μl PBS or culture media was added in each well, and then 15 μl of Matrigel microgel suspension (50 v/v% in PBS) was added. The plate was centrifuged at 6 g for 15 s, 15 μl of Matrigel microgel suspension was added, and then the plate was centrifuged at 6 g for 15 s in the opposite direction.

2.4. Microscopy imaging

All confocal imaging was performed with a Leica SP5 inverted microscope. To visualize the 3D structure of granular Matrigel, 2 v/v% of concanavalin A (Alexa Fluor® 488 Con A, Molecular Probes Inc., OR, US) was added into each well containing the granular Matrigel, washed with PBS after one minute [36, 37], and imaged using confocal microscopy.

2.5. Structural analysis of granular Matrigel

Effects of Matrigel microgel size and centrifugation force on the packed structure of granular Matrigel were investigated. Microgels of 100, 150, 200, and 250 μm diameter were fabricated and packed by centrifugation at 6, 250, 500, 750, 1000, 2000, 3000 g for 15 s, not including the acceleration and deceleration time. To observe the structure of granular Matrigel, we imaged *XY* planes 300 and 800 μm above of the well bottom using back-scattered laser light. We use back-scattered microscopy instead of a fluorescent dye to avoid any effect that a dye might have on microgel surface chemistry. To assess the homogeneity of granular Matrigel structure, images were taken from the center and corner of the well at each XY plane. Image analysis software (ImageJ, National Institute of Health, US [38]) was then used to measure the 2D microgel area fraction ϕ_{2D}. The 3D microgel area fraction ϕ_{3D} was estimated as $\frac{2}{3}\phi_{2D}$ as described in figure S2 (available online at stacks.iop.org/BMM/17/045020/mmedia). To assess microgel interactions, we performed time-lapse back-scattered imaging for 10.5 h 300 μm from the bottom of plates. The 384-well plates containing the granular Matrigel were kept at 37 °C, 95% humidity, and 5% CO_2 during imaging to represent typical cell culture conditions.

2.6. Permeability experiments

Microspheres were prepared by adding a drop of 2.5% aqueous suspension (1 μm diameter, Fluorespbrite® Yellow Green Microspheres, PolyScience Inc., PA, US) into 500 μl PBS. Next, 50 μl of the microsphere particle suspension was added to the supernatant above the granular Matrigel ($\bar{D} \approx 150$ μm). DCs were obtained from heparinized whole blood samples randomly selected from a pool of approximately 20 healthy male and female adult volunteers aged 21–60. Blood was obtained with informed consent and institutional review board approval. DCs were prepared by isolating $CD14^+$ monocytes from peripheral blood mononuclear cells from human blood donation by gradient centrifugation with Histopaque®-1077 (10 771, Sigma, MA, US) and CD14 MACS beads (130-050-201, Miltenyi Biotec, Cologne, Germany), as previously described [39]. Next, the isolated monocytes were cultured in RPMI-1640 (SH30027.01, Cytiva, UT, US) with 10% human AB serum (35 060 CI, Corning, VA, US), 100 U l^{-1} penicillin, 100 mg l^{-1} streptomycin (Gibco, MD, US), 50 mg ml^{-1} gentamycin (IBI Scientific, IA, US), 0.25 μg ml^{-1} Amphotericin B (Omega Scientific, CA, US), and 2 mmol l^{-1} L-glutamine (Hyclone, UT, US). Monocytes were differentiated to DCs by culture with 7 ng ml^{-1} rhIL-4 (204-IL-050) and 25 ng ml^{-1} recombinant human granulocyte-macrophage colony-stimulating factor (215 GM-050) (R&D Systems, MN, US). After four days of culture, DCs were recovered by vigorous pipetting followed by washing with PBS. DCs were stained with CellTracker Deep Red (C34565) (ThermoFischer, MA, US), using the protocol suggested by the manufacturer. A 30 μl suspension of human blood monocyte-derived DCs (6×10^9 cells ml^{-1} media) was added to the supernatant of granular Matrigel in a 384-well plate. For both microspheres and DCs, time-lapse microscopy was used to image a 400 μm thick sample volume (100 μm above the well bottom and 1100 μm below the granular Matrigel surface) using fluorescent time-lapse microscopy ($\Delta t = 3$ min for 12 h). Particle movement over time was tracked using Imaris.

2.7. Cell migration experiments

Chemokine solution was prepared by mixing 3 μl of 5 μg ml^{-1} chemokine (CXCL1, 300–11, PeproTech, NJ, US) and 7 μl of Matrigel at 4 °C. 5 μl of the chemokine/Matrigel solution was added into a corner of the well 3 h after addition of DCs (30 μl of DC suspension). Migration of DCs through a 400 μm thick volume (100 μm above the bottom of the well) was imaged using time-lapse confocal microscopy ($\Delta t = 4$ min for 4 h). A negative control sample was prepared and imaged in the same manner, but no chemokine was included in the 5 μl Matrigel added. To ensure minimal disruption of the granular Matrigel structure solutions were added gently using narrow pipet tips and imaging was performed far from the injection site to avoid any possible effect caused by addition of solutions. Similar conditions were used for bulk Matrigel migration experiments. After imaging, individual cells were tracked using Imaris to quantify cell motion. To determine the migration direction of each tracked cell, the following parameters were used: automatic background object subtraction; cell size = 11 μm; maximum cell displacement between each frame = 100 μm. The 'autoregressive motion' tracking algorithm was selected and maximum gap size of three set by Imaris. No extra filter was selected. Individual x and y track displacement, which is defined in Imaris as the distance between the first and last cell's position along the selected axis, was used to calculate the migration angle of each cell track. Cell velocity of each track was determined from the xy displacement length over the time of each track.

2.8. Organoid and DC culture

Gastric organoids were generated from gastric glands isolated from human tissue as previously described [40]. Human gastric tissue was obtained from sleeve

gastrectomy surgeries with institutional review board approval. Lentiviral transduction was used to generate mCherry or GFP fluorescent organoids as previously described [41]. Organoids were cultured for 4–6 d in Matrigel with L-WRN media: advanced DMEM/F12 (12 634 010, Gibco, MD, US) with 10% FBS (FB-02, Omega Scientific Tarzana, CA, US), 2 mmol l^{-1} L-glutamine (SH30034.1, Hyclone, UT, US), 50 mg ml^{-1} gentamycin (IB2030; IBI Scientific, IA, US), 0.25 μg ml^{-1} Amphotericin B (# FG-70, Omega Scientific, CA, US), 10 μM ROCK-inhibitor Y-27 632 (1254, Tocris Biosciences, Bristol, UK) and 10 μM TGF-beta-inhibitor SB431542 (1614, Tocris Biosciences, Bristol, UK), with 50% conditioned media from L-cells constituently expressing Wnt3a, R-spondin 3, and Noggin, as previously described [42]. Afterward, whole organoids were removed from Matrigel by incubation on ice with Cell Recovery Solution (354 253, Corning, Az, US) for 30 min. After incubation, organoids were gently resuspended with a wide bore tip to prevent aggregation and centrifuged at 200 g for 2 min. Cell Recovery Solution was removed, and organoids washed with cold PBS (<4 °C) to remove any remaining Matrigel before use. For organoid culture, organoids were added to 30 μl suspension of Matrigel microgels in L-WRN media and centrifuged in 384-well plates to form granular Matrigel. Organoids were cultured for eight days in granular Matrigel and media (20 μl) was refreshed daily. Daily confocal microscopy was performed to evaluate the growth and integrity of organoids. For co-culture experiments, organoids were first cultured in granular Matrigel for four days. Afterward, 50 μl of DC suspension (2×10^6 cells μl^{-1} L-WRN media) was added to the organoid culture. Migration of DCs (stained with CellTracker deep red) was imaged using time-lapse confocal microscopy for 40 h at 15 min time intervals.

3. Results and discussion

3.1. Matrigel microgels of various diameters

To fabricate Matrigel microgels, we use a microfluidic flow-focusing drop-maker [33] to create monodisperse drops of Matrigel in fluorinated oil at $T = 4$ °C, as shown in figure 1(A). This temperature is below the gelation temperature of Matrigel subjected to shear in a microfluidic device ($T_{gel} = 6$ °C) [43]; thus, the Matrigel remains liquid during the drop making process. To gel the liquid drops, we warm the drops to 37 °C for 45–60 min and then use successive washing and centrifugation steps to remove the oil and surfactant from the system. A representative brightfield microscopy image of monodisperse Matrigel microgels is shown in figure 1(B). To produce microgels of different sizes, we systematically vary the characteristic channel dimension, W. We find that by varying W in increments of 50 μm over the range $100 \leqslant W \leqslant 250$ we can produce monodisperse Matrigel microgels of average diameter, $\bar{D} \approx 100$, 150, 200, and 250 μm, as shown by the drop size probability distributions in figure 1(C). Plotting $\bar{D}$ as a function of W reveals that drop size scales linearly with W over this range (figure 1(D)).

3.2. Porous structure of granular Matrigel

To concentrate Matrigel microgels, we use centrifugation. We find that the density difference between the Matrigel microgels and suspension media is sufficiently large that mild centrifugation can be used to concentrate the microgels (figure S1). This is illustrated by the fluorescence microscopy images of different sized microgel particles in figures 2(A)–(D). To explore the effect of centrifugation on the concentration of microgels, we systematically vary the effective gravity, g_{eff} over the range: $6\ g \leqslant g_{eff} \leqslant 3000\ g$ by varying the centrifuge rotational frequency, ω over the approximate range: 211 rpm $\leqslant \omega \leqslant$ 4725 rpm (see Methods). To quantify the concentration of the microgels after centrifugation at each ω, we capture 2D microscopy images, and use a simple geometric approximation to estimate the microgel volume fraction, ϕ in 3D (figure S2). We find that ϕ increases with g_{eff} from approximately 0.25–0.35 as shown in figure 2(E). This ϕ range is well below ϕ for random closed packing of repulsive spheres, $\phi_{RCP} \approx 0.64$, which provides strong evidence that the microgels are interacting attractively. We also observe that the data in figure 2(E) exhibits power law scaling with $\phi \sim g_{eff}^{0.062}$. A theoretical description of this scaling, while beyond the scope of this study, would require consideration of all the microgel-microgel bonds that are broken and formed during compression of a dense attractive gel.

To better understand the interactions between Matrigel microgels and the impact of these interactions on the dynamics of the packing, we perform time-lapse microscopy imaging of granular Matrigel. We observe minimal internal movement, even over 10 h, and observe stable linear particle 'strings', as shown by the series of microscopy images in (figures 2(F)–(H), video S1). Near the edges of a microgel packing, we observe that tenuous particle clusters occasionally break away and rotate slowly as rigid bodies (figures 2(I)–(M), video S2). These observations provide additional evidence that Matrigel microgel particles interact attractively and also that the bonds between microgels are shear-rigid [44]. This behavior contrasts with that of most granular hydrogels reported in the literature, which interact repulsively and approach volume fractions $\phi_{RCP} \approx 0.64$ through settling. These attractive interactions between Matrigel microgels will have implications in the rheology, dynamics, and applications of granular Matrigel systems.

IOP Publishing Biomed. Mater. 17 (2022) 045020 Z Mahdieh et al

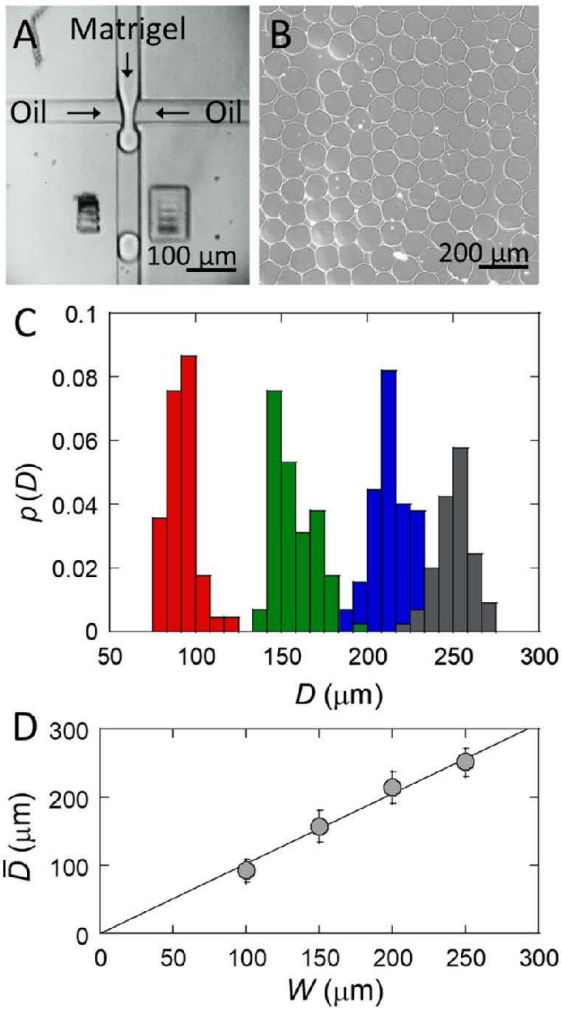


Figure 1. Production of monodisperse Matrigel drops with drop-based microfluidics. (A) High-speed video micrograph of microfluidic drop-maker producing Matrigel drops. (B) Representative brightfield microscopy image of monodisperse Matrigel microgels made using channel width, $W = 150$ μm. (C) Measured probability distribution, $p(D)$ of Matrigel microgel diameter, D produced by four different drop-makers with varying channel widths, $W = 100$ μm (red), 150 μm (green), 200 μm (blue), and 250 μm (grey). (D) Average Matrigel microgel diameter, $\bar{D}$ as a function of W. Error bars represent one standard deviation. Straight line is linear fit ($S = 8.9531$, p-value $= 0.00003$).

3.3. Improved permeability of granular Matrigel

The porous structure of granular Matrigel should enhance material transport and cell migration relative to bulk Matrigel. To assess this, we introduce fluorescent colloidal microspheres and fluorescently tagged human monocyte-derived DCs to both granular Matrigel and bulk Matrigel and track their motion using time-lapse confocal microscopy. We observe that the colloidal microspheres, with average particle diameter, $d \approx 1$ μm and density, $\rho = 1.05$ g cm^{-3}, exhibit Brownian motion and settle slowly (video S3), distributing throughout the granular Matrigel (thickness, $h = 1.6$ mm) over the course of the imaging period ($\Delta t = 10$ h), as shown by the microscopy image in figure S3(B). By contrast, the microspheres do not penetrate the surface of bulk Matrigel, as shown by the microscopy image in figure S3(A). Similarly, we observe that DCs fail to penetrate the surface of bulk Matrigel, even after 10 h (figure 3(A), video S4), but rapidly penetrate and migrate through granular Matrigel by attaching to the surface of the microgels and migrating along their surfaces (figure 3(B),

IOP Publishing Biomed. Mater. 17 (2022) 045020 Z Mahdieh et al

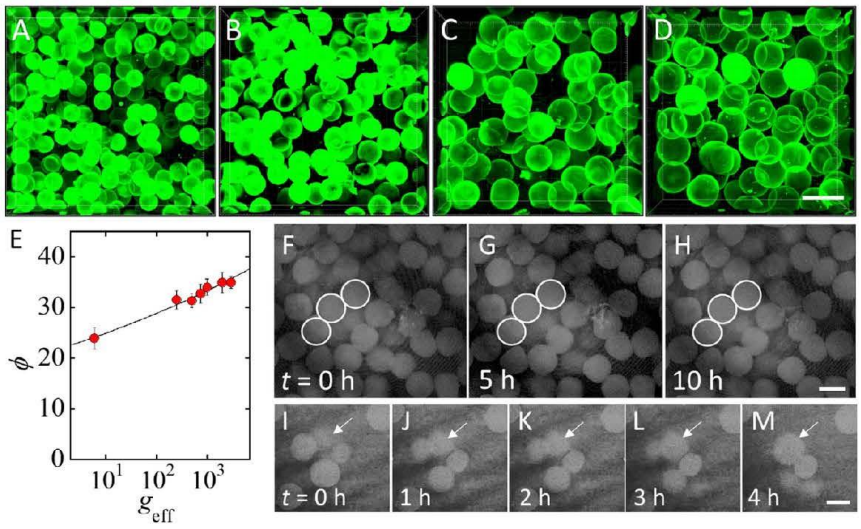


Figure 2. Structure and dynamics of dense, attractive gels formed by concentrated Matrigel microgels. (A)–(D) 3D volume projections obtained with fluorescence confocal microscopy after low-speed centrifugation (effective gravity, $g_{eff} = 6$) of microgels with $\bar{D} \approx 100$, 150, 200, and 250 μm, respectively, from left to right. Microgels labelled with green fluorescent lectin. Void spaces indicate microgel-microgel interaction is attractive. (E) Microgel volume fraction, ϕ for microgels in (A) plotted as function of g_{eff}. At the highest g_{eff}, $\phi \approx 0.35$, well below $\phi \approx 0.64$ associated with random close packing. Data is fit to a power law (black line, R = 0.9867). Error bars represent standard deviation. (F)–(H) Time-lapse imaging of concentrated microgels using back-scattered laser light reveals minimal internal movement over 10 h. Linear particle strings (white outline) and open (dark) voids indicate that the particle-particle interaction is attractive and not repulsive. (I)–(M) Rotation of particle cluster behaving as a rigid body provides additional evidence of attractive interaction. White arrow points to particle moving into the imaging plane during rotation. Image series beginning with F and I were started approximately 2 h after centrifugation at $g_{eff} = 6$ for 30 s (see Methods). Scale bars in (D), (H), and (M) correspond to 300, 200, and 100 μm, respectively.

video S5). Enhanced mobility of particles could prove beneficial for nutrient [45] and drug delivery applications [46, 47]. Enhanced cell migration is important for stem cell therapy [48–50], tissue engineering [51, 52], cancer research [53, 54], organ development applications [55, 56], and basic immunology research [11, 57].

Here, DCs are chosen because of their migratory capacity and their central role in tissue immunosurveillance [58–62]. In the body, DCs and other immune cells migrate through the ECM in response to chemotactic gradients [63]. To explore this capability in granular Matrigel, we prepare granular systems containing DCs, impose a chemokine gradient using recombinant CXCL1, and image DC dynamics over 4 h by time-lapse confocal microscopy. We observe clear directed motion in the presence of the chemokine gradient but not in the no-chemokine control. This is shown qualitatively by the representative microscopy images and DC migration tracks in figures 4(A), (B) and figures 4(E), (F) (videos S6 and S7). We quantify DC chemotaxis through granular Matrigel using image analysis, as shown by the DC displacement vectors and Rose graphs in figures 4(C), (G) and figures 4(D), (H), respectively. We also observe increased DC migration speed in the presence of the chemokine, relative to the non-chemokine control, as shown by the probability distribution of DC velocities in figure 4(I). As an additional test, we embed DCs in bulk Matrigel and impose a chemokine gradient; under these conditions we do not observe DC migration (video S8). This lack of migration is likely due to limited DC mobility, but could also be caused by limited diffusion of the chemokine in Matrigel, which has been shown for other proteins like VGEF [64].

3.4. Granular Matrigel application for 3D cell culture scaffold

To evaluate granular Matrigel for long-term 3D cell culture applications, we culture human gastric epithelial organoids (HGOs) in granular Matrigel for multiple days. We select organoids due to their growing importance in various research areas such as human physiology [65, 66], disease modeling [67, 68], and drug development [69, 70]. We find that HGOs remain apparently viable and maintain their integrity for multiple days after transfer from bulk Matrigel cultures to granular Matrigel of all sizes ($100\ \mu m \leqslant \bar{D} \leqslant 250\ \mu m$). Representative brightfield and fluorescent image time series for HGOs grown in granular Matrigel ($\bar{D} \approx 250\ \mu m$) over eight days

IOP Publishing Biomed. Mater. 17 (2022) 045020 Z Mahdieh et al

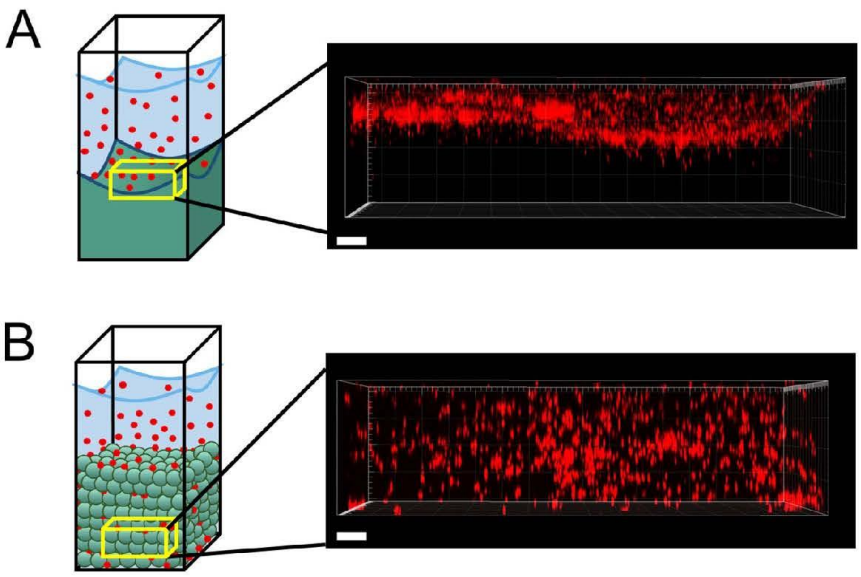


Figure 3. Human blood monocyte-derived dendritic cells (DCs) migrate into granular Matrigel but not bulk Matrigel. (A) Left: illustration of DCs (red spheres) added to liquid media above bulk Matrigel. Right: fluorescence confocal microscopy volume projection image 10 h after addition of DCs shows they remain on the surface of the Matrigel and do not migrate into the bulk. (B) Left: illustration of DCs (red spheres) added to liquid media above granular Matrigel. Right: fluorescence confocal microscopy volume projection 10 h after addition of DCs shows DCs migrate deep into the granular Matrigel (top of imaging volume > 1 mm from surface of granular Matrigel). Granular Matrigel composed of microgels of $\bar{D} \approx 200$ μm concentrated at 6 g. Micrographs in (A) and (B) constructed of 450 μm z-stacks. DCs labelled with CellTracker Deep Red. Scale bars correspond to 100 μm.

are shown in figure 5. We observe that HGOs exhibit many of the same behaviors reported in bulk Matrigel [71]; for example, small organoids (yellow arrows, figure 5) fuse together to form larger organoids (red arrows figure 5). In cases where imaging time was freely available, we observed HGO growth for much longer than eight days; for example, images of a 19 day culture are provided in figure S4. While we hesitate to report conclusions comparing growth of HGOs in granular Matrigel with bulk Matrigel (figure S5) without further studies, our results indicate that granular Matrigel provides sufficient nutrient transport and mechanical support for long-term organoid cultures.

3.5. Granular Matrigel for co-culture model applications

To better understand human physiology and disease, the ability to co-culture more than one cell type in the same matrix material to enable physiological cell interactions is critical [62–69]. We previously used co-cultures of HGOs and DCs embedded in Matrigel to analyze mechanisms of DC recruitment and antigen uptake [58]; however, subsequent studies revealed that DC migration in bulk Matrigel varied significantly from batch to batch and was most often highly limited [11]. We found that higher-permeability, synthetic hydrogels allowed for increased DC migration, but did not support robust HGO growth [11]. Thus, to demonstrate the utility of granular Matrigel for co-culture applications, here we combine DCs and HGOs together in granular Matrigel. We begin by culturing HGOs for four days and then adding DCs. Following the addition of DCs, we image the system using confocal microscopy for 40 h. Images of the HGOs immediately following the addition of DCs and 30 h after their introduction are shown in figures 6(A) and (B). Importantly, we find that DCs migrate through the granular Matrigel and interact closely with the basolateral surface of the HGOs. DC migration is illustrated by a microscopy image volume projection overlaid with DC migration pathways in figure 6(C). DC interaction with the basolateral surface of an HGO is illustrated by the image series in figures 6(D)–(G). A full 40 h video of DC migration in the co-culture is shown in videos S9 and S10. The mechanical stability of granular Matrigel can be clearly seen in video S10. Our results here show the promising potential of granular Matrigel for applications that require both a solid matrix to support 3D cell culture and high permeability to allow for migration and interaction of cells.

IOP Publishing Biomed. Mater. 17 (2022) 045020 Z Mahdieh et al

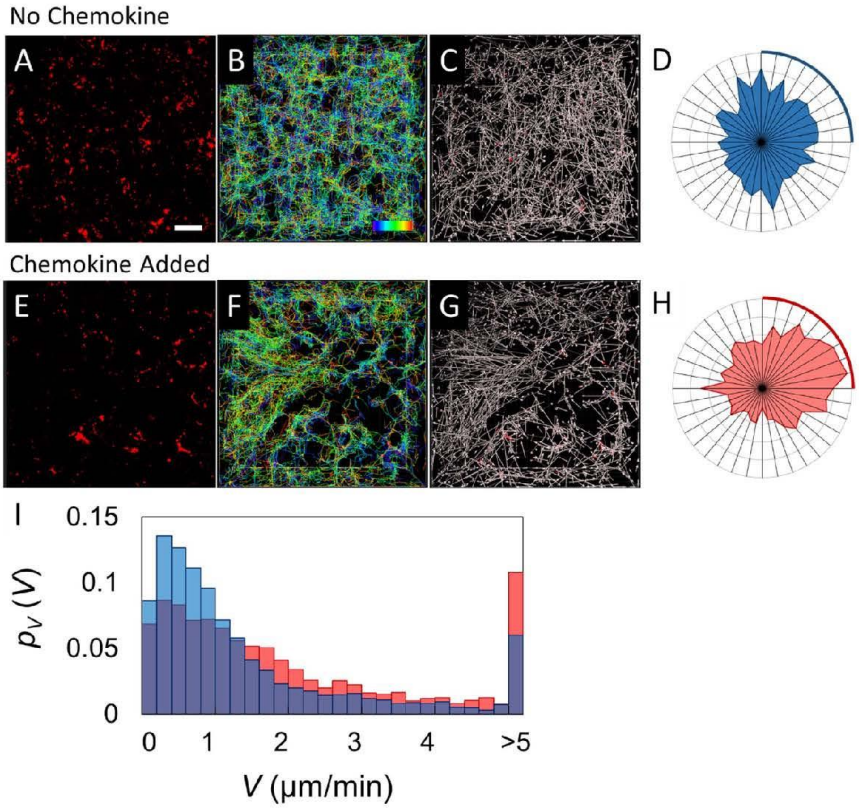


Figure 4. Time lapse microscopy of DC migration in granular Matrigel in response to a CXCL1 chemokine gradient. (A), (E) Fluorescence confocal micrographs of two granular Matrigel samples containing DCs (red; microgels not labelled). Matrigel (5 μl) without chemokine (A) and with chemokine (E) added to the top right corner (arrow) in each sample, ≈1 mm from the top right corner in the field of view. Images correspond to t = 0, before 4 h time-lapse imaging. (B), (F) DC migration tracks extracted from 4 h video. (C), (G) DC displacement vectors extracted from 4 h video. (D), (H) Rose graph histograms of DC migration angle reveal biased migration in the direction of the chemokine gradient. (I) Probability distribution of DC velocity, V in the presence (red) and absence (blue) of a chemokine gradient reveals an increase DC velocity in presence of chemokine gradient. Histogram bins are overlaid on the same scale, not additive in y. Scale bar in (A) represents 200 μm and applies to all images.

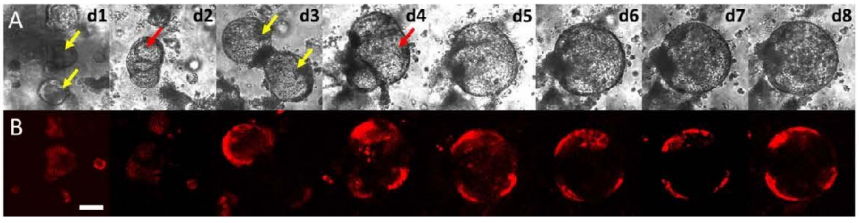


Figure 5. Granular Matrigel as a scaffold for long-term, 3D organoid culture applications. Representative brightfield (A) and fluorescence (B) time-lapse confocal image series of mCherry-expressing HGOs cultured for eight days in granular Matrigel ($\bar{D} \approx 250$ μm) reveals robust growth. Yellow arrows denote the small HGOs fusing together and forming larger HGOs shown with red arrows. Scale bar is 100 μm for all images.

IOP Publishing Biomed. Mater. 17 (2022) 045020 Z Mahdieh et al

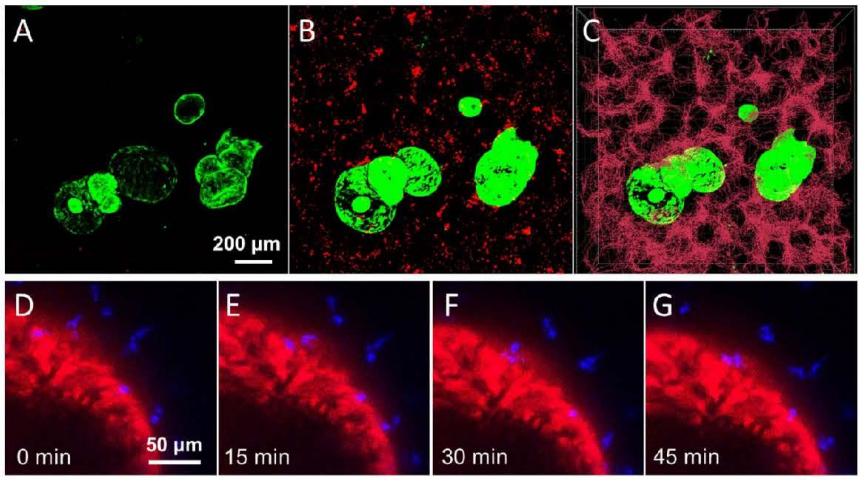


Figure 6. Granular Matrigel for organoid-immune cell co-culture. Fluorescence confocal microscopy max projection images of (A) GFP-expressing HGOs (green) after four days of culture in granular Matrigel (not fluorescently labelled), and (B) the same culture in (A) after the addition of human blood monocyte-derived DCs stained with CellTracker Deep Red. Image taken 30 h after DC addition. (C) 3D volume projection depicting the migration of DCs (red lines) over 40 h tracked with Imaris software. (D)–(G) Time series of confocal images show DCs (CellTracker Deep Red stained, pseudo-colored blue) interacting with the basolateral surface of an mCherry-expressing HGO (red). Scale bars in (A) and (D) apply to images (A)–(C) and (D)–(G), respectively. Imaging volume depth for (A)–(C) is 340 µm.

4. Conclusions

Here we present an approach for restructuring bulk Matrigel into a porous, three-dimensional culture material we call granular Matrigel. This approach is important because it provides a means to change the physical properties of the hydrogel without altering the composition. We fabricate monodisperse Matrigel microgels using drop-based microfluidics and control the size of the microgels by controlling the characteristic channel dimension; large quantities of polydisperse microgels could also be made using bulk emulsification. We use a standard lab centrifuge to concentrate the microgels to volume fractions as high as $\phi \approx 0.35$. Higher ϕ could be achieved by compressing the microgels with a simple filter. We find that the granular Matrigel allows for free diffusion of microsphere particles and migration of DCs; the open, interconnected pore structure will likely enhance the diffusion of other materials that have limited transport in bulk Matrigel as well. We also show that granular Matrigel supports culture of HGOs and co-culture with human DCs. In future studies, culture of other cells and tissues in granular Matrigel should also be explored.

Data availability statement

The data that support the findings of this study are available upon reasonable request from the authors.

Acknowledgments

The authors thank Thomas Sebrell for help with cell culture, Kristen Brileya for general lab support, and Heidi Smith for assistance and training with confocal imaging.

Conflict of interest

Authors declare no conflict of interest.

Author contributions

Conceptualization: Z M, J P F, B S, J N W.
Methodology: Z M, J N W.
Validation: C B C, D B, J N W.
Formal analysis: Z M, J N W.
Investigation: Z M, M D C, J P F, B S, H S S.
Data Curation: Z M, J N W.
Writing-Original Draft: Z M, M D C, J P F, H S S, J N W.
Writing-Review & Editing: Z M, M D C, J P F, B S, H S S, C B C, D B, J N W.
Supervision: J N W.
Funding Acquisition: D B, C B C, J N W.

Funding

NIH, National Institute of Biomedical Imaging and Bioengineering (5-UO1-EB029242).

ORCID iD

James N Wilking https://orcid.org/0000-0002-7255-7209

References

[1] Benton G, Arnaoutova I, George J, Kleinman H K and Koblinski J 2014 Matrigel: from discovery and ECM mimicry to assays and models for cancer research *Adv. Drug. Deliv. Rev.* **79** 3–18

[2] Kleinman H K and Martin G R 2005 Matrigel: basement membrane matrix with biological activity *Seminars in Cancer Biology* vol 15 (New York: Academic) pp 378–86

[3] Hughes C S, Postovit L M and Lajoie G A 2010 Matrigel: a complex protein mixture required for optimal growth of cell culture *Proteomics* **10** 1886–90

[4] Benton G, Kleinman H K, George J and Arnaoutova I 2011 Multiple uses of basement membrane-like matrix (BME/Matrigel) *in vitro* and *in vivo* with cancer cells *Int. J. Cancer* **128** 1751–7

[5] Lewis M T, Landua J D, Adams H C, Medina D and Mystery A 2012 Wrapped in an enigma: Matrigel enhancement of mammary cell growth and morphogenesis *J. Mammary Gland Biol. Neoplasia* **17** 99–101

[6] Smith B D, Martin G R, Miller E J, Dorfman A and Swarm R 1975 Nature of the collagen synthesized by a transplanted chondrosarcoma *Arch. Biochem. Biophys.* **166** 181–6

[7] Ranga A, Gobaa S, Okawa Y, Mosiewicz K, Negro A and Lutolf M P 2014 3D niche microarrays for systems-level analyses of cell fate *Nat. Commun.* **5** 4324

[8] Wang J, Chu R, Ni N and Nan G 2020 The effect of Matrigel as scaffold material for neural stem cell transplantation for treating spinal cord injury *Sci. Rep.* **10** 1–11

[9] Ouyang M *et al* 2020 Sensing traction force on the matrix induces cell-cell distant mechanical communications for self-assembly *ACS Biomater. Sci. Eng.* **6** 5833–48

[10] Sugimoto S and Sato T 2017 Establishment of 3D intestinal organoid cultures from intestinal stem cells *Methods in Molecular Biology* (New York: Humana Press Inc.) pp 97–105

[11] Cherne M D *et al* 2021 A synthetic hydrogel, VitroGel® ORGANOID-3, improves immune cell-epithelial interactions in a tissue chip co-culture model of human gastric organoids and dendritic cells *Front. Pharmacol.* **12** 2279

[12] Qian X *et al* 2016 Brain-region-specific organoids using mini-bioreactors for modeling ZIKV exposure *Cell* **165** 1238–54

[13] Lancaster M A *et al* 2013 Cerebral organoids model human brain development and microcephaly *Nature* **501** 373–9

[14] Davoudi Z *et al* 2018 Intestinal organoids containing poly(lactic-co-glycolic acid) nanoparticles for the treatment of inflammatory bowel diseases *J. Biomed. Mater. Res.* A **106** 876–86

[15] Qian X *et al* 2020 Sliced human cortical organoids for modeling distinct cortical layer formation *Cell Stem Cell* **26** 766–81.e9

[16] Wake H, Mori S, Liu K, Takahashi H K and Nishibori M 2009 Histidine-rich glycoprotein inhibited high mobility group box 1 in complex with heparin-induced angiogenesis in Matrigel plug assay *Eur. J. Pharmacol.* **623** 89–95

[17] Widener A E, Bhatta M, Angelini T E and Phelps E A 2021 Guest–host interlinked PEG-MAL granular hydrogels as an engineered cellular microenvironment *Biomater. Sci.* **9** 2480–93

[18] Tomasetti L, Liebl R, Wastl D S and Breunig M 2016 Influence of PEGylation on nanoparticle mobility in different models of the extracellular matrix *Eur. J. Pharm. Biopharm.* **108** 145–55

[19] Yu X and Machesky L M 2012 Cells assemble invadopodia-like structures and invade into Matrigel in a matrix metalloprotease dependent manner in the circular invasion assay *PLoS One* **7** e30605

[20] Shaw L M 2005 Tumor cell invasion assays *Methods Mol. Biol.* **294** 97–105

[21] Haralabopoulos G C, Grant D S, Kleinman H K and Maragoudakis M E 1997 Thrombin promotes endothelial cell alignment in Matrigel *in vitro* and angiogenesis *in vivo* *Am. J. Physiol.* **273** C239–45

[22] Anguiano M *et al* 2020 The use of mixed collagen-Matrigel matrices of increasing complexity recapitulates the biphasic role of cell adhesion in cancer cell migration: ECM sensing, remodeling and forces at the leading edge of cancer invasion *PLoS One* **15** e0220019

[23] Akashi T *et al* 2005 Basement membrane matrix modifies cytokine interactions between lung cancer cells and fibroblasts *Pathobiology* **72** 250–9

[24] Borries M, Barooji Y F, Yennek S, Grapin-Botton A, Berg-Sørensen K and Oddershede L B 2020 Quantification of visco-elastic properties of a Matrigel for organoid development as a function of polymer concentration *Front. Phys.* **0** 475

[25] Kulchar R J, Denzer B R, Chavre B M, Takegami M and Patterson J 2021 A review of the use of microparticles for cartilage tissue engineering *Int. J. Mol. Sci.* **22** 10292

[26] Cheng W, Zhang J, Liu J and Yu Z 2020 Granular hydrogels for 3D bioprinting applications *View* **1** 20200060

[27] Griffin D R, Weaver W M, Scumpia P O, Di Carlo D and Segura T 2014 Accelerated wound healing by injectable microporous gel scaffolds assembled from annealed building blocks *Nat. Mater.* **14** 737–44

[28] Riley L, Schirmer L and Segura T 2019 Granular hydrogels: emergent properties of jammed hydrogel microparticles and their applications in tissue repair and regeneration *Curr. Opin. Biotechnol.* **1** 1–8

[29] Daly A C, Riley L, Segura T and Burdick J A 2020 Hydrogel microparticles for biomedical applications *Nat. Rev. Mater.* **5** 20–43

[30] Griffin D R, Weaver W M, Scumpia P O, Di Carlo D and Segura T 2015 V Accelerated wound healing by injectable microporous gel scaffolds assembled from annealed building block *Nat Mater* **14** 737–44 (available at: www.nature.com/naturematerials)

[31] Bhattacharjee T and Angelini T E 2019 3D T cell motility in jammed microgels *J. Phys. D: Appl. Phys.* **52** 024006

[32] Gehlen D B *et al* 2020 Granular cellulose nanofibril hydrogel scaffolds for 3D cell cultivation *Macromol. Rapid Commun.* **41** 2000191

[33] Anna S L, Bontoux N and Stone H A 2003 Formation of dispersions using "flow focusing" in microchannels *Appl. Phys. Lett.* **82** 364–6

[34] Duffy D C, McDonald J C, Schueller O J A and Whitesides G M 1998 Rapid prototyping of microfluidic systems in poly(dimethylsiloxane) *Anal. Chem.* **70** 4974–84

[35] Rueden C T *et al* 2017 ImageJ2: imageJ for the next generation of scientific image data *BMC Bioinform.* **18** 1–26

[36] Kastana P *et al* 2019 Matrigel plug assay for *in vivo* evaluation of angiogenesis *Methods in Molecular Biology* (New York: Humana Press) pp 219–32

[37] Beuth J, Ko H L, Pulverer G, Uhlenbruck G and Pichlmaier H 1995 Importance of lectins for the prevention of bacterial infections and cancer metastases *Glycoconj. J.* **12** 1–6

[38] Schneider C A, Rasband W S and Eliceiri K W 2012 NIH Image to ImageJ: 25 years of image analysis *Nat. Methods* **9** 671–5

[39] Bimczok D, Grams J M, Stahl R D, Waites K B, Smythies L E and Smith P D 2011 Stromal regulation of human gastric dendritic cells restricts the Th1 response to helicobacter pylori *Gastroenterology* **141** 929–38

[40] Bimczok D *et al* 2013 Helicobacter pylori infection inhibits phagocyte clearance of apoptotic gastric epithelial cells *J. Immunol.* **190** 6626–34

[41] Sebrell T A *et al* 2018 Live imaging analysis of human gastric epithelial spheroids reveals spontaneous rupture, rotation and fusion events *Cell Tissue Res.* **371** 293–307

[42] Miyoshi H, Ajima R, Luo C T, Yamaguchi T P and Stappenbeck T S 2012 Wnt5a potentiates TGF-β signaling to promote colonic crypt regeneration after tissue injury *Science* **338** 108–13

[43] Kane K I W *et al* 2018 Determination of the rheological properties of Matrigel for optimum seeding conditions in microfluidic cell cultures *AIP Adv.* **8** 125332

[44] Wilking J N, Graves S M, Chang C B, Meleson K, Lin M Y and Mason T G 2006 Dense cluster formation during aggregation and gelation of attractive slippery nanoemulsion droplets *Phys. Rev. Lett.* **96** 015501

[45] Yao M H *et al* 2014 Directed self-assembly of polypeptide-engineered physical microgels for building porous cell-laden hydrogels *Chem. Commun.* **50** 9405–8

[46] Li G *et al* 2010 Permeability of endothelial and astrocyte cocultures: *in vitro* Blood-brain barrier models for drug delivery studies *Ann. Biomed. Eng.* **38** 2499–511

[47] Mahdieh Z and Holian A 2020 Electrospun fibers loaded with ball-milled poly(n-isopropylacrylamide) microgel particles for smart delivery applications *J. Appl. Polym. Sci.* **137** 49786

[48] Koh J *et al* 2019 Enhanced *in vivo* delivery of stem cells using microporous annealed particle scaffolds *Small* **15** 1903147

[49] van Pul K M, Fransen M F, van de Ven R and de Gruijl T D 2021 Immunotherapy goes local: the central role of lymph nodes in driving tumor infiltration and efficacy *Front. Immunol.* **12** 643291

[50] Xia P, Zhang K, Gong Y, Li G, Yan S and Yin J 2017 Injectable stem cell laden open porous microgels that favor adipogenesis: *in vitro* and *in vivo* evaluation *ACS Appl. Mater. Interfaces* **9** 34751–61

[51] Mandal B B and Kundu S C 2009 Cell proliferation and migration in silk fibroin 3D scaffolds *Biomaterials* **30** 2956–65

[52] Wang C Y *et al* 2020 Cell migration of preosteoblast cells on a clinical gelatin sponge for 3D bone tissue engineering *Biomed. Mater.* **15** 015005

[53] Nabeshima K, Inoue T, Shimao Y and Sameshima T 2002 Matrix metalloproteinases in tumor invasion: role for cell migration *Pathol. Int.* **52** 255–64

[54] Ning Y *et al* 2020 HDAC9 deficiency promotes tumor progression by decreasing the CD8 + dendritic cell infiltration of the tumor microenvironment *J. Immunother. Cancer* **8** e000529

[55] Worbs T, Hammerschmidt S I and Förster R 2016 *Nature Reviews Immunology* Dendritic cell migration in health and disease (Nat Publ Gr.) (https://doi.org/10.1038/nri.2016.116) (available at: www.nature.com/nri)

[56] Franz C M, Jones G E and Ridley A J 2002 Cell migration in development and disease *Developmental Cell* vol 2 pp 153–8

[57] Noel G *et al* 2017 A primary human macrophage-enteroid co-culture model to investigate mucosal gut physiology and host-pathogen interactions *Sci. Rep.* **7** 1–14

[58] Sebrell T A *et al* 2019 A novel gastric spheroid co-culture model reveals chemokine-dependent recruitment of human dendritic cells to the gastric epithelium *Cell. Mol. Gastroenterol. Hepatol.* **8** 157–71.e3

[59] Banchereau J *et al* 2000 Immunobiology of dendritic cells *Annu. Rev. Immunol.* **18** 767–811

[60] Mellman I and Steinman R M 2001 Dendritic cells: specialized and regulated antigen processing machines *Cell* **106** 255–8

[61] Constantino J, Gomes C, Falcão A, Neves B M and Cruz M T 2017 Dendritic cell-based immunotherapy: a basic review and recent advances *Immunol. Res.* **65** 798–810

[62] De Figueiredo J A P *et al* 2018 Dendritic cells and their relation to apical peridontitis *Braz. Oral Res.* **32** 119–25

[63] Iglesias P A and Devreotes P N 2008 Navigating through models of chemotaxis *Curr. Opin. Cell Biol.* **20** 35–40

[64] Miura T and Tanaka R 2009 *In vitro* vasculogenesis models revisited-measurement of VEGF diffusion in Matrigel *Math. Model Nat. Phenom.* **4** 118–30

[65] Del Dosso A, Urenda J P, Nguyen T and Quadrato G 2020 Upgrading the physiological relevance of human brain organoids *Neuron* **107** 1014–28

[66] Takebe T and Wells J M 2019 Organoids by design *Science* **364** 956–9

[67] Sachs N *et al* 2019 Long-term expanding human airway organoids for disease modeling *EMBO J.* **38** e100300

[68] Sun Y and Ding Q 2017 Genome engineering of stem cell organoids for disease modeling *Protein Cell* **8** 315–27

[69] Devarasetty M, Mazzocchi A R and Skardal A 2018 Applications of bioengineered 3D tissue and tumor organoids in drug development and precision medicine: current and future *BioDrugs* **32** 53–68

[70] Ranga A, Gjorevski N and Lutolf M P 2014 Drug discovery through stem cell-based organoid models *Adv. Drug. Deliv. Rev.* **69–70** 19–28

[71] Sidar B, Jenkins B R, Huang S, Spence J R, Walk S T and Wilking J N 2019 Long-term flow through human intestinal organoids with the gut organoid flow chip (GOFlowChip) *Lab Chip* **19** 3552–62

REFERENCES CITED

REFERENCES CITED

Akashi, Takumi, Junko Minami, Yuki Ishige, Yoshinobu Eishi, Touichiro Takizawa, Morio Koike, and Masaki Yanagishita. 2005. “Basement Membrane Matrix Modifies Cytokine Interactions between Lung Cancer Cells and Fibroblasts.” Pathobiology: Journal of Immunopathology, Molecular and Cellular Biology 72 (5): 250–59.

Alexopoulos, Leonidas G., Mansoor A. Haider, Thomas P. Vail, and Farshid Guilak. 2003. “Alterations in the Mechanical Properties of the Human Chondrocyte Pericellular Matrix with Osteoarthritis.” Journal of Biomechanical Engineering 125 (3): 323–33.

Amr, Mahmoud, Alia Mallah, Samina Yasmeen, Bernard Van Wie, Arda Gozen, Juana Mendenhall, and Nehal I. Abu-Lail. 2022. “From Chondrocytes to Chondrons, Maintenance of Phenotype and Matrix Production in a Composite 3D Hydrogel Scaffold.” Gels (Basel, Switzerland) 8 (2). https://doi.org/10.3390/gels8020090.

Andersson-Engels, S., J. Johansson, K. Svanberg, and S. Svanberg. 1991. “Fluorescence Imaging and Point Measurements of Tissue: Applications to the Demarcation of Malignant Tumors and Atherosclerotic Lesions from Normal Tissue.” Photochemistry and Photobiology 53 (6): 807–14.

Anguiano, María, Xabier Morales, Carlos Castilla, Alejandro Rodríguez Pena, Cristina Ederra, Martín Martínez, Mikel Ariz, et al. 2020. “The Use of Mixed Collagen-Matrigel Matrices of Increasing Complexity Recapitulates the Biphasic Role of Cell Adhesion in Cancer Cell Migration: ECM Sensing, Remodeling and Forces at the Leading Edge of Cancer Invasion.” PloS One 15 (1): e0220019.

Anna, Shelley L., Nathalie Bontoux, and Howard A. Stone. 2003. “Formation of Dispersions Using ‘Flow Focusing’ in Microchannels.” Applied Physics Letters 82 (3): 364–66.

Arnold, Katherine M., Delphine Sicard, Daniel J. Tschumperlin, and Jennifer J. Westendorf. 2023. “Atomic Force Microscopy Micro-Indentation Methods for Determining the Elastic Modulus of Murine Articular Cartilage.” Sensors 23 (4). https://doi.org/10.3390/s23041835.

Balgude, A. P., X. Yu, A. Szymanski, and R. V. Bellamkonda. 2001. “Agarose Gel Stiffness Determines Rate of DRG Neurite Extension in 3D Cultures.” Biomaterials 22 (10): 1077–84.

Banchereau, J., F. Briere, C. Caux, J. Davoust, S. Lebecque, Y. J. Liu, B. Pulendran, and K. Palucka. 2000. “Immunobiology of Dendritic Cells.” Annual Review of Immunology 18: 767–811.

Basiri, Arefeh, Arash Heidari, Melina Farshbaf Nadi, Mohammad Taha Pahlevan Fallahy, Sasan Salehi Nezamabadi, Mohammadreza Sedighi, Amene Saghazadeh, and Nima Rezaei. 2021. “Microfluidic Devices for Detection of RNA Viruses.” Reviews in Medical Virology 31 (1): 1–11.

Bassett, David C., Armend G. Håti, Thor B. Melø, Bjørn T. Stokke, and Pawel Sikorski. 2016. "Competitive Ligand Exchange of Crosslinking Ions for Ionotropic Hydrogel Formation." Journal of Materials Chemistry. B, Materials for Biology and Medicine 4 (37): 6175–82.

Batty, Lachlan, Samuel Dance, Sarvottam Bajaj, and Brian J. Cole. 2011. "Autologous Chondrocyte Implantation: An Overview of Technique and Outcomes." ANZ Journal of Surgery 81 (1–2): 18–25.

Benton, Gabriel, Irina Arnaoutova, Jay George, Hynda K. Kleinman, and Jennifer Koblinski. 2014. "Matrigel: From Discovery and ECM Mimicry to Assays and Models for Cancer Research." Advanced Drug Delivery Reviews 79–80 (December): 3–18.

Benton, Gabriel, Hynda K. Kleinman, Jay George, and Irina Arnaoutova. 2011. "Multiple Uses of Basement Membrane-like Matrix (BME/Matrigel) in Vitro and in Vivo with Cancer Cells." International Journal of Cancer. Journal International Du Cancer 128 (8): 1751–57.

Benya, P. D., S. R. Padilla, and M. E. Nimni. 1978. "Independent Regulation of Collagen Types by Chondrocytes during the Loss of Differentiated Function in Culture." Cell 15 (4): 1313–21.

Benya, P. D., and J. D. Shaffer. 1982. "Dedifferentiated Chondrocytes Reexpress the Differentiated Collagen Phenotype When Cultured in Agarose Gels." Cell 30 (1): 215–24.

Beuth, J., H. L. Ko, G. Pulverer, G. Uhlenbruck, and H. Pichlmaier. 1995. "Importance of Lectins for the Prevention of Bacterial Infections and Cancer Metastases." Glycoconjugate Journal 12 (1): 1–6.

Bhattacharjee, Tapomoy, and Thomas E. Angelini. 2018. "3D T Cell Motility in Jammed Microgels." Journal of Physics D: Applied Physics 52 (2): 024006.

Bimczok, Diane, Jayleen M. Grams, Richard D. Stahl, Ken B. Waites, Lesley E. Smythies, and Phillip D. Smith. 2011. "Stromal Regulation of Human Gastric Dendritic Cells Restricts the Th1 Response to Helicobacter Pylori." Gastroenterology 141 (3): 929–38.

Bimczok, Diane, Lesley E. Smythies, Ken B. Waites, Jayleen M. Grams, Richard D. Stahl, Peter J. Mannon, Shajan Peter, et al. 2013. "Helicobacter Pylori Infection Inhibits Phagocyte Clearance of Apoptotic Gastric Epithelial Cells." Journal of Immunology 190 (12): 6626–34.

Borries, Mads, Younes Farhangi Barooji, Siham Yennek, Anne Grapin-Botton, Kirstine Berg-Sørensen, and Lene B. Oddershede. 2020. "Quantification of Visco-Elastic Properties of a Matrigel for Organoid Development as a Function of Polymer Concentration." Frontiers in Physics 8. https://doi.org/10.3389/fphy.2020.579168.

Broguiere, Nicolas, Luca Isenmann, Christian Hirt, Till Ringel, Silja Placzek, Emma Cavalli, Femke Ringnalda, et al. 2018. "Growth of Epithelial Organoids in a Defined Hydrogel." Advanced Materials 30 (43): e1801621.

Caen, Ouriel, Simon Schütz, M. S. Suryateja Jammalamadaka, Jérémy Vrignon, Philippe Nizard, Tobias M. Schneider, Jean-Christophe Baret, and Valérie Taly. 2018. “High-Throughput Multiplexed Fluorescence-Activated Droplet Sorting.” Microsystems & Nanoengineering 4 (October): 33.

Caldwell, Alexander S., Brian A. Aguado, and Kristi S. Anseth. 2020. “Designing Microgels for Cell Culture and Controlled Assembly of Tissue Microenvironments.” Advanced Functional Materials 30 (37). https://doi.org/10.1002/adfm.201907670.

Caliari, Steven R., and Jason A. Burdick. 2016. “A Practical Guide to Hydrogels for Cell Culture.” Nature Methods 13 (5): 405–14.

Carlson, A. K., R. A. Rawle, C. W. Wallace, E. G. Brooks, E. Adams, M. C. Greenwood, M. Olmer, M. K. Lotz, B. Bothner, and R. K. June. 2019. “Characterization of Synovial Fluid Metabolomic Phenotypes of Cartilage Morphological Changes Associated with Osteoarthritis.” Osteoarthritis and Cartilage / OARS, Osteoarthritis Research Society 27 (8): 1174–84.

Cheng, Wei, Jing Zhang, Ji Liu, and Ziyi Yu. 2020. “Granular Hydrogels for 3D Bioprinting Applications.” View (Beijing, China) 1 (3): 20200060.

Cherne, Michelle D., Barkan Sidar, T. Andrew Sebrell, Humberto S. Sanchez, Kody Heaton, Francis J. Kassama, Mandi M. Roe, et al. 2021. “A Synthetic Hydrogel, VitroGel® ORGANOID-3, Improves Immune Cell-Epithelial Interactions in a Tissue Chip Co-Culture Model of Human Gastric Organoids and Dendritic Cells.” Frontiers in Pharmacology 12. https://doi.org/10.3389/fphar.2021.707891.

Ch’ng, Toh Hean, E. Alexander Flood, and Lynn William Enquist. 2005. “Culturing Primary and Transformed Neuronal Cells for Studying Pseudorabies Virus Infection.” Methods in Molecular Biology 292: 299–316.

Chowdhury, T. T., S. Arghandawi, J. Brand, O. O. Akanji, D. L. Bader, D. M. Salter, and D. A. Lee. 2008. “Dynamic Compression Counteracts IL-1β Induced Inducible Nitric Oxide Synthase and Cyclo-Oxygenase-2 Expression in Chondrocyte/Agarose Constructs.” Arthritis Research & Therapy 10 (2): R35.

Cohen, Efrat M., and Oren Kobiler. 2016. “Gene Expression Correlates with the Number of Herpes Viral Genomes Initiating Infection in Single Cells.” PLoS Pathogens 12 (12): e1006082.

Colombini, Alessandra, F. Libonati, S. Lopa, G. M. Peretti, M. Moretti, and L. de Girolamo. 2022. “Autologous Chondrocyte Implantation Provides Good Long-Term Clinical Results in the Treatment of Knee Osteoarthritis: A Systematic Review.” Knee Surgery, Sports Traumatology, Arthroscopy: Official Journal of the ESSKA, June. https://doi.org/10.1007/s00167-022-07030-2.

Constantino, João, Célia Gomes, Amílcar Falcão, Bruno Miguel Neves, and Maria Teresa Cruz. 2017. “Dendritic Cell-Based Immunotherapy: A Basic Review and Recent Advances.” Immunologic Research 65 (4): 798–810.

Costa, Elisa, Cristina González-García, José Luis Gómez Ribelles, and Manuel Salmerón-Sánchez. 2018. “Maintenance of Chondrocyte Phenotype during Expansion on PLLA Microtopographies.” Journal of Tissue Engineering 9 (August): 2041731418789829.

Cullen, D. Kacy, M. Christian Lessing, and Michelle C. LaPlaca. 2007. “Collagen-Dependent Neurite Outgrowth and Response to Dynamic Deformation in Three-Dimensional Neuronal Cultures.” Annals of Biomedical Engineering 35 (5): 835–46.

Daly, Andrew C., Lindsay Riley, Tatiana Segura, and Jason A. Burdick. 2020. “Hydrogel Microparticles for Biomedical Applications.” Nature Reviews. Materials 5 (1): 20–43.

Danalache, M., R. Kleinert, J. Schneider, A. L. Erler, M. Schwitalle, R. Riester, F. Traub, and U. K. Hofmann. 2019. “Changes in Stiffness and Biochemical Composition of the Pericellular Matrix as a Function of Spatial Chondrocyte Organisation in Osteoarthritic Cartilage.” Osteoarthritis and Cartilage / OARS, Osteoarthritis Research Society 27 (5): 823–32.

Daniel, J. C., B. U. Pauli, and K. E. Kuettner. 1984. “Synthesis of Cartilage Matrix by Mammalian Chondrocytes in Vitro. III. Effects of Ascorbate.” The Journal of Cell Biology 99 (6): 1960–69.

Darling, E. M., S. Zauscher, and F. Guilak. 2006. “Viscoelastic Properties of Zonal Articular Chondrocytes Measured by Atomic Force Microscopy.” Osteoarthritis and Cartilage / OARS, Osteoarthritis Research Society 14 (6): 571–79.

Darling, Eric M., and Kyriacos A. Athanasiou. 2005. “Rapid Phenotypic Changes in Passaged Articular Chondrocyte Subpopulations.” Journal of Orthopaedic Research: Official Publication of the Orthopaedic Research Society 23 (2): 425–32.

Darling, Eric M., Rebecca E. Wilusz, Michael P. Bolognesi, Stefan Zauscher, and Farshid Guilak. 2010. “Spatial Mapping of the Biomechanical Properties of the Pericellular Matrix of Articular Cartilage Measured in Situ via Atomic Force Microscopy.” Biophysical Journal 98 (12): 2848–56.

Davoudi, Zahra, Nathan Peroutka-Bigus, Bryan Bellaire, Michael Wannemuehler, Terrence A. Barrett, Balaji Narasimhan, and Qun Wang. 2018. “Intestinal Organoids Containing Poly(Lactic-Co -Glycolic Acid) Nanoparticles for the Treatment of Inflammatory Bowel Diseases.” Journal of Biomedical Materials Research. Part A 106 (4): 876–86.

Del Dosso, Ashley, Jean-Paul Urenda, Tuan Nguyen, and Giorgia Quadrato. 2020. “Upgrading the Physiological Relevance of Human Brain Organoids.” Neuron 107 (6): 1014–28.

Devarasetty, Mahesh, Andrea R. Mazzocchi, and Aleksander Skardal. 2018. “Applications of Bioengineered 3D Tissue and Tumor Organoids in Drug Development and Precision Medicine: Current and Future.” BioDrugs: Clinical Immunotherapeutics, Biopharmaceuticals and Gene Therapy 32 (1): 53–68.

Drayman, Nir, Parthiv Patel, Luke Vistain, and Savaş Tay. 2019. “HSV-1 Single-Cell Analysis Reveals the Activation of Anti-Viral and Developmental Programs in Distinct Sub-Populations.” ELife 8 (May). https://doi.org/10.7554/eLife.46339.

Duarte, Luisa F., Mónica A. Farías, Diana M. Álvarez, Susan M. Bueno, Claudia A. Riedel, and Pablo A. González. 2019. “Herpes Simplex Virus Type 1 Infection of the Central Nervous System: Insights Into Proposed Interrelationships With Neurodegenerative Disorders.” Frontiers in Cellular Neuroscience 13. https://doi.org/10.3389/fncel.2019.00046.

Duffy, D. C., J. C. McDonald, O. J. Schueller, and G. M. Whitesides. 1998. “Rapid Prototyping of Microfluidic Systems in Poly(Dimethylsiloxane).” Analytical Chemistry 70 (23): 4974–84.

Eschweiler, Joerg, Nils Horn, Bjoern Rath, Marcel Betsch, Alice Baroncini, Markus Tingart, and Filippo Migliorini. 2021. “The Biomechanics of Cartilage-An Overview.” Life 11 (4). https://doi.org/10.3390/life11040302.

Esdaille, Caldon J., Kenyatta S. Washington, and Cato T. Laurencin. 2021. “Regenerative Engineering: A Review of Recent Advances and Future Directions.” Regenerative Medicine 16 (5): 495–512.

Figueiredo, José Antonio Poli de, Audrey Moraes Machado, Vinícius Pasqualotti de Oliveira, Rafael Hartmann, Silvana Beltrami Gonçalves Waltrick, Maristela Gutierrez de Borba, Myrian Câmara Brew, Cyntia Rodrigues de Araújo Estrela, and Daiana Elisabeth Böttcher. 2018. “Dendritic Cells and Their Relation to Apical Peridontitis.” Brazilian Oral Research 32 (suppl 1): e71.

Franz, Clemens M., Gareth E. Jones, and Anne J. Ridley. 2002. “Cell Migration in Development and Disease.” Developmental Cell 2 (2): 153–58.

Franze, Kristian, Paul A. Janmey, and Jochen Guck. 2013. “Mechanics in Neuronal Development and Repair.” Annual Review of Biomedical Engineering 15 (May): 227–51.

Fredrikson, Jacob P., Priyanka P. Brahmachary, Ayten E. Erdoğan, Zachary K. Archambault, James N. Wilking, Ronald K. June, and Connie B. Chang. 2022. “Metabolomic Profiling and Mechanotransduction of Single Chondrocytes Encapsulated in Alginate Microgels.” Cells 11 (5). https://doi.org/10.3390/cells11050900.

Frega, Monica. 2016. “3D Neuronal Networks: State of the Art.” In Neuronal Network Dynamics in 2D and 3D in Vitro Neuroengineered Systems, edited by Monica Frega, 45–57. Cham: Springer International Publishing.

———. n.d. Neuronal Network Dynamics in 2D and 3D in Vitro Neuroengineered Systems. Springer International Publishing. Accessed April 5, 2023.

Gaharwar, Akhilesh K., Irtisha Singh, and Ali Khademhosseini. 2020. “Engineered Biomaterials for in Situ Tissue Regeneration.” Nature Reviews Materials 5 (9): 686–705.

García Alonso, Daniel, Mengchao Yu, Haijun Qu, Liang Ma, and Feng Shen. 2019. “Advances in Microfluidics-Based Technologies for Single Cell Culture.” Advanced Biosystems 3 (11): e1900003.

Gavara, N. (2017). A beginner’s guide to atomic force microscopy probing for cell mechanics. Microscopy Research and Technique, 80(1), 75–84.

Gebauer, M., J. Saas, F. Sohler, J. Haag, S. Söder, M. Pieper, E. Bartnik, J. Beninga, R. Zimmer, and T. Aigner. 2005. “Comparison of the Chondrosarcoma Cell Line SW1353 with Primary Human Adult Articular Chondrocytes with Regard to Their Gene Expression Profile and Reactivity to IL-1beta.” Osteoarthritis and Cartilage / OARS, Osteoarthritis Research Society 13 (8): 697–708.

Gehlen, David B., Niklas Jürgens, Abdolrahman Omidinia-Anarkoli, Tamás Haraszti, Julian George, Andreas Walther, Hua Ye, and Laura De Laporte. 2020. “Granular Cellulose Nanofibril Hydrogel Scaffolds for 3D Cell Cultivation.” Macromolecular Rapid Communications 41 (18): e2000191.

Ghosh, Soham, Adrienne K. Scott, Benjamin Seelbinder, Jeanne E. Barthold, Brittany M. St Martin, Samantha Kaonis, Stephanie E. Schneider, Jonathan T. Henderson, and Corey P. Neu. 2022. “Dedifferentiation Alters Chondrocyte Nuclear Mechanics during in Vitro Culture and Expansion.” Biophysical Journal 121 (1): 131–41.

Griffin, Donald R., Westbrook M. Weaver, Philip O. Scumpia, Dino Di Carlo, and Tatiana Segura. 2015. “Accelerated Wound Healing by Injectable Microporous Gel Scaffolds Assembled from Annealed Building Blocks.” Nature Materials 14 (7): 737–44.

Guerrero, C. R., Garcia, P. D., & Garcia, R. (2019). Subsurface Imaging of Cell Organelles by Force Microscopy. ACS Nano, 13(8), 9629–9637.

Guo, Feng, Sixing Li, Mehmet Umut Caglar, Zhangming Mao, Wu Liu, Andrew Woodman, Jamie J. Arnold, Claus O. Wilke, Tony Jun Huang, and Craig E. Cameron. 2017. “Single-Cell Virology: On-Chip Investigation of Viral Infection Dynamics.” Cell Reports 21 (6): 1692–1704.

Haralabopoulos, G. C., D. S. Grant, H. K. Kleinman, and M. E. Maragoudakis. 1997. “Thrombin Promotes Endothelial Cell Alignment in Matrigel in Vitro and Angiogenesis in Vivo.” The American Journal of Physiology 273 (1 Pt 1): C239-45.

Harris, Michael D., Andrew E. Anderson, Corinne R. Henak, Benjamin J. Ellis, Christopher L. Peters, and Jeffrey A. Weiss. 2012. “Finite Element Prediction of Cartilage Contact Stresses in Normal Human Hips.” Journal of Orthopaedic Research: Official Publication of the Orthopaedic Research Society 30 (7): 1133–39.

Håti, Armend G., David C. Bassett, Jonas M. Ribe, Pawel Sikorski, David A. Weitz, and Bjørn T. Stokke. 2016. “Versatile, Cell and Chip Friendly Method to Gel Alginate in Microfluidic Devices.” Lab on a Chip 16 (19): 3718–27.

Häuselmann, H. J., R. J. Fernandes, S. S. Mok, T. M. Schmid, J. A. Block, M. B. Aydelotte, K. E. Kuettner, and E. J. Thonar. 1994. “Phenotypic Stability of Bovine Articular Chondrocytes after Long-Term Culture in Alginate Beads.” Journal of Cell Science 107 (Pt 1) (January): 17–27.

Heath, Joseph R., and Jill A. Dembowski. 2022. “Fashionably Late: Temporal Regulation of HSV-1 Late Gene Transcription.” PLoS Pathogens 18 (6): e1010536.

Heldt, Frank S., Sascha Y. Kupke, Sebastian Dorl, Udo Reichl, and Timo Frensing. 2015. “Single-Cell Analysis and Stochastic Modelling Unveil Large Cell-to-Cell Variability in Influenza A Virus Infection.” Nature Communications 6 (November): 8938.

Herr, Alix E., Kyle S. Hain, and Matthew P. Taylor. 2017. “Limitations on the Multiplicity of Cellular Infection During Human Alphaherpesvirus Disease.” Current Clinical Microbiology Reports 4 (3): 167–74.

Hoell, T., G. Huschak, A. Beier, G. Hüttmann, Y. Minkus, H. J. Holzhausen, and H. J. Meisel. 2006. “Auto Fluorescence of Intervertebral Disc Tissue: A New Diagnostic Tool.” European Spine Journal: Official Publication of the European Spine Society, the European Spinal Deformity Society, and the European Section of the Cervical Spine Research Society 15 Suppl 3 (Suppl 3): S345-53.

Hu, Hui-Lan, Kalanghad P. Srinivas, Shuoshuo Wang, Moses V. Chao, Timothee Lionnet, Ian Mohr, Angus C. Wilson, Daniel P. Depledge, and Tony T. Huang. 2022. “Single-Cell Transcriptomics Identifies Gadd45b as a Regulator of Herpesvirus-Reactivating Neurons.” EMBO Reports 23 (2): e53543.

Huang, Brian J., Jerry C. Hu, and Kyriacos A. Athanasiou. 2016. “Cell-Based Tissue Engineering Strategies Used in the Clinical Repair of Articular Cartilage.” Biomaterials 98 (August): 1–22.

Huang, S-C, J. C-C Wei, D. J. Wu, and Y-C Huang. 2010. “Vitamin B6 Supplementation Improves Pro-Inflammatory Responses in Patients with Rheumatoid Arthritis.” European Journal of Clinical Nutrition 64 (9): 1007–13.

Hughes, Chris S., Lynne M. Postovit, and Gilles A. Lajoie. 2010. “Matrigel: A Complex Protein Mixture Required for Optimal Growth of Cell Culture.” Proteomics 10 (9): 1886–90.

Iglesias, Pablo A., and Peter N. Devreotes. 2008. “Navigating through Models of Chemotaxis.” Current Opinion in Cell Biology 20 (1): 35–40.

Jacobi, Matthias, Vincent Villa, Robert A. Magnussen, and Philippe Neyret. 2011. “MACI - a New Era?” Sports Medicine, Arthroscopy, Rehabilitation, Therapy & Technology: SMARTT 3 (1): 10.

Jeon, June E., Karsten Schrobback, Christoph Meinert, Viviana Sramek, Dietmar W. Hutmacher, and Travis J. Klein. 2013. “Effect of Preculture and Loading on Expression of Matrix Molecules, Matrix Metalloproteinases, and Cytokines by Expanded Osteoarthritic Chondrocytes.” Arthritis and Rheumatism 65 (9): 2356–67.

Jgamadze, Dennis, Jamie Bergen, Daniel Stone, Jae-Hyung Jang, David V. Schaffer, Ehud Y. Isacoff, and Sophie Pautot. 2012. “Colloids as Mobile Substrates for the Implantation and Integration of Differentiated Neurons into the Mammalian Brain.” PloS One 7 (1): e30293.

Ju, Yo-El, Paul A. Janmey, Margaret E. McCormick, Evelyn S. Sawyer, and Lisa A. Flanagan. 2007. “Enhanced Neurite Growth from Mammalian Neurons in Three-Dimensional Salmon Fibrin Gels.” Biomaterials 28 (12): 2097–2108.

Jutila, Aaron A., Donald L. Zignego, Bradley K. Hwang, Jonathan K. Hilmer, Timothy Hamerly, Cody A. Minor, Seth T. Walk, and Ronald K. June. 2014. “Candidate Mediators of Chondrocyte Mechanotransduction via Targeted and Untargeted Metabolomic Measurements.” Archives of Biochemistry and Biophysics 545 (March): 116–23.

Jutila, Aaron A., Donald L. Zignego, William J. Schell, and Ronald K. June. 2015. “Encapsulation of Chondrocytes in High-Stiffness Agarose Microenvironments for in Vitro Modeling of Osteoarthritis Mechanotransduction.” Annals of Biomedical Engineering 43 (5): 1132–44.

Kane, K. I. W., E. Lucumi Moreno, C. M. Lehr, S. Hachi, R. Dannert, R. Sanctuary, C. Wagner, R. M. T. Fleming, and J. Baller. 2018. “Determination of the Rheological Properties of Matrigel for Optimum Seeding Conditions in Microfluidic Cell Cultures.” AIP Advances 8 (12): 125332.

Kanehisa, Minoru, Miho Furumichi, Yoko Sato, Mari Ishiguro-Watanabe, and Mao Tanabe. 2021. “KEGG: Integrating Viruses and Cellular Organisms.” Nucleic Acids Research 49 (D1): D545–51.

Kastana, Pinelopi, Fatema Tuz Zahra, Despoina Ntenekou, Stamatiki Katraki-Pavlou, Dimitris Beis, Michail S. Lionakis, Constantinos M. Mikelis, and Evangelia Papadimitriou. 2019. “Matrigel Plug Assay for In Vivo Evaluation of Angiogenesis.” Methods in Molecular Biology 1952: 219–32.

Kleinman, Hynda K., and George R. Martin. 2005. “Matrigel: Basement Membrane Matrix with Biological Activity.” Seminars in Cancer Biology 15 (5): 378–86.

Koh, Jaekyung, Donald R. Griffin, Maani M. Archang, An-Chieh Feng, Thomas Horn, Michael Margolis, David Zalazar, Tatiana Segura, Philip O. Scumpia, and Dino Di Carlo. 2019. “Enhanced In Vivo Delivery of Stem Cells Using Microporous Annealed Particle Scaffolds.” Small 15 (39): e1903147.

Kollias, Christina M., Richard B. Huneke, Brian Wigdahl, and Stephen R. Jennings. 2015. “Animal Models of Herpes Simplex Virus Immunity and Pathogenesis.” Journal of Neurovirology 21 (1): 8–23.

Kontomaris, S. V., A. Malamou, and A. Stylianou. 2022. “The Hertzian Theory in AFM Nanoindentation Experiments Regarding Biological Samples: Overcoming Limitations in Data Processing.” Micron 155 (April): 103228.

Kratchmarov, R., L. W. Enquist, and M. P. Taylor. 2015. “Us9-Independent Axonal Sorting and Transport of the Pseudorabies Virus Glycoprotein GM.” Journal of Virology 89 (12): 6511–14.

Kulchar, Rachel J., Bridget R. Denzer, Bharvi M. Chavre, Mina Takegami, and Jennifer Patterson. 2021. “A Review of the Use of Microparticles for Cartilage Tissue Engineering.” International Journal of Molecular Sciences 22 (19): 10292.

Kupke, Sascha Young, Lam-Ha Ly, Stefan Thomas Börno, Alexander Ruff, Bernd Timmermann, Martin Vingron, Stefan Haas, and Udo Reichl. 2020. “Single-Cell Analysis Uncovers a Vast Diversity in Intracellular Viral Defective Interfering RNA Content Affecting the Large Cell-to-Cell Heterogeneity in Influenza A Virus Replication.” Viruses 12 (1). https://doi.org/10.3390/v12010071.

Lancaster, Madeline A., Magdalena Renner, Carol-Anne Martin, Daniel Wenzel, Louise S. Bicknell, Matthew E. Hurles, Tessa Homfray, Josef M. Penninger, Andrew P. Jackson, and Juergen A. Knoblich. 2013. “Cerebral Organoids Model Human Brain Development and Microcephaly.” Nature 501 (7467): 373–79.

Lee, D. A., T. Noguchi, M. M. Knight, L. O’Donnell, G. Bentley, and D. L. Bader. 1998. “Response of Chondrocyte Subpopulations Cultured within Unloaded and Loaded Agarose.” Journal of Orthopaedic Research: Official Publication of the Orthopaedic Research Society 16 (6): 726–33.

Lewis, Michael T., John D. Landua, Homer C. Adams 3rd, and Daniel Medina. 2012. “A Mystery Wrapped in an Enigma: Matrigel Enhancement of Mammary Cell Growth and Morphogenesis.” Journal of Mammary Gland Biology and Neoplasia 17 (2): 99–101.

Li, Guanglei, Melissa J. Simon, Limary M. Cancel, Zhong-Dong Shi, Xinying Ji, John M. Tarbell, Barclay Morrison 3rd, and Bingmei M. Fu. 2010. “Permeability of Endothelial and Astrocyte Cocultures: In Vitro Blood-Brain Barrier Models for Drug Delivery Studies.” Annals of Biomedical Engineering 38 (8): 2499–2511.

Lieleg, Oliver, and Katharina Ribbeck. 2011. “Biological Hydrogels as Selective Diffusion Barriers.” Trends in Cell Biology 21 (9): 543–51.

Liu, Wu, Hongzhang He, and Si-Yang Zheng. 2020. “Microfluidics in Single-Cell Virology: Technologies and Applications.” Trends in Biotechnology 38 (12): 1360–72.

Loveday, Emma Kate, Humberto S. Sanchez, Mallory M. Thomas, and Connie B. Chang. 2022. “Single-Cell Infection of Influenza A Virus Using Drop-Based Microfluidics.” Microbiology Spectrum 10 (5): e0099322.

Loveday, Emma Kate, Geoffrey K. Zath, Dimitri A. Bikos, Zackary J. Jay, and Connie B. Chang. 2021. “Screening of Additive Formulations Enables Off-Chip Drop Reverse Transcription Quantitative Polymerase Chain Reaction of Single Influenza A Virus Genomes.” Analytical Chemistry 93 (10): 4365–73.

Luke Domanico, Matthew Taylor. n.d. “A Dual Fluorescent Recombinant for Live Cell Observation of HSV-1 Replication.”

Ma, Qinyu, Mengmeng Liang, Xiangyu Tang, Fei Luo, and Ce Dou. 2019. “Vitamin B5 Inhibit RANKL Induced Osteoclastogenesis and Ovariectomy Induced Osteoporosis by Scavenging ROS Generation.” American Journal of Translational Research 11 (8): 5008–18.

Mahdieh, Zahra, Michelle D. Cherne, Jacob P. Fredrikson, Barkan Sidar, Humberto S. Sanchez, Connie B. Chang, Diane Bimczok, and James N. Wilking. 2022. “Granular Matrigel: Restructuring a Trusted Extracellular Matrix Material for Improved Permeability.” Biomedical Materials 17 (4). https://doi.org/10.1088/1748-605X/ac7306.

Mahdieh, Zahra, and Andrij Holian. 2020. “Electrospun Fibers Loaded with Ball-milled Poly(N-isopropylacrylamide) Microgel Particles for Smart Delivery Applications.” Journal of Applied Polymer Science 137 (44): 49786.

Mandal, Biman B., and Subhas C. Kundu. 2009. “Cell Proliferation and Migration in Silk Fibroin 3D Scaffolds.” Biomaterials 30 (15): 2956–65.

Mark, K. von der, V. Gauss, H. von der Mark, and P. Müller. 1977. “Relationship between Cell Shape and Type of Collagen Synthesised as Chondrocytes Lose Their Cartilage Phenotype in Culture.” Nature 267 (5611): 531–32.

Mayne, R., M. S. Vail, P. M. Mayne, and E. J. Miller. 1976. “Changes in Type of Collagen Synthesized as Clones of Chick Chondrocytes Grow and Eventually Lose Division Capacity.” Proceedings of the National Academy of Sciences of the United States of America 73 (5): 1674–78.

McCutchen, Carley N., Donald L. Zignego, and Ronald K. June. 2017. “Metabolic Responses Induced by Compression of Chondrocytes in Variable-Stiffness Microenvironments.” Journal of Biomechanics 64 (November): 49–58.

McGuigan, Alison P., Derek A. Bruzewicz, Ana Glavan, Manish J. Butte, and George M. Whitesides. 2008. “Cell Encapsulation in Sub-Mm Sized Gel Modules Using Replica Molding.” PloS One 3 (5): e2258.

McLeod, Morgan A., Rebecca E. Wilusz, and Farshid Guilak. 2013. “Depth-Dependent Anisotropy of the Micromechanical Properties of the Extracellular and Pericellular Matrices of Articular Cartilage Evaluated via Atomic Force Microscopy.” Journal of Biomechanics 46 (3): 586–92.

Mellman, I., and R. M. Steinman. 2001. “Dendritic Cells: Specialized and Regulated Antigen Processing Machines.” Cell 106 (3): 255–58.

Minas, T., and L. Peterson. 1999. “Advanced Techniques in Autologous Chondrocyte Transplantation.” Clinics in Sports Medicine 18 (1): 13–44, v–vi.

Miura, T., and R. Tanaka. 2009. “In Vitro Vasculogenesis Models Revisited - Measurement of VEGF Diffusion in Matrigel.” Mathematical Modelling of Natural Phenomena 4 (4): 118–30.

Miyoshi, Hiroyuki, Rieko Ajima, Christine T. Luo, Terry P. Yamaguchi, and Thaddeus S. Stappenbeck. 2012. “Wnt5a Potentiates TGF-β Signaling to Promote Colonic Crypt Regeneration after Tissue Injury.” Science 338 (6103): 108–13.

Muir, H. 1995. “The Chondrocyte, Architect of Cartilage. Biomechanics, Structure, Function and Molecular Biology of Cartilage Matrix Macromolecules.” BioEssays: News and Reviews in Molecular, Cellular and Developmental Biology 17 (12): 1039–48.

Nabeshima, Kazuki, Teruhiko Inoue, Yoshiya Shimao, and Tetsuro Sameshima. 2002. “Matrix Metalloproteinases in Tumor Invasion: Role for Cell Migration.” Pathology International 52 (4): 255–64.

Nelson, David L., Albert L. Lehninger, and Michael M. Cox. 2008. Lehninger Principles of Biochemistry. Macmillan.

Ng, Laurel, Han-Hwa Hung, Alexander Sprunt, Susan Chubinskaya, Christine Ortiz, and Alan Grodzinsky. 2007. “Nanomechanical Properties of Individual Chondrocytes and Their Developing Growth Factor-Stimulated Pericellular Matrix.” Journal of Biomechanics 40 (5): 1011–23.

Ning, Yongling, Jun Ding, Xiao Sun, Yewen Xie, Mingming Su, Chenglong Ma, Jie Pan, Jie Chen, Hua Jiang, and Chunjian Qi. 2020. “HDAC9 Deficiency Promotes Tumor Progression by Decreasing the CD8+ Dendritic Cell Infiltration of the Tumor Microenvironment.” Journal for Immunotherapy of Cancer 8 (1). https://doi.org/10.1136/jitc-2020-000529.

Noel, Gaelle, Nicholas W. Baetz, Janet F. Staab, Mark Donowitz, Olga Kovbasnjuk, Marcela F. Pasetti, and Nicholas C. Zachos. 2017. “Erratum: A Primary Human Macrophage-Enteroid Co-Culture Model to Investigate Mucosal Gut Physiology and Host-Pathogen Interactions.” Scientific Reports 7 (May): 46790.

Ouyang, Mingxing, Zhili Qian, Bing Bu, Yang Jin, Jiajia Wang, Yiming Zhu, Lei Liu, Yan Pan, and Linhong Deng. 2020. “Sensing Traction Force on the Matrix Induces Cell–Cell Distant

Mechanical Communications for Self-Assembly." ACS Biomaterials Science & Engineering 6 (10): 5833–48.

Pautot, Sophie, Claire Wyart, and Ehud Y. Isacoff. 2008. "Colloid-Guided Assembly of Oriented 3D Neuronal Networks." Nature Methods 5 (8): 735–40.

Pratt, Shawna L., Geoffrey K. Zath, Tatsuya Akiyama, Kerry S. Williamson, Michael J. Franklin, and Connie B. Chang. 2019. "DropSOAC: Stabilizing Microfluidic Drops for Time-Lapse Quantification of Single-Cell Bacterial Physiology." Frontiers in Microbiology 10 (September): 2112.

Qian, Xuyu, Ha Nam Nguyen, Mingxi M. Song, Christopher Hadiono, Sarah C. Ogden, Christy Hammack, Bing Yao, et al. 2016. "Brain-Region-Specific Organoids Using Mini-Bioreactors for Modeling ZIKV Exposure." Cell 165 (5): 1238–54.

Qian, Xuyu, Yijing Su, Christopher D. Adam, Andre U. Deutschmann, Sarshan R. Pather, Ethan M. Goldberg, Kenong Su, et al. 2020. "Sliced Human Cortical Organoids for Modeling Distinct Cortical Layer Formation." Cell Stem Cell 26 (5): 766-781.e9.

Rafael, Dor, Enosh Tomer, and Oren Kobiler. 2022. "A Single Herpes Simplex Virus 1 Genome Reactivates from Individual Cells." Microbiology Spectrum 10 (4): e0114422.

Randau, Thomas M., Frank A. Schildberg, Mauro Alini, Matthias D. Wimmer, El-Mustapha Haddouti, Sascha Gravius, Keita Ito, and Martin J. Stoddart. 2013. "The Effect of Dexamethasone and Triiodothyronine on Terminal Differentiation of Primary Bovine Chondrocytes and Chondrogenically Differentiated Mesenchymal Stem Cells." PloS One 8 (8): e72973.

Ranga, A., S. Gobaa, Y. Okawa, K. Mosiewicz, A. Negro, and M. P. Lutolf. 2014. "3D Niche Microarrays for Systems-Level Analyses of Cell Fate." Nature Communications 5 (July): 4324.

Ranga, Adrian, Nikolche Gjorevski, and Matthias P. Lutolf. 2014. "Drug Discovery through Stem Cell-Based Organoid Models." Advanced Drug Delivery Reviews 69–70 (April): 19–28.

Rigacci, Luigi, Renato Alterini, Pietro Antonio Bernabei, Pierluigi Rossi Ferrini, Giovanni Agati, Franco Fusi, and Monica Monici. 2007. "Multispectral Imaging Autofluorescence Microscopy for the Analysis of Lymph-Node Tissues." Photochemistry and Photobiology 71 (6): 737–42.

Riley, Lindsay, Lucas Schirmer, and Tatiana Segura. 2019. "Granular Hydrogels: Emergent Properties of Jammed Hydrogel Microparticles and Their Applications in Tissue Repair and Regeneration." Current Opinion in Biotechnology 60 (December): 1–8.

Roizman, Bernard, and Guoying Zhou. 2015. "The 3 Facets of Regulation of Herpes Simplex Virus Gene Expression: A Critical Inquiry." Virology 479–480 (May): 562–67.

Rueden, Curtis T., Johannes Schindelin, Mark C. Hiner, Barry E. DeZonia, Alison E. Walter, Ellen T. Arena, and Kevin W. Eliceiri. 2017. “ImageJ2: ImageJ for the next Generation of Scientific Image Data.” BMC Bioinformatics 18 (1): 529.

Russell, Alistair B., Elizaveta Elshina, Jacob R. Kowalsky, Aartjan J. W. Te Velthuis, and Jesse D. Bloom. 2019. “Single-Cell Virus Sequencing of Influenza Infections That Trigger Innate Immunity.” Journal of Virology 93 (14). https://doi.org/10.1128/JVI.00500-19.

Russell, Alistair B., Cole Trapnell, and Jesse D. Bloom. 2018. “Extreme Heterogeneity of Influenza Virus Infection in Single Cells.” ELife 7 (February). https://doi.org/10.7554/eLife.32303.

Sachs, Norman, Angelos Papaspyropoulos, Domenique D. Zomer-van Ommen, Inha Heo, Lena Böttinger, Dymph Klay, Fleur Weeber, et al. 2019. “Long-Term Expanding Human Airway Organoids for Disease Modeling.” The EMBO Journal 38 (4): e100300.

Sader, J. E., Chon, J. W. M., & Mulvaney, P. (1999). Calibration of rectangular atomic force microscope cantilevers. The Review of Scientific Instruments, 70(10), 3967–3969.

Safiri, Saeid, Ali-Asghar Kolahi, Emma Smith, Catherine Hill, Deepti Bettampadi, Mohammad Ali Mansournia, Damian Hoy, et al. 2020. “Global, Regional and National Burden of Osteoarthritis 1990-2017: A Systematic Analysis of the Global Burden of Disease Study 2017.” Annals of the Rheumatic Diseases 79 (6): 819–28.

Salinas, Daniel, Brendan M. Mumey, and Ronald K. June. 2019. “Physiological Dynamic Compression Regulates Central Energy Metabolism in Primary Human Chondrocytes.” Biomechanics and Modeling in Mechanobiology 18 (1): 69–77.

Scheffold, Frank. 2020. “Pathways and Challenges towards a Complete Characterization of Microgels.” Nature Communications 11 (1): 4315.

Schmitz, Christian H. J., Amy C. Rowat, Sarah Köster, and David A. Weitz. 2009. “Dropspots: A Picoliter Array in a Microfluidic Device.” Lab on a Chip 9 (1): 44–49.

Schneider, Caroline A., Wayne S. Rasband, and Kevin W. Eliceiri. 2012. “NIH Image to ImageJ: 25 Years of Image Analysis.” Nature Methods 9 (7): 671–75.

Sciambi, Adam, and Adam R. Abate. 2015. “Accurate Microfluidic Sorting of Droplets at 30 KHz.” Lab on a Chip 15 (1): 47–51.

Sebrell, T. Andrew, Barkan Sidar, Rachel Bruns, Royce A. Wilkinson, Blake Wiedenheft, Paul J. Taylor, Brian A. Perrino, Linda C. Samuelson, James N. Wilking, and Diane Bimczok. 2018. “Live Imaging Analysis of Human Gastric Epithelial Spheroids Reveals Spontaneous Rupture, Rotation and Fusion Events.” Cell and Tissue Research 371 (2): 293–307.

Sebrell, Thomas A., Marziah Hashimi, Barkan Sidar, Royce A. Wilkinson, Liliya Kirpotina, Mark T. Quinn, Zeynep Malkoç, Paul J. Taylor, James N. Wilking, and Diane Bimczok. 2019. "A Novel Gastric Spheroid Co-Culture Model Reveals Chemokine-Dependent Recruitment of Human Dendritic Cells to the Gastric Epithelium." Cellular and Molecular Gastroenterology and Hepatology 8 (1): 157-171.e3.

Shaw, Leslie M. 2005. "Tumor Cell Invasion Assays." Methods in Molecular Biology 294: 97–105.

Shipley, Mackenzie M., Colleen A. Mangold, Chad V. Kuny, and Moriah L. Szpara. 2017. "Differentiated Human SH-SY5Y Cells Provide a Reductionist Model of Herpes Simplex Virus 1 Neurotropism." Journal of Virology 91 (23). https://doi.org/10.1128/JVI.00958-17.

Sidar, Barkan, Brittany R. Jenkins, Sha Huang, Jason R. Spence, Seth T. Walk, and James N. Wilking. 2019. "Long-Term Flow through Human Intestinal Organoids with the Gut Organoid Flow Chip (GOFlowChip)." Lab on a Chip 19 (20): 3552–62.

Simpson, Caitlin, Sung Sik Lee, Chang-Soo Lee, and Yohei Yamauchi. 2018. "Microfluidics: An Untapped Resource in Viral Diagnostics and Viral Cell Biology." Current Clinical Microbiology Reports 5 (4): 245–51.

Smith, B. D., G. R. Martin, E. J. Miller, A. Dorfman, and R. Swarm. 1975. "Nature of the Collagen Synthesized by a Transplanted Chondrosarcoma." Archives of Biochemistry and Biophysics 166 (1): 181–86.

Sophia Fox, Alice J., Asheesh Bedi, and Scott A. Rodeo. 2009. "The Basic Science of Articular Cartilage: Structure, Composition, and Function." Sports Health 1 (6): 461–68.

Stoddart, M. J., L. Ettinger, and H. J. Häuselmann. 2006. "Generation of a Scaffold Free Cartilage-like Implant from a Small Amount of Starting Material." Journal of Cellular and Molecular Medicine 10 (2): 480–92.

Stokke, Bjørn T., Kurt I. Draget, Olav Smidsrød, Yoshiaki Yuguchi, Hiroshi Urakawa, and Kanji Kajiwara. 2000. "Small-Angle X-Ray Scattering and Rheological Characterization of Alginate Gels. 1. Ca−Alginate Gels." Macromolecules 33 (5): 1853–63.

Sugimoto, Shinya, and Toshiro Sato. 2017. "Establishment of 3D Intestinal Organoid Cultures from Intestinal Stem Cells." In 3D Cell Culture: Methods and Protocols, edited by Zuzana Koledova, 97–105. New York, NY: Springer New York.

Sun, Jiayi, J. Cristobal Vera, Jenny Drnevich, Yen Ting Lin, Ruian Ke, and Christopher B. Brooke. 2020. "Single Cell Heterogeneity in Influenza A Virus Gene Expression Shapes the Innate Antiviral Response to Infection." PLoS Pathogens 16 (7): e1008671.

Sun, Yingmin, and Qiurong Ding. 2017. "Genome Engineering of Stem Cell Organoids for Disease Modeling." Protein & Cell 8 (5): 315–27.

Takebe, Takanori, and James M. Wells. 2019. “Organoids by Design.” Science 364 (6444): 956–59.

Tao, Ye, Assaf Rotem, Huidan Zhang, Connie B. Chang, Anindita Basu, Abimbola O. Kolawole, Stephan A. Koehler, et al. 2015. “Rapid, Targeted and Culture-Free Viral Infectivity Assay in Drop-Based Microfluidics.” Lab on a Chip 15 (19): 3934–40.

Tao, Ye, Assaf Rotem, Huidan Zhang, Shelley K. Cockrell, Stephan A. Koehler, Connie B. Chang, Lloyd W. Ung, et al. 2015. “Artifact-Free Quantification and Sequencing of Rare Recombinant Viruses by Using Drop-Based Microfluidics.” Chembiochem: A European Journal of Chemical Biology 16 (15): 2167–71.

Team, R. D. C. 2009. “A Language and Environment for Statistical Computing.” Http://Www.R-Project.Org. https://cir.nii.ac.jp/crid/1570854175843385600.

Theberge, Ashleigh B., Fabienne Courtois, Yolanda Schaerli, Martin Fischlechner, Chris Abell, Florian Hollfelder, and Wilhelm T. S. Huck. 2010. “Microdroplets in Microfluidics: An Evolving Platform for Discoveries in Chemistry and Biology.” Angewandte Chemie 49 (34): 5846–68.

Tierney, Wesley M., Ian A. Vicino, Stella Y. Sun, Wah Chiu, Esteban A. Engel, Matthew P. Taylor, and Ian B. Hogue. 2022. “Methods and Applications of Campenot Trichamber Neuronal Cultures for the Study of Neuroinvasive Viruses.” Methods in Molecular Biology 2431: 181–206.

Timm, Andrea, and John Yin. 2012. “Kinetics of Virus Production from Single Cells.” Virology 424 (1): 11–17.

Tinevez, Jean-Yves, Nick Perry, Johannes Schindelin, Genevieve M. Hoopes, Gregory D. Reynolds, Emmanuel Laplantine, Sebastian Y. Bednarek, Spencer L. Shorte, and Kevin W. Eliceiri. 2017. “TrackMate: An Open and Extensible Platform for Single-Particle Tracking.” Methods 115 (February): 80–90.

Tomasetti, Luise, Renate Liebl, Daniel S. Wastl, and Miriam Breunig. 2016. “Influence of PEGylation on Nanoparticle Mobility in Different Models of the Extracellular Matrix.” European Journal of Pharmaceutics and Biopharmaceutics: Official Journal of Arbeitsgemeinschaft Fur Pharmazeutische Verfahrenstechnik e.V 108 (November): 145–55.

Utech, Stefanie, Radivoje Prodanovic, Angelo S. Mao, Raluca Ostafe, David J. Mooney, and David A. Weitz. 2015. “Microfluidic Generation of Monodisperse, Structurally Homogeneous Alginate Microgels for Cell Encapsulation and 3D Cell Culture.” Advanced Healthcare Materials 4 (11): 1628–33.

Vacanti, J. P., and R. Langer. 1999. “Tissue Engineering: The Design and Fabrication of Living Replacement Devices for Surgical Reconstruction and Transplantation.” The Lancet 354 Suppl 1 (July): SI32-4.

Van Pul, K. M., M. F. Fransen, and R. Van de Ven. 2021. “Immunotherapy Goes Local: The Central Role of Lymph Nodes in Driving Tumor Infiltration and Efficacy.” Frontiers In. https://www.frontiersin.org/articles/10.3389/fimmu.2021.643291/full?&utm_source=Email_to_authors_&utm_medium=Email&utm_content=T1_11.5e1_author&utm_campaign=Email_publication&field=&journalName=Frontiers_in_Immunology&id=643291.

Wake, Hidenori, Shuji Mori, Keyue Liu, Hideo K. Takahashi, and Masahiro Nishibori. 2009. “Histidine-Rich Glycoprotein Inhibited High Mobility Group Box 1 in Complex with Heparin-Induced Angiogenesis in Matrigel Plug Assay.” European Journal of Pharmacology 623 (1–3): 89–95.

Wang, Chi-Yun, Zong-Keng Kuo, Ming-Kai Hsieh, Ling-Yi Ke, Chih-Chen Chen, Chao-Min Cheng, and Po-Liang Lai. 2019. “Cell Migration of Preosteoblast Cells on a Clinical Gelatin Sponge for 3D Bone Tissue Engineering.” Biomedical Materials 15 (1): 015005.

Wang, Jiuling, Ruiliang Chu, Na Ni, and Guoxin Nan. 2020. “The Effect of Matrigel as Scaffold Material for Neural Stem Cell Transplantation for Treating Spinal Cord Injury.” Scientific Reports 10 (1): 2576.

Wickham, H. n.d. “Tidyverse: Easily Install and Load the ‘Tidyverse’. 2017.” Accessed March 1, 2022. https://tidyverse.tidyverse.org/.

Widener, Adrienne E., Mallika Bhatta, Thomas E. Angelini, and Edward A. Phelps. 2021. “Guest–Host Interlinked PEG-MAL Granular Hydrogels as an Engineered Cellular Microenvironment.” Biomaterials Science 9 (7): 2480–93.

Wilking, J. N., S. M. Graves, C. B. Chang, K. Meleson, M. Y. Lin, and T. G. Mason. 2006. “Dense Cluster Formation during Aggregation and Gelation of Attractive Slippery Nanoemulsion Droplets.” Physical Review Letters 96 (1): 015501.

Wilson, Angus C. 2022. “Impact of Cultured Neuron Models on α-Herpesvirus Latency Research.” Viruses 14 (6). https://doi.org/10.3390/v14061209.

Wilusz, Rebecca E., Johannah Sanchez-Adams, and Farshid Guilak. 2014. “The Structure and Function of the Pericellular Matrix of Articular Cartilage.” Matrix Biology: Journal of the International Society for Matrix Biology 39 (October): 25–32.

Witten, Jacob, and Katharina Ribbeck. 2017. “The Particle in the Spider’s Web: Transport through Biological Hydrogels.” Nanoscale 9 (24): 8080–95.

Worbs, Tim, Swantje I. Hammerschmidt, and Reinhold Förster. 2017. “Dendritic Cell Migration in Health and Disease.” Nature Reviews. Immunology 17 (1): 30–48.

Xia, Pengfei, Kunxi Zhang, Yan Gong, Guifei Li, Shifeng Yan, and Jingbo Yin. 2017. “Injectable Stem Cell Laden Open Porous Microgels That Favor Adipogenesis: In Vitro and in Vivo Evaluation.” ACS Applied Materials & Interfaces 9 (40): 34751–61.

Xu, Yufan, Hongjia Zhu, Akhila Denduluri, Yangteng Ou, Nadia A. Erkamp, Runzhang Qi, Yi Shen, and Tuomas P. J. Knowles. 2022. “Recent Advances in Microgels: From Biomolecules to Functionality.” Small 18 (34): e2200180.

Yao, Ming-Hao, Jie Yang, Ji-Tao Song, Dong-Hui Zhao, Ming-Shuo Du, Yuan-Di Zhao, and Bo Liu. 2014. “Directed Self-Assembly of Polypeptide-Engineered Physical Microgels for Building Porous Cell-Laden Hydrogels.” Chemical Communications 50 (66): 9405–8.

Yu, Xinzi, and Laura M. Machesky. 2012. “Cells Assemble Invadopodia-like Structures and Invade into Matrigel in a Matrix Metalloprotease Dependent Manner in the Circular Invasion Assay.” PloS One 7 (2): e30605.

Yuguchi, Y., H. Urakawa, K. Kajiwara, K. I. Draget, and B. T. Stokke. 2000. “Small-Angle X-Ray Scattering and Rheological Characterization of Alginate Gels. 2. Time-Resolved Studies on Ionotropic Gels.” Journal of Molecular Structure 554 (1): 21–34.

Zath, Geoffrey K., Ralph A. Sperling, Carter W. Hoffman, Dimitri A. Bikos, Reha Abbasi, Adam R. Abate, David A. Weitz, and Connie B. Chang. 2022. “Rapid Parallel Generation of a Fluorescently Barcoded Drop Library from a Microtiter Plate Using the Plate-Interfacing Parallel Encapsulation (PIPE) Chip.” Lab on a Chip 22 (23): 4735–45.

Zelenski, Nicole A., Holly A. Leddy, Johannah Sanchez-Adams, Jinzi Zhang, Paolo Bonaldo, Wolfgang Liedtke, and Farshid Guilak. 2015. “Type VI Collagen Regulates Pericellular Matrix Properties, Chondrocyte Swelling, and Mechanotransduction in Mouse Articular Cartilage.” Arthritis & Rheumatology (Hoboken, N.J.) 67 (5): 1286–94.

Zhai, Guangju. 2019. “Alteration of Metabolic Pathways in Osteoarthritis.” Metabolites 9 (1). https://doi.org/10.3390/metabo9010011.

Zhang, Huidan, Shelley K. Cockrell, Abimbola O. Kolawole, Assaf Rotem, Adrian W. R. Serohijos, Connie B. Chang, Ye Tao, et al. 2015. “Isolation and Analysis of Rare Norovirus Recombinants from Coinfected Mice Using Drop-Based Microfluidics.” Journal of Virology 89 (15): 7722–34.

Zhang, Zijun. 2015. “Chondrons and the Pericellular Matrix of Chondrocytes.” Tissue Engineering. Part B, Reviews 21 (3): 267–77.

Zhu, Ying, Andrew Yongky, and John Yin. 2009. “Growth of an RNA Virus in Single Cells Reveals a Broad Fitness Distribution.” Virology 385 (1): 39–46.

Zignego, Donald L., Jonathan K. Hilmer, Brian Bothner, William J. Schell, and Ronald K. June. 2019. “Primary Human Chondrocytes Respond to Compression with Phosphoproteomic Signatures That Include Microtubule Activation.” Journal of Biomechanics 97 (December): 109367.

Zignego, Donald L., Jonathan K. Hilmer, and Ronald K. June. 2015. “Mechanotransduction in Primary Human Osteoarthritic Chondrocytes Is Mediated by Metabolism of Energy, Lipids, and Amino Acids.” Journal of Biomechanics 48 (16): 4253–61.

Zignego, Donald L., Aaron A. Jutila, Martin K. Gelbke, Daniel M. Gannon, and Ronald K. June. 2014. “The Mechanical Microenvironment of High Concentration Agarose for Applying Deformation to Primary Chondrocytes.” Journal of Biomechanics 47 (9): 2143–48.